Analysis of Shale-Water Interactions and Flowback Water Chemistry for Fracture Characterization

By

Ashkan Zolfaghari Sharak

A THESIS SUBMITTED IN PARTIAL FULFILLMENT OF
THE REQUIREMENTS FOR THE DEGREE OF

DOCTOR OF PHILOSOPHY

in

Petroleum Engineering

Department of Civil and Environmental Engineering

UNIVERSITY OF ALBERTA

Abstract

Unconventional hydrocarbon resources such as tight and shale reservoirs have become an additional source of oil and gas. Recent developments in hydraulic fracturing and horizontal drilling technologies have paved the way toward economic exploitation of these unconventional resources. The induced fracture network by hydraulic fracturing operations facilitates hydrocarbon flow to wellbore. Fracture network characterization is essential for evaluation of future hydrocarbon production. There are several fracture characterization methods such as rate-transient-analysis, pressure-transient-analysis, microseismic analysis, and tracer analysis. Each of these methods have their own pros and cons. This study aims at interpretation of flowback chemical data by conducting shale-water interaction experiments. The primary focus of this research is to investigate the source of ions in the flowback water. This study also investigates the possibility of fracture network characterization by interpretation of the laboratory and field data of ion concentration.

Extensive imbibition experiments are performed to investigate shale-water interactions at different conditions. Effects of rock-surface area, rock volume, temperature, and pressure are investigated on the ion concentration during the imbibition experiments. The experimental results of ion concentration are compared with the flowback chemical data to characterize the fracture network complexity, fracture surface area (A_f), and invaded reservoir volume (IRV).

Experimental results indicate that the barium ions in the flowback water of wells drilled in the Horn River Basin (HRB) are primarily originated from natural fractures. The results from this study suggest that the barium ion concentration profile during the flowback process is a signature of the connectivity between the natural fractures and the induced primary fractures. The well with a steep increase in the barium concentration profile has a more complex fracture network compared with the well with a slow increase in the barium concentration profile and a more simple fracture network. Furthermore, a model is proposed to characterize the fracture network complexity using flowback salt concentration transient. According to the model results and during the flowback process, the wells with a continuous increase in their salinity profile have more complex fracture network as opposed to the wells with a plateau in their salinity profile. Comparison between the ion concentration data in the flowback water and in the seawater suggests that Na^+, Cl^-, and Mg^{2+}

ions primary originate from formation water, while dissolution of rock constituents in the fracturing fluid is potentially the major source of K^+ and Ca^{2+} ions in the flowback water.

Experimental results indicate that the total ion produced (TIP) increases by increasing rock surface area, rock volume, and temperature, while pressure has negligible impact on TIP. A scale-up procedure is proposed to estimate A_f and IRV using the experimental results of ion concentration during the imbibition experiments. The estimated A_f values for two wells completed in the HRB are $\approx 5 \times 10^6 m^2$ which have similar orders of magnitude to those calculated from rate-transient analysis ($\approx 10^6 m^2$). The estimated IRV values for the target wells are about $5 \times 10^5 m^3$. The well with higher estimated IRV value has lower water recovery in the field as opposed to the well with lower estimated IRV value and higher water recovery in the field.

A modified water sorption isotherm is proposed (a) to investigate the role of clays on water adsorption and desorption and (b) to characterize the organic and inorganic pore size distributions ($PSDs$) of gas shales. Experimental results indicate that clays tend to adsorb and retain most of the capacity for water at low relative humidity conditions. Moreover, hydrophilic pores have wider $PSDs$ compared with those of hydrophobic pores. Also, majority of the hydrophobic pores are smaller than 5 nm, while majority of the large pores (>10 nm) belong to the hydrophilic pore system.

Preface

All or parts of Chapters 2, 4, 6, and 7 have been published as peer reviewed journal papers. Chapter 2 is published in Journal of Unconventional Oil and Gas Resources (Zolfaghari et al., 2016a), Chapter 4 is published in SPE Journal (Zolfaghari et al., 2016b), and Chapters 6 and 7 are published in International Journal of Coal Geology (Zolfaghari et al., 2017a,b). The contents of Chapter 5 is submitted for publication in SPE Journal in March 2018. Chapter 3 is the extension of a SPE conference paper (SPE-175154-MS), and is ready for submission to a peer-review journal. All or parts of the published/submitted journal papers were initially published/highlighted in international/national conferences or non-peer reviewed journals, and they are: Zolfaghari et al. 2014a,b; Zolfaghari and Dehghanpour, 2015 a,b; Zolfaghari et al., 2015a-c; Zolfaghari et al., 2017c; Binazadeh et al., 2015; and Yassin et al., 2017.

I was responsible for experimental design, running the experiments, model development, computer programming, writing, and editing the papers. My co-authors were responsible for providing relevant data from their respective companies, helping me with the experiments, providing useful comments and discussions on field practices, and reviewing the manuscript drafts. The necessary approvals to include the journal papers as chapters in this work are provided in sequential order in the Copyright Permissions section.

Dedication

I would like to dedicate this work to

my beautiful, caring, and loving wife, Fatemeh, for her love, kindness, patience, and endless supports.

my parents and my brother for their unconditional love, encouragements, and ultimate supports.

Acknowledgement

I would like to express my special thanks to my advisor Dr. Hassan Dehghanpour. Hassan, you have been a tremendous mentor for me. I would like to thank you for encouraging my research and for allowing me to grow as a research scientist. Your advice on both research as well as on my career has been invaluable.

I would like to also thank my supervisory committee members, Dr. Juliana Leung and Dr. Daniel Alessi for their guidance through this work. The discussion, ideas, and feedback have been absolutely invaluable.

I would like to thank Mr. Doug Bearinger for his thoughtful technical advices to improve this work.

I am grateful to Alberta Innovates Technology Futures, Vanier Canada Graduate Scholarship Committee, Natural Resources Canada, Natural Sciences and Engineering Research Council of Canada, FMC Technologies, and Nexen Energy ULC for providing field data and financial support for this work.

I would like to appreciate my colleagues (Yingkun Fu, Obinna Ezulike, Yanmin Xu, Ali Habibi, Mahmood Yassin, Lin Yuan, Momotaj Begum, Hamidreza Yarveicy, Ali Javaheri, Son Tran, Khan Athar, Tobi Adefidipe, Mingxiang Xu, Serge Pegov, Sara Eghbali, Ebrahim Ghanbari, Mahdie Mojarad, Mojtaba Binazadeh, Taregh Soleiman Asl, Mike Noel, Jordan Holyk, Jia He, Qing Lan) for their insightful contributions and fruitful discussions. Also, I appreciate the help of Mr. Todd Kinnee, our lab technician for helping me in my experiments. I am also thankful to the administrative staff members of the civil and environmental engineering department (Anne Jones, Arlene Figley, Jomana Haymour and Trina Cattral) for helping me through this journey.

Table of Content

List of Figures

List of Tables

Chapter 1

General Literature

1.1. Overview

This part of the chapter briefly describes the key technologies and common field practices mentioned in Chapters 2-7.

1.1.1. Unconventional Reservoirs

Unconventional reservoirs usually refer to gas and oil shales, tight oil and gas, coalbed methane, oil sands, and gas-hydrate deposits. Figure 1-1 compares the conventional and unconventional reservoir rocks based on the rock matrix permeability.

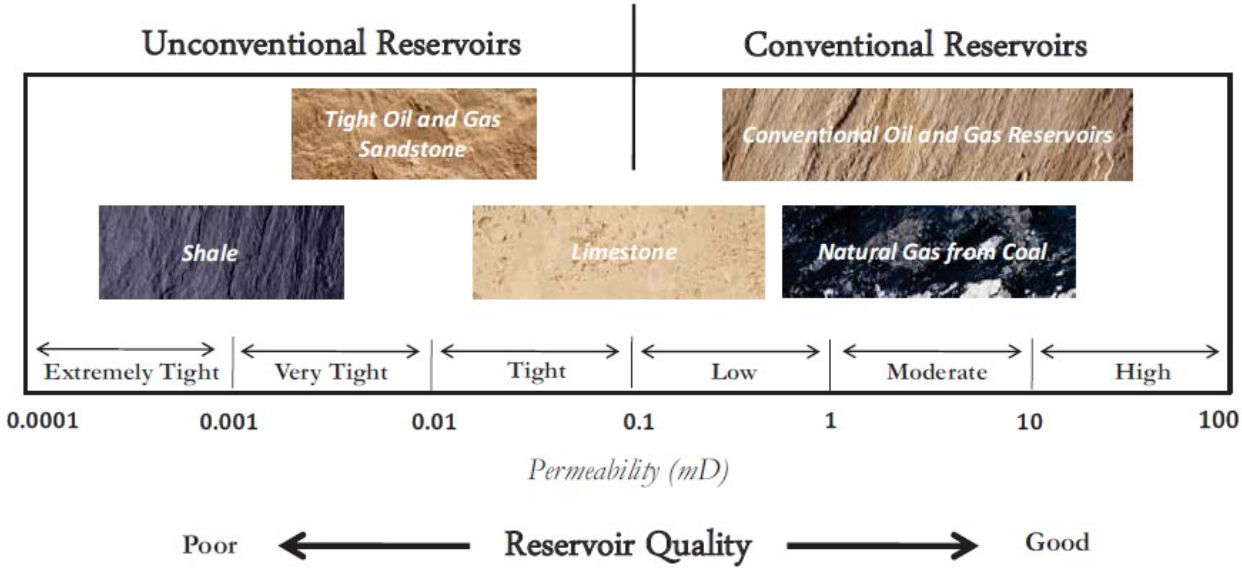

Figure 1-1. Categorization of conventional and unconventional reservoirs based on the rock matrix permeability (Understanding Tight Oil, 2012).

The experiments and field results presented in this study belong to gas shale samples/reservoirs. According to Figure 1-1, gas shales are categorized among very/extremely tigh rocks with approximate matrix permeability of smaller than 0.005 mD.

Figure 1-2 shows the geographical distribution of major unconventional basins in North America. Major basins are mainly concentrated in central and south part of the United States and the Western Canadian Sedimentary Basin. The shale rock and water samples used in this study

belong to the Horn River Basin, which is located in the north eastern part of British Columbia, Canada (shown in red circle on Figure 1-2).

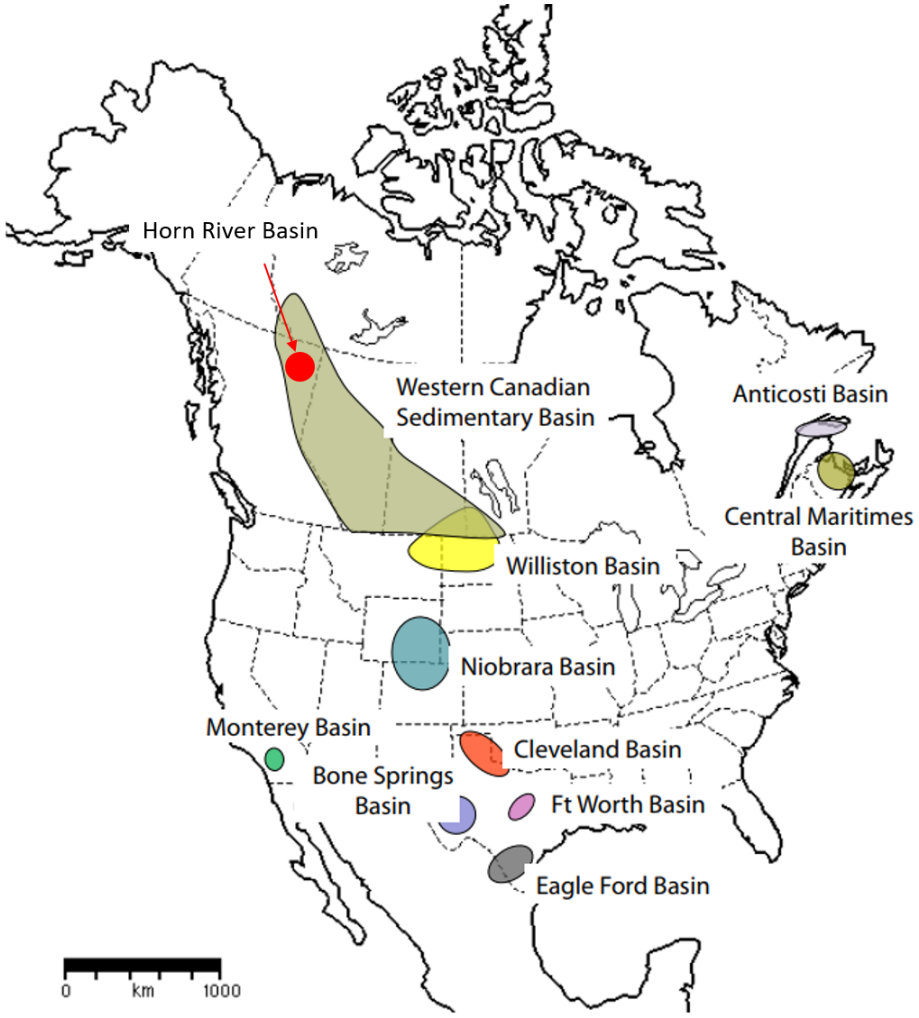

Figure 1-2. Geographical distribution of major unconventional basins in North America (Canadian Society for Unconventional Resources, 2011). The approximate location of the Horn River Basing is shown by the red circle, and is added to the original map.

1.1.2. Horizontal Drilling and Multi-Stage Hydraulic Fracturing

Hydrocarbon recovery from unconventional resources such as shale reservoirs is challenging mainly because of their low permeability and porosity. Recent developments in horizontal drilling and multi-stage hydraulic fracturing operations (Figure 1-3) have paved the way for economic exploitation of these resources.

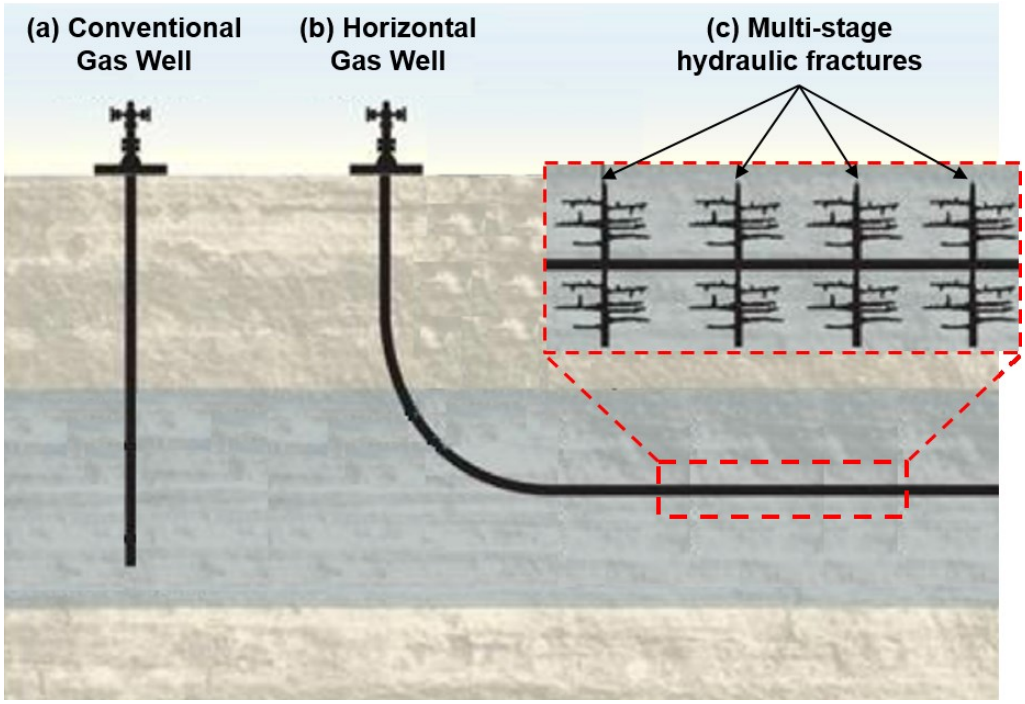

Figure 1-3. Schematic cross-sectional view of (a) a conventional vertical well and (b) a horizontal well (Clover Global Solutions, 2012). The original image is modified to depict (c) the top view of the multi-stage hydraulic fractures.

Horizontal drilling, and in general "directional drilling", refers to practice of drilling non-vertical wells. Horizontal drilling can be done in three general steps of (i) vertical drilling until the wellbore reaches to a point above the target pay zone, (ii) kick off and start the directional drilling until the wellbore runs into the pay zone horizontally, and (iii) drilling horizontally to the desired target length.

Horizontal drilling is of great interest especially for thin pay zones as this technology provides more contact area between the wellbore and the target reservoir (Ezulike, 2017).

Additionally, horizontal drilling reduces the associated environmental footprints of the hydrocarbon recovery (i.e., fewer wells and access roads and less surface disruption).

Multi-state hydraulic fracturing is a common practice to ensure economic exploitation of unconventional gas/oil shale reservoirs. During hydraulic fracturing operations, high pressure fracturing fluid (usually water) is injected into the reservoir to create fractures. The induced fracture network acts as an artificial pipeline system facilitating hydrocarbon flow from low-permeable matrix to the wellbore. During fracturing operations, in addition to induction of new hydraulic fractures, pre-existing natural fractures (Gale, 2014) may also reactivated. In other words, fracturing operations creates a complex network of primary (i.e., induced hydraulic) fractures and secondary (i.e., natural) fractures.

Multi-stage fracturing is a wide spread completion practice to create a network of fractures along the horizontal well. Fracturing usually starts from the toe of the horizontal section of the well, and ends with the heel. Majority of the wells have minimum of 10 fracturing stages per well (Figure 1-4a), and the number of fracturing stages per well is increasing over time (Figure 1-4b).

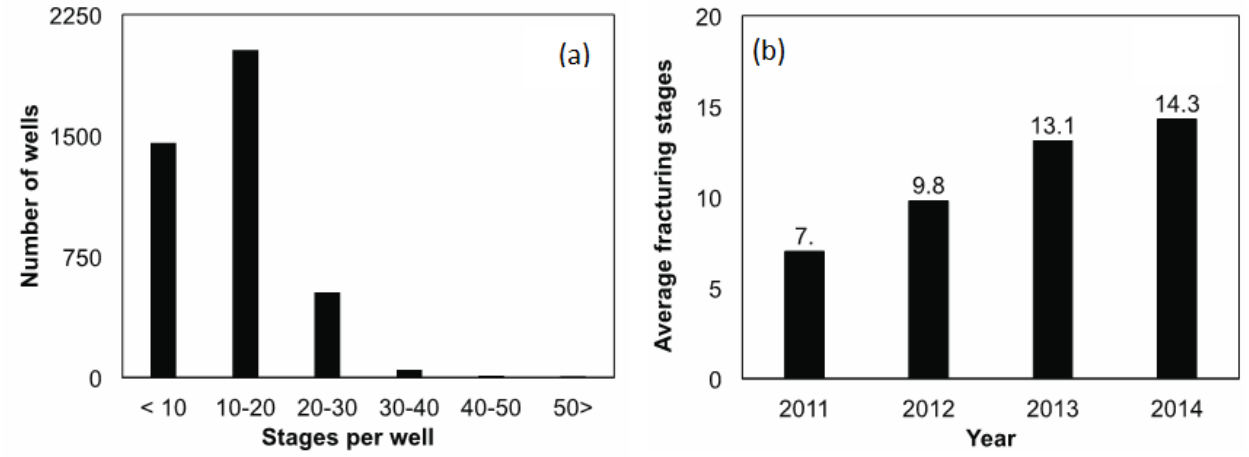

Figure 1-4. (a) Number of wells versus hydraulic fracturing stages per well, and (b) average number of fracturing stages per well by year (Alessi et al., 2017). The reported data in this figure belong to wells completed in Alberta and British Columbia between November 2011 and March 2014.

1.1.3. Fracturing Process

During fracturing operations, a relatively large amount of water, proppants, and chemical additives are injected into the reservoir to create fractures. The total injected volume (TIV) depends on the rock mineralogy, completion practice, and surface facilities. Figure 1-5 shows the geographical distribution of TIV for wells drilled in in Alberta and British Columbia between November 2011 and March 2014. The target wells in this study belong to the Horn River Basin, where the TIV is generally greater than 10000 m^3.

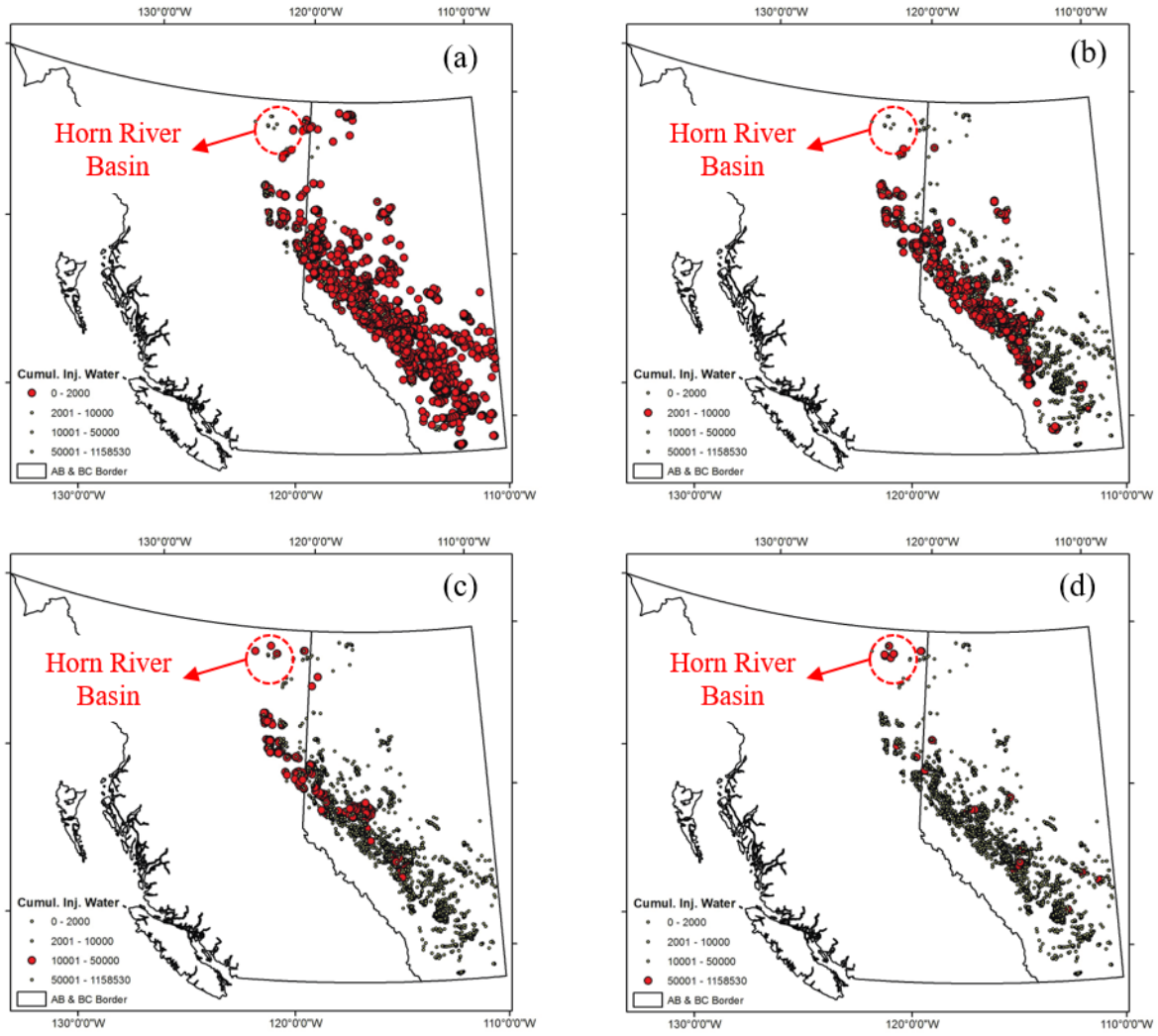

Figure 1-5. Distribution of the TIV per well for wells completed in Alberta and British Columbia between November 2011 and March 2014 (Alessi et al., 2017). (a) $TIV = 1 - 2{,}000\ m^3$, (b)

$TIV = 2001 - 10{,}000\ m^3$, (c) $TIV = 10{,}001 - 50{,}000\ m^3$, and (d) $TIV > 50{,}000\ m^3$. The original maps are modified to depict the approximate location of Horn River Basin.

Fracturing fluids contain proppants (usually silica sand or ceramics) to keep the fractures open. More specifically, fracture pressure drops during the shut-in and production periods (Ezulike, 2017), which can lead to fracture closure (Ezulike, 2017). In order to keep the fractures open, proppants (Figure 1-6) are added to the fracturing fluid to wedge the fractures. One of the main properties of the fracturing fluid is the ability to transport the proppants to fractures. As a general rule of thumb, increasing the viscosity of fracturing fluid increases it ability to transport the proppants (Ezulike, 2017).

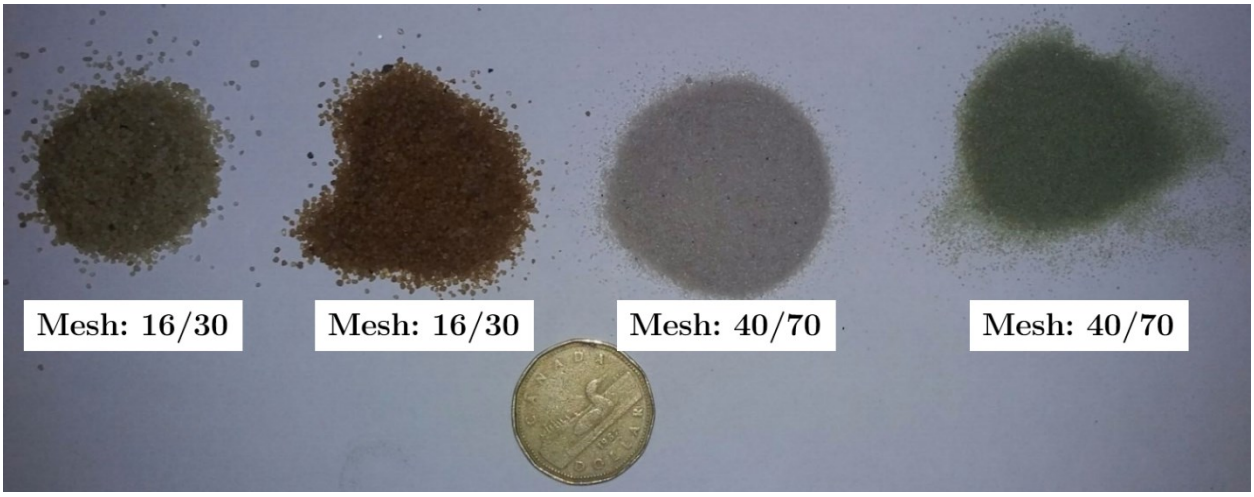

Figure 1-6. Proppants of different sizes used in hydraulic fracturing operations to keep the fractures open.

Different additives are added to the fracturing fluid to optimize the fracturing operations (Table 1-1). According to Council of Canadian Academies (CCA) (2014), there has been at least 750 chemicals that added to fracturing fluids of different wells. Depending on local regulations, reservoir geology, and fracturing treatment a dozen of these chemicals might be added to the fracturing fluid for the fracturing operations.

Fracturing fluid treatments are generally classified into three types (Goss et al., 2015) of

(i) ***Slickwater stimulation***, which is mainly consist of fresh water and relatively large amount of proppants. Slickwater stimulation is usually used for fracturing of

reservoirs with brittle rocks. A large number of wells in Barnette and Horn River Basin are stimulated using slickwater (Alessi et al., 2017).

(ii) ***Energized stimulation***, which uses relatively smaller amount of water compared with the slickwater stimulation. In addition to water, the fracturing fluid also contains large amount of proppants and compressed gas (such as CO_2 and N_2). Energized stimulation is better suited for reservoirs with less brittle rocks, and is a common practice in Haynesville (Alessi et al., 2017).

(iii) ***Energized-slickwater stimulation***, which is a hybrid of the first two stimulation processes. In other words, a large amount of water and compressed gas is injected into the reservoir to create fractures. This treatment process is more suitable for reservoirs with semi-brittle rocks, and is a common practice in Marcellus (Alessi et al., 2017).

Table 1-1. Typical chemical additives used in the fracturing operations (Petrowiki, 2016)

Additive	Function	Typical product
Biocide	Killing the bacteria	Gluteraldehyde carbonate
Breaker	Viscosity reduction	Acid, oxidizer. enzyme breaker
Buffer	Controlling the pH	Sodium bicarbonate, fumaric acid
Clay stabilizer	Clay swelling prevention	KCl, NHCl, KCl substitutes
Fluid loss additive	Improving fluid efficiency	Diesel, particulates, fine sand
Friction reducer	Reducing friction	Polyacrylamide derivatives
Iron controller	Prevent iron precipitation	Acetic and citric acid
Surfactant	Reducing surface tension	Fluorocarbon, Isopropanol
Gel stabilizer	Controlling the thermal degradation of gels	MEOH, sodium thiosulphate
Scale Inhibitors	Reducing scale formation	Inorganic and organic phosphates

1.1.4. Shut-in Process

After fracturing, the well is shut-in (or soak) for some time. The duration of the shut-in process mainly depends on (i) the knowledge about leak-off of fracturing fluid into rock matrix and (ii) the time required for arrange the surface facilities for production (Ezulike, 2017). During shut-in period, the fracturing fluid (primarily water) can leak-off into the rock matrix (Figure 1-7) mainly through imbibition (Makhanov et al., 2014; Ghanbari and Dehghanpour, 2016), clay adsorption (Santos et al., 1996), and osmosis processes (Binazadeh et al., 2016; Wang et al., 2017). There are disputes about the role of water leak-off on the hydrocarbon recovery. Some researchers believe that leak-off can reduce hydrocarbon production by adversely affecting the effective hydrocarbon permeability (Holditch, 1979; Bennion et al., 1999; Bertoncello et al., 2014; Shen et al., 2017). Some other researchers on the other hand believe that osmotic forces (Fakcharoenphol et al., 2013) and counter-current imbibition (Ghanbari et al., 2013) during shut-in period may help hydrocarbon production.

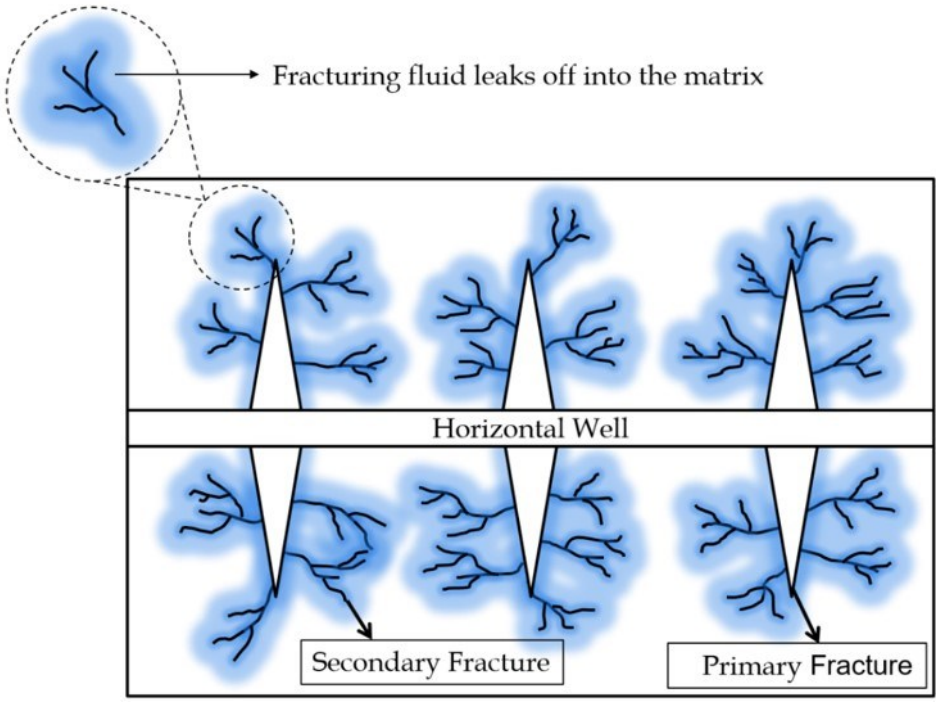

Figure 1-7. Fracturing fluid can leak-off into the rock matrix and potentially cause water blockage.

1.1.5. Flowback Process

After the shut-in period, the well is placed on production. The early stages of the production process is usually referred to as flowback process. Flowback sometimes is referred to as cleanup process, which cleans up the fractures and wellbore from the fracturing fluid. Generally, water rate is relatively high at early flowback process and declines over time (Figure 1-8).

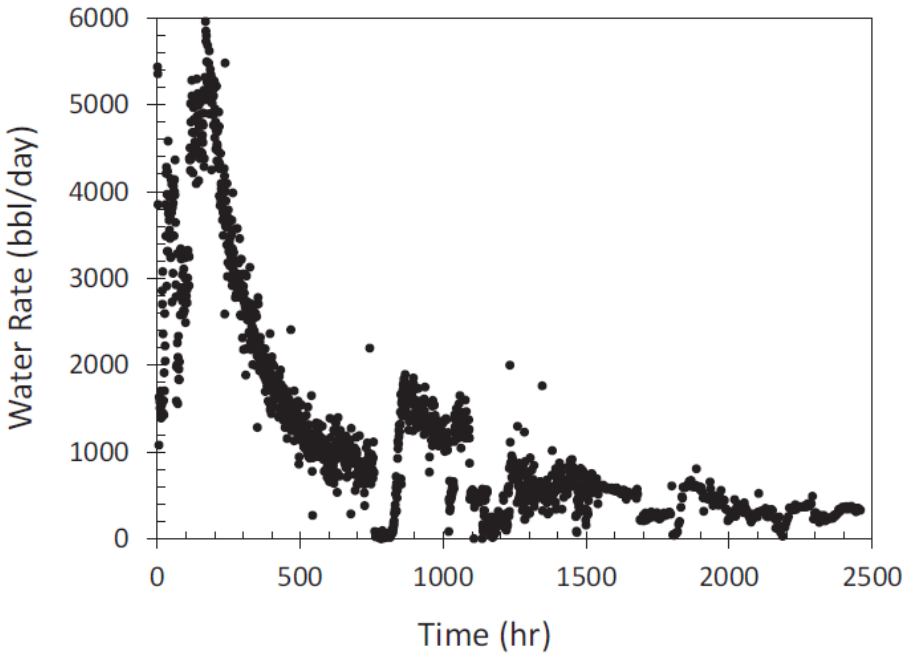

Figure 1-8. Water rate during flowback process for a well completed in the Horn River Basin (Ezulike, 2017).

1.1.6. Production Process

The fluid (oil/gas/water) recovery after flowback is usually referred to as the production period which can last for years. Majority of hydrocarbon recovery occurs during the long-term production period (Ezulike, 2017). Long-term production forecast has been the focus of many studies. Production data (such as water flowrate, hydrocarbon flowrate, and pressure) analysis is a common practice to predict the long-term hydrocarbon recovery (Makinde and Lee, 2017).

1.1.7. Fracture Network Characterization

For the particular case of low-permeable shales and hydraulic fracturing, the created fracture network greatly influences the long-term hydrocarbon recovery. The most common methods for fracture characterization are pressure transient analysis (PTA), rate transient analysis (RTA), micro seismic analysis, and tracer test.

1.1.7.1. R/PTA

Production data are usually available for all wells. Thus, many past studies applied rate/pressure-transient-analysis (R/PTA) analysis to characterize the fracture network. Fisher et al. (2005) characterized fracture parameters (such as fracture length) by analyzing the production data. Ezulike (2017) presented a complementary workflow for analysis of the production data (flowback and post-flowback) to characterize the fracture network parameters (such as fracture half length). Although, RTA and PTA are widely used to characterize the fracture network, they consider several simplifications that sometimes lead to unrealistic results. For instance, Hoffman and Chang (2009) indicate that since RTA does not consider the fracturing fluid properties, the estimated fracture length is too long and unrealistic. Furthermore, computational time in the production analysis methods is sometimes very high. The reason is that the production data analysis models are sometimes very finely gridded in an attempt to capture the dimension of the fracture (Karimi-Fard et al., 2004). However, the fractures are usually less than an inch wide, and the reservoir models require many grids to avoid the numerical convergence problems (Hoffman and Chang, 2009) which increases the computational time.

1.1.7.2. Microseismic analysis

Microseismic monitoring is also broadly used in the field to characterize the fracture network during hydraulic fracturing operations (Figure 1-9). Fracture characterization using microseismic

analysis is mainly based on the determination of the source, location, and geometry of microseismic events (Fan, 2014). Tafti et al. (2012) proposed a workflow to characterize the fracture network using microseismic data. Aside from all the benefits of the microseismic monitoring, active microseismic imaging is expensive (National Research Council, 2011). Also, fluid-filled porosity and clay minerals in the alteration zone around the fractures could cause anomalies in the microseismic data (National Research Council, 2011). Moreover, the stimulated reservoir volume (SRV) obtained from the microseismic interpretation does not provide propped fracture volume and its conductivity, and there is a difference between the SRV that is open for the gas flow and SRV obtained from microseismic diagnosis (Ahn et al., 2014).

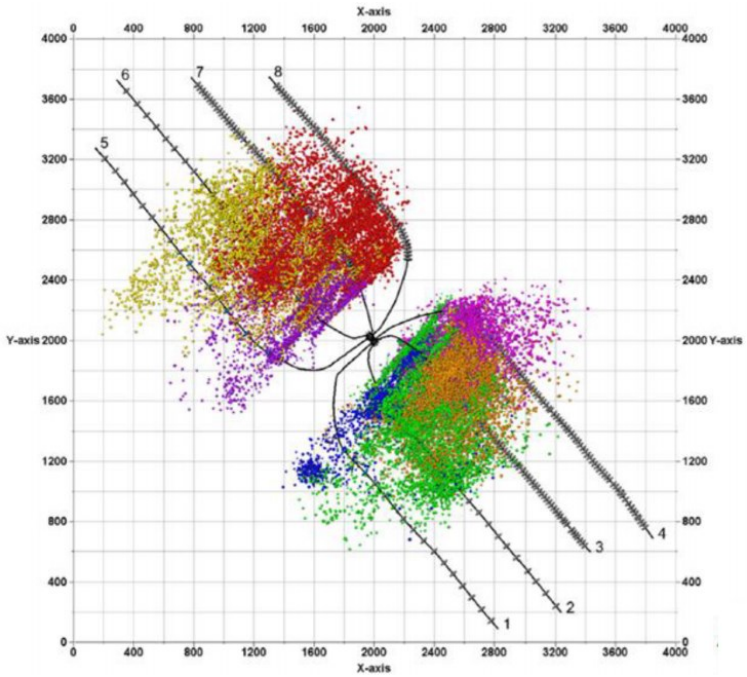

Figure 1-9. Recorded microseismic events during stimulation of a well-pad in the Horn River Basin (Xu et al., 2016).

1.1.7.3. Tracer test

Tracer test is commonly used to characterize the fracture network (Smith et al., 1987; Ramirez et al. 1993; Ramirez et al., 1995; Lange et al., 2005; Mulkern et al., 2010; Poulsen et al., 2012). For instance, Smith et al. (1987) estimated fracture aperture, distance between fracture

walls, using hydraulic and tracer tests. Although it is desirable to determine the tracer distribution in space and time, this goal is usually not achievable by tracer test. The reason is that the number of sampling points in the field is limited and the tracer concentration versus time is only available for the sampling points (National Research Council, 2011). Moreover, it is possible for the tracer to bypass the sampling point if the fluid mainly transmits through pre-existing open fractures around the sampling point.

1.1.7.4. Flowback chemical analysis

Flowback chemical analysis is an alternative approach which can extend/complement the available methods. Recently, Ghanbari et al. (2013) analyzed flowback salt concentration data from hydraulically fractured horizontal wells completed in the Horn River Basin. This comparative field study infers that the complexity of the fracture network can affect the shape of the salt concentration-load recovery profile. Bearinger (2013) qualitatively explained the relationship between the salinity profile and the complexity of the fracture network.

1.2. Research Motivation and Hypothesis

The chemistry of flowback water is usually only reported to the government/environmental agencies. However, flowback water chemistry provides an early data set from reservoir. The interactions between fracturing fluid and reservoir rock may contain information about the host fractures.

Although the flowback water is highly saline, the source of produced ions during flowback process is poorly understood. An improved understanding of the source/s of ions in the flowback water is essential for accurate interpretation of flowback chemical data. It is also hypothesised that flowback chemical analysis can be used as an alternative approach to extend/complement other available fracture characterization methods.

1.3. Research Objectives

Primary objectives of this research are:

- Investigating the source/s of ions in the flowback water by comparative analysis of laboratory and field data of ion concentration. This part of the study also investigates the possibility of characterizing the fracture network complexity using the concentration of individual ions in the flowback water.
- Characterizing the fracture network (fracture network complexity, fracture surface area, and invaded reservoir volume) using the total salt concentration in the flowback water. The model would account for the net ion transfer from rock matrix to water-filled fractures in order to mathematically explain the variation of salt concentration in the flowback water over time.
- Performing shale-water interaction (i.e., water imbibition) experiments and scaling-up the laboratory results of ion concentration to estimate fracture network/reservoir properties (i.e., fracture surface area and invaded reservoir volume).
- Performing shale-water interaction (i.e., water sorption) experiments to (i) investigate the role of clay minerals in water uptake of gas shale samples and (ii) to characterize the organic and inorganic pore size distributions of gas shale samples.

In this research, the "complexity" of fracture network is referred to the dendritic nature of the fracture network. In other words, for the same fracture volume, the fracture network with higher surface-to-volume ratio of the fractures is considered to be more complex than that with smaller surface-to-volume ratio of the fractures.

1.4. Organization of Dissertation

This work is divided into eight chapters. Chapters 2, 4, 6, and 7 have been published as peer-reviewed journal papers. Therefore, there might be some repetition of texts or figures in the chapters. Chapter 3 is the extended version of an SPE conference paper, and is ready for

submission to a peer-review journal. Chapter 5 is submitted for peer-review publication in March 2018, and it is currently under-review. Although each chapter forms a distinct unit of study with its own nomenclature, the chapters can still be read sequentially without loss of coherence.

Chapter 1 describes a general introduction about the prospective of this study, and provides the research motivation and objectives. Chapter 2 focuses on identifying the sources of ions in the flowback water by analyzing the laboratory and field data of ion concentration. The individual ion concentration data are also interpreted to qualitatively characterize the fracture network complexity. Chapter 3 presents the experimental results of acid digestion and sequential-ion extraction on both flowback water and downhole shale rock samples to investigate the source of ions in the flowback water. Chapter 4 combines all ions in the flowback water to characterize the fracture network complexity using salt concentration profile during flowback process. Chapter 5 investigates the effects of rock surface area, rock volume, temperature, and pressure on the total ion produced during water imbibition experiments. This chapter also proposes a procedure to scale-up the laboratory results of ion concentration in order to estimate fracture surface area and invaded reservoir volume. Chapter 6 presents a modified water sorption technique to investigate the role of clays on water uptake of gas shale samples. Chapter 7 provides a model to characterize the inorganic and organic pore size distributions using the modified water sorption isotherms. Chapter 8 lists the key conclusions of this work and presents recommendations for future studies. The references for all chapters are combined together and presented after Chapter 8. Similarly, the appendices from all chapters are combined and provided after the references section.

Chapter 2

Laboratory and Field Analysis of Flowback Water from Gas Shales

2.1. Introduction

Low permeability shale gas reservoirs are rapidly emerging as a vital source of natural gas (Frantz and Jochen, 2005). Multi-lateral horizontal drilling and multi-stage hydraulic fracturing technologies have paved the way for economical exploitation of these shale resources. In hydraulic fracturing, a large volume of fracturing fluid (mainly water) is injected into the reservoir to create multiple fractures and increase reservoir contact per well (King, 2012). Then, the wells are sometimes shut-in for a period of time (soaking period) (King, 2012; Lan et al., 2014a; Makhanov et al., 2014). During the production phase, a portion of the injected fracturing fluid returns to the surface, i.e. flowback water, alongside the produced hydrocarbons (Dehghanpour et al., 2012; King, 2012; Dehghanpour et al., 2013; Abbasi et al., 2014; Bai et al., 2015).

The field data indicate that the chemistry of flowback water is substantially different than that of the injected water (Rimassa et al., 2009; Haluszczaket al., 2012; Bearinger, 2013; Engle and Rowan, 2014; Capo et al., 2014). For instance, in the Horn River Basin (HRB), slick water (which has similar salinity levels as fresh water) is injected into the reservoir to create fractures (Johnson and Jonson, 2012), while the recovered flowback water is highly saline (40,000-70,000 ppm) (Bearinger, 2013; Engle and Rowan, 2014; Capo et al., 2014).

Several past studies focused on the flowback chemical analysis to evaluate the hydraulic fracturing operations and characterize the fractured reservoir. Chemical analysis models for optimizing fracturing fluid cleanup have been developed by Woodroof et al. (2003), Sullivan et al. (2004), and Asadi et al. (2006). Gdanski (2010) incorporated a chemistry layer to a 2-D numerical simulator to history match the composition of the flowback fluid. Engle and Rowan (2014) applied a multivariate data analysis approach to investigate the geochemical evolution of flowback water (Engle and Rowan, 2014). Flowback salt concentration data from hydraulically fractured wells in the HRB were analyzed by Ghanbari et al. (2013); and their results indicate that the architecture of the induced fracture network affects the load recovery and the shape of the salt concentration profiles. Bearinger (2013) developed a qualitative theory explaining the relationship between shape of the salt concentration profile and the complexity of the fracture network. In Chapter 4 a model is presented to mathematically describe the Bearinger's qualitative theory. This model

characterizes the complexity of the fracture network using the salinity profile measured during the flowback process.

Despite the previous studies that analyze the chemistry of flowback water to assess the hydraulic fracturing operations, the origin of flowback salts is still a matter of dispute. Blaunch et al. (2009) reported that the production of salts during the flowback process is due to the dissolution of shale constituents in injected water; while Haluszczak et al. (2013) claimed that the saline flowback water is mainly caused by interaction of injected water with the in situ formation brine. Furthermore, shales are composed of clay minerals (Carman and Lant, 2010) that can alter the chemistry of the water through ion exchange reactions. Moreover, shales have mineral-filled natural fractures (Gale et al., 2014). Reactivation of these mineral-filled natural fractures and dissolution of minerals into the water during hydraulic fracturing operations is another possible source for flowback salts.

This chapter presents a laboratory and field analysis to investigate the origin of salts in the flowback water. The salinity and individual ion concentration are measured for three wells completed in the HRB. X-ray diffraction (XRD) analysis is utilized to characterize the mineralogy of the rock samples. Cation exchange capacity (CEC) of the shale samples are measured using the ammonium acetate method. Oil and water imbibition experiments are performed on samples of three different surface-to-volume ratios (i.e. specific area or "A_{sp}") to investigate the effects of fluid-rock interface on the liquid uptake and diffusion rate of individual ions. Electrical conductivity (EC) and individual ion concentration are measured during the water imbibition process. Furthermore, elemental maps from energy-dispersive X-ray spectroscopy (EDS) analysis are used to visualize the distribution of individual ions on the fresh break and on the natural fracture surfaces of the samples.

2.2. Methodology

Interactions of injected water with in situ formation brine and shale rock are the possible sources of the flowback salts. Since the shale formations in the HRB are at sub-irreducible water saturation state (Dehghanpour et al., 2013), there is a possibility for ions to precipitate in the form

of salts in the pore structure or on the surface of natural fractures. To identify the origin of the flowback water salts, we first analyze the field flowback data including salinity and individual ion concentration. The elemental maps of the fresh break and natural fracture surfaces from EDS analysis are compared to identify the nature of the locally occurring minerals. The EDS results are further compared with the bulk-rock mineralogy, CEC, and the flowback water chemistry to identify the source of the ions.

2.2.1. Horn River Basin

The flowback water and downhole shale samples are collected from three wells completed in the Muskwa (Mu), Otter-Park (OP), and Evie (Ev) formations in the HRB. HRB is an unconventional shale play and is located in the north eastern part of British Columbia, Canada. Figure 2-1a shows the location of the HRB and the target wells investigated in this study.

HRB covers about 3 million acres (Reynolds and Munn, 2010) and is confined by Bovie Lake Fault Zone and Devonian Carbonate Barrier Complex from west and south, respectively (BC Oil and Gas Commission, 2014). HRB is an over-pressured dry gas play with an initial gas in place of approximately 500 Tcf (Reynolds and Munn, 2010). Shale members of HRB (i.e., Mu, OP, and Ev) are grey to plack organic rich (1-4%) pyritic, and variably calcareous and siliceous minerals (BC Oil and Gas Commission, 2014).

Horizontal drilling and multi-stage hydraulic fracturing operations began in 2005 in the HRB. By the end of 2013, there were more than 350 vertical and horizontal wells drilled in the HRB, with the daily gas production of about 580 mmcf per day. In 2012, the gas production from the Mu, OP, and Ev formations in the HRB accounted for nearly 10% of the total gas production in British Columbia (BC Oil and Gas Commission, 2014).

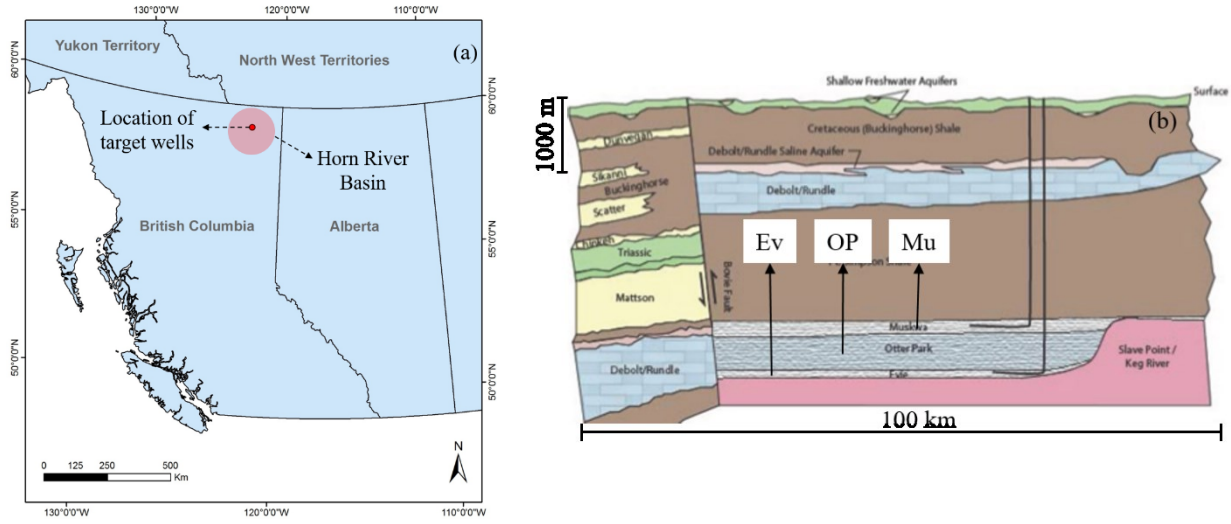

Figure 2-1. (a) Location of the target wells and (b) stratigraphic cross-section of shale members in the Horn River Basin (BC Oil and Gas Commission, 2014)

2.2.2. Field Data

The salinity of the flowback water is frequently measured during the flowback process. Figure 2-2 shows the field data of flowback water salinity versus time for three target wells. The salinity profiles of Mu and OP initially show a gradual increase, and then reach to a plateau at around 40000 ppm; the salinity profile of Ev continuously increases even after 70000 ppm.

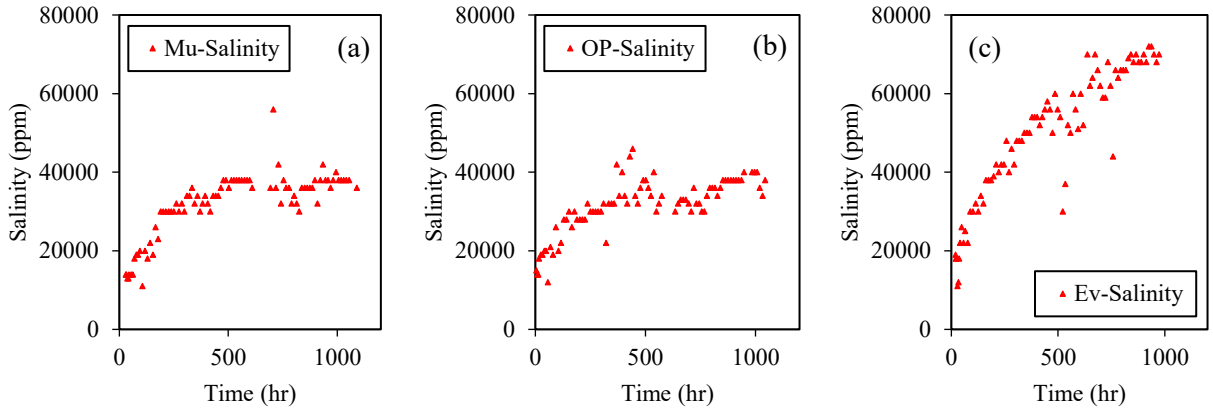

Figure 2-2. Field data of flowback water salinity versus time for three wells completed in the (a) Mu, (b) OP, and (c) Ev formations in the HRB.

The individual ion concentrations are measured during the flowback process for the three focus wells. Figure 2-3 shows the concentration trends for barium, iron, sulfate, and chloride ions measured during the flowback process.

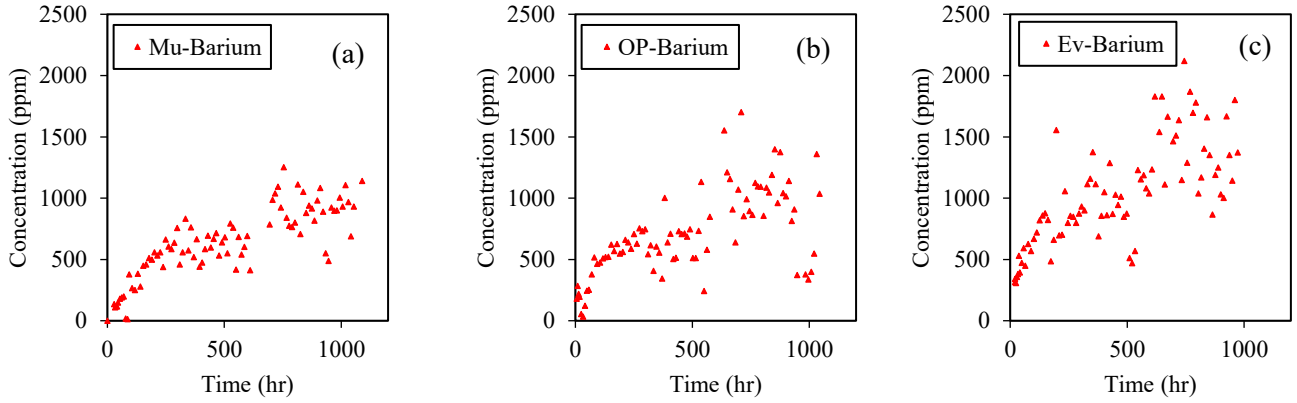

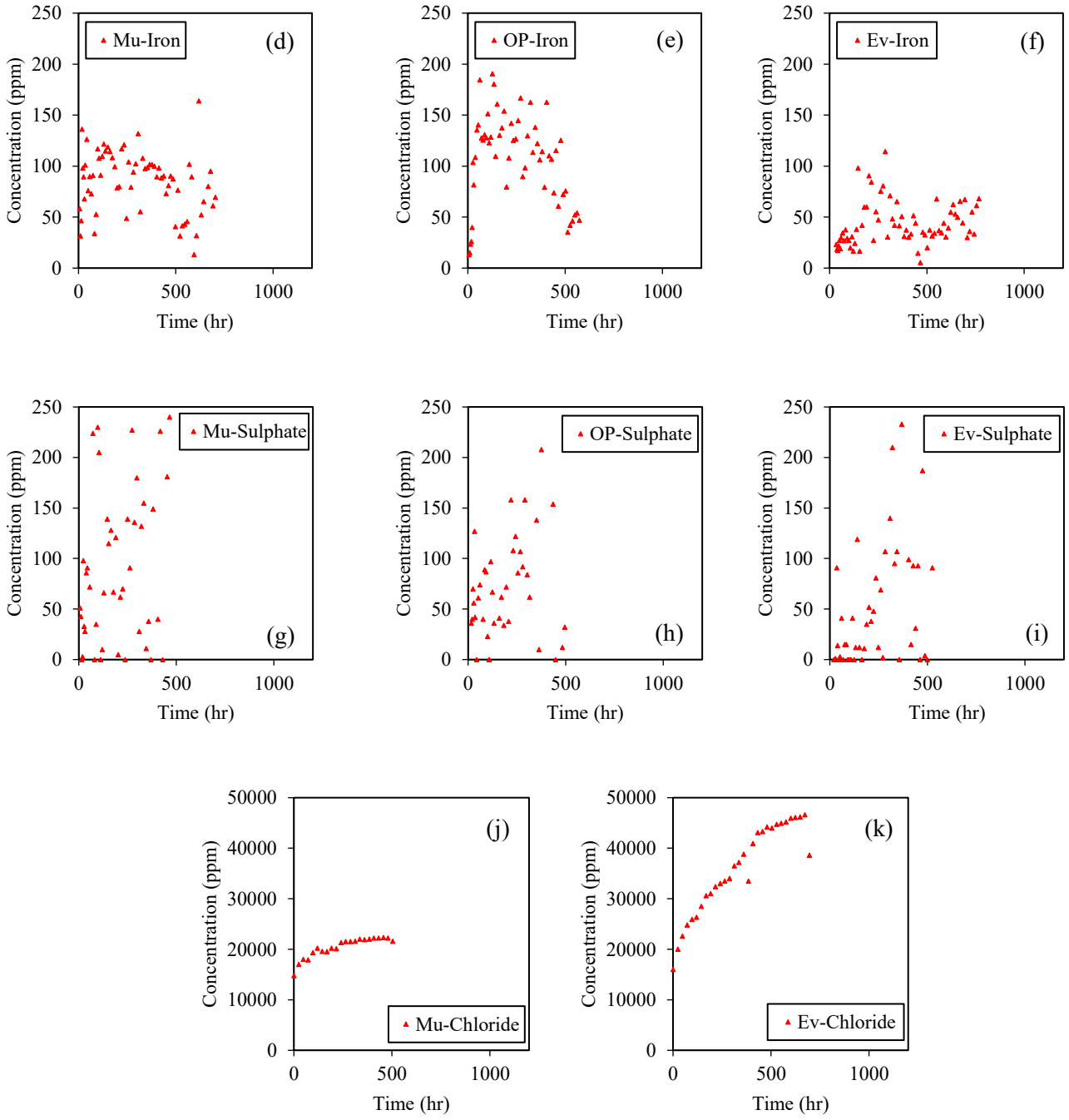

Figure 2-3. Field data of flowback water concentration versus time for barium, iron, sulfate, and chloride ions for three wells completed in the (a, d, g, j) Mu, (b, e, h) OP, and (c, f, I, k) Ev formations in the HRB. The accuracy of measured ion concentration is ± 0.1 ppm.

Over the course of the flowback process, a general increase of the barium and sulfate concentration is observed for all three wells. A similar increase in the concentration of chloride

ion is also observed for the Mu and Ev wells (no data was available for the OP well). The iron and sulfate concentration profiles are relatively scattered. The concentration of iron ions in OP shows a gradual increase over the first 200 hours during the flowback process, after which the concentration decreases with time.

During the hydraulic fracturing operations, the injected water interacts with the reservoir rock. For instance, leaching of clay minerals and dissolution of rock constituents could impact the water chemistry. Therefore, the primary steps in identifying the origin of the flowback salts are to characterize the bulk-rock mineralogy. Liquid uptake and ion transfer into/out of the shale also impact the chemistry of the flowback water. The injected water could also interact with in situ formation brine and precipitated salt crystals in natural fractures or pore space. The shale formations in the HRB are at sub-irreducible water saturation state (Dehghanpour et al., 2013). Therefore, there is a possibility for ions to precipitate in the form of salts in the pore structure or on the surface of natural fractures. Thus, a comparative analysis of elemental distribution in the matrix and natural fractures will help to better understand the origin of the flowback salts. In Section 2.1.3.5, the surfaces of fresh break and natural fractures are explored for local mineral-concentrated areas using EDS.

2.2.3. Laboratory Analysis

2.2.2.1. Bulk-Rock Mineralogy

One of the current hypotheses about the origin of the flowback salts is that the salts in the flowback water are the shale constituents that have been dissolved in the injected water (Blaunch et al., 2009). XRD analysis is applied to characterize the rock mineralogy of the shale samples.

2.2.2.2. Contact Angle Measurement

During fracturing operation water imbibes into the rock matrix. The water present in the pore network provides a medium for ion transfer into/out of the rock. Thus, the rock affinity for water

uptake impacts the ion transfer between the rock and water. On the other hand, the wettability of shale rock impacts the liquid uptake by shales (Xu and Dehghanpour, 2014; Lan et al., 2014b). Fluid-rock contact angle is a simple way to characterize the wettability of the shales (Andrew et al., 2014; Mirchi et al., 2015; Yarveicy and Javaheri, 2017; Yarveicy and Haghtalab, 2018; Yarveicy et al., 2018). This chapter also presents the equilibrium water and oil contact angles for both the Ev and OP samples to characterize their affinity for liquid uptake.

2.2.2.3. Imbibition Experiments

It has been previously shown that the fluid-rock interface impacts the flowback water chemistry (Bearinger, 2013). Therefore, imbibition experiments are carried out for samples of different specific surface area (A_{sp}) values. A_{sp} is defined as the surface-to-volume ratio of the samples. The sample with high A_{sp} ($A_{sp,high}$) value is prepared by sifting the crushed rock with 2 mm mesh size sieve. The sample with medium A_{sp} ($A_{sp,medium}$) value is prepared by dry cutting the rock in smaller cubed-shape samples of approximately 1-2 cm in edge length. The samples with low A_{sp} ($A_{sp,low}$) value are a large cubed-shape sample with the side size of approximately 5-7 cm. For all samples of different A_{sp} values, it is tried to keep the sample mass at around 380 g. Figure 2-4 demonstrates the pictures of the prepared OP samples of three A_{sp} values for the water imbibition experiment.

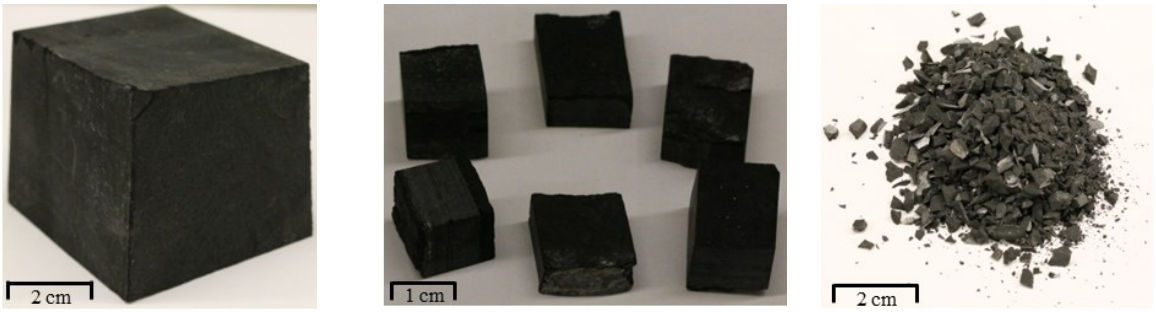

(a) (b) (c)

Figure 2-4. Pictures of OP samples of three A_{sp} values for the water imbibition experiments; (a) OP-$A_{sp,Low}$, (b) OP-$A_{sp,Medium}$, (c) OP-$A_{sp,High}$

For the water/oil imbibition experiments, the samples are placed into 700 ml of DI-water/kerosene. Since it was not possible to measure the weight change of the $A_{sp,high}$ sample, water and oil imbibition tests are only reported for $A_{sp,low}$ and $A_{sp,medium}$ samples. Physical specifications of the prepared samples for the imbibition experiments are reported in Table 2-1. The measurement accuracy for surface area and mass measurements are 0.25 cm^2 and 0.01 g, respectively.

Table 2-1. Physical specifications of the OP and Ev samples prepared for the water and oil imbibition experiments

Sample	Formation	Interacting Fluid	A_{sp}	Surface Area (cm^2)	Mass (g)
1	OP	DI Water	Low	57.2 ± 0.25	383.20 ± 0.01
2	OP	DI Water	Medium	108.1 ± 0.25	381.90 ± 0.01
3	OP	DI Water	High	∞	380.20 ± 0.01
4	Ev	DI Water	Low	75.2 ± 0.25	378.40 ± 0.01
5	Ev	DI Water	Medium	109.9 ± 0.25	382.40 ± 0.01
6	Ev	DI Water	High	∞	380.50 ± 0.01
7	OP	Oil	Low	64.8 ± 0.25	385.80 ± 0.01
8	OP	Oil	Medium	101.2 ± 0.25	380.10 ± 0.01
9	Ev	Oil	Low	59.4 ± 0.25	377.60 ± 0.01
10	Ev	Oil	Medium	107.7 ± 0.25	384.60 ± 0.01

2.2.2.4. Ion Diffusion Analysis

The electrical conductivity (EC) and individual ion concentration are measured during the water imbibition experiments. The experimental set-up is schematically illustrated in Figure 2-5. Since DI water is used in these experiments, EC of the solution is considered as a proxy for the net ion transfer from the shale sample to water. ICP-OES and IC are used to determine the concentration of cations and anions in water, respectively.

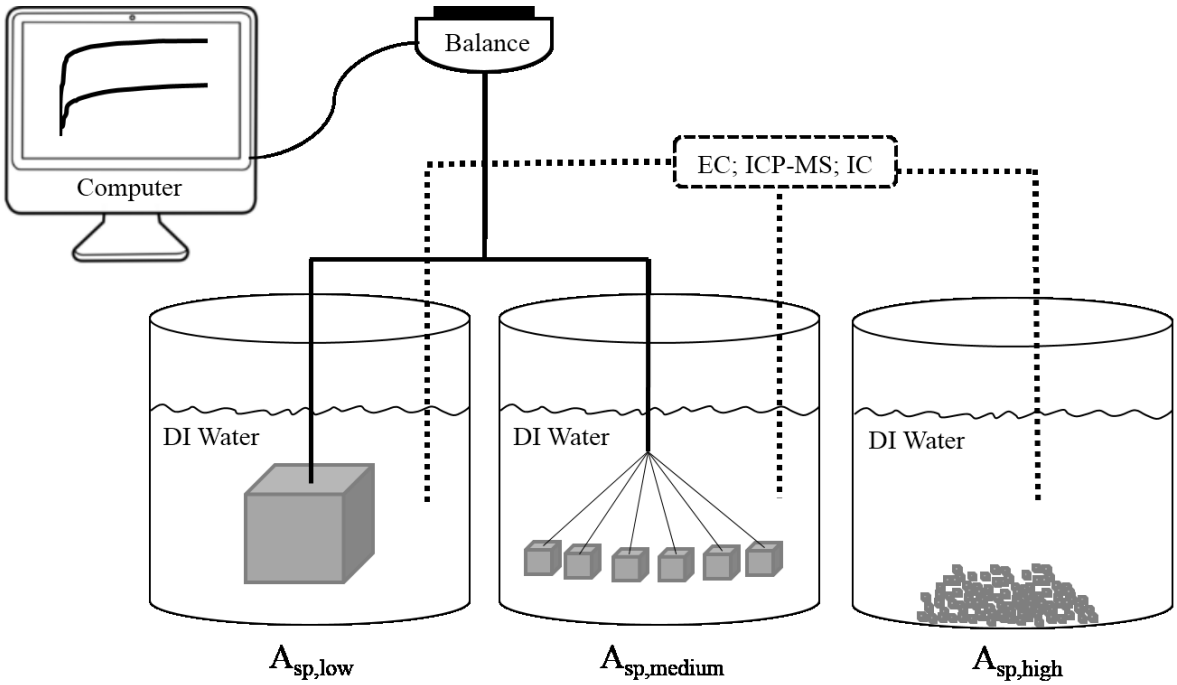

Figure 2-5. A schematic representation of the experimental set-up for the imbibition/diffusion experiments. EC and individual ion concentration are measured over time for the water imbibition experiments.

2.2.2.5. Surface Element Analysis

XRD uses a very small volume of rock, so it is possible to miss minerals that occur in local areas such as in natural fractures. Natural fractures are very common in the HRB and they are mostly sealed (Gale et al., 2014). EDS analysis is conducted as a complementary test for XRD analysis to explore the surfaces of the natural fractures for the possible mineral-concentrated areas. Furthermore, the fresh break surfaces of the samples are also analyzed using EDS to compare the elemental distribution in the rock matrix and on the natural fracture surfaces. The selected natural fractures are identified by their visually distinct coloration caused by mineral fill. Figure 2-6 shows natural fractures in an OP shale sample.

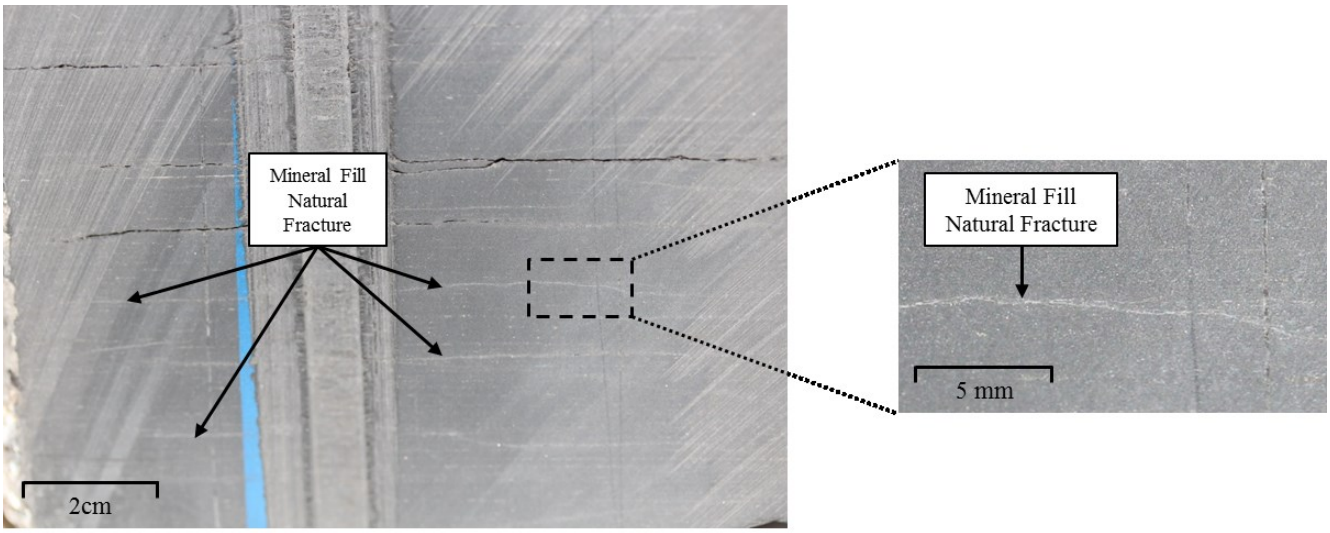

Figure 2-6. Natural fractures in the OP sample. The natural fractures in the samples were almost horizontal (perpendicular to the blue scratch test mark) and they have a visually distinct coloration (whiter area) caused by mineral fill.

2.2.2.6. CEC

CEC is the capacity of a rock to hold exchangeable cations (Essington, 2005). The exchangeable cations in the clay fraction of the shales can take part in the ion exchange reactions and alter the chemistry of the flowback water. More specifically, the surface of clay minerals is negatively charged. These negative charges are balanced by exchangeable cations (such as Na^{+}, K^{+}, Ca^{2+}, Mg^{2+}) residing in the interlayer space of the clay minerals (Hensen and Smit, 2002). The exchangeable cations in the interlayer space of the clay minerals are schematically illustrated in Figure 2-7.

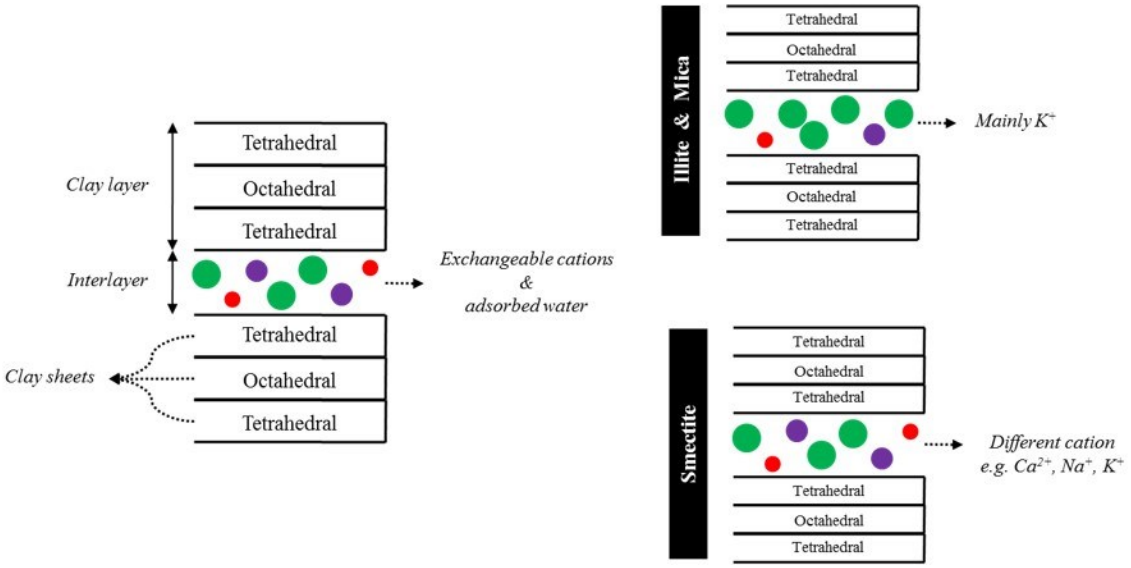

Figure 2-7. Schematic of clay (2:1 type) structure and the common exchangeable cations in the interlayer of the clay minerals

The exchangeable cations can take part in the ion exchange reactions during hydraulic fracturing operations (including the soaking period)/imbibition experiment. The CEC of our shale samples are measured using the ammonium acetate method to characterize their capacity for ion exchange reactions (Sumner and Miller, 1996). To do so, 1 molar ammonium acetate is added to the crushed samples (sifted with 2 mm mesh size sieve). After 24 hours, the solution is filtered in a Buchner vacuum. Then, the rock samples were rinsed with 1 M KCl solution in a Buchner vacuum. The final solution is analyzed for ammonium concentration to obtain the CEC.

2.3. Results and Discussion

2.3.1. Bulk-Rock Mineralogy Results

Table 2-2 shows the bulk-rock mineralogy of the OP and Ev samples from XRD analysis. It must be noted the shales are heterogeneous and their mineralogy can significantly vary even in small scales (Diaz et al., 2010). Furthermore, XRD uses small amount of rock samples for its analysis. Therefore, the results presented in Table 2-2 might not be an accurate representation of all samples from the OP and Ev formations.

Table 2-2. The bulk-rock mineralogy of the OP and Ev samples from XRD analysis. The XRD used for characterization of rock mineralogy has a signal-to-noise ratio of 400.

Sample	OP	Ev
Depth (m)	2608.75	2682.48
Non-Clay Content (wt.%)		
Quartz	77	32
K-Feldspar	2	6
Plagioclase	2	6
Calcite	0	10
Siderite	0	0
Ankerite/Fe-Dolomite	1	5
Dolomite	0	4
Pyrite	1	5
Fluorapatite	0	0
Barite	0	0
Magnetite	0	0
Total Non-Clay	84	67
Clay Content (wt.%)		
Smectite	0	0
Illite/Smectite (I/S)	5	14
Illite+Mica	11	19
Kaolinite	0	0
Chlorite	0	0
Total Clay	16	33

According to the XRD results, the OP samples are composed of 77 wt.% quartz and 16 wt.% clay while the Ev samples have 32 wt.% quartz and 33 wt.% clay minerals. The quartz content in the OP samples is more than twice that of the Ev samples, and the clay content of the Ev samples is almost twice that of the OP samples. Furthermore, Ev samples contain 10 wt.% calcite and 5 wt.% pyrite while the concentration of these components is negligible in the OP samples. According to the XRD analysis pyrite and ankerite/Fe-dolomite are the iron-bearing components. Furthermore, although there is a significant amount of barium in the flowback water (Figure 2-3a-c), XRD analysis does not detect any barium-bearing component in the bulk-rock. It must be noted that the shales are heterogeneous and their properties can significantly vary even in small scales (Diaz et al., 2010). On the other hand, XRD uses a very small volume of rock for its analysis.

Therefore, the rock mineralogy presented in Table 2-2 might not be an accurate representation of the formation mineralogy.

The clay fraction in the rock samples could take part in the ion exchange reactions during and after hydraulic fracturing operations. According to the XRD results, the clay fraction of our shale samples is mainly composed of illite, mica, and mixed-layer illite/smectite (I/S) minerals. The CEC ranges between 10-40 $cmol_c kg^{-1}$ for illite and mica, and 60-150 $cmol_c kg^{-1}$ for smectite (Essington, 2005). Therefore, during and after the hydraulic fracturing operations, the smectite in the mixed I/S layers has higher tendency to take part in the cation exchange reactions and affect the flowback water chemistry than illite and mica.

2.3.2. Contact Angle Measurement Results

Figure 2-8 compares the water and oil droplets equilibrated on the fresh break surfaces of the Ev and OP samples. The water contact angle on the fresh break surface is smaller for the Ev sample as compared with the OP sample, suggesting that the surface of the Ev sample has a greater affinity to adsorb water compared with that of the OP sample. This result is in agreement with the previous contact angle measurements conducted on the HRB's shale samples (Dehghanpour et al., 2012; Lan et al., 2014b; Ghanbari et al., 2015). For both samples, the oil droplet spreads out over the surface (approximately zero contact angle) which indicates that the clean surface of both formations is oil-wet. Similar observations are also reported for the HRB's shale samples (Ghanbari and Dehghanpour, 2015; Dehghanpour et al., 2013; Dehghanpour et al., 2012).

It must be noted that the reported contact angle values for both OP and Ev samples (Figure 2-8) are the average value of three contact angle values with the standard deviation (σ_{st}) of 4.1º and 2.2º, respectively. The standard deviation is calculated by

$$\sigma_{st} = \sqrt{\frac{\sum_i^n \theta_i^2 - \frac{(\sum_i^n \theta_i)^2}{n}}{n-1}} \quad (2\text{-}1)$$

Where θ is contact angle and n is the number of measurements.

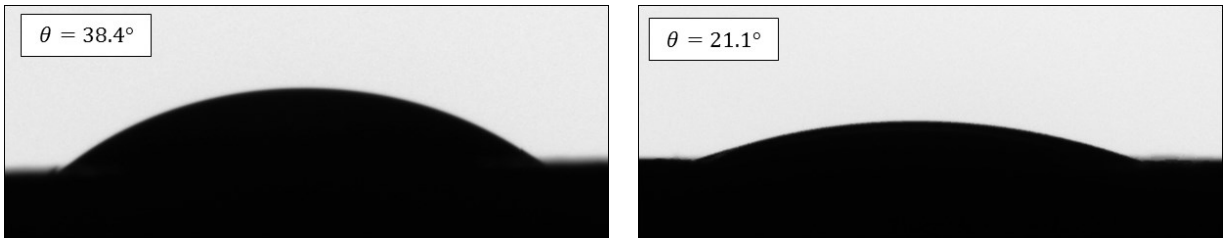

(a) (b)

Figure 2-8. Pictures of water droplets equilibrated on the fresh break surface of the (a) OP and (b) Ev samples.

2.3.3. Imbibition Experiment Results

Figure 2-9 shows the water and oil imbibition versus time for the OP and Ev samples of low specific surface value. Despite the lower contact angle of oil compared with that of water (favourable wettability conditions for oil), both Ev and OP samples show lower oil uptake compared to water. Similar observations were also reported for high water uptake in the HRB shales by other researchers (Dehghanpour et al., 2012; Dehghanpour et al., 2013; Makhanov et al., 2014; Ghanbari and Dehghanpour, 2015). These results suggest that capillarity force is not the sole mechanism that controls the imbibition process. Other parameters such as rock mineralogy, osmotic effect, natural fractures, induced fractures during the water imbibition, and adsorption of water molecules by clays could also impact the total liquid uptake (Xu and Dehghanpour, 2014).

The difference between water and oil imbibition is higher for the Ev sample compared with that for the OP sample. This difference, along with the high water imbibition of Ev, is in agreement with its mineralogy (higher clay content compared with OP). Furthermore, these results complies with field observations of higher leak-off rate and lower water recovery from Ev (compared to the higher water recovery from OP) (Figure 4-10).

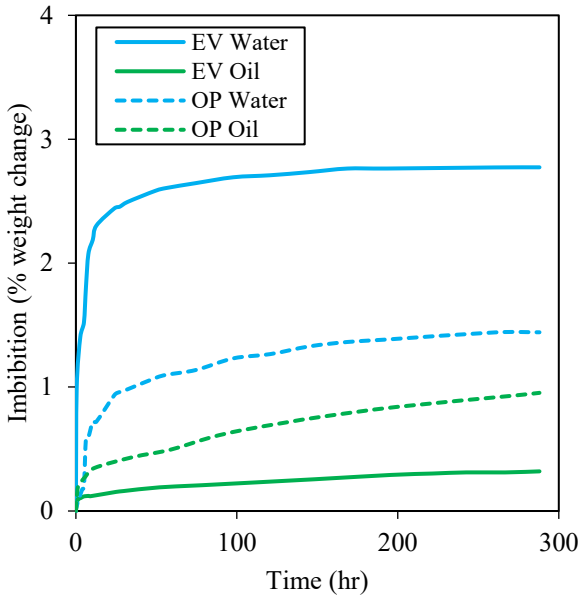

Figure 2-9. Water and oil imbibition versus time for the OP and Ev samples of low specific surface value ($A_{sp,low}$). The scale used for measuring the mass of the rock samples during the imbibition experiments has an accuracy of ± 0.01 g.

Figure 2-10 represents the oil and water imbibition versus time for the OP and Ev samples of different specific surface values. The experimental results indicate that A_{sp} has significant impact on water imbibition (Figure 2-10a) while its impact on oil imbibition is negligible (Figure 2-10b). Higher A_{sp} values increases both the rate and the amount of the imbibed water which shows that water imbibition strongly depends on the water-rock interface. Higher interface area also improves accessibility to the clay-rich zones, which further promotes the water uptake.

The difference between the water uptakes of the samples with different A_{sp} values is more prominent in the Ev samples. Since, the Ev sample has more clay content compared with the OP sample, probably higher interface area enhanced accessibility to the clay rich zones. The water molecules could adsorb in interlayer space of the clay minerals (Figure 2-7). Also, clay expansion could induce micro-fractures (Dehghanpour et al., 2013; Ghanbari and Dehghanpour, 2015) that can further increase the water uptake.

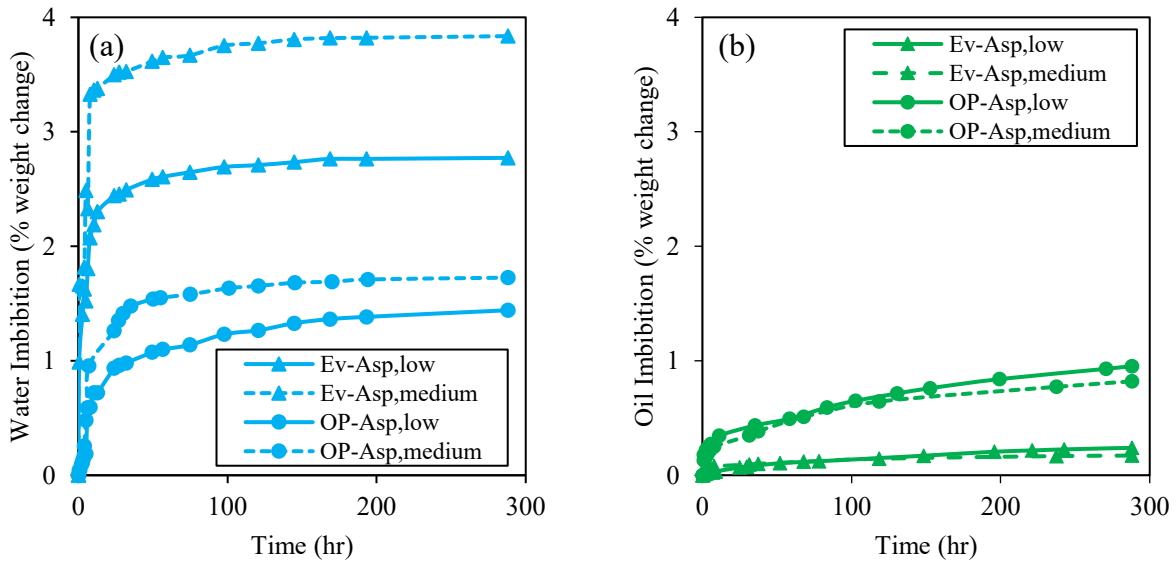

Figure 2-10. (a) Water and (b) oil imbibition versus time for the OP and Ev samples of low and medium specific surface area (A_{sp}). The scale used for measuring the mass of the rock samples during the imbibition experiments has an accuracy of ± 0.01 g.

2.3.4. Ion Diffusion and CEC Results

Figure 2-11 shows the increase in the EC of the solution for the OP and Ev samples of three A_{sp} values during the water imbibition experiments.

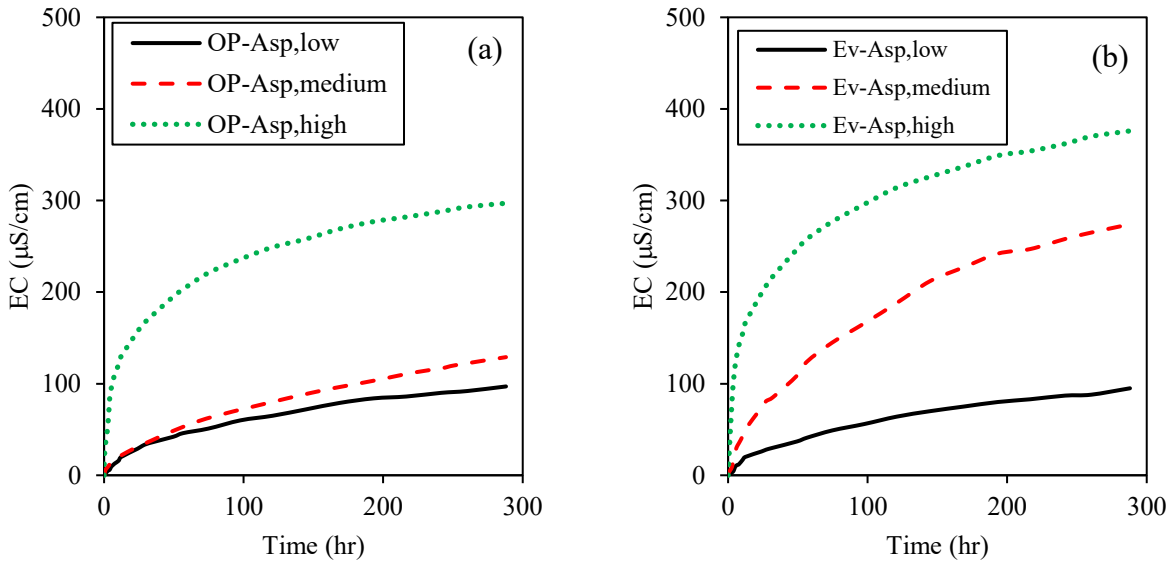

Figure 2-11. The EC of water versus time during the water imbibition experiment for the (a) OP and (b) Ev samples of three A_{sp} values. The accuracy of measured EC is ± 0.1 µS/cm.

The EC of the solution increases during the water imbibition experiments for all samples. During the water imbibition process, as the water imbibes into the rock, the ions diffuse into the water. As the ion concentration increases over time, the EC of the solution increases accordingly. Furthermore, for both of the OP and Ev samples, the EC is higher for the samples with higher A_{sp} values. Moreover, the difference between the EC of samples of different A_{sp} values is more prominent for the Ev sample. In addition, the absolute values of EC are higher for the Ev ample compared with that for the OP sample.

During the water imbibition process, the ions can be sourced from either of the dissolution of precipitated salts (remaining from the formation water), leaching of clay minerals, and reactions between water and rock. The greater EC values of the samples with higher A_{sp} values can be explained by the higher water-rock interface. More water-rock interface promotes the water-rock reactions. Also, it can improve the accessibility to the clay-rich zones which facilitates the ion exchange reactions. More specifically, the exchangeable cations can leach out from the clays during the water imbibition experiment. The tendency of the shale samples for CEC is measured experimentally and the results are presented in Figure 2-12.

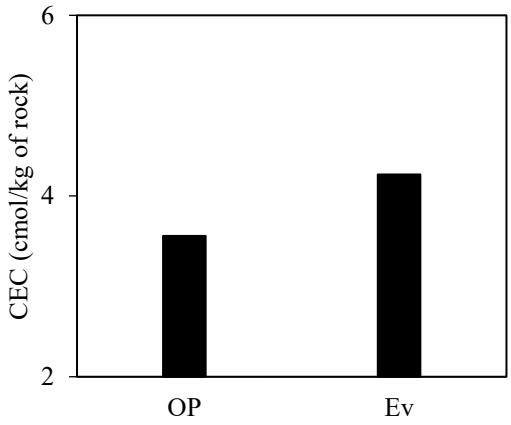

Figure 2-12. CEC of the OP and Ev samples measured using the ammonium acetate method.

The CEC of the Ev sample is higher than that of the OP sample, suggesting that the Ev sample has more exchangeable cations than the OP sample. According to Table 2-2, the clay content of the Ev sample is almost double that of the OP sample. There are exchangeable cations in the interlayer space of the clay minerals (Figure 2-7). Therefore, the higher clay content of Ev could be one of the reasons for its higher CEC compared with that of OP. The higher CEC of the Ev samples promotes the ion exchange reactions, which causes the higher and faster ion transfer (Figure 2-11b) compared with that of OP samples (Figure 2-11a).

The concentrations of individual ions versus time during the water imbibition experiments are measured for Ev and OP samples of three A_{sp} values using ICP-MS and IC, and are illustrated in Figures 2-13 and 2-14, respectively. In general ion concentration increases over time, which is in agreement with the field observations presented in Section 2.1.2.1. It is worth mentioning that the ion concentration obtained in the laboratory (Figure 2-13) is very smaller than that obtained in the field (Figure 2-3); which can be due to the difference between the experimental and reservoir conditions (such as temperature, pressure, redox state). The effects of temperature, pressure, rock volume, and rock surface area on the total ion produced is investigated in chapter 5. The effect of redox state on water imbibition and ion concentration can be found elsewhere (Xu et al., 2018).

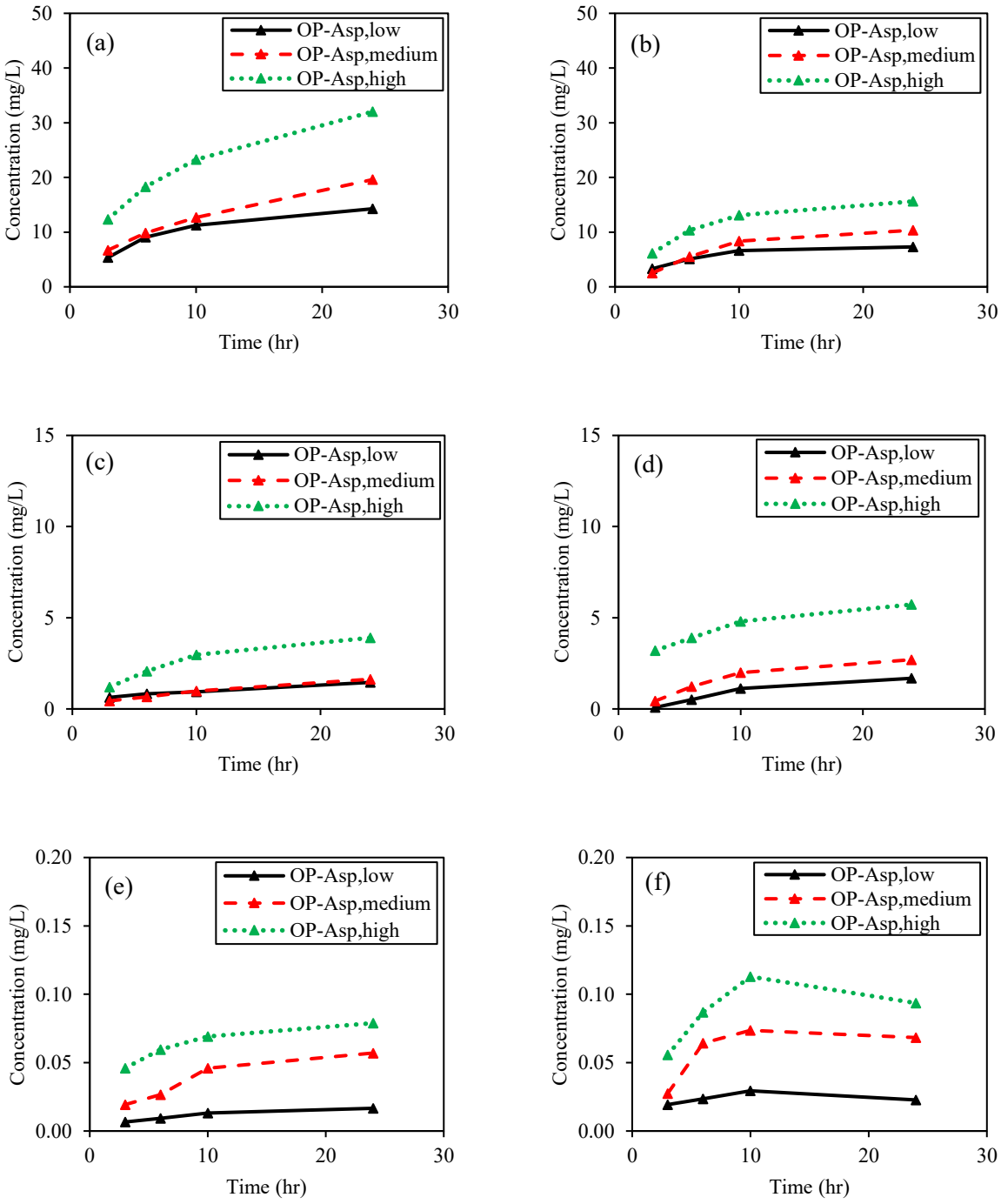

Figure 2-13. Individual ion concentrations versus time during the water imbibition experiments for the OP samples of three A_{sp} values, (a) sodium, (b) potassium, (c) chloride, (d) sulfate, (e) barium, and (f) iron. The accuracy of measured ion concentration is ± 0.1 mg/L.

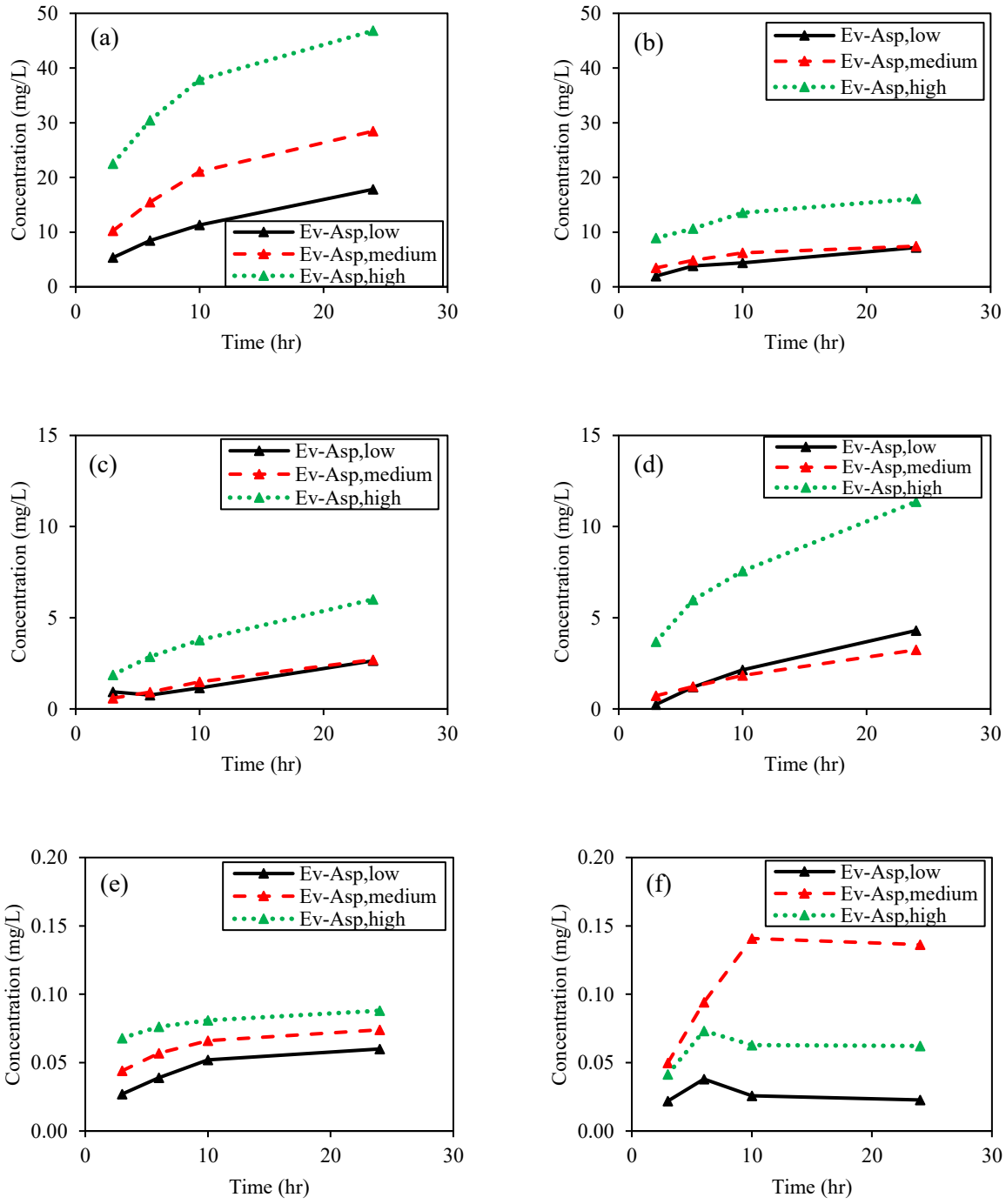

Figure 2-14. Individual ion concentrations versus time during the water imbibition experiments for the Ev samples of three A_{sp} values, (a) sodium, (b) potassium, (c) chloride, (d) sulfate, (e) barium, and (f) iron. The accuracy of measured ion concentration is ± 0.1 mg/L.

Sodium and chloride: The concentration of sodium and chloride ions increase during the water imbibition experiments. Sodium is the dominant cation in the solution, and its concentration is higher than the concentration of chloride. The average Na/Cl molar ratio for the OP and Ev samples is 10.9 and 11.0, respectively. Similar observations were also reported by Ghanbari et al. (2013). Figure 2-15 shows the Na/Cl molar ratio during the water imbibition experiments.

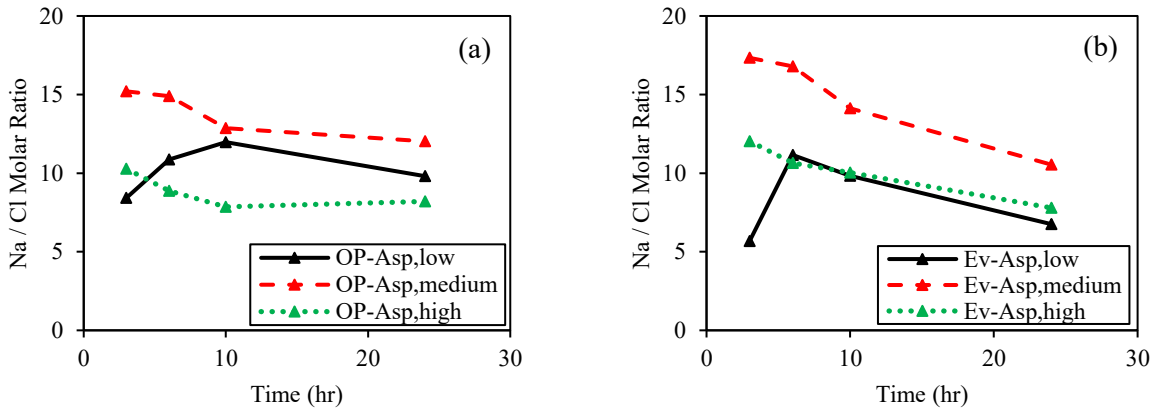

Figure 2-15. The Na/Cl molar ratio measured during the water imbibition experiments for (a) OP and (b) Ev samples of three A_{sp} values. The accuracy of measured ion concentration is ± 0.1 mg/L.

Dissolution of sodium-bearing rock minerals is a possible source for sodium. According to the XRD results (Table 2-2), plagioclase is the only non-clay sodium-bearing mineral in our rock samples. However, dissolution of plagioclase in water and at room temperature is very slow (Huang and Kiang, 1972). A possible source for high Na/Cl is the sodium mobilized from the exchangeable sites caused by leaching of clay minerals in the shales (Keller and Da-Costa, 1989). According to Table 2-2, the clay fraction of our shale samples is composed of mica, illite and mixed I/S layer. Sodium is not the major cation in the interlayer of mica and illite (Figure 2-7) (Essington, 2005). Therefore, leaching of the exchangeable sodium in the interlayer of smectite (in the mixed I/S layer) is a possible source for high Na/Cl molar ratio.

For $A_{sp,low}$ samples, the Na/Cl molar ratio shows an initial increase and it declines at later time. For $A_{sp,medium}$ and $A_{sp,high}$ samples, the Na/Cl molar ratio decreases by time. This could be due to the net effect between leaching of exchangeable sodium from the clay minerals and dissolution-diffusion of chloride-bearing components (such as halite and potassium chloride). The initial high

Na/Cl molar ratio might be resulted from fast leaching of exchangeable sodium from the clay minerals. According to the imbibition results (Figure 2-10a), the sample with the higher clay content (Ev) has faster and higher water intake compared to the sample with lower clay content (OP). Fast water adsorption by clays facilitates leaching of interlayer cations into the solution. The later-time decrease in the Na/Cl profile could be the result of the dissolution of chloride-bearing components. Furthermore, over the course of the imbibition process, the water imbibes into the pore structure. The possible precipitated chloride-bearing salts (such as halite and potassium chloride) in the pore space could dissolve in water and diffuse back into the solution. The diffused chloride ions decrease the Na/Cl molar ratio of the solution at later times.

Potassium and chloride: The concentration of potassium increases during the water imbibition experiments, and its concentration is higher than the chloride concentration. The average K/Cl molar ratio for the OP and Ev samples is 5.9 and 3.9 respectively. The K/Cl profile during the water imbibition experiment is illustrated in Figure 2-16. The high K/Cl molar ratio could also be described in the similar way that Na/Cl profiles were described. The initial high K/Cl molar ratio might be resulted from fast leaching of exchangeable potassium from interlayer of illite and mica (Figure 2-7); and the later-time decrease in the K/Cl profile could be the result of the dissolution of chloride-bearing components.

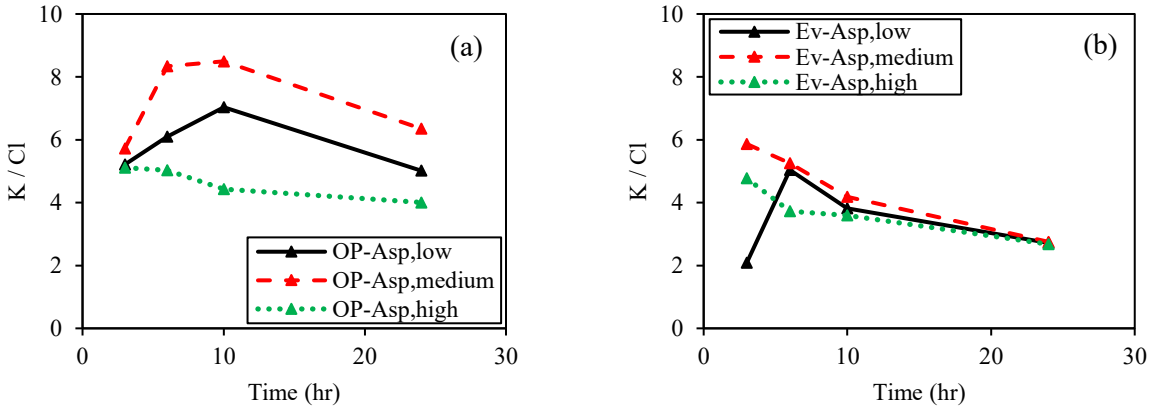

Figure 2-16. The K/Cl molar ratio during the water imbibition experiment for (a) OP and (b) Ev samples of three A_{sp} values. The accuracy of measured ion concentration is ± 0.1 mg/L.

Iron and sulfate: Both the imbibition experiments and field observations show a general increasing trend in the sulfate concentration profile (Figures 2-3g-I, 2-13d, and 2-14d); while the

iron concentration profile shows an initial increase followed by a gradual decrease over time (Figures 2-3d-f, 2-13f, and 2-14f). The laboratory sulfate concentration profile shows two distinct rate of increase (Figures 2-13d and 2-14d). During the imbibition experiments, the sulfate concentration experiences a sharp increase initially. The concentration increases slowly at later times as the imbibition progresses. A possible explanation describing both the sulfate and iron concentration profiles is the formation of iron and sulfur-bearing complexes such as iron sulfate (Reaction 2-2):

$$Fe^{2+} + SO_4^{2-} \rightarrow FeSO_4 \tag{2-2}$$

It must be noted that the field data of sulfate concentration is scattered and it is difficult to make judgment about the change in the slope of the concentration profile (Figures 2-3g-i). Iron is very reactive (Essington, 2005) and its reaction with sulfate could decrease the sulfate concentration in the solution. High reactivity of iron promotes complexation (and precipitation) of iron ions. For instance, depending on the oxidation state of the elements, it is possible for iron to precipitate in the form of iron (II) oxide (Reactions 2-3, 2-4), iron (III) oxide (Reaction 2-5), goethite (Reaction 2-6), hematite (Reaction 2-7), and magnetite (Reaction 2-8):

$$FeSO_4 + 2OH^- \rightarrow Fe(OH)_2 + SO_4^{2-} \tag{2-3}$$

$$Fe^{2+} + 2OH^- \rightarrow Fe(OH)_2 \tag{2-4}$$

$$Fe^{3+} + 3OH^- \rightarrow Fe(OH)_3 \tag{2-5}$$

$$Fe^{3+} + 3OH^- \rightarrow FeOOH + H_2O \tag{2-6}$$

$$2FeOOH \rightarrow Fe_2O_3 + H_2O \tag{2-7}$$

$$Fe(OH)_2 + 2FeOOH \rightarrow Fe_3O_4 + 2H_2O \tag{2-8}$$

Precipitation of iron-bearing components could be the reason for decrease in the iron concentration at later times during the flowback/imbibition processes. Further investigation of redox potential of the solution will provide supplementary information to address the aqueous complexations during the water imbibition and flowback processes.

Barium: The barium concentration increases during the water imbibition experiments (Figures 2-13e and 2-14e). Similarly, the barium concentration increases over the course of the flowback process (Figures 2-3a-c). However, the XRD analysis (Table 2-2) does not detect any barium-bearing component in the bulk-rock. One of the limitations of XRD is that it uses small volume of rock sample for its analysis. Therefore, it is very possible to miss local mineral-concentrated areas such as the precipitated salt crystals. Section 2.1.3.5 presents the results of EDS analysis as a complementary test for XRD analysis to explore the surfaces of the natural fractures for the possible mineral-concentrated areas.

2.3.5. Surface Element Analysis Results

Although both the field and laboratory data indicate the presence of barium in the flowback/imbibition water, XRD does not detect any barium-bearing component in the bulk-rock mineralogy. The negligible barium in the bulk rock mineralogy of the OP and Ev samples are also in agreement with the acid digestion experimental results presented in Chapter 3. In order to investigate the possible mineral-concentrated spots in local areas, EDS analysis is performed on the surface of natural fractures. Moreover, to compare the elemental distribution in the rock matrix and natural fracture surfaces, the fresh break surfaces of the samples are also analyzed by EDS. The EDS analysis of the fresh break surface of the rock samples can also be a qualitative representative of the bulk rock mineralogy. Figures 2-17 and 2-18 show the EDS results for both the fresh break and the natural fracture surfaces of the OP and Ev samples, respectively.

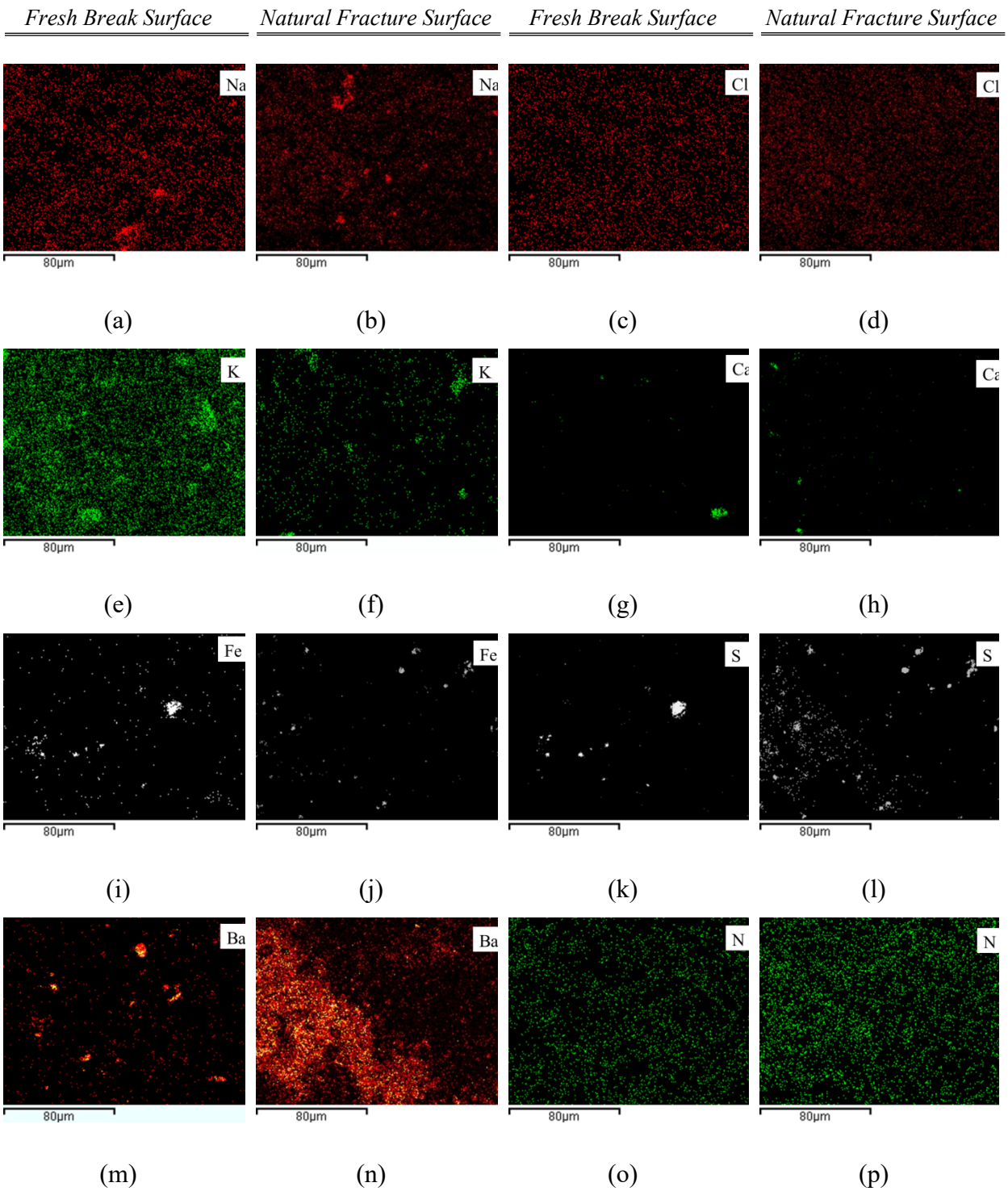

Figure 2-17. Elemental maps from EDS analysis of the fresh break and natural fracture surfaces of a sample from the OP formation.

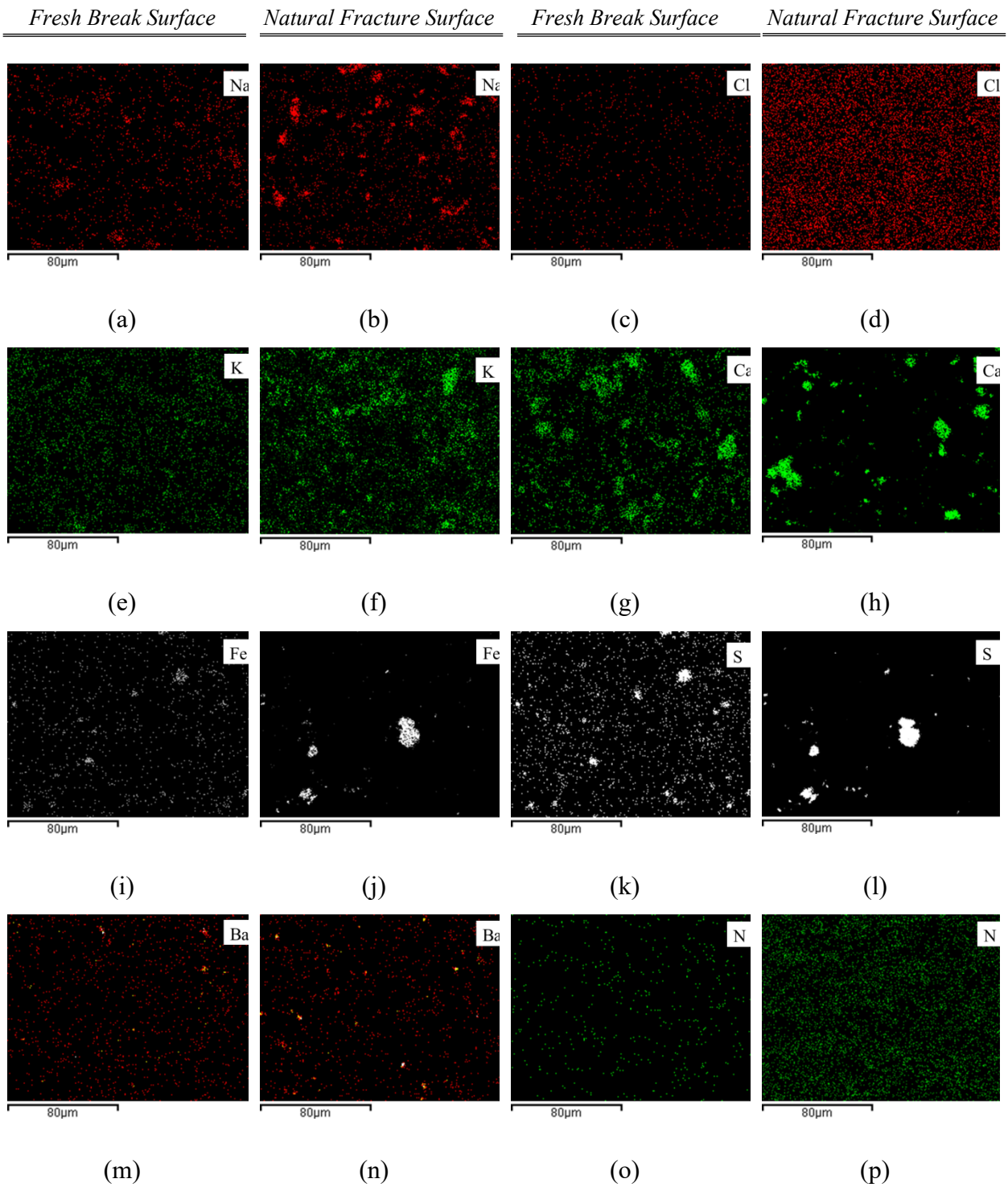

Figure 2-18. Elemental maps from EDS analysis of the fresh break and natural fracture surfaces of a sample from the Ev formation.

The elemental maps for both iron and sulfur (Figures 2-17i-l and 2-18i-l) indicate that the iron and sulphur elements occur in the similar areas. The barium map for the OP sample (Figure

2-17n) shows barium-concentrated areas on the surface of natural fractures. The other ions are almost uniformly distributed on both the fresh break and natural fracture surfaces.

Figure 2-17n shows a noticeable barium-concentrated area on the surface of a natural fracture in the OP sample. A visually notable barium vein was also found on the surface of a natural fracture in one of the samples of the Lower Evie (LEv) formation (located below the Ev formation). Figure 2-19 shows this barium vein and the EDS results of the barium distribution for this zone. It is worth mentioning that the results of SIMS (secondary ion mass spectrometry) analysis suggest that the precipitated barium-bearing minerals on the surface of natural fractures are likely mainly consist of witherite ($BaCO_3$) (Section 3.3.3).

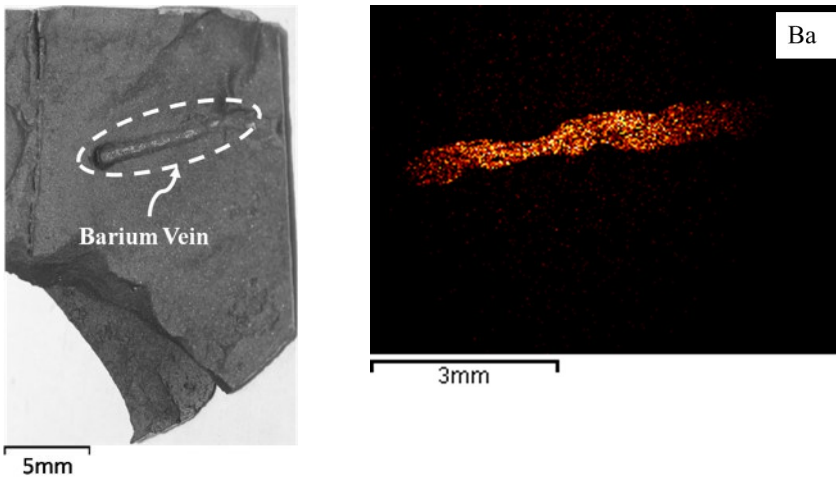

(a) (b)

Figure 2-19. (a) Picture of a barium vein found on the surface of a natural fracture in a sample from the LEv Formation and (b) the corresponding barium map from EDS analysis of the barium vein zone.

Since the barium concentration is high in the natural fractures and negligibly low in the bulk-rock mineralogy, the barium ions in the flowback water might have been originated from the natural fractures (formation water or precipitated salt crystals in the natural fractures). It is worth mentioning that barite is also a common additive to the drilling fluid to increase its density (Tehrani et al., 2009; Nguyen et al., 2011). The target wells in this research are drilled with oil-based drilling fluids, and among them, there are some wells that are drilled with no barium-bearing additives. However, the produced flowback water from almost all wells are relatively high.

Co-presence of Fe and S might be an indication of iron-sulfur-bearing components. Considering the XRD results (Table 2-2), ankerite/Fe-dolomite and pyrite are the possible sources of iron in the bulk-rock, and the only source of sulfur is pyrite. Since ankerite/Fe-dolomite does not have sulfur, pyrite is likely located in the white areas of Figures 2-17i-l and 2-18i-l.

According to Table 2-2, the concentration of pyrite in the Ev formation is five times higher than that in the OP formation. Pyrite oxidation could increase mineral dissolution through an acid generation-neutralization process (Chermak and Schreiber, 2014; Descourvières, 2010; Schieber, 2007; Shaver et al., 2006).

In Figure 2-20, we plot the pH and dissolved oxygen (DO) of the flowback water samples collected at different times during the flowback of the Mu, OP, and Ev wells. The measured pH values are slightly above 8 ($pH \approx 8 - 8.5$). It must be noted that the pH values plotted in Figure 2-20 are measured in the laboratory, where the samples were in contact with air. The measured DO in the flowback water samples ($\mathrm{DO} \approx 8 - 8.5$ mg/l) is slightly smaller than the measured DO for the DI water ($\mathrm{DO} = 8.58$ mg/l), which can be due to the ions present in the flowback water samples. Presence of oxygen promotes oxidation reactions which could impact the dissolution/precipitation of salts in the water samples, and ultimately the pH values.

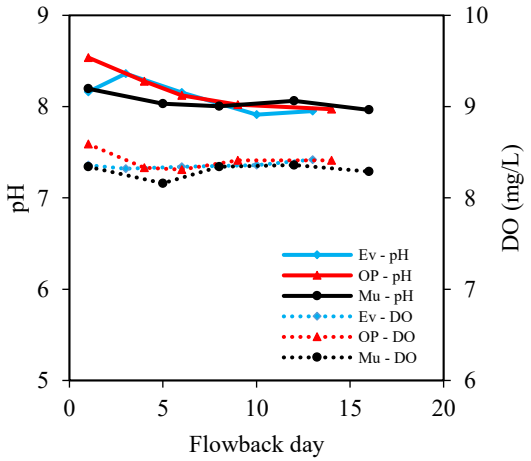

Figure 2-20. The pH and DO of the flowback water samples collected at different times during the flowback of the Mu, OP, and Ev wells. σ_{st} for pH and DO measurements are 0.16 and 0.35 mg/l respectively.

Some researchers have crossed out the possibility of mineral dissolution as a source for highly saline flowback water because the pH of the flowback water remains around neutrality range (Haluszczak et al., 2013). However, being near neutral range of pH does not necessarily guaranty that the mineral dissolution is negligible. For instance, simultaneous pyrite oxidation and calcite dissolution processes increase mineral dissolution while keep the pH around the neutral range. In this particular case, pyrite may undergo oxidation and produce acids which can dissolve rock constituents (Chermak and Schreiber, 2014; Chou, 2012; Descourvières, 2010; Schieber, 2007). One of the possible sources for the oxygen required for pyrite oxidation is the air carried alongside the injected fracturing water and proppant into the reservoir. The oxygen reacts with pyrite in presence of water and generates sulfate and acid:

$$FeS_2 + \frac{7}{2}O_2 + H_2O \rightarrow Fe^{2+} + 2SO_4^{2-} + 2H^+ \quad (2\text{-}9)$$

$$Fe^{2+} + \frac{1}{4}O_2 + \frac{5}{2}H_2O \rightarrow Fe(OH)_3 + 2H^+ \quad (2\text{-}10)$$

Calcite has the potential to neutralize the acidity generated by pyrite oxidation (Chermak and Schreiber, 2014; Descourvières, 2010; Schieber, 2007):

$$CaCO_3 + H^+ \rightarrow Ca^{2+} + HCO_3^- \quad (2\text{-}11)$$

Both reactions 2-9 and 2-11 increase the mineral dissolution. The acid generated by reaction 2-9 is consumed by reaction 2-11 to dissolve calcite. In the other words, the presence of calcite acts as a buffer system (Descourvières, 2010; Schieber, 2007).

In addition to calcite, dolomite could also play as a buffer helping the system to neutralize the acid produced by the pyrite oxidation (Descourvières, 2010). The dolomite dissolution reaction is (Lund et al., 1973):

$$CaMg(CO_3)_2 + 4H^+ \rightarrow Ca^{2+} + Mg^{2+} + 2CO_2 + 2H_2O \quad (2\text{-}12)$$

The acid produced by the pyrite helps the dissolution of calcite (Reaction 2-11) and dolomite (Reaction 2-12) and increases the ion content in the water. Presence of natural buffer systems such as calcite and dolomite can potentially neutralize the produced acid by the acidic reactions (such as reactions 2-9 and 2-10). Therefore, neutrality of the flowback water does not necessarily guaranty that the mineral dissolution has minor effect on the chemistry of the flowback water. More investigations are required to investigate the role of natural buffer systems on the mineral dissolution and the solution pH. Also, thermodynamic simulation of water-rock interactions can provide detailed analysis about the effect of reservoir/experimental conditions on elemental speciation and solution pH.

Since the concentrations of pyrite, calcite and dolomite are higher in Ev compared with that in OP (Table 2-2), the acid generation-neutralization process could possibly contribute to the higher salinity of the flowback water in Ev as compared to that in OP.

Reactions of pyrite with calcite and dolomite in the presence of oxygen and water could be a possible source of the sulfate ions production. The general buffering reactions of calcite and dolomite for pyrite oxidation are:

$$FeS_2 + 4CaCO_3 + \frac{15}{2}O_2 + \frac{7}{2}H_2O \rightarrow Fe(OH)_3 + 2SO_4^{2-} + 4Ca^{2+} + 4HCO_3^- \quad (2\text{-}13)$$

$$FeS_2 + \frac{15}{4}O_2 + \frac{3}{2}H_2O + CaMg(CO_3)_2 \rightarrow Fe(OH)_3 + Ca^{2+} + Mg^{2+} + 2SO_4^{2-} + 2CO_2 \quad (2\text{-}14)$$

Sulfate reduction at later stages of the flowback process could be one of the possible reasons for high barium concentration in later flowback water (Engle and Rowan, 2014). During the flowback process, the produced methane may react with sulfate and increase alkalinity, which

further enhances the barium solubility. Reaction 2-15 shows the sulfate reduction reaction in the presence of methane that could occur during the flowback process:

$$CH_4 + SO_4^{2-} \rightarrow H_2O + HS^- + HCO_3^- \quad (2\text{-}15)$$

Since barium primarily originates from natural fractures, the barium concentration profile during the flowback process can be a signature of the connectivity between natural and induced fractures. In this context, a steep slope in the barium concentration profile for the Ev well (Figure 2-3c) could be an indication of more complex fracture network. Conversely, the barium concentration profiles for Mu and OP exhibit smaller slopes compared to that of Ev (Figures 2-3a,b), and their fracture networks are likely simpler and less dendritic. Moreover, the initial barium concentration in the flowback water for Mu and OP is almost zero (Figures 2-3a,b) while the initial barium concentration is about 300 ppm in the flowback water from Ev (Figure 2-3c). Higher initial concentration of barium ions in the flowback water from the Ev well compared to that from the Mu and OP wells also complies with the statement that the fracture network is more complex in Ev compared with that in Mu and OP. These findings are also in agreement with the model results presented in Chapter 4. In Chapter 4 the salinity profile is used to characterize the fracture network complexity, and it was also shown that the fracture network is more complex in Ev as compared to that in Mu and OP.

2.4. Summary

This chapter presents laboratory and field analyses to investigate the origin of flowback salts. Field flowback water samples are collected at different flowback times from three different wells completed in the Horn River Basin. Flowback water samples are analyzed for pH, dissolved oxygen, and individual ion concentrations. The ion concentration measurements are conducted by inductively coupled plasma mass spectrometry (ICP-MS) and ion chromatography (IC). Laboratory experiments include (i) rock mineralogy characterization using X-ray diffraction (XRD), (ii) water and oil contact angle measurements, (iii) water and oil imbibition tests, (iv) ion diffusion analysis during water imbibition by ICP-MS and IC, (v) electrical conductivity (EC)

measurements during water imbibition tests, (vi) cation exchange capacity (CEC) analysis of the shale rock samples, (vii) energy-dispersive X-ray spectroscopy (EDS) analysis of the surface of natural fractures and the fresh-break surface of the rock matrix.

According to the ICP-MS and IC results, there are significant amount of barium ion in the field flowback water samples. However, according to the XRD results, there is no barium-bearing component in the shale rock samples. The results from EDS analysis of surface of natural fractures indicate that barium ions in the flowback water are primarily originated from mineral-filled natural fractures. Thus, the barium concentration profile during flowback process can be an indication of the connectivity between the induced and the pre-existing natural fractures. In other words, the shape of the barium concentration profile during flowback can be a signature of the complexity of fracture network.

During water imbibition experiments, EC and individual ion concentrations increase over time. The increasing EC trend is higher and faster for samples with higher clay content, which corresponds to their higher CEC values. Additionally, the average Na/Cl and K/Cl molar ratios are about 11 and 5 during the water imbibition experiments, respectively. Furthermore, both Na/Cl and K/Cl molar ratios show an increasing trend at early times, and a gradual decreasing trend at later times during imbibition experiments. These results suggest that leaching of clay minerals can be a key mechanism for ion transfer from rock to water at early stage of the imbibition process. The dissolution-diffusion of chloride-bearing minerals (i.e., NaCl and KCl) can be responsible for the decreasing trends in Na/Cl and K/Cl molar ratios at later times during imbibition experiments.

The pH of the flowback water samples (measured in laboratory) is slightly above the neural value (pH~8). Presence of natural buffer systems (such as calcite and dolomite) can be responsible for the neutrality of the produced flowback water. More specifically, dissolution of buffering minerals (i.e., calcite and dolomite) can increase the ion concentration in the flowback water while keeping the pH of the water (i.e., flowback water) near the neutral range. It must be noted that the pH of the flowback water samples are measured at laboratory, where the water samples exposed to air for a long time. Thus, the reported pH values of the flowback water samples may not necessarily reflect the pH of the water at reservoir conditions. Future studies should account for the differences between reservoir and laboratory conditions (such as redox-state, temperature, and pressure) to better understand the role of natural buffer systems at downhole conditions.

Nomenclatures

A_{sp}	Specific surface area
$A_{sp,high}$	High specific surface area
$A_{sp,low}$	Low specific surface area
$A_{sp,medium}$	Medium specific surface area
CEC	Cation exchange capacity
DI	Deionized
EC	Electrical conductivity
EDS	Energy-dispersive X-ray spectroscopy
Ev	Evie
HRB	Horn River Basin
IC	Ion chromatography
ICP-MS	Inductively coupled plasma mass spectrometry
LEv	Lower Evie
Mu	Muskwa
n	Number of measurements
OP	Otter-Park
SIMS	Secondary ion mass spectrometry
XRD	X-ray diffraction
σ_{st}	Standard deviation
θ	Contact angle

Chapter 3

Chemical Analysis of Flowback Water and Gas Shale Rock: Acid Digestion and Sequential-Ion Extraction Experiments

3.1. Introduction

Unconventional oil and gas reservoirs are emerging as an important source of energy in the United States and Canada (Frantz et al. 2005). These low-permeability reservoirs are commonly developed using multi-fractured horizontal wells (Ning et al. 1993). During fracturing operations, fracturing fluid (which mainly consists of water) is injected into the well to induce fractures (Engelder et al., 2014). The well is then sometimes shut-in (soaking period) to improve the hydrocarbon production (King, 2012; Lan et al., 2014; Makhanov et al., 2014). Later on, the wells are put on flowback to recover the injected fracturing fluid at the surface facilities (Abbasi et al., 2014). Depending on the reservoir properties (such as rock mineralogy) and the operational conditions (such as fracturing fluid type), 10% to 70% of the total injected fluid may be recovered during the flowback process (Hillard et al., 2013; Ghanbari and Dehghanpour, 2016).

The field data show that the chemistry of the water recovered during the flowback operations is significantly different than that of the water injected for hydraulic fracturing (Rimassa et al., 2009; Haluszczak et al., 2012). For instance, in the Horn River Basin (HRB), slick water, with similar salinity levels as fresh water, is injected into the reservoir during fracturing (Johnson and Johnson, 2012), while the recovered flowback water is highly saline (40,000-70,000 ppm) (Bearinger, 2013; Engle and Rowan, 2014; Capo et al., 2014), containing both soluble ions and insoluble complexes that increase in concentration over time (Balaba and Smart, 2012; Ziemkiewicz and He, 2015; Roshan et al., 2016).

Several past studies focused on the flowback chemical analysis to evaluate the hydraulic fracturing operations and to forecast reservoir performance. For instance, flowback chemical data have been used for quick characterization of the induced fracture network (Ghanbari et al., 2013; Bearinger 2013; Gdanski, 2010). A qualitative correlation was developed between fracture network complexity and salt concentration profiles measured during the flowback period by Bearinger (2013). Analysis of flowback data from the HRB wells indicates that the shape of the salt concentration profiles is related to the fracture network complexity (Ghanbari et al. 2013). A mathematical model is proposed in Chapter 4 to characterize the complexity of fracture network using flowback salinity profiles.

Despite the economic justification of hydraulic fracturing, its adverse environmental impacts have raised serious concerns about the contamination of ground and surface water as well as the consequential hazards to environment and public health (Wellman et al., 2009; Cheng and Saiers, 2009; Howarth et al., 2011; Jackson et al., 2013; Vengosh, 2014; Subramani and Jacangelo, 2015; Reagan et al., 2015; Gallegos et al., 2015; Li et al., 2016). Osborn et al. (2011) analyzed samples from water wells located near hydraulic fracturing sites. They found that the water was contaminated with methane from the deep shale formations due to hydraulic fracturing operations. Furthermore, flowback water is highly saline and may contain toxic elements such as strontium, arsenic, selenium, and barium (Warner et al., 2012; Balaba and Smart, 2012; Sun et al., 2013; Haluszczak et al., 2013). Therefore, knowledge of flowback water composition and the origin of flowback ions are helpful for environmental assessment and selection of appropriate remediation strategies.

Despite the fact that flowback chemical analysis is used in assessing fracturing operations, the shale-water interactions are still poorly understood. For instance, the source of ions in flowback water is still a matter of debate. It has been proposed that dissolution of rock constituents is the major reason for altered chemical composition in the flowback water (Blaunch et al. 2009). However, Haluszczak et al. (2013) suggested that mixing of the injected fracturing fluid with in-situ formation brine may result in saline flowback water. Moreover, shales have clay minerals (Carman and Lant, 2010) which may undergo ion exchange reactions in the presence of water. Such reactions can further impact chemical composition of the flowback water. Furthermore, mineral filled natural fractures and local precipitated salts (Ali and Hascakir, 2015; Gale et al., 2014) can react with water and impact the flowback water chemistry during the hydraulic fracturing operations. Additionally, experimental analysis of flowback water may not necessarily represent the flowback water chemistry as the reservoir conditions are different than the laboratory conditions. For instance, different pressure, temperature, and redox state in the laboratory compared with those in the reservoir alters the thermodynamic equilibrium of the flowback water.

This chapter analyzes flowback water and downhole shale rock samples from the HRB to investigate the role of shale-water interactions on the flowback water chemistry. The intact flowback water samples are tested over the flowback period for their electrical conductivity (EC), total salts concentration, pH, and dissolved oxygen (DO), and individual ion concentration.

Different equilibrium states at the laboratory and reservoir conditions leads to the precipitation of some ions in the intact flowback water samples. In order to account for these precipitated salts (which were a part of the original flowback water), the flowback water samples are digested in acid. The rock composition is determined using XRD. Furthermore, two extraction methods are used to characterize the nature of the leachable ions from the shale rock samples.

3.2. Experiments

Materials: The field flowback water samples are collected from wells drilled in the Muskwa (Mu), Otter-Park (OP), and Evie (Ev) members of the HRB. The shale rock samples belong to the EV and OP formations. Shale rock samples from the Mu formation were unavailable for rock analysis. Details of reservoir geology and HRB shales can be found in Section 2.2.1.

Experimental Workflow: Figure 3-1 illustrates the experimental workflow performed on the flowback water and shale rock samples.

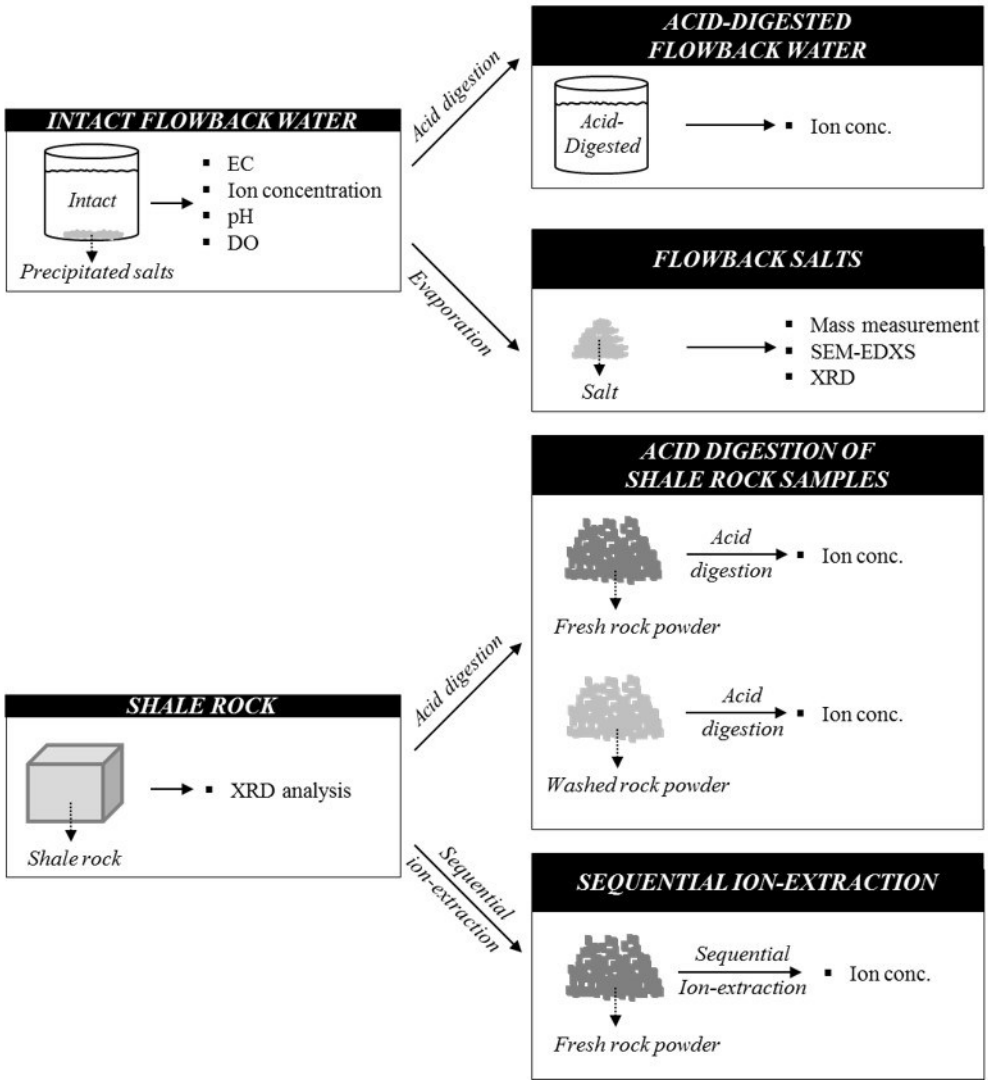

Figure 3-1. Experimental workflow for analysis of the flowback water and shale rock samples

3.2.1. Intact Flowback Water Samples

The EC, pH, DO, and the concentration of individual ions are measured for the intact flowback water samples collected at different flowback times. ICP-MS analysis is used to determine the ion concentration. Furthermore, the total mass of the salts are measured after drying the intact water samples. For this purpose, the samples were first shaken for 5 minutes. Afterwards, a 1 ml sample is taken from the homogenous suspension and dried overnight at 200°F. The mass of the remaining salts is reported for different flowback times. The salts are further analyzed using

XRD and SEM-EDS to investigate the type of the flowback salts, and the results are presented in the Appendix A.

3.2.2. Acid-Digested Flowback Water Samples

There are visible precipitated salts in the intact flowback water samples (Figure 3-2). Therefore, the chemistry of the intact flowback water, under the laboratory conditions, may not be a good representation of the original flowback water chemistry. Nitric acid is used to digest the intact flowback water samples (including the precipitated salts). ICP-MS analysis is used for determination of the ions in the acid-digested flowback water samples.

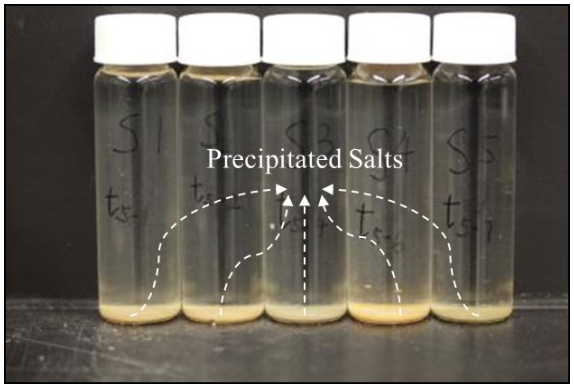

Figure 3-2. Precipitated salts in the intact flowback water samples. The flowback water samples belong to the Mu well and represent different flowback times.

3.2.3. Shale Rock Analysis

Leaching of the shale constituents into the fracturing fluid is one of the mechanisms impacting the flowback water chemistry (Blaunch et al. 2009; Balaba and Smart, 2012). In order to investigate how strongly the ions are attached to shale matrix, first, the rock composition is determined by XRD. Then two different extraction experiments are performed on the shale rock samples: (i) acid digestion of fresh and washed rock samples and (ii) sequential ion-extraction.

To evaluate the ability of deionized (DI) water to leach out the ions from shale rocks; acid digestion is performed on both fresh and washed shale rock samples. The fresh samples are prepared by milling down the shale rock samples into powders with an average particle diameter of about 1 μm. Acid digestion requires the addition of 4 ml of concentrate HNO_3 (trace metal grade 205L A509-1212Lot No. 1114100) and 1 ml of concentrate HCl (trace metal grade 4L A508-4 Lot 4114020) to each sample. The digestion process is then carried out at 1600W for 9.5 min. Next, the volume is increased to 25 ml using DI water. Afterwards, the solution was filtered and analyzed using ICP-MS. The washed sample preparation starts off with the same milling technique used for the fresh samples. Subsequently, 20 g of rock powder and 80 g of DI water are stirred for 2 hrs to wash the sample. The suspension is then filtered, and the remaining rock powder is dried out at 200°F. Each washed sample went through 10 cycles of washing and drying during sample preparation. The same procedure used for acid digestion of the fresh samples is used for the rock powder obtained at the end of the 10^{th} washing cycle. The 10 step washing process is selected as further washing stages does not alter the chemistry of the extracted solution (Binazadeh et al., 2016).

In order to determine what percentage of the ions can be leached out from the shale, the sequential ion-extraction method developed by Tessier et al. (1979) is applied on the shale powders. This method uses extractants of different strengths to preferentially extract the ions from the powdered shale samples. To do this, shale rocks are milled down into powders of about 1 μm diameter. Five extractans of different strengths are sequentially used to extract the ions: (1) For the first extraction stage, 20 ml of 1.0 M $MgCl_2$ solution is added to 5 g of shale powder, and the resulted mixture is agitated at 200 rpm for 1 h at room temperature. The mixture is stored for 24 h to allow particle settle down; then it is filtered by filter paper of 1-5 μm mesh size. The ionic concentration of the filtered solution is measured by ICP-MS. The particle settle down, filtering, and ion concentration procedures are the same in all steps. (2) For the second extraction stage, 20 ml of 1.0 M sodium acetate solution is added to the residual rock powders obtained in step 1. The solution is agitated at 200 rpm for 4 h at room temperature. The resulted mixture went through particle settle down, filtering, and ion concentration measurement processes. (3) For the third extraction stage, 50 ml of 0.04 M $NH_2OH.HCl$ is added to the residual rock powder obtained in step 2. The solution is agitated at 200 rpm for 5.5 h at 96°C. The resulted mixture went through particle settle down, filtering, and ion concentration measurement processes. (4) For the fourth

extraction stage, 7.5 ml of 0.02 M HNO_3 is added to 12.5 ml of a 30% H_2O_2 solution and the pH is adjusted to 2.0. The resulting solution is added to the residual rock powder obtained in step 3. The solution is agitated at 85°C at 200 rpm. After 2 h, 7.5 ml of 30 % H_2O_2 is added to the solution. The solution is further agitated at 200 rpm for 3 h at 85°C. The resulted mixture went through particle settle down, filtering, and ion concentration measurement processes. (5) For the fifth extraction stage, 7 ml HCl (32% - 35%) and 2.3 ml HNO_3 (1 N) is added to the residual powder obtained in step 4. The mixture is agitated at 200 rpm for 2 h at room temperature. The resulted mixture went through particle settle down, filtering, and ion concentration measurement processes. The schematics of the sequential ion-extraction set-up and the experimental procedure are presented in Figure 3-3.

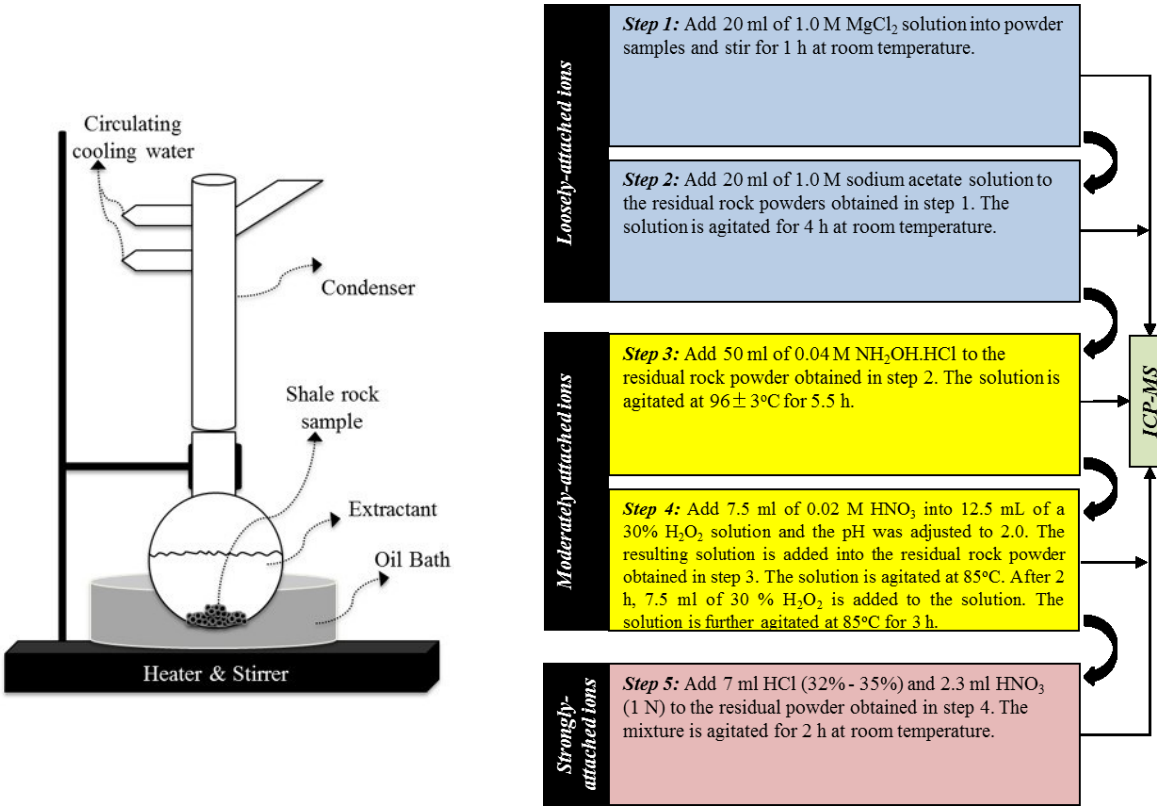

Figure 3-3. The schematics of set-up (left) and the experimental procedure (right) for the sequential ion-extraction experiment.

We categorized the extracted ions from the sequential ion-extraction experiment into three tiers of (i) loosely-attached ions: which includes the extracted ions from steps 1 and 2, (ii) moderately-attached ions: which includes the extracted ions from steps 3 and 4, and (iii) strongly-attached ions: which includes the extracted ions from step 5.

3.3. Results and Discussion

3.3.1. Flowback Water Analysis

In Figure 3-4a, we plot the EC and mass of the flowback salts (after evaporation) for the intact flowback samples collected at different flowback times for the Mu, OP, and Ev wells. The EC curve and flowback salt concentration curve show similar trends over time for all wells. On day one of the flowback process all three formations have a similar initial EC of around 45 mS/cm and approximately a total salts concentration of 25 g/L. Within the first 15 days of flowback the EC and flowback salts for Mu slightly increase, then reach a plateau at 56 mS/cm and 33 g/L, respectively. OP shows the similar trend as Mu, reaching plateaus of 60 mS/cm and 36 g/L. However, even 13 days after starting the flowback process, Ev shows a continuous increase with respect to time for both EC and total salts concentration. The maximum values recorded were 82.2 mS/cm and 50.5 g/L. Similar observations were also reported previously (Bearinger, 2013).

Figure 3-4b shows a plot of pH and DO of the intact flowback samples collected at different flowback times for the Mu, OP, and Ev wells. The measured pH for the intact flowback water samples of different times is around neutral range ($\mathrm{pH} \approx 7 - 7.5$). Presence of natural buffer systems such as calcite and dolomite (Chermak and Schreiber, 2014; Descourvières, 2010; Schieber, 2007; Lund et al., 1973) provides a possible explanation for the neutral pH range of the flowback water. Also, it must be noted that the pH values plotted in Figure 3-4b are measured for the intact flowback samples in the laboratory, which were in contact with air. The measured DO in our intact flowback water samples ($\mathrm{DO} \approx 8 - 8.5\ \mathrm{mg/l}$) is slightly smaller than the measured DO for the DI water ($\mathrm{DO} = 8.58\ \mathrm{mg/l}$), possibly due to the ions present in the intact flowback water samples. The presence of oxygen promotes oxidation reactions which could impact the dissolution/precipitation of salts in the water samples, and ultimately the pH values.

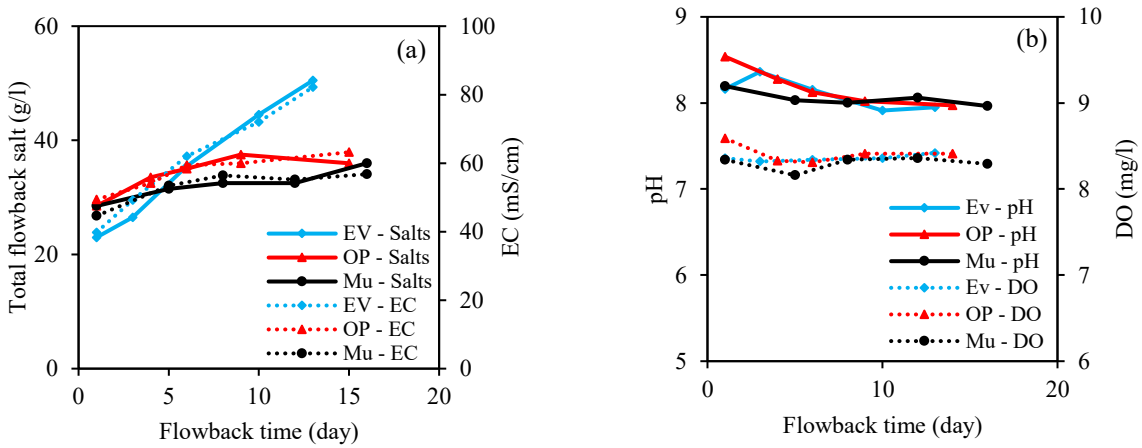

Figure 3-4. Intact flowback water analysis. (a) Total flowback salts (solid line) and EC (dashed line) versus flowback time. (b) pH (solid line) and DO (dashed line) versus flowback time. The standard deviation (σ_{st}) for the reported pH and DO values are 0.16, 0.35 mg/l, respectively. The accuracy of measured EC is ± 0.1 µS/cm.

The concentration of Na^+, K^+, Ca^{2+}, and Ba^{2+} versus flowback time for the intact flowback water samples are plotted in Figure 3-5. The intact flowback water contains visible precipitated salts (Figure 3-2). These precipitated salts were a part of the solution in the original flowback water under the reservoir conditions. However, different experimental conditions compared with that in the reservoir (such as temperature, pressure, and redox conditions) dictates different thermodynamic equilibrium for the flowback water in the laboratory; leading to precipitation of ions in the form of salts. In order to have a better representation of the chemistry of the original flowback water, the intact flowback water samples are digested in acid to dissolve the precipitated salts. The acid-digested solutions are then analyzed by ICP-MS and the results are presented in Figure 3-5.

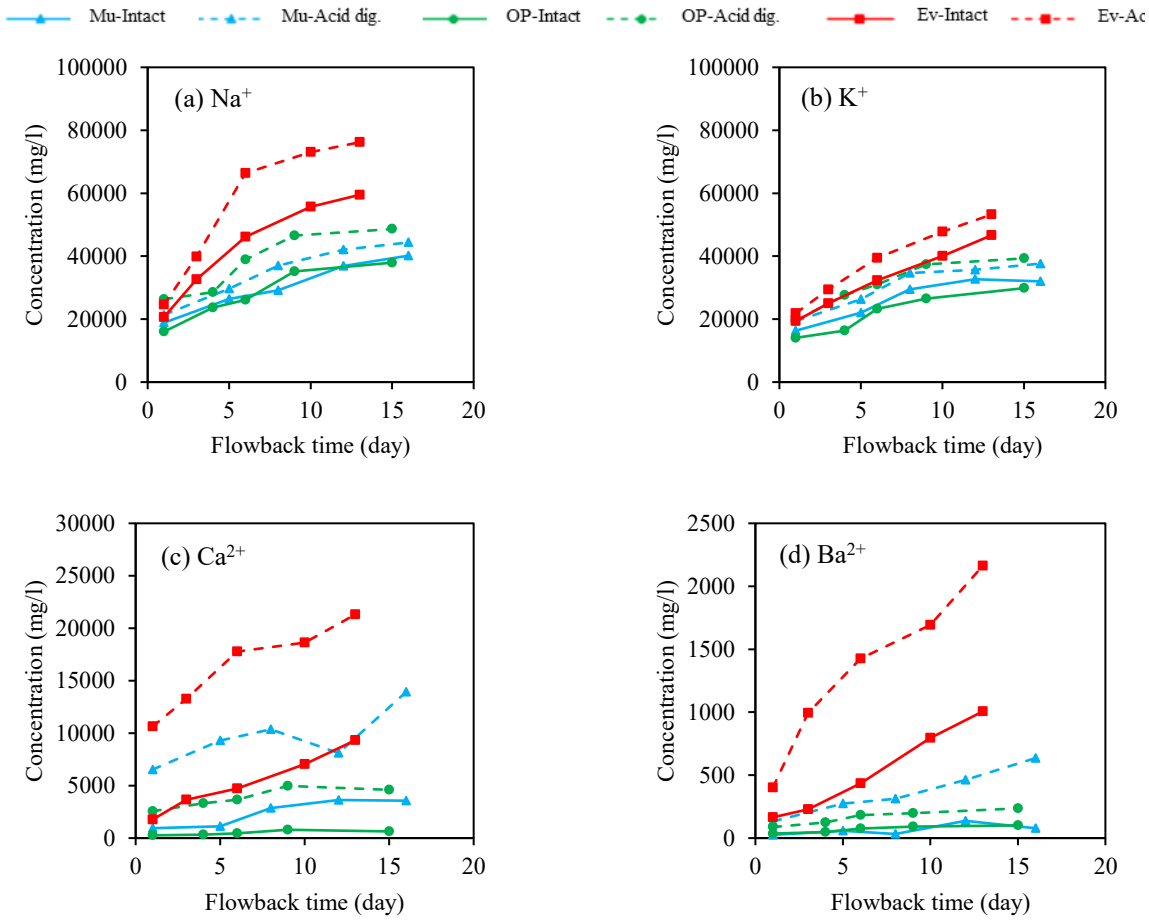

Figure 3-5. Individual ion concentration in the intact and acid digested flowback water versus flowback time: (a) Na^+, (b) K^+, (c) Ca^{2+}, and (d) Ba^{2+}. Different scales are selected for the Y-axis in order to show the difference between the ion concentration in the intact and acid-digested flowback water samples. The accuracy of measured ion concentration is ± 0.1 mg/l.

The main cation in the flowback water is Na^+. The concentration of ions generally increases over flowback time for both of the intact and acid-digested flowback water samples. Similar observations were also reported by other researchers (Roshan et al., 2016; Ziemkiewicz and He, 2015; Bearinger 2013; Ghanbari et al. 2013; Haluszczak et al., 2012). Mixing of fracturing fluid with in situ formation brine (Haluszczak et al., 2012), dissolution of rock constituents (Blaunch et al. 2009), water producing from fractures with smaller aperture (see Chapter 4), and extended shale-water exposure time (Roshan et al., 2016; Blaunch et al. 2009) have been suggested for increasing ion concentration over time during the flowback process.

Due to the digestion of the precipitated salts in acid, the concentration of ions is higher in the acid-digested samples compared with that in the intact samples (Figure 3-2). The ion concentration in the acid-digested flowback water samples is calculated using the ion concentration determined from ICP-MS, and from the original volume of the intact flowback water samples (including the precipitated salts).

For most of the wells, a general trend in the ion concentration in the acid-digested samples (dash lines in Figure 3-5) is that the monovalent cations show a sharp increase initially. The increase rate declines at later flowback times. The concentration of divalent cations however, shows a continuous increase over the course of the flowback process. In other words, the contribution of divalent cations in the flowback water chemistry increases over the course of the flowback process. This can be due to the slow dissolution rate of salts containing divalent cations. In fact, the high surface charge density of divalent cations (Essington, 2005) helps them to form a stable salt (Table A-1), which dissolve (in water) at a slow rate. The later flowback water produces from deeper fractures with smaller aperture size (see Chapter 4), with higher surface to volume ratio and also higher exposure time. More exposure time promotes the dissolution of stable divalent-based precipitated salts at later flowback times.

The difference between the ion concentration in the acid-digested and intact water samples is smaller and remains relatively constant over the flowback time for the monovalent cations. However, for divalent cations, this difference is relatively large and increases over the flowback time. These results suggest that (i) the divalent cations have a higher precipitation rate compared to the monovalent cations and (ii) the precipitation rate is more prominent at later times when the flowback water is more saline. Higher surface charge density of the divalent cations as opposed to that of the monovalent cations (Essington, 2005) is a possible reason for this behavior. The surface charge densities are 1.9594 and 1.1470 C/m^2 for Ca^{2+} and Ba^{2+} respectively, which are comparably larger than 0.9462 and 0.5511 C/m^2 for Na^+ and K^+ respectively (Essington, 2005). High surface charge density increases the affinity of the divalent cations for anions, and therefore, increases the chance to create complex ions precipitating in the form of salts (e.g. $CaCO_3$) in the intact flowback water samples. After evaporating the intact flowback water samples, the remaining salts are analyzed by XRD and SEM-EDS analyzes, and their results are presented in the Appendix A.

3.3.2. Shale Rock Analysis

The rock samples are analyzed using XRD and the results are presented in Table 1. The quartz content is 77 Wt.% and 32Wt.% in the OP and Ev samples, respectively. Also, the clay content of OP and Ev samples are 16 Wt.% and 33 Wt.%, respectively. The quartz content in the OP samples is over twice that of the Ev samples, and the clay content in the Ev samples is over twice that of the OP samples. Furthermore, no source of barium is found according to the XRD results. It must be noted the shales are heterogeneous and their mineralogy can significantly vary even in small scales (Diaz et al., 2010). Furthermore, XRD uses small amount of rock samples for its analysis. Therefore, the results presented in Table 3-1 might not be an accurate representation of all samples from the OP and Ev formations.

Table 3-1. The composition of the example OP and Ev shale rock samples by XRD analysis. The XRD used for characterization of rock mineralogy has a signal-to-noise ratio of 400.

Sample	OP	Ev
Non-Clay Content (Wt.%)		
Quartz	77	32
K-Feldspar	2	6
Plagioclase	2	6
Calcite	0	10
Ankerite/Fe-Dolomite	1	5
Dolomite	0	4
Pyrite	1	5
Total Non-Clay	84	67
Clay Content (Wt.%)		
Illite/Smectite (I/S)	5	14
Illite+Mica	11	19
Total Clay	16	33

In order to evaluate the ability of fracturing fluid for leaching out the ions from the reservoir rock, a 10-step ion-extraction procedure is designed using DI water. The rock samples before and after the washing process are digested in acid. The solution is then analyzed by ICP-MS to identify

the elemental composition of the rock samples. The elemental distribution of the shale samples before and after the washing process is compared in Figure 3-6. The Si element is excluded from the results as the digestion method described in Section 3-2 is not able to digest the silicate phase of the rock samples (Pena-Icart et al., 2011; Tessier et al., 1979).

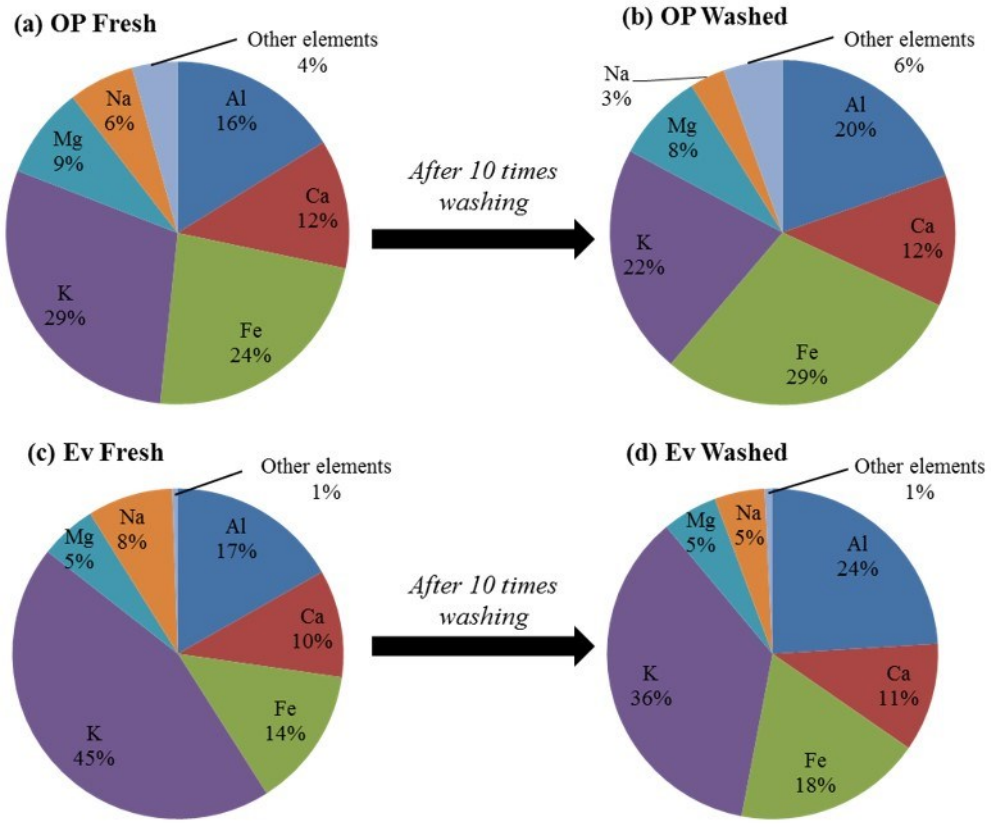

Figure 3-6. A comparison between the elemental distributions of the fresh and washed shale samples of (a,b) OP and (c,d) Ev obtained by the acid-digestion analysis. Si element is excluded from the acid digestion results. The accuracy of measured ion concentration is ± 0.1 mg/l.

According to Figure 3-6, potassium, iron, aluminum, and calcium are the major elements (that comprise ≥ 10% of the rock elemental composition) in the fresh OP and Ev shale samples. After the washing process, the contribution of potassium and sodium in the rock mineralogy is reduced compared with that of other elements (Figure 3-6b, 3-6d). In order to compare the rock and flowback water analysis results, the elemental concentration of major monovalent and divalent cations for the fresh and washed samples are shown in Figure 3-7. It must be noted that selection of the shale samples was based on having minimal or no visual natural fractures in the sample.

This is probably the reason for negligible barium concentration in the shale samples (Table 3-1 and Figure 3-6); as barium possibly originates from natural fractures (see Chapter 2).

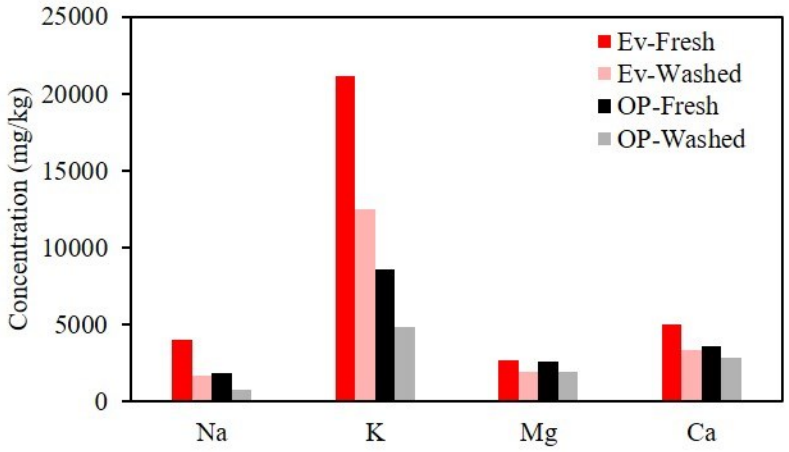

Figure 3-7. Elemental concentration of Na, K, Mg, and Ca for the fresh and washed samples of (a) OP and (b) Ev obtained by acid digestion. ICP-MS is used to analyze the acid-digested samples, with accuracy of ± 0.1 mg/l.

According to Figure 3-7, the difference between the concentration of elements in the fresh and washed samples is higher for the monovalent cations compared with that for the divalent cations. The surface charge density of the monovalent cations impacts their selectivity for the negatively-charged surfaces. The cations selectivity for the negatively charged surfaces (such as clays) is: $Ca^{2+}>Mg^{2+}>K^{+}>Na^{+}$ (Essington, 2005). Easier extraction of monovalent cations compared with that of divalent cations complies with the sharp increase in the concentration of monovalent cations in the early flowback water (Figure 3-4).

Potassium is the major element in both of the fresh OP and Ev shale samples, and its concentration is about five times higher than the sodium concentration. While, according to Figure 3-5, Na^{+} is the major cation in the flowback water, and its concentration is higher than K^{+} concentration. The sequential ion-extraction method is used to investigate how easily we can extract the ions from the shale samples, and the results are presented in Figure 3-8.

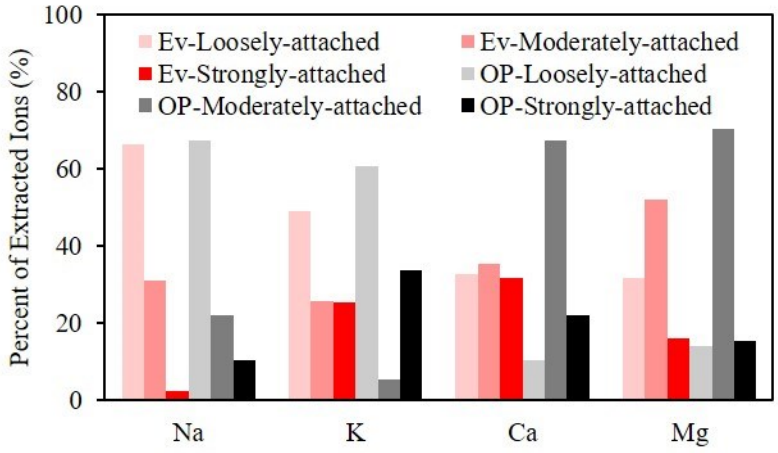

Figure 3-8. The results of the sequential ion-extraction on the OP and Ev shale rock samples. ICP-MS is used to analyze the acid-digested samples, with accuracy of ± 0.1 mg/l.

According to Figure 3-8, less than 75% of potassium belongs to the loosely- or moderately-attached tier. This value is over 90% for sodium; which indicates that it is easier to leach out sodium than potassium. This is also in agreement with the lower selectivity of sodium compared with potassium for negatively-charged shale particles (Binazadeh et al. 2016) and clay surfaces (Essington, 2005). This can be one of the reasons explaining that although potassium is the major component in the shale rock samples (Figures 3-6 and 3-7), Na^+ is the major cation in the flowback water (Figure 3-5) as it can be leached out from the shale samples easier than potassium.

Majority of the monovalent cations (Na^+ and K^+) belong to the loosely-attached tier. However, divalent cations (Ca^{2+} and Mg^{2+}) are mainly associated with the moderately- and strongly-attached tires. This complies with the cations selectivity for negative surfaces: $Ca^{2+}>Mg^{2+}>K^+>Na^+$ (Essington, 2005). Moreover, the portion of the loosely-attached monovalent cations is larger in the OP sample compared with that in the Ev sample. However, the portion of the loosely-attached divalent cations is larger for the Ev sample compared with that for the OP sample.

In this research it is believed that the loosely-attached ions can be mainly produced from (i) mixing with in-situ formation brine, (ii) dissolution of the precipitated soluble salts, and (iii) the leaching of the exchangeable cations from clay minerals. Analysis of field data suggests that the shale formations might be at the state of sub-irreducible water saturation (King, 2012), and this increases the possibility for the presence precipitated salts under in-situ conditions. NaCl and KCl

are among the major flowback salts (Figures A-2 and A-3). Both salts are very soluble in water (Table A-1). Therefore, dissolution of these soluble salts can be another possible source for the extraction of Na^+ and K^+ at the initial steps of the ion-extraction experiments. It must be noted that there are other parameters controlling the ion dissolution/precipitation. For instance, pH, DO, ion activity, ionic strength, and temperature play a key role on the thermodynamic equilibrium of the shale-water. The thermodynamic simulation of the shale-water interactions remains the subject of future studies to provide further information about the nature of the precipitated salts at different conditions.

In this research it is believed that the moderately-attached ions can be mainly produced from (i) the multivalent exchangeable cations in the clay minerals (e.g. Ca^{2+}, and Mg^{2+}), (ii) weakly-soluble salts (e.g. K_2SO_4), and (iii) relatively slow shale-water reactions. The multivalent cations have higher selectivity to the clay surface compared with the monovalent cations. Thus, they have less chance to be produced at the initial steps of the sequential ion-extraction experiment. One must note that, although we categorized the weakly-soluble salts and relatively slow shale-water reactions in the second tier (the moderately-attached ions); these mechanisms might be different at different conditions. For example, redox state, pH, and temperature are key parameters controlling the reactions and mineral solubility (Green and Perry, 2008). These parameters need to be further investigated for the shale-water systems.

One should note that the water chemistry also influences the shale-water interactions. For instance, according to Figure 3-5, for most of the ions, the concentration increases during the flowback process. The higher ion concentration at later flowback times increases the ionic strength of the flowback water. Higher ionic strength enhances the mineral dissolution through decreasing activity coefficients of the ions (Essington, 2005). In other words, the role of the dissolution of rock constituents is more pronounced at the later flowback stages. Another example is the ion exchange reactions in clays which depend on the water chemistry. At early flowback times, monovalent cations have relatively high concentration compared with the divalent cations (Figure 3-5). The elevated concentration of monovalent cations enhances leaching of divalent cations from the interlayer of the clay minerals.

3.3.3. Comparison with Seawater Composition

HRB shale samples are at sub-irreducible water saturation state (Dehghanpour et al., 2013), and therefore, it is challenging to extract and analyze the composition of formation water. On the other hand, HRB shale is marine sediments belonging to the Devonian age. Thus, seawater composition can possibly be an indication of the formation water composition. Table 3-2 compares the average ion concentration molar ratios (MR) in our flowback water and shale rock samples with the average values reported in the seawater (Benedict et al., 2012).

Table 3-2. Ion concentration ratios for intact and acid-digested flowback water and shale rock samples. The values of ionic molar ratio for seawater are the average values reported by Benedict et al. (2012). The absolute deviation from seawater composition is calculated from Eq. 3-1.

Molar ratio (MR)	Intact flowback water	Acid-digested flowback water	Acid-digested intact shale	Acid-digested washed shale	Seawater
Cl^-/Na^+	0.64 ± 0.035	0.96 ± 0.050	0.09 ± 0.001	0.31 ± 0.025	1.17
K^+/Na^+	0.80 ± 0.030	0.82 ± 0.070	4.92 ± 0.020	6.21 ± 0.045	0.02
Mg^{2+}/Na^+	0.03 ± 0.001	0.15 ± 0.015	0.93 ± 0.035	1.46 ± 0.025	0.23
Ca^{2+}/Na^+	0.07 ± 0.004	0.24 ± 0.020	1.86 ± 0.015	2.32 ± 0.040	0.04
Absolute deviation (σ_{abs}) from seawater composition					
Cl^-/Na^+	0.45	0.17	0.92	0.73	0
K^+/Na^+	39.01	40.00	245.00	309.50	
Mg^{2+}/Na^+	0.89	0.34	3.04	5.34	
Ca^{2+}/Na^+	0.75	5.00	45.50	57.00	

The absolute deviation (σ_{abs}) of ionic molar ratios from the seawater composition is calculated by Eq. 3-1.

$$\sigma_{abs} = \left| \frac{(MR)_{rock/flowback} - (MR)_{seawater}}{(MR)_{seawater}} \right| \quad (3\text{-}1)$$

where $(MR)_{rock/flowback}$ is the molar ratio of ions in shale rock or flowback water from either of intact or acid-digested samples, and $(MR)_{seawater}$ is the molar ratio of ions in the seawater. It must be noted that σ_{abs} is zero for seawater.

According to Table 3-2, the values of σ_{abs} are smaller for flowback water samples compared with those for the shale rock samples. Assuming that the formation water composition is similar to seawater composition, this result may suggest that mixing of formation water with fracturing fluid is more influencing the composition of the fracturing fluid compared with the dissolution of rock constituents.

σ_{abs} values are relatively small for Cl^-/Na^+ and Mg^{2+}/Na^+ molar ratios. These results may suggest that chloride, sodium, and magnesium ions in the flowback water may primarily originate from the formation water through either of (i) mixing of fracturing fluid with formation water or (ii) dissolution of precipitated salts in the pores or on the surface of natural fractures.

σ_{abs} values are relatively large for K^+/Na^+ and Ca^{2+}/Na^+ molar ratios. According to Figure 3-6, both potassium and calcium are among the major elements in our shale rock samples. Therefore, dissolution of Ca-/K-bearing rock constituents in the fracturing fluid is possibly a major source for the K^+ and Ca^{2+} ions in the flowback water.

Paytan et al. (2007) conducted sequential leaching experiments to extract barite ($BaSO_4$) from the seawater samples. They concluded that Sr^{2+}/Ba^{2+} molar ratio for marine barite is between 0.03 and 0.08. Figure 3-9 shows the plot of Sr^{2+}/Ba^{2+} molar ratio in flowback water samples of 48 wells completed in the Horn River Basin. According to Figure 3-9, the molar ratio of Sr^{2+}/Ba^{2+} in flowback water is higher than that in marine barite. This may suggest that the barium ions in the flowback water could have other sources than barite. This is in agreement with our secondary ion mass spectrometry (SIMS) analysis on the barium vein that is shown in Figure 2-19. More specifically, helium ion beam is used to etch the surface of the barium vein and analyze the composition versus depth. According to SIMS results (Figure 3-10), the barium vein is probably comprised of witherite ($BaCO_3$). It must be noted that the shale samples were not preserved, and therefore, the SIMS results presented in Figure 3-10 might be different if the analysis was conducted on preserved samples.

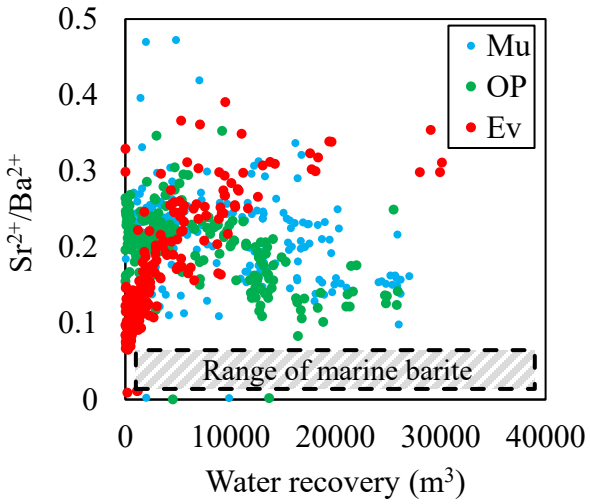

Figure 3-9. Molar ratio of Sr^{2+}/Ba^{2+} for 48 wells completed in the Mu, OP, and Ev formations of the Horn River Basin. The approximate range of Sr^{2+}/Ba^{2+} molar ratio is about 0.03 – 0.08 if barium is sourced from marine barite. The accuracy of measured ion concentration is ± 0.1 mg/l.

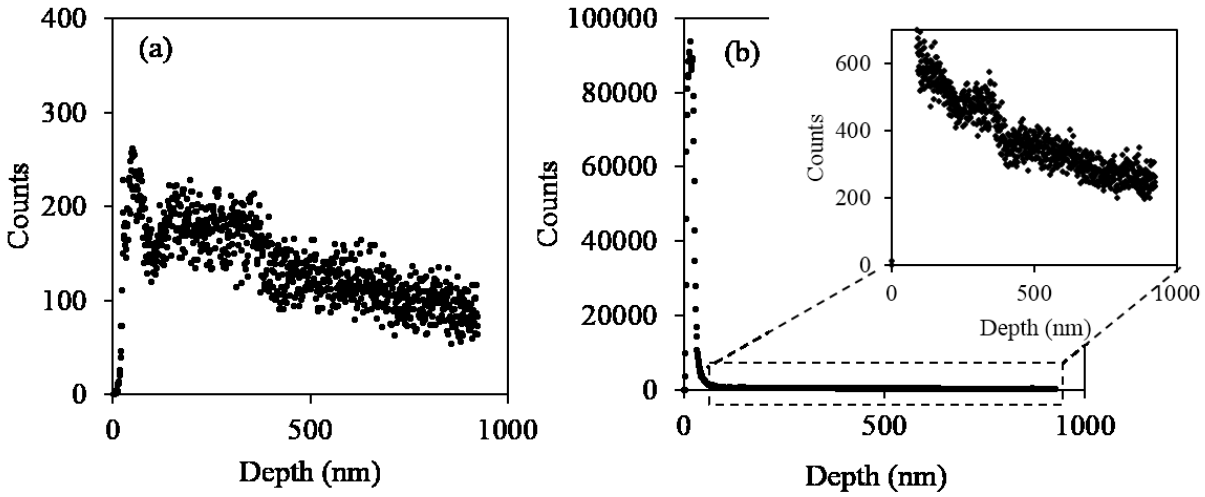

Figure 3-10. The results of secondary ion mass spectrometry analysis on the barium vein that is shown in Figure 2-19. Helium ion beam is used to etch the surface of the barium vein and analyze the composition versus depth. The trends for (a) barium and (b) carbon elements are similar versus depth, suggesting that witherite could be the main component in the barium vein.

3.3.4. Ion Concentration Cross-Plots

Several past studies investigated the source of ions in the produced brine from both conventional and unconventional reservoirs. Past studies showed that there is a linear relationship between the sodium and chloride ion concentrations in the produced wastewater from both conventional and unconventional reservoirs (Vidic, 2015; Hu and Mackay, 2017). Vidic (2015) concluded that the source of sodium and chloride ions in the flowback water and that in the brine produced from conventional reservoirs are similar if their Na:Cl ratios are similar. Figure 3-11a shows the logarithmic cross-plot of sodium ion concentration as a function of chloride ion concertation in the flowback water of 48 wells completed in HRB. The wells are completed in three different formations of Mu, OP, and Ev. There is almost a 1:1 linear relationship for Na:Cl ratio (in logarithmic scale) for all target wells/formations. This observation may suggest that the primary source of sodium and chloride ions in the flowback water is possibly the same, regardless of the formation and the well location. According to Table 3-2, the molar ratios of sodium-to-chloride in the flowback water is similar to that in the seawater. Assuming that the formation water has similar composition to seawater, the primary source of sodium and chloride ions in the flowback water from HRB is probably the mixing of formation water with the injected fracturing fluid. It must be noted that the observed trend and subsequent interpretations are specific to target wells of this study, and may not be applicable to other wells and formations.

According to Figure 3-11b-d, the logarithmic cross-plots of potassium, calcium, and magnesium ion concentrations versus chloride ion concertation is formation-dependent in the target 48 wells. The wells drilled in the Mu and OP formations have similar trends, while the wells drilled in the Ev formation behave differently. Ev wells also show different trends in their salinity profiles compared with that in Mu and OP wells (Sections 2.2.1 and 4.2.3).

The formation-dependency of flowback chemical data can be leveraged for characterization of fracture network complexity (Chapters 2 and 4). For the target 48 wells in HRB, the cross-plot of normalized monovalent and divalent cations also shows a distinct trend for Ev wells compared with that for Mu and OP wells. More specifically, the cross-plot of $Log[Na^+/K^+]$ versus $Log[Ca^{2+}/Mg^{2+}]$ is almost one order of magnitude smaller for Ev wells compared with that for Mu and OP wells (Figure 3-12). Future studies may combine this signature trend with other

characterization methods to evaluate the fracturing operations. For instance, the signature ion concentration cross-plots can complement the tracer test results for investigation of inter-well communications.

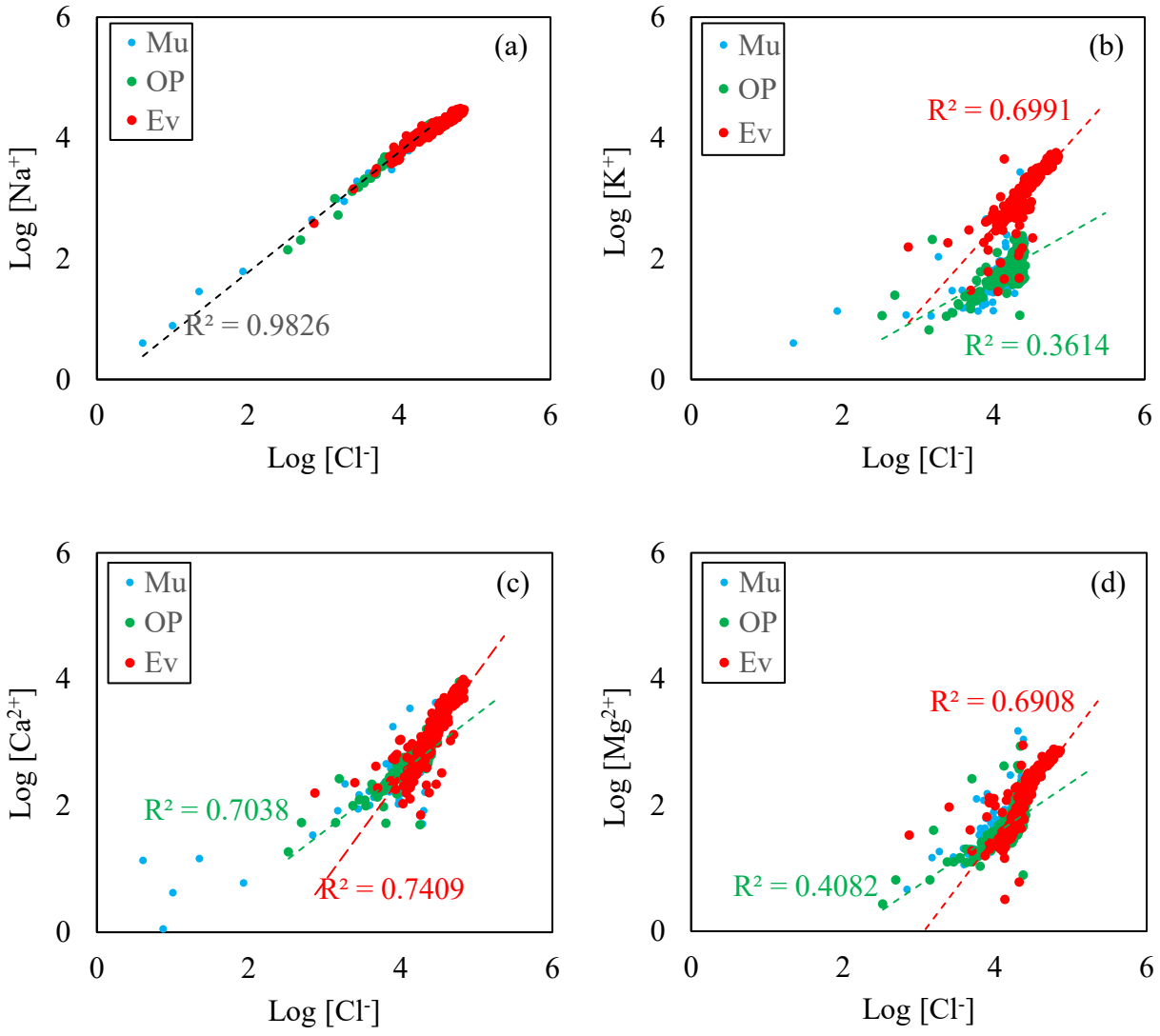

Figure 3-11. Logarithmic cross-plot of (a) sodium, (b) potassium, (c) calcium, and (d) magnesium ion concentrations versus chloride ion concentration in flowback water samples from 48 wells completed in the Horn River Basin. The accuracy of measured ion concentration is ± 0.1 mg/l.

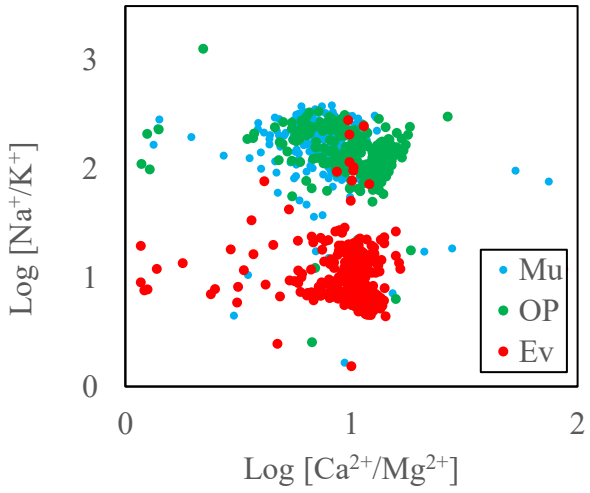

Figure 3-12. Logarithmic cross-plot of Na^+/K^+ versus Ca^{2+}/Mg^{2+} in flowback water samples from 48 wells completed in the Horn River Basin. The accuracy of measured ion concentration is ± 0.1 mg/l.

HRB is a marine shale with sub-irreducible water saturation (Dehghanpour et al., 2013). Dehydration and desiccation phenomenon are possible reasons for the sub-irreducible water saturation in low-permeable gas reservoirs (Bennion et al., 1999; Economides and Martin, 2007). On the other hand, it has been shown that bromide ion ($i.e., Br^-$) concentrates conservatively during evaporation of seawater (McCaffrey et al., 1987). Thus, assuming that evaporation of seawater is the primary reason for the sub-irreducible water state in HRB shales, Br^- concentration can be a proxy for evaluation of mixing of fracturing fluid with in situ formation brine (Haluszczak, 2011).

Figure 3-13 shows the logarithmic cross-plots of sodium, potassium, calcium, and magnesium as a function of bromide ion concentration in flowback water of 11 wells completed in HRB. The concentration profiles for wells drilled in Mu and OP formations show a consistent trend in the logarithmic scale, where the concentration of ions (i.e., Na^+, K^+, Ca^{2+}, and Mg^{2+}) increases (i.e., increasing tale) with $Log[Br^-]$ and reaches to a plateau (i.e., plateau tale) at $Log[Br^-] \approx 2.1$. For Ev wells, sodium ion follows the plateau tale of $Log[Na^+] - Log[Br^-]$ profile that observed for Mu and OP wells (Figure 1-13a). For other ions (i.e., K^+, Ca^{2+}, and Mg^{2+}), Ev wells somehow extend the increasing tale of $Log[Na^+] - Log[Br^-]$ profile that observed for Mu and OP wells (Figure 1-13b-d).

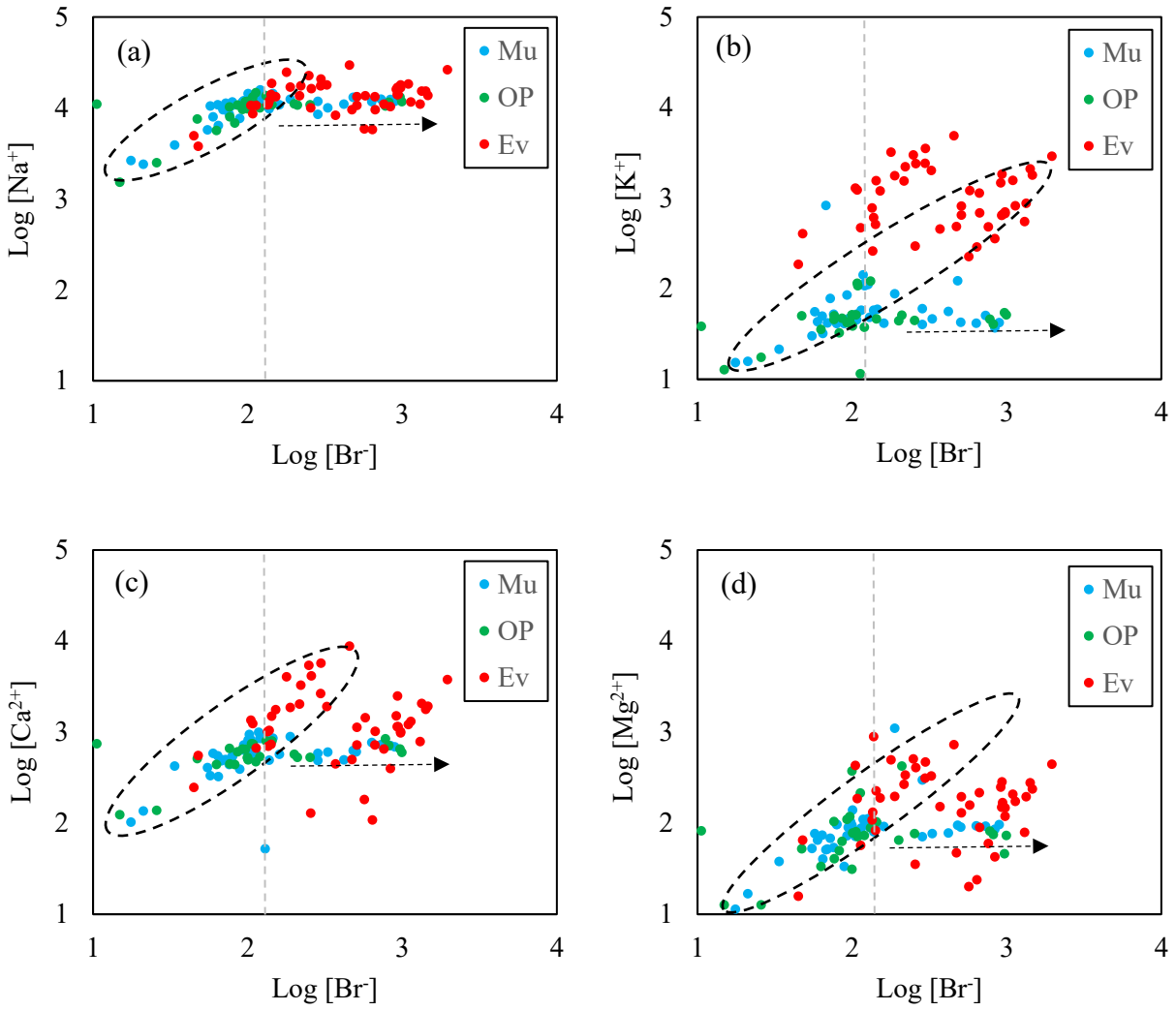

Figure 3-13. Logarithmic cross-plot of (a) sodium, (b) potassium, (c) calcium, and (d) magnesium ion concentrations versus bromide ion concentration in flowback water samples from 11 wells completed in the Horn River Basin. The accuracy of measured ion concentration is ± 0.1 mg/l.

3.4. Summary

This chapter presents the experimental results of acid digestion and sequential-ion extraction on the flowback water and gas shale samples. There are visible precipitations in the collected field flowback water samples. These salts were likely a part of the flowback water at the reservoir

conditions. The flowback water samples are digested in nitric acid, and the solutions are analyzed for ion concentration using ICP-MS and IC. The ion concentration is higher in the acid-digested flowback water samples compared with that in the intact flowback water samples.

Mineralogy of shale rock samples are characterized using XRD. Two extraction experiments are performed on the shale rock samples to investigate the role of shale-water interactions in the flowback water chemistry: (i) acid digestion of fresh and washed (with deionized water) rock samples and (ii) sequential ion-extraction.

Comparison between the composition of the intact and acid-digested flowback water samples suggests that divalent cations have a higher precipitation rate compared to monovalent cations. The precipitation rate is higher at later times as flowback water becomes more saline. Furthermore, the contribution of divalent cations in the flowback water chemistry increases at later flowback times. Late flowback water is mainly produced from deep small fractures which have more exposure time for the shale-water interactions. More exposure time promotes dissolution of stable divalent-based precipitated salts.

Acid digestion of the fresh shale rock samples indicates that potassium is the major element in our shale samples. However, sodium appears to be the major cation present in the flowback water samples based on our analysis of both intact and acid-digested flowback samples. Greater selectivity for K^+ over Na^+ for negative surfaces is a possible explanation for these results.

Formation water in the Horn River Basin is at sub-irreducible water saturation. Thus, it is challenging to characterize the composition of formation water. Compared with shale rock samples, the molar ratios of Cl^-/Na^+ and Mg^{2+}/Na^+ in the flowback water samples are closer to those in seawater. Thus, chloride, sodium, and magnesium ions in the flowback water for wells drilled in the Horn River Basin is likely to source from the mixing of formation water with fracturing fluid or dissolution of precipitated salts (in pore network or on the surface of natural fracture) in the fracturing fluid. The molar ratios of K^+/Na^+ and Ca^{2+}/Na^+ in the flowback water samples is significantly larger than that in seawater. Relatively large ratios of K^+/Na^+ and Ca^{2+}/Na^+ in the rock samples may suggest that K^+ and Ca^{2+} ions in the flowback water samples may originate from dissolution of rock constituents in fracturing fluid.

There is a 1:1 logarithmic-scale relationship between sodium and chloride ions in the flowback water produced from three formations of Mu, OP, and Ev. This observation may suggest that the primary source of sodium and chloride ions (likely formation brine) is not formation-specific. For other primary cations (i.e., K^+, Ca^{2+}, and Mg^{2+}), the cross-plots against Cl^- is formation-dependent. Although there is a general increasing trend for all wells, the slope is smaller for Mu and OP wells compared with that for the Ev wells. The formation-dependency of ion concentration in the flowback water is clearer when Na^+/K^+ is plotted against Ca^{2+}/Mg^{2+}, where in this plot, the Ev wells' data points are about one order of magnitude smaller than that of Mu and OP wells. The similarity between the flowback water of Mu and OP wells can also be observed from the logarithmic-scale cross-plots of Na^+, K^+, Ca^{2+}, and Mg^{2+} versus Br^-. For both formations, all profiles show an increasing trend with $Log[Br^-]$ up to $Log[Br^-] \approx 2.1$, and after that they approached to a plateau.

Chapter 4

Fracture Characterization using Flowback Salt Concentration Transient

4.1. Introduction

Unconventional oil and gas reservoirs are emerging as an important source of energy in the United States and Canada (Frantz et al. 2005). These low-permeability reservoirs are commonly developed using multi-fractured horizontal wells (Ning et al. 1993). A large volume of fracturing fluid is injected to create multiple fractures and increase the reservoir contact per well (Cheng, 2012; King, 2012). This fracturing fluid pumped into the formation needs to be recovered before placing the well on production, preparing the fractured well for long-term hydrocarbon production (Crafton and Gunderson, 2007).

A common challenge for shale oil and gas reservoirs is the characterization of the fracture network for evaluating fracturing operations and predicting reservoir performance. Characterizing stimulated shale reservoirs is challenging due to complexities such as dual porosity effects, multi-phase flow, complex flow regimes, non-static absolute permeability and porosity, complex fracture geometry, the role of natural fractures, liquid loading, and operational complexities (Clarkson et al., 2007; Cipolla et al., 2008; Soliman et al., 2010; Gale et al., 2014).

The most common methods for fracture characterization are pressure transient analysis (PTA), rate transient analysis (RTA), micro seismic analysis, and tracer test. These methods have been widely used by industries and each has its own pros and cons.

RTA and PTA Methods: Since production data are available for almost every well many researchers used PTA and RTA to characterize the fracture network (Fisher et al., 2005; Bello, 2009; Cheng et al., 2009; Medeiros et al., 2008, 2010; Song and Ehlig-Economides, 2011; Samandarli et al., 2012; Behmanesh et al., 2013). For instance, Fisher et al. (2005) characterized the induced fracture network using fracture-mapping technologies, and presented correlations between production response and various fracture parameters. Although, RTA and PTA are widely used to characterize the fracture network, these methods consider several simplifications that sometimes lead to unrealistic results. For instance, Hoffman and Chang (2009) indicate that since RTA does not consider the fracturing fluid properties, the estimated fracture length is too long and unrealistic. Furthermore, computational time in the production analysis methods is sometimes very high. The reason is that the production data analysis models are sometimes very finely gridded in an attempt to capture the dimension of the fracture (Karimi-Fard et al., 2004). However, the

fractures are usually less than an inch wide, and the reservoir models require many grids to avoid the numerical convergence problems (Hoffman and Chang, 2009) which increases the computational time.

Micro Seismic Analysis Method: Microseismic monitoring is also broadly used in the field to characterize the fracture network during the hydraulic fracturing operations (Quirein et al., 2006; Maxwell, 2012; Tafti et al., 2012; Van der Baan, 2013). For instance, Tafti et al. (2012) investigated the importance of different microseismic methods in shale reservoirs. They proposed a workflow to characterize the fracture network using microseismic data. Aside from all the benefits of the microseismic monitoring, active microseismic imaging is expensive (National Research Council, 2011). Also, fluid-filled porosity and clay minerals in the alteration zone around the fractures could cause anomalies in the microseismic data (National Research Council, 2011). Moreover, the stimulated reservoir volume (SRV) obtained from the microseismic interpretation does not provide propped fracture volume and its conductivity, and there is a difference between the SRV that is open for the gas flow and SRV obtained from microseismic diagnosis (Ahn et al., 2014).

Tracer Test Method: Tracer test is another method that is commonly used to characterize the fracture network (Smith et al., 1987; Ramirez et al. 1993; Ramirez et al., 1995; Lange et al., 2005; Mulkern et al., 2010; Poulsen et al., 2012). For instance, Smith et al. (1987) estimated fracture aperture, distance between fracture walls, using hydraulic and tracer tests. Although it is desirable to determine the tracer distribution in space and time, this goal is usually not achievable by tracer test. The reason is that the number of sampling points in the field is limited and the tracer concentration versus time is only available for the sampling points (National Research Council, 2011). Moreover, it is possible for the tracer to bypass the sampling point if the fluid mainly transmits through pre-existing open fractures around the sampling point.

Flowback Chemical Analysis Method: Flowback chemical analysis is an alternative approach which can extend/complement the previous methods. Chemical analysis of the flowback water has been previously studied by many researchers. For instance, Woodroof et al. (2003), Sullivan et al. (2004) and Asadi et al. (2008) presented chemical analysis models for monitoring and optimizing fracturing fluid cleanup. Gdanski et al. (2007) incorporated a chemistry layer to a 2-D numerical simulator that was used to history-match the composition of flowback fluids.

Ghanbari et al. (2013) analyzed flowback salt concentration data from hydraulically fractured horizontal wells completed in the Horn River Basin. This comparative field study infers that the complexity of the fracture network can affect the shape of the salt concentration-load recovery profile. The experimental results presented in Chapter 2 also suggest that the barium concentration profile during flowback process maybe a signature for the complexity of fracture network.

This chapter analyzes the flowback salt concentration transient of three different wells in the Horn River Basin to characterize the fracture network. We believe that the flowback salinity is likely a reflection of the complexity of the fracture network. A model is proposed to mathematically describe the behaviors of the salinity profile during the flowback process. Two approaches are used to present the relationship between the salinity and cumulative water production. The first approach provides the volumetric fraction of the recovered water as a probability density function (PDF) of each fracture aperture. The second approach considers a bundle of fractures in series to derive the PDF. At the end, a comparative analysis of the model results and the flowback salinity data is used to characterize the fracture network.

4.2. Reservoir Geology and Field Data

4.2.1. Horn River Basin (HRB)

The Muskwa (Mu), Otter Park (OP), and Evie (Ev) formations belong to the Devonian age of the HRB (Figure 4-1). The total thickness of these shale members ranges from 160 to 180 meters, and the total organic content is approximately 4% (Rogers et al., 2010). Most of the observed fractures in the HRB samples are sealed and few are partly open (Gale et al., 2014). The substantial natural gas resources in the Horn River Basin make it the third largest North American natural gas accumulation discovered before 2010 (Horn River News, 2009).

4.2.2. Field Data

Chemical flowback data are collected from a pad of 18 hydraulically fractured horizontal wells completed in the Mu, OP, and Ev formations. Three wells are placed at the right side of the pad, and three wells are placed at the left side of the pad in each formation as schematically shown in Figure 4-2. The fracturing fluid used for the treatment is the same for all wells and mainly consists of fresh water. During the flowback operation, high frequency water samples taken from the wells in the well pad that were analyzed in a high quality water lab. In this chapter, the field data and calculation results are only presented for three wells that are completed in Mu, OP, and Ev. More details about the well pad and production are presented elsewhere (Abbasi, 2013, Ghanbari et al., 2013).

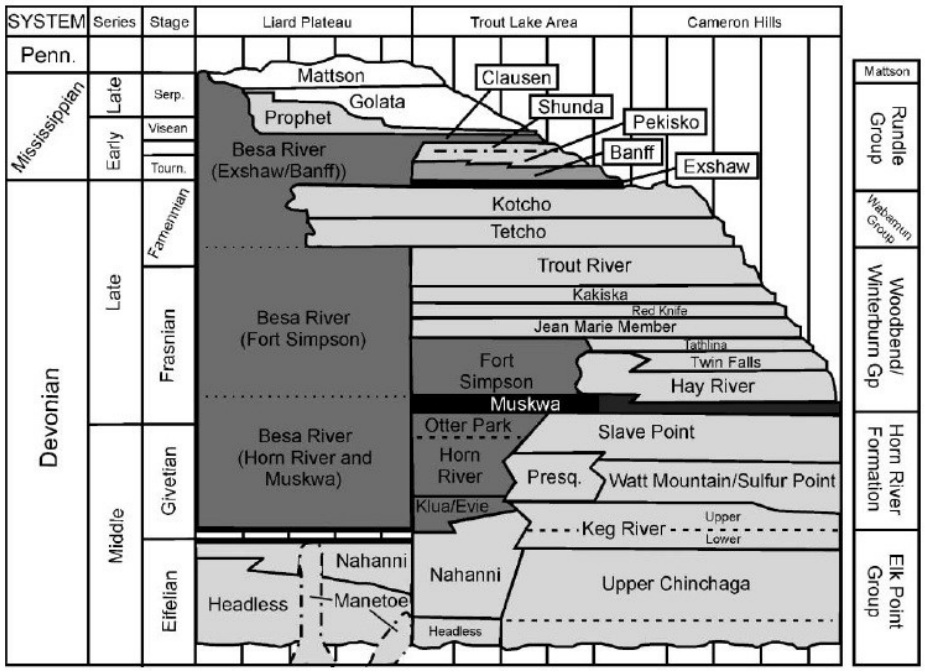

Figure 4-1. Stratigraphic section of Devonian-Mississippian (Gal and Jones 2003).

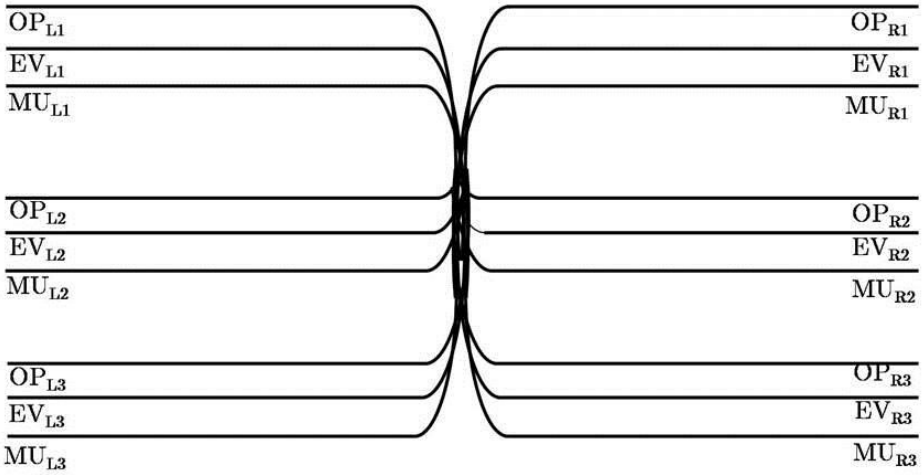

Figure 4-2. Layout of a well pad drilled and completed in the Horn River Basin. A total of 18 wells were drilled; nine wells on the right side of the pad, and nine wells on the left side of the pad.

4.2.3. Key Observations

Figures 4-3 shows the variations in the salt concentration (salinity) of flowback water during the flowback process for three wells completed in the Mu, OP, and Ev formations. The salinity profiles of Mu and OP initially show a gradual increase, and then reach to a plateau at around 40000 ppm. However, the salinity profile of Ev keeps increasing even after 70000 ppm.

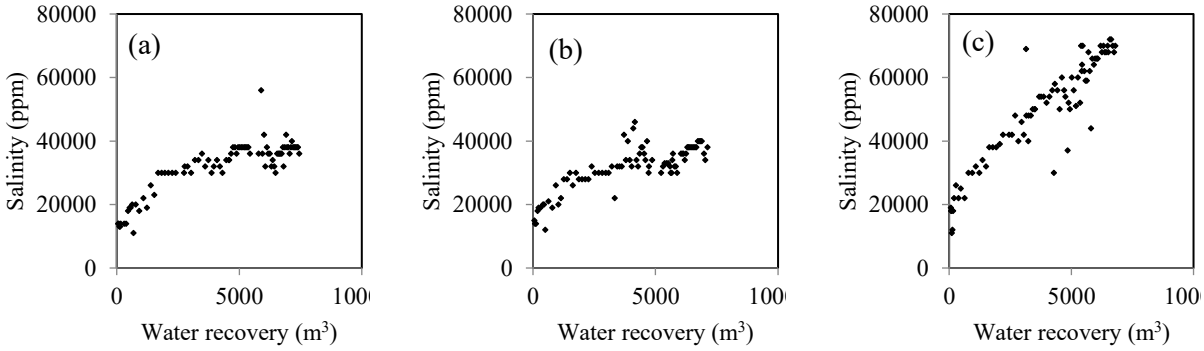

Figure 4-3. Flowback salt concentration transient (salinity) versus water recovery for wells completed in (a) Mu, (b) OP and (c) Ev.

4.2.4. Conceptual Model

We hypothesise that the shape of the salinity versus load recovery profile during the flowback process reflects fracture network complexity. We believe that the gradual increase in salinity concentration of Ev, as opposed to those of Mu and OP, may indicate that the stimulated fracture network for Ev is more dendritic than those for Mu and OP. Put simply, the early water is recovered from the newly formed hydraulic fractures that have an aperture size larger than that of the secondary fractures. Therefore, salt concentration in hydraulic fractures with a low surface to volume ratio is expected to be lower than that in secondary fractures with a relatively higher surface to volume ratio. As the flowback process progresses, the water from secondary fractures with a relatively higher salt concentration will be produced. This qualitative interpretation of the fracture network complexity from the flowback salinity data are in agreement with the conclusions of the previous studies on these shale members in Horn River Basin (Bearinger, 2013). Therefore, in the following section we propose a model to mathematically describe the behavior of the flowback salinity profile.

4.3. Modeling

This section provides a model to describe the behaviors of the salinity profile during the flowback process. Section 4.3.1 describes the relationship between the flowback salinity and the fracture aperture. In our model, we apply two approaches to calculate the PDF for the fracture aperture. The first approach gives the volumetric fraction as a PDF of each fracture aperture (Section 4.3.2), and the second approach considers a bundle of fractures in series to derive the PDF (Section 4.2.3).

4.3.1. Theory

A network of slit-shape fractures of different aperture size is considered as the fracture network. A schematic view of the complex fracture network and the simplified network of slit-shape fractures are illustrated in Figure 4-4.

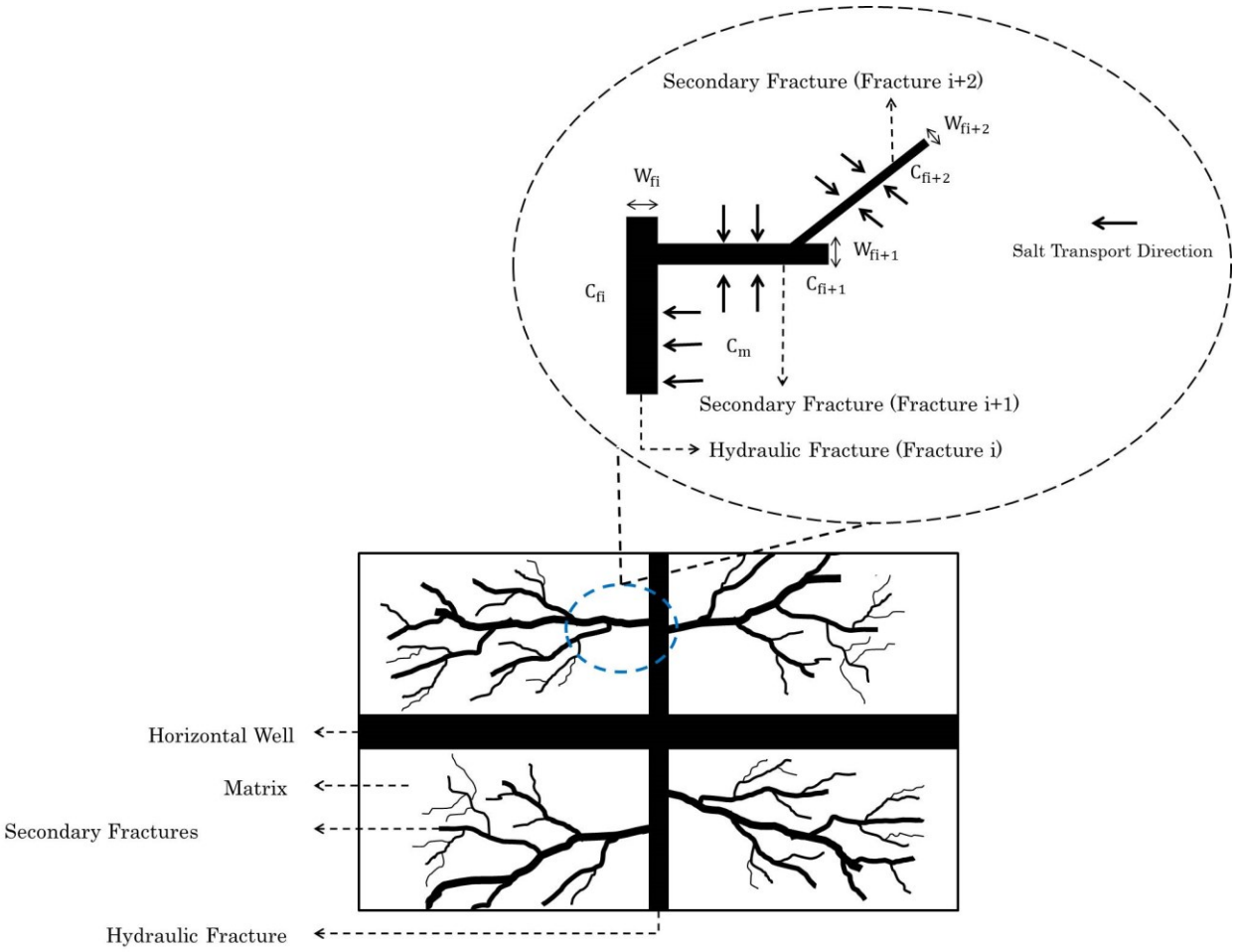

Figure 4-4. A schematic view of the complex fracture network created by a multi-fractured horizontal well (magnified area illustrates the simplified network of slit-shape fractures of different aperture size)

Flowback water is highly saline and the salinity changes over time. Let us assume that salt is transported from matrix to fracture and the transport rate can be described by Fick's first law of diffusion (Treybal 1980):

$$J_i = 2\,D\,A_{f,i}\frac{C_m - C_{f,i}}{L_m} \tag{4-1}$$

Where J is the diffusion rate, $A_{f,i}$ is the interface between matrix and i^{th} fracture, D is diffusion coefficient, C_m and $C_{f,i}$ are the salt concentration within the matrix and the i^{th} fracture, respectively, and L_m is the characteristic length. The characteristic length is the effective distance from the middle of the fracture's aperture to a point within the matrix that contributes to the salt

transfer due to the concentration gradient. The salt concentration in the matrix decreases locally due to the salt diffusion to the fracture. However, the overall salt concentration in the matrix is considered to be constant because the volume of rock is much higher than the volume of injected fracking fluid (mainly water). The huge volume of rock compare to small volume of water in the fractures acts as an infinite source of salts. In the other words, although the local salt concentration decreases near the fracture walls, the bulk rock acts as an infinite source of salts to compensate for the salt loss due to the diffusion into water. It must be noted that the salt transfer occurs from both sides of the fracture to the water, and thus the right hand side of Eq. 4-1 is multiplied by 2.

During fracturing operation and soaking period, the salt transfers from matrix to the water in the fractures. Since huge rock system acts as an infinite source for salts, it is assumed that C_m remains constant and it is much higher than $C_{f,i}$. Therefore, the effective concentration difference can be approximated by:

$$C_m \gg C_{f,i} \Rightarrow \quad C_m - C_{f,i} \approx C_m \tag{4-2}$$

So, Eq. 4-1 can be rewritten as:

$$J_i = 2DA_{f,i}\frac{C_m}{L_m} \tag{4-3}$$

The next step is to find the concentration within each individual fracture ($C_{f,i}$) by multiplying Eq. 4-3 by $\Delta t/V_{f,i}$, where Δt is the exposure time, and $V_{f,i}$ is the volume of fracture *i*. To find $V_{f,i}$, fractures are assumed to have a slit (rectangular) shape with the aperture of W and area of A, so the volume of fracture is given by $V_{f,i} = A_{f,i}W_{f,i}$.

$$C_{f,i}(W_{f,i}) = \frac{2DC_m\Delta t/L_m}{W_{f,i}} \tag{4-4}$$

Interestingly, Eq. 4-4 shows that $C_{f,i}$ is inversely proportional to $W_{f,i}$ ($C_{f,i} \propto {}^{1}/_{W_{f,i}}$). Therefore, the smaller the aperture size, the higher the salt concentration within the fracture. This mathematical relationship between fracture aperture and salt concentration is similar to that

between capillary pressure and pore size of a porous medium through the Young-Laplace equation ($P_c = 2\sigma|cos\theta|/r$). $C_{f,i}$, measured during a flowback process, is inversely proportional to W of the depleted fracture, while P_c measured during a mercury injection process is inversely proportional to r of the invaded pore space. The numerator of the Young-Laplace equation ($2\sigma|cos\theta|$) does not depend on the pore size. Similarly, the numerator of Eq. 4-4 ($2DC_m\Delta t/L_m$) does not depend on fracture size. The mathematical similarities between $C_{f,i} - W_{f,i}$ in a flowback process are analogous to the $P_c - r$ relationship in a mercury injection test. One can interpret the flowback concentration data to describe the fracture aperture size distribution in a similar way that mercury injection data are interpreted to describe the rock pore size distribution. It must be noted that the physics behind the Eq. 4-4 and Young-Laplace equation are different. Eq. 4-4 is developed based on the Fick's first law of diffusion while, Young-Laplace equation is the fundamental equation of capillarity for a curved surface (Huang et al., 2011). However, both equations are mathematically similar. In the following, we use the mathematical analogy to develop an approach for calculation of the ASD from the flowback salinity data.

The rest of this section demonstrates that a plot of cumulative produced water versus salt concentration can be interpreted as a cumulative probability density function (CDF) for the aperture size of the fracture network. Let us consider depletion of water from three connected fractures of the complex system shown in the magnified part of Figure 4-4. Figure 4-5a schematically shows the gradual increase in salt concentration versus cumulative produced water. Figure 4-5b shows the discretized form of the gradual trend shown in Figure 4-5a. The volume of the produced water $(Q_w)_i$ with the concentration of $2DC_m\Delta t/L_m W_{f,i}$ is equal to the volume of fracture *i* which is $A_{f,i}W_{f,i}$. As the flowback process progresses, fracture *i+1* starts depleting and the salt concentration reaches $2DC_m\Delta t/L_m W_{f,i+1}$. Therefore, total volume of the produced water after depletion of fracture *i+1* is $A_{f,i}W_{f,i} + A_{f,i+1}W_{f,i+1}$. Thus, salt concentration-load recovery profile can be interpreted as a basis for the cumulative probability density function (CDF) of fracture aperture size.

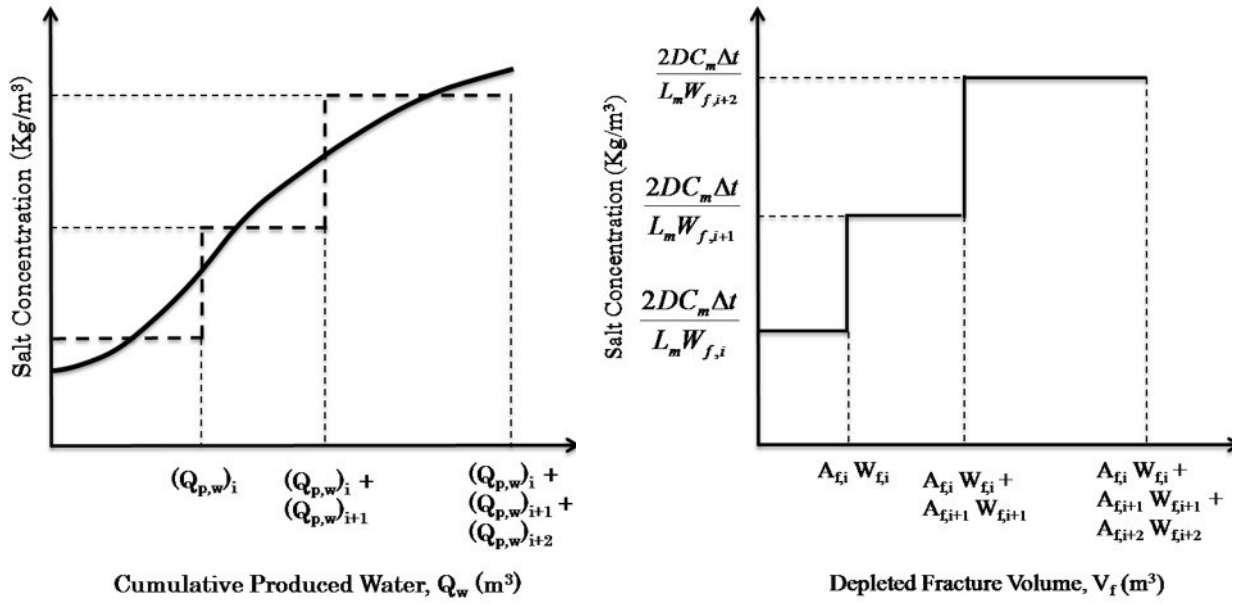

(a) (b)

Figure 4-5. Schematic illustration of salt concentration versus cumulative produced water

Let us build a schematic plot of cumulative produced water versus salt concentration as shown in Figure 4-6. Each arbitrary concentration point on the horizontal axis (such as C_f^*) corresponds to a fracture aperture $\left(W_f^*\right)$ according to Eq. 4-4. As salt concentration increases from left to right, fracture aperture decreases. Therefore, any value such as Q_w^* on the vertical axis represents the total volume of fractures with the aperture size equal or larger than W_f^* $\left(W_f \geq W_f^*\right)$.

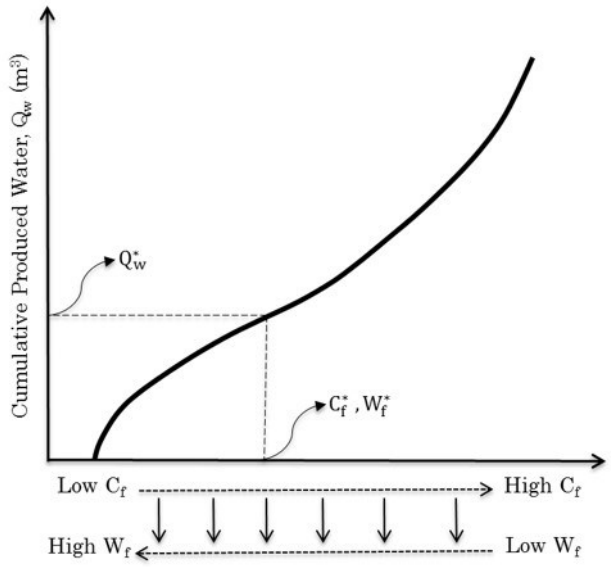

Figure 4-6. A schematic plot of cumulative produced water versus C_f and W_f during the flowback process

Cumulative produced water versus salt concentration can be interpreted as a CDF for the aperture size of the fracture network. If the total facture volume is known, one can normalize the produced water volume to obtain an approximate CDF for aperture size. The derivative of CDF gives the PDF which can be interpreted as fracture aperture size distribution.

The non-recovered water can be trapped in the rock matrix and/or in the complex fracture network (Parmar et al, 204). If we neglect the volume of the fractures that contain non-recoverable water, the total connected fracture volume that contribute in the water production during recovery process, V_{f_t}, can be approximated by the total water production at the end of the flowback process. Therefore, Q_w^*/V_{f_t} represents the normalized volume of depleted fractures. Q_w^*/V_{f_t} can also be interpreted as the volumetric fraction of fractures with $W_f \geq W_f^*$.

The capillary and osmotic forces propel the fracturing water into the rock matrix (Engelder et al., 2014). Moreover, the imbibition experiments on the shale samples of HRB indicates that the water tend to imbibe more into these shale samples compare to oil (see Chapter 2). Therefore, the water influx from matrix to the fractures is considered to be negligible. If we assume that the initial gas saturation within the fractures, $S_{g,ini}$, is negligible, the average gas saturation, $\bar{S}_g$, in the fracture network during the flowback process can be estimated by:

$$\overline{S_g} = S_{g,ini} + \frac{Q_w}{V_{f_t}} \xrightarrow{S_{g,ini} \approx 0} \overline{S_g} = \frac{Q_w}{V_{f_t}} \tag{4-5}$$

Where, Q_w is the cumulative produced water and V_{f_t} is the total volume of the connected fractures that contribute in the water production during recovery process. Also, average water saturation within the fractures can be calculated using $\overline{S_w} = \left(1 - \overline{S_g}\right)$. For any value of W_f, $\overline{S_w}$ is the fraction of the water existing in fractures with aperture equal or less than W_f ($W \leq W_f$).

Although V_{f_t} is an uncertain parameter, it can be estimated as the total produced water volume at the end of the flowback process if the cumulative produced water eventually stabilizes over time; this indeed needs the assumption of negligible water influx from the matrix.

4.3.2. Approach 1: Aperture size distribution using probability density function

In the previous section, we showed that $\overline{S_g}$ can be interpreted as the volumetric fraction of depleted fractures and $\overline{S_w} = \left(1 - \overline{S_g}\right)$ can be interpreted as the volumetric fraction of fractures filled with water. If we assume that $f(W)$ is the probability density function for the fracture aperture, then:

$$\overline{S_w} = \left(1 - \overline{S_g}\right) = \int_{W_{f,min}}^{W_f} f(W) dW \tag{4-6}$$

Where,

$$\int_{W_{f,min}}^{W_{f,max}} f\left(W_f\right) dW_f = 1 \tag{4-7}$$

Where $W_{f,min}$ and $W_{f,max}$ are the minimum and maximum fracture aperture size respectively. Differentiating Eq. 4-6 using Leibnitz's rule for integral differentiation (Kate et al. 2006), the resulting probability density function can be written as:

$$f(W_f) = \frac{d\overline{S_w}}{dW_f} \tag{4-8}$$

We also know from Eq. 4-4 that

$$C_f W_f = 2DC_m \Delta t / L_m \tag{4-9}$$

The right-hand side of Eq. 4-9 is constant. Therefore, differentiating Eq. 4-9 results in:

$$W_f dC_f + C_f dW_f = 0 \quad \Rightarrow \quad dW_f = \frac{-W_f dC_f}{C_f} \tag{4-10}$$

Substituting Eq. 4-10 into Eq. 4-8 gives:

$$f(W_f) = -\frac{2DC_m \Delta t / L_m}{W_f^2} \frac{d\overline{S_w}}{dC_f} \tag{4-11a}$$

We also know that $\overline{S_w} = 1 - N_{P,w}$, where $N_{P,w}$ is the normalized water recovery and it is defined as $N_{P,w} = \frac{Q_w}{V_{f_t}}$. Therefore, $\frac{d\overline{S_w}}{dC_f} = -\frac{dN_{P,w}}{dC_f}$, and the probability density function for fracture aperture in terms of measureable parameters is given by:

$$f(W_f) = \frac{{C_f}^2 L_m}{2DC_m \Delta t} \frac{dN_{P,w}}{dC_f} \tag{4-11b}$$

Eq. 4-11b shows that differentiating the normalized water production ($N_{P,w}$) with respect to salt concentration (C_f) can represent the aperture size distribution. Since the field data are usually scattered and noisy, the five-point central difference formula (Akima, 1970) is used to have more accurate and smooth plots.

$N_{P,w}$ versus C_f (salinity) plots of the three wells are demonstrated in Figure 4-7. These plots and their derivatives can be interpreted as a CDF and PDF for the fracture aperture, respectively. $N_{P,w}$-C_f plots of Mu and OP are sharper than that of Ev. The interpretation of this phenomenon is that the aperture size distribution of Ev is wider than those of Mu and OP. It must be noted that to obtain $N_{P,w}$, the cumulative produced water is divided by the total produced water (Eq. 4-5).

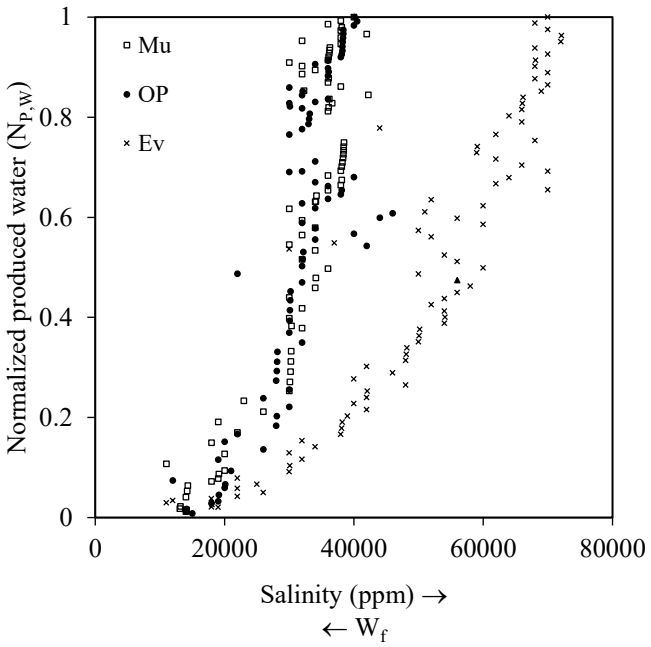

Figure 4-7. Normalized produced water versus salinity (Cf) for the three wells completed in the Mu, OP, and Ev formations.

4.3.3. Approach 2: Aperture size distribution using fractures in series method

Considering Eq. 4-4, lower concentrations are attributed to the primary fractures with larger aperture size. Thus, primary fractures are initially depleted. During the recovery process, the contribution of secondary fractures with smaller aperture size increases; therefore, the name "fractures in series method" is selected to depict the fact that primary fractures have a major effect at the beginning of the process and the smaller fractures become more important as the flowback process progresses. In this approach, a bundle of fractures in series is considered to derive the PDF

for a connected fracture network. The final correlation for PDF using the fractures in series method is shown in Eq. 4-12. The detailed derivation procedure is presented in the Appendix B.

$$f(W_f) = \frac{{C_f}^3 L_m^2 \overline{V}_f}{(2DC_m\Delta t)^2 \times A_f} \frac{dN_{P,w}}{dC_f} \tag{4-12}$$

Both the derived PDFs from approaches 1 and 2 (Eqs. 11-b and 12) are correlated to $dN_{P,w}/dC_f$ which can be calculated based on the field data of salt concentration-load recovery. The derived PDFs are a function of C_f, Δt, C_m, L_m, and D but with different exponents. C_f and Δt are field data and the values of D, C_m, and L_m are assumed (see Section 4.4.1 for the assumed values) to calculate the ASD.

The PDF obtained form approach 2 (Eq. 4-12) also depends on the average fracture volume ($\overline{V}_f$) and the interface between matrix and fracture (A_f). The step-by-step solution procedure for ASD calculations using approach 2 is given in the Appendix B.

4.4. Results

This section provides a comparative analysis of the calculated ASD and the field data of salinity to characterize the fracture network complexity (Section 4.4.1). Also, sensitivity analysis of the uncertain parameters and the limitations for the application of the proposed approaches are discussed in Sections 4.4.2 and 4.4.3, respectively.

4.4.1. Results of the ASD Calculations

The proposed model presents the ASD for three wells completed in Mu, OP, and Ev. The calculated ASD by approaches 1 and 2 for the three focus wells are compared in Figure 4-8. The majority of the fractures have an aperture size of less than 2 mm. Gale et al. (2014) also reported the fracture ASDs for different formations. Their study also shows that the majority of the fractures in the shale formations have aperture size of less than 2 mm. One should note that the calculated

ASDs are based on the assumptions and the values assumed for D, C_m, and L_m. Sodium and chloride are the major cation and anion in the flowback water respectively (Ghanbari et al., 2013). Therefore, sodium chloride diffusion coefficient in water, $D = 1.484 \times 10^{-9} m^2 s^{-1}$ (Weast 1974), is used in the calculations. The formation water is usually hyper-saline (Vengosh et al., 2014) and also there are localized precipitated salt areas (see Chapter 2). Therefore, mixing of the injected water with formation water and salt dissolution could increase the salinity of the water. In our calculations, the lump effects these phenomena are considered in the assumed value for C_m. The value for the salt concentration within the matrix is considered to be higher than the maximum value obtained from the field data of flowback salinity. The assumed value for each well is $C_{m,Mu} = C_{m,OP} = 50000ppm$, $C_{m,Ev} = 75000ppm$. L_m depends on the reservoir and it shows the effective distance from the middle of the fracture's aperture to a point within the matrix that contributes to the mass transfer due to the concentration gradient. Although the characteristic length is an unknown parameter, its value is fixed at $L_m = 10W_f$ to compare the modeling results using both approaches. The calculated ASDs from both approaches are compared in Figure 4-8. It must be noted that the ASDs plotted in Figure 4-8 are based on the assumed values for the uncertain parameters however; the comparative analysis demonstrates meaningful differences between the shapes of the ASDs of the three wells. Additionally, the sensitivity analysis of the uncertain parameters for the ASD calculations is further investigated in Section 4.4.2.

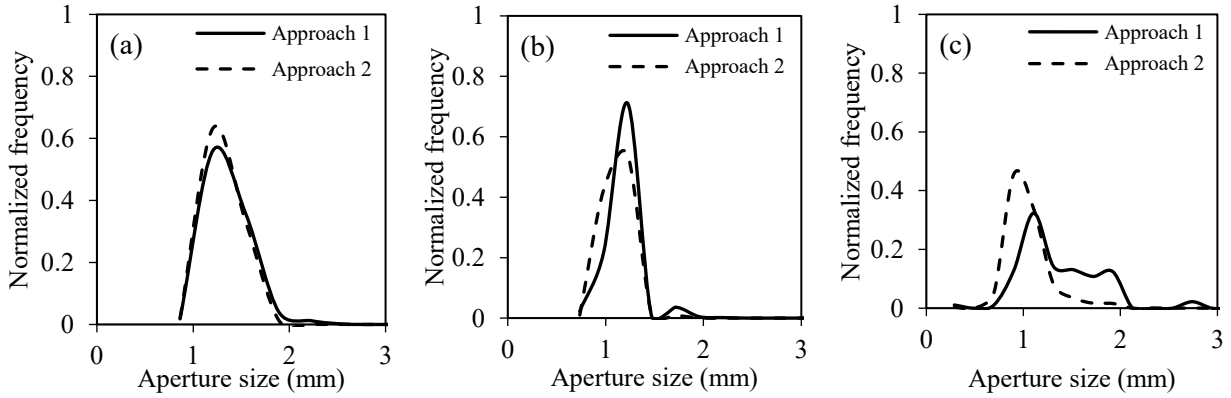

Figure 4-8. A comparison between the calculated ASDs by approaches 1 and 2 for three different wells completed in (a) Mu, (b) OP, and (c) Ev. The calculations assumed a constant diffusion coefficient of salt in water ($D = 1.484 \times 10^{-9} m^2 s^{-1}$). Also, the characteristic length is fixed at $L_m = 10W_f$.

Figure 4-8 shows that both approaches have calculated similar ASD for the Mu well; however, there are some trivial differences in the ASDs calculated by approach l and approach 2 for the OP and Ev wells. Since the calculated PFDs in both approaches are different (Eqs. 11-b and 12), the calculated ASD from both approaches can be different as well.

The modeling results present a narrower ASD for the Mu and OP wells, while the distribution curve for Ev is wider. Comparing the modeling results (Figure 4-8) with the flowback salinity data (Figure 4-3) reveals that the wells with a plateau in the salt concentration-load recovery curve (Mu and OP wells) have a narrower ASD. However, ASD is wider for the well with a steady increase in the salt concentration-load recovery curve (Ev well). Since ASD is wider for Ev, the fracture network is expected to be more dendritic than those in Mu and OP. The simple and complex fracture networks are schematically illustrated in Figure 4-9.

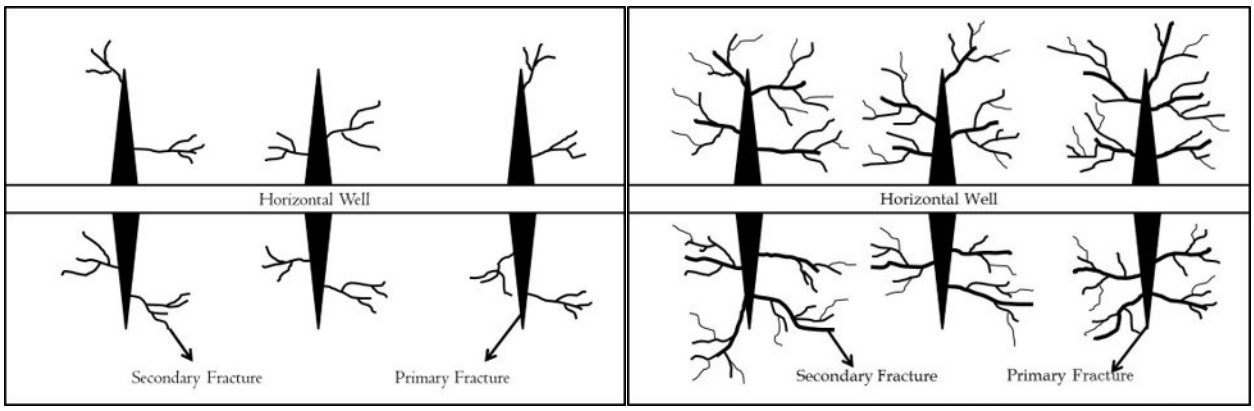

(a) (b)

Figure 4-9. Schematic illustration of (a) simple and (b) complex fracture networks

More complex fracture network for Ev in compare to simpler fracture networks in Mu and OP is also in agreement with the field observations of lower water recovery and higher gas production in Ev (compare to the higher water recovery and lower gas production in Mu and OP). Figure 4-10 shows the gas recovery versus water recovery for the wells completed in these three formations.

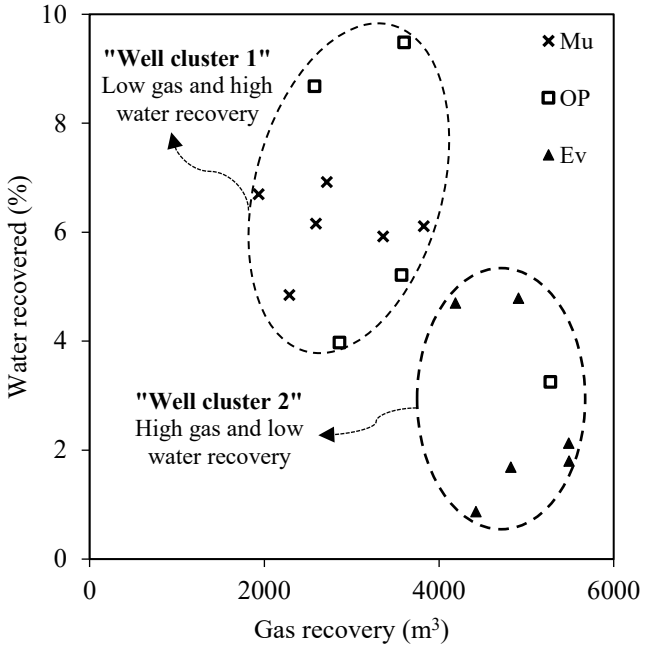

Figure 4-10. Water recovery versus gas recovery 300 hours after placing the wells on flowback for the wells with (1) low gas and high water recovery and (2) high gas and low water recovery

Two well clusters can be distinguished in the plots of water recovery versus gas recovery. The first well cluster has low gas and high water recovery and all the wells in this cluster are completed in the either Mu or OP formations. However, the second well cluster has high gas and low water recovery and all the wells completed in the Ev formation are covered in this cluster. To explain the higher gas and lower water recovery in Ev (compare to those in Mu and OP) we consider a more complex fracture network (in contrast to a simpler fracture networks for Mu and OP) similar to the one shown in Figure 4-9b.

In a more dendritic and complex fracture network, the available surface area for water-rock interactions is higher. Higher surface area increases the imbibition rate (see Chapter 2). Higher imbibition rate is one of the reasons for higher leak-off and lower water recovery in Ev. In a more complex fracture system, the tortuous nature of the secondary fractures can also increase the possibility of water trapping (Ghanbari, 2014). The water retained in the secondary fractures can imbibed into the matrix (more leak-off) due to the capillarity, chemical osmosis and water adsorption by clay minerals (Dehghanpour et al., 2013, Dehghanpour et al, 2012, Chenevert, 1970).

On the other hand, water imbibition can also result in the counter-current expelling of gas from matrix into the fractures (Dehganpour et al., 2012). As the complexity of the fracture network increases, the water trapping and counter current imbibition rate increase, potentially resulting in low water and high gas recoveries. This means that the cluster 2 wells (mostly Ev wells) have more complex fracture network compare to the cluster 1 wells (most of the Mu and OP wells).

A comparative analysis of the modeling results and the flowback salinity data along with the water and gas recovery data indicate that the fracture network is simpler when the salt concentration-load recovery curve reaches a plateau (compared with the well with continuous increase in the salinity profile). Similarly, the fracture network is more complex when the salt concentration-load recovery curve continuously increases over the course of the flowback process (compared with the well with a plateau in its salinity profile). Considering the salinity profiles in Figure 4-3 for the focus wells, the fracture network in Ev is more complex compare to that in Mu and OP. Similar conclusion can also be made based on the results presented in Chapter 2. More specifically, interpretation of the barium concentration profile during flowback period suggest that the fracture network is more complex in Ev compare to that of Mu and OP (see Chapter 2).

The presented model for describing the behaviour of the salinity profile during the flowback process and its meaningful relationship to the fracture network complexity provides an alternative approach for reservoir characterization. Reservoir characterization using flowback chemical data along with other characterization methods (PTA, RTA, microseismic monitoring, tracer test, etc.) help industry to better understand the flowback process and control the fracking operations.

4.4.2. Sensitivity Analysis

Since properties (like rock mineralogy, permeability, porosity, etc.) of shale formations can significantly vary even in small scales (Diaz et al., 2010), attributing an absolute value to the diffusion coefficient, D, and the characteristic length, L_m, could impact the calculations. In order to investigate the sensitivity of our calculations to these parameters, first L_m was fixed at 0.1m and the diffusion coefficient varied between $5 \times 10^{-10}\, m^2/s$ and $10^{-8}\, m^2/s$. Next, to analyze the effect of characteristic length on ASD, D was fixed at $10^{-9}\, m^2/s$ and L_m varied between 0.1m and

1.5m. Since the sensitivity analysis for all formations shows the similar trends, only the results for the Ev formation are presented in Figures 4-11 and 4-12.

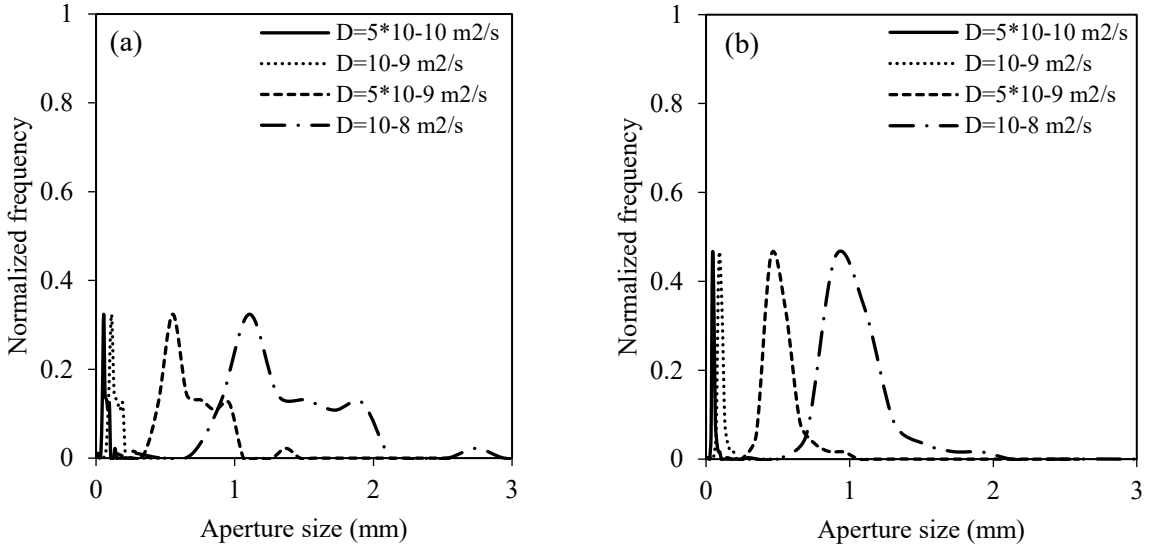

Figure 4-11. Effect of diffusion coefficient, D, on the ASD in the Ev formation [$L_m = 0.1m$] (a) approach 1, (b) approach 2.

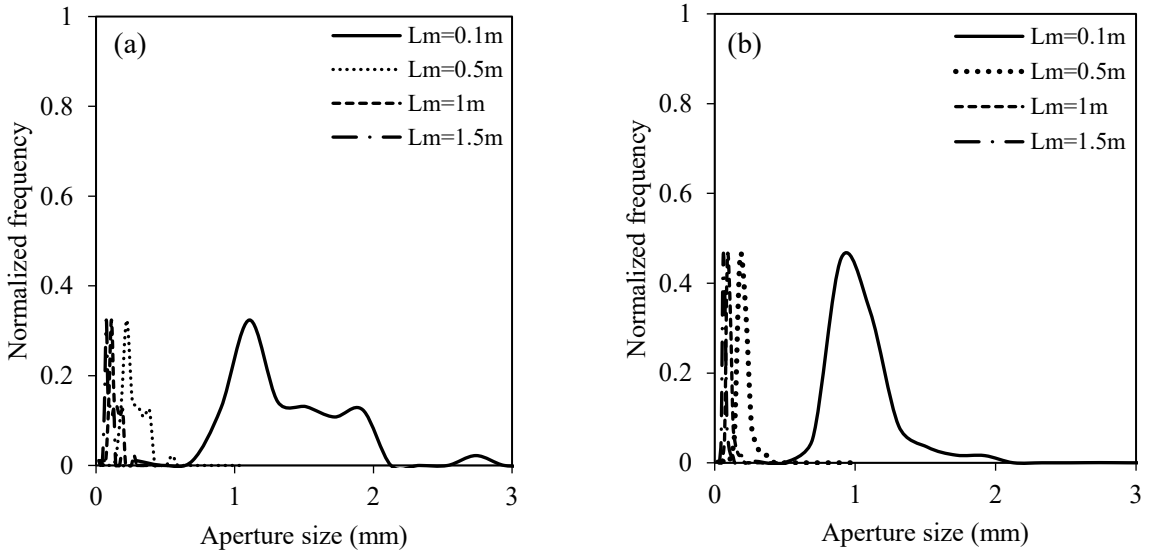

Figure 4-12. Effects of characteristic length, Lm, on the ASD in the Evie formation [$D = 10^{-9}\, m^2/s$] (a) approach 1, (b) approach 2.

For both approaches, the ASD curve shifts to the higher aperture size values at larger diffusion coefficient values. According to Eq. 4-3, larger values of *D* lead to greater salt diffusion

flux, J, from matrix to fracture. Therefore, for a certain salt concentration in the flowback water, larger fractures are required for the larger diffusion flux (large D values). This is why the ASD curve shifts to the greater aperture size values when the diffusion coefficient is larger. When D is smaller however, fracture aperture should also be smaller in order to compensate for the smaller corresponding diffusion flux. This is why the ASD curve shifts to the lower aperture size values when the diffusion coefficient is smaller.

Similar reason could explain the effect of characteristic length on the calculated ASD. According to Eq. 4-3, for the smaller L_m values diffusion flux is higher, and, in order to reach to a certain salt concentration, the fracture aperture should be larger. Therefore, ASD curves shift to the larger aperture size at greater diffusion coefficient and lower characteristic length values.

4.4.3. Limitations of the proposed model

Although the proposed model is able to describe the salinity profile behaviors during the flowback process, the derivations are based on the several assumptions and also both approaches have uncertain input parameters. For instance, since the volume of rock available per fracture surface area is huge, in our models C_m is considered to be constant. L_m is used to account for the effective distance within the matrix that contributes to the salt transfer. However, these assumptions should be modified for the stimulated reservoirs with highly complex fracture network.

The formation water is usually hyper-saline (Vengosh et al., 2014) and also there are localized precipitated salt areas (see Chapter 2). Therefore, mixing with formation water and mineral dissolution are possible mechanisms for high salt concentration in flowback water. To account for these mechanisms, in our calculations, the value for C_m is considered to be higher than the maximum value obtained from the field data of flowback salinity. This assumption provide salt gradient from matrix to the fractures. However, this assumption should be corrected for modeling of reservoirs with low halite content and low saline formation water.

The proposed model is also developed based on the assumption that the salt transport only occurs from matrix to fractures. However, the chemistry of the flowback water could change due

to several phenomena such as mixing of fracking water with saline formation water (Haluszczak et al., 2013), dissolution of the shale constituents (Blaunch et al., 2009), cation exchange with clay minerals (Josh et al., 2012), etc. In our calculations, the lump effects all of these phenomena are considered in the assumed value for C_m. Therefore, if the effect of each of the individual phenomenon is the goal, a separate model should be developed.

In our calculations, the clay leaching effect is lumped with other sources for ions in the flowback water (formation water, precipitated salts, etc.) and the net effect is reflected in the assumed values for C_m. However, leaching of the clay minerals from the exchangeable sites (Keller and Da-Costa, 1989) and cation exchange capacity (CEC) of clays (Josh et al., 2012) impact the ion transfer rate, which could influence the interpretation of the results. Therefore, the proposed approaches should be modified for the high clay content reservoirs to account for the CEC of the clays. Moreover, chemical reactions could add/consume components (such as ions and elements) into/out of the rock/water. Furthermore, the formation itself could be chemically altered if there are active reactions with fracturing fluid (Liao et al., 2014). Therefore, the model should also be modified if the rock formation has active chemical interaction with fracturing fluid.

The proposed model is also considered a constant diffusion coefficient for a single component. However, in reality, different ions have different diffusion rates and various parameters (such as concentration, temperature, pressure, etc.) affect their diffusion coefficients (Treybal 1980). Moreover, leaching of the clay minerals (Keller and Da-Costa, 1989) and their CEC (Josh et al., 2012) impact individual ion concentration (and also their diffusion coefficients). Thus, for a more precise calculation, the proposed approaches should be modified to account for individual ion diffusion coefficient and the parameters that impact their values.

It has been shown that during the production process, pressure draw down along with gas expansion can evaporate the water (i.e., flowback water) (Singh, 2016). Water vaporization can potentially increase the salinity of the produced flowback water. More specifically, water molecules leave the flowback water during the flowback/production process, concentrating the solution. Future studies should also take into account for the role of water evaporation mechanism in the flowback water chemistry for a more accurate interpretation of the flowback chemical data.

4.5. Summary

The concentration of different ions, and in general the salt concentration, in the flowback water changes over time during the flowback process. For some wells, the salt concentration shows a continuous increase over time, while for some other wells it shows a plateau at later flowback times. This chapter presents a model to mathematically describe the salt concentration transient during the flowback process. The model considers mass (i.e., salt) transfer from matrix to the water-filled fractures over time (i.e., soaking time plus flowback time). The model results indicate that the wells with a continuous increase in their salinity profile have more complex fracture network compared with the wells with a plateau in their salinity profile and more simple fracture network.

The model results comply with the field data of water and gas recoveries. The wells with more complex fracture network have more gas production and lower water recovery compared with the wells with more simple fracture network. A complex fracture network provides high fracture-matrix contact area, increasing the gas production. Furthermore, high fracture-matrix area increases the chance of water leak-off into the matrix, leading to low water recovery for wells with a complex fracture network.

The qualitative fracture network complexity results presented in this chapter also agree with the estimated fracture surface area values presented in Chapter 5. In this chapter, the model results indicate that the Ev well has more complex fracture network compared with the OP well. As presented in Chapter 5, the estimated fracture surface area for Ev well is higher compared with that estimated for the OP well (Figure 4-11).

Nomenclatures

$A_{f,i}$	Interface between matrix and i^{th} fracture (m^2)
A_g	Area under the graph of $\delta(W_f)/\overline{V_f}$ versus W_f (m^2)
C_f	Salt concentration within the fracture (mol/m^3)
C_m	Salt concentration within the matrix (mol/m^3)
D	Diffusion coefficient of salt in water (m^2/s)
$f(W_f)$	Probability density function
J	Diffusion rate (mol/s)
L_m	Characteristic length (m)
N_f	Total number of fractures
$N_{P,w}$	Normalized water recovery
P_c	Capillary pressure (Pa)
Q_w	Cumulative produced water (m^3)
$(Q_{p,w})_i$	Produced water from fracture i (m^3)
r	Pore radius in the porous medium (m)
$\overline{S_g}$	Average gas saturation
$S_{g,Ini}$	Initial gas saturation
$\overline{S_w}$	Average water saturation
t	Time (s)
V_d	Volume of depleted fractures (m^3)
V_f	Fracture volume (m^3)
$\overline{V_f}$	Average fracture volume (m^3)
V_{f_t}	Total fractures's volume (m^3)
V_w	Volume of water in the fracture (m^3)

W_f	Fracture aperture size (m)
Greek symbols	
Δt	Exposure time (s)
$\delta(W_f)$	Probability density function
σ	Interfacial tension (N/m)
θ	Wetting angle (°)
Subscripts	
c	Capillary
d	Depleted fractures
f	Fracture
g	Gas/Graph
ini	Initial
max	Maximum
min	Minimum
w	Water

Chapter 5

Produced Flowback Salts versus Induced Fracture Interface: A Field and Laboratory Study

5.1. Introduction

Recent developments in horizontal drilling and hydraulic fracturing operations have paved the way toward economic exploitation of unconventional resources such as tight and shale oil/gas reservoirs (King, 2012). During fracturing operations, huge amount of fracturing fluid (~10,000-75,000 m^3 per well) is injected in the reservoir to create fractures (King, 2012; Goss et al., 2015). The induced fracture network acts as an artificial pipeline system facilitating hydrocarbon flow to the wellbore. Characterization of stimulated fracture network is challenging mainly due to low porosity and permeability of shale matrix (King, 2012; Cao et al., 2017), fracture network complexity (Zho et al., 20114; Ghanbari and Dehghanpour, 2016), presence of clay minerals (Bai et al., 2013; Le at al., 2016), natural fractures (Gale et al., 2014; Taleghani and Olsen, 2014), and fault systems (Suliman et al., 2013; Stabile et al., 2014).

The recovered water at early production period (i.e., flowback water) is highly saline and toxic (Alessi et al., 2017; He et al., 2017). Several past studies focused on chemical analysis of flowback water to evaluate the hydraulic fracturing operations and characterize the fractured reservoirs. Woodroof et al. (2013) developed a chemical analysis model to optimize the fracturing fluid cleanup. Gdanski (2010) developed a numerical model to history match the composition of flowback fluid. Engle and Rowan (2014) applied a multivariate data analysis approach to investigate the geochemical evolution of flowback water. Roshan et al. (2015) calculated the surface area of shale powders by analyzing extracted exchangeable cations. They suggested that fracture surface area (A_f) can be estimated by tracking exchangeable cations in the flowback water. Shook and Suzuki (2017) analyzed tracer data to estimate A_f in engineered geothermal systems. Ghanbari et al. (2013) analyzed flowback salt concentration data of three wells completed in the Horn River Basin (HRB). They concluded that the induced fracture network affects the load recovery and the shape of the salt concentration profiles. Bearinger (2013) qualitatively explained the relationship between the shape of the salt concentration profile and the complexity of fracture network. In Chapter 4, a model is developed to mathematically describe the Bearinger's qualitative theory. This model characterizes the complexity of fracture network using the salinity profile measured during the flowback process.

Several past studies investigated shale-water interactions to study the source of ions in the flowback water. Jones et al. (1992) performed leaching experiments and simulation study to investigate potential effects of acidification in Rundle oil shale. They concluded that dissolution of calcite and siderite controls the leachate's chemistry. Blaunch et al. (2009) analyzed over 100 flowback water samples from the Marcellus shale play. They concluded that production of highly-saline flowback water is mainly due to the dissolution of shale constituents in injected water. However, Haluszczak et al. (2013) showed that mixing of the fracturing fluid with in-situ formation brine is the main reason for highly-saline flowback water in the Marcellus shale play. Thomson et al. (2016) identified abnormally high concentration of barium ion in the field flowback water from Marcellus shale play. The experimental results shown in Chapter 2 suggest that the barium ions in the flowback water of wells drilled in the HRB are possibly originated from natural fractures.

The reported ion concentration during water imbibition experiments are significantly smaller than those reported in the field flowback water (Langille et al., 2014; Xiong et al., 2016; He et al., 2016; Estrada and Bhamidimarri, 2016; Shrestha et al., 2017). Majority of the studies aiming at ion concertation during leaching/imbibition experiments are performed at low-temperature and low-pressure ($LTLP$) laboratory conditions (Shook and Suzuki, 2017; Ghanbari et al., 2013; Binazadeh et al., 2016; Xu et al., 2018), whereas the reservoir usually has high-temperature and high-pressure ($HTHP$) conditions. The different temperature and pressure values dictates different thermodynamic pathways (Shahrak et al., 2007; Fogler, 2010; Tabrizi et al., 2012; Ebrahimi et al., 2012) for shale-water interactions in laboratory and in reservoir conditions. Furthermore, the laboratory imbibition experiments are usually conducted using small rock samples with limited surface area (A_s) and volume (V_s), which are significantly smaller compared with the A_f and the rock volume in the reservoir.

This chapter presents the results of $LTLP$ and $HTHP$ water imbibition experiments to investigate the effects of A_s, temperature, and pressure on the total ion produced (TIP). Also, A_f is estimated by scaling-up the experimental results of ion concentration for two wells completed in the HRB.

5.2. Materials

Flowback water and downhole shale samples are collected from two wells completed in the Otter-Park (OP) and Evie (Ev) Formations in the HRB. The approximate reservoir temperature and pressure for both wells are ~140℃ and ~4500 $psia$, respectively. Figure 1 shows the location of the target wells.

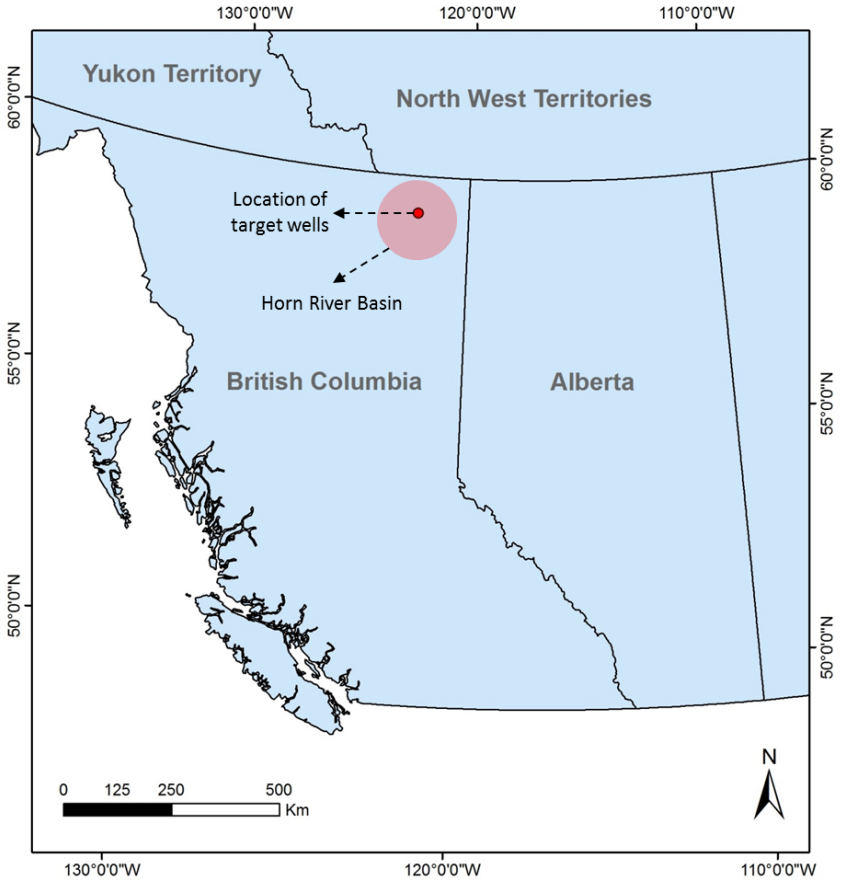

Figure 5-1. Location of the target wells in the Horn River Basin.

Table 5-1 shows the average rock mineralogy of OP and Ev samples measured by X-ray diffraction (XRD) analysis. Quartz is the primary mineral in both of the OP and Ev samples. OP samples has about two-times more clay minerals compared with the Ev sample. It must be noted that the gas shales are heterogeneous and their properties can significantly vary even in small scales (Diaz et al., 2010). Moreover, XRD uses a very small volume of rock for its analysis. Therefore, the rock mineralogy presented in Table 5-1 might not be an accurate representation of the mineralogy of the target formations.

Table 5-1. The average bulk-rock mineralogy of the OP and Ev samples from XRD analysis. The XRD used for characterization of rock mineralogy has a signal-to-noise ratio of 400.

Sample	OP	Ev
Depth (m)	2605	2681
Non-Clay Content (wt.%)		
Quartz	55.3	51.9
K-Feldspar	1.6	4.9
Plagioclase	3.7	5.7
Calcite	0.9	13.3
Ankerite/Fe-Dolomite	0.7	0.0
Dolomite	0.4	2.6
Pyrite	3.5	2.9
Barite	0.1	0.0
Total Non-Clay	66.2	81.3
Clay Content (wt.%)		
Illite/Smectite (I/S)	10.8	6.6
Illite+Mica	22.8	12.1
Kaolinite	0.2	0.0
Total Clay	33.8	18.7

Flowback water samples are collected from both OP and Ev wells. Electrical conductivity (EC) and the ionic composition of the produced flowback water is measured over time. The ionic composition is measured using inductively coupled plasma mass spectrometry ($ICP-MS$) and ion chromatography (IC).

5.3. Experiments

$HTHP$ reactor (Figure 5-2) is used to conduct the imbibition experiments at low-pressure and high-pressure conditions. Tables 5-2 and 5-3 show the physical properties of selected OP samples that are used in low-pressure and high-pressure experiments, respectively. The physical

properties of Ev samples are not shown in Tables 5-2 and 5-3 as they have similar properties to that of OP samples.

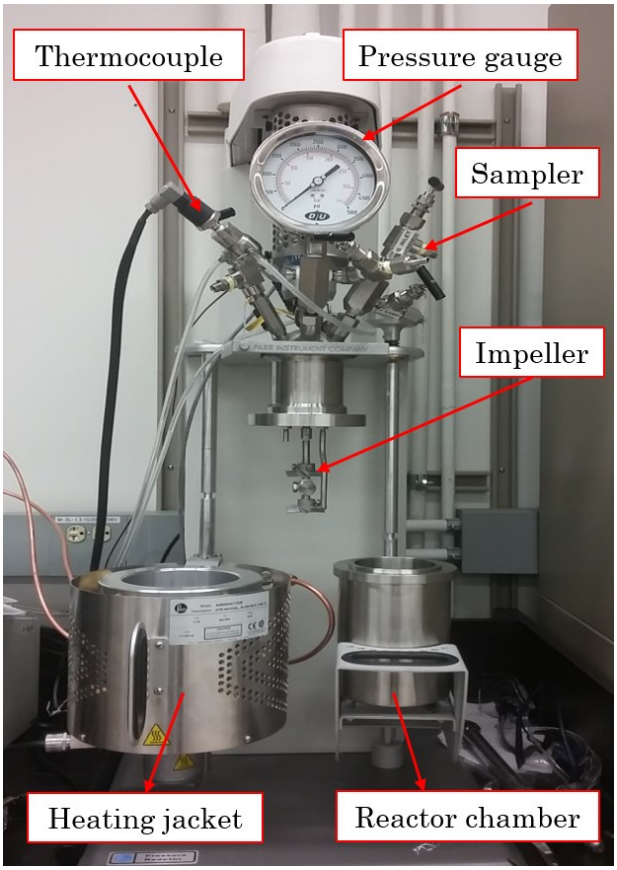

Figure 5-2. Picture of the high-temperature and high-pressure reactor (Parr-Reactor model 4540) used for shale-water interaction experiments.

Table 5-2. Physical properties of selected OP samples used for low-pressure shale-water interaction experiments.

Sample	Mass (g)	$A_s(cm^2)$	$V_s(cm^3)$	T(℃)	$P(psia)$
OP_1	346.9 ± 0.1	97.0 ± 0.25	138.3 ± 0.05	23 ± 0.5	14.7
OP_2	340.2 ± 0.1	108.0 ± 0.25	135.6 ± 0.05		
OP_3	343.1 ± 0.1	134.0 ± 0.25	136.8 ± 0.05		
OP_4	345.2 ± 0.1	165.0 ± 0.25	137.6 ± 0.05		
OP_5	343.9 ± 0.1	198.0 ± 0.25	137.1 ± 0.05		
OP_6 (known)*	345.1 ± 0.1	344.0 ± 0.25	137.6 ± 0.05		
OP_7	376.2 ± 0.1	96.0 ± 0.25	150.0 ± 0.05	45 ± 0.5	14.7
OP_8	369.6 ± 0.1	94.0 ± 0.25	147.4 ± 0.05		
OP_9	365.4 ± 0.1	118.0 ± 0.25	145.7 ± 0.05		
OP_{10}	373.3 ± 0.1	168.0 ± 0.25	148.8 ± 0.05		
OP_{11}	377.6 ± 0.1	189.0 ± 0.25	150.6 ± 0.05		
OP_{12} (known)*	376.3 ± 0.1	373.0 ± 0.25	150.0 ± 0.05		
OP_{13}	316.8 ± 0.1	92.0 ± 0.25	126.3 ± 0.05	65 ± 0.5	14.7
OP_{14}	328.2 ± 0.1	116.0 ± 0.25	130.9 ± 0.05		
OP_{15}	312.7 ± 0.1	141.0 ± 0.25	124.7 ± 0.05		
OP_{16}	320.9 ± 0.1	174.0 ± 0.25	128.0 ± 0.05		
OP_{17}	318.5 ± 0.1	205.0 ± 0.25	127.0 ± 0.05		
OP_{18} (known)*	316.7 ± 0.1	364. 0 ± 0.25	126.3 ± 0.05		

* Samples with known surface area used for verification of empirical $TIP - A_s$ correlation (red points in Figure 5-9a).

Table 5-3. Physical properties of selected OP samples used for high-pressure shale-water interaction experiments.

Sample	Mass (g)	$A_s(cm^2)$	$V_s(cm^3)$	T(℃)	$P(psia)$
OP_{19}	48.2 ± 0.01	24.0 ± 0.25	19.2 ± 0.005	140 ± 0.5	2550 ± 5
OP_{20}	52.6 ± 0.01	35.0 ± 0.25	21.0 ± 0.005		
OP_{21}	53.7 ± 0.01	54.0 ± 0.25	21.4 ± 0.005		
OP_{22}	57.8 ± 0.01	92.0 ± 0.25	23.0 ± 0.005		
OP_{23}	50.7 ± 0.01	108.0 ± 0.25	20.2 ± 0.005		
OP_{24} (known)*	47.6 ± 0.01	211.0 ± 0.25	19.0 ± 0.005		
OP_{25}	79.4 ± 0.01	67.0 ± 0.25	31.7 ± 0.005	140 ± 0.5	500 - 2550
OP_{26}	88.2 ± 0.01	59.0 ± 0.25	35.2 ± 0.005	23 -140	2550 ± 5

* Sample with known surface area used for verification of empirical $TIP - A_s$ correlation (red point in Figure 5-10a).

5.3.1. Low-Pressure Experiments

Temperature: We conduct isothermal imbibition experiments using samples of similar A_s and V_s in deionized (DI) water. Isothermal tests are performed at $T = 23, 45, and\ 65°C$ and $P = 14.7\ psia$. During the experiments, we measure the EC of the solution over time. Since the temperature impacts the EC value (Dauphinee and Klein, 1977; Mukerjee et al., 1985), we measure the EC of the solution at the reference temperature of $T = 23°C$. So, for high temperature experiments $(i.e., T = 45\ and\ 65°C)$, the water samples are first cooled down to $T = 23°C$ before the EC measurement. At the end of the experiments, we analyze the ion concentration using $ICP - MS$ and IC.

Rock Surface Area: We conduct isothermal imbibition experiments by placing shale samples of different A_s, but similar V_s, in DI water at $P = 14.7\ psia$. We repeat the experiments at different temperatures values $(T = 23, 45, and\ 65°C)$ to simultaneously investigate the effects of temperature and A_s on the TIP. During the experiments, the EC and also the individual ion concentration of the solution is measured over time.

5.3.2. High-Pressure Experiments

Pressure: The temperature is set to a constant value of $T = 140℃$, which is the average reservoir temperature for the wells drilled in the OP and Ev Formations. Pressure increases incrementally every five days, and we monitor the EC of the solution over time. The experimental pressure values are $P = 500, 1000, 1500\ and\ 2550\ psia$. At the end of the experiments, we analyze the ion concentration using $ICP - MS$ and IC.

Temperature: The pressure is set to a constant value of $P = 2250\ psia$, which is the maximum allowable pressure in our $HTHP$ reactor. Temperature increases incrementally every five days, and the EC of the solution is monitored over time. The experimental temperature values are $T = 23, 65, 100, and\ 140°C$. At the end of the experiments, the ion concentration is analyzed using $ICP - MS$ and IC.

Rock Surface Area: Shale samples of different A_s, but similar V_s, are placed in DI water at constant temperature and pressure values of $T = 140°C$ and $P = 2250\ psia$, respectively. The EC of the solution is measured during the experiments. At the end of the experiments, the ion concentration is analyzed using $ICP - MS$ and IC.

5.3.3. TIP Calculations

Calculation of TIP from Ion Concentration Data: In the field, one can plot the concentration of ion i (C_i) in the flowback water versus the cumulative produced water $(V_{w,cum.})$ (schematically illustrated in Figure 5-3a). The area under $C_i - V_{w,cum.}$ represents the TIP for ion i in the field flowback water $(TIP_{Field,i})$. Eq. 5-1 can be used to calculate the total mass of all ions in the flowback water.

$$TIP_{Field,tot} = \sum_{i=1}^{n} TIP_{Field,i} \tag{5-1}$$

where n is the number of ions in the water sample.

In the laboratory and during the imbibition experiments, we measure C_i over time (schematically illustrated in Figure 5-3b). Once C_i stabilizes over time, one can use Eq. 5-2 to calculate the total mass of all ions in the solution.

$$TIP_{Lab,tot} = \sum_{i=1}^{n} C_{i,eqm.} V_w \tag{5-2}$$

where $C_{i,eqm.}$ and V_w are the equilibrium concentration for ion i and the volume of water used in experiments, respectively.

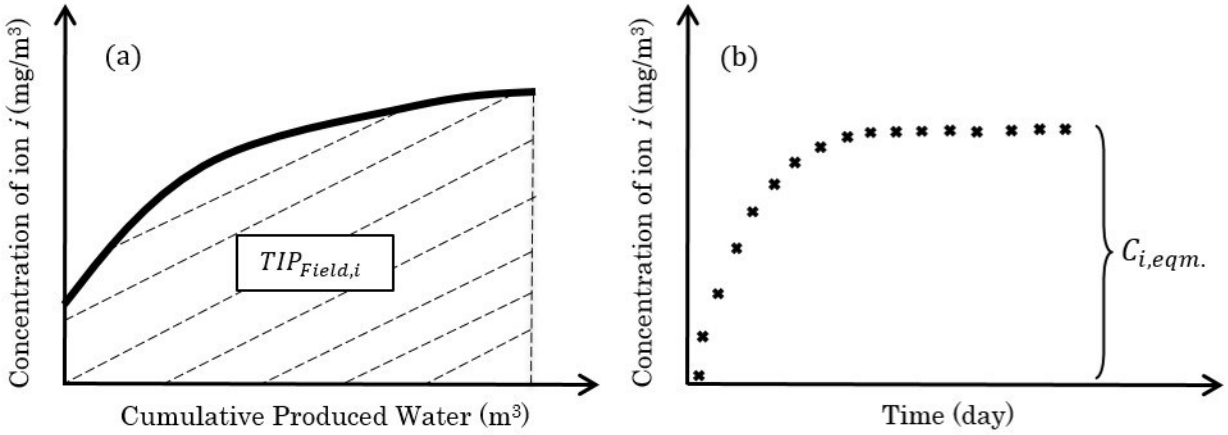

Figure 5-3. Schematic illustration of the concentration of ion i versus (a) cumulative produced water during flowback process and (b) time during isothermal shale-water interaction experiments.

Calculation of TIP from EC Data: One can use Eqs. 5-1 and 5-2 to calculate $TIP_{Field,tot}$ and $TIP_{Lab,tot}$ based on the field and laboratory data of ion concentrations measure by $ICP-MS$ and IC. However, both $ICP-MS$ and IC analyzes are relatively expensive and time consuming. We also measure the EC of aqueous solutions to approximate the values of $TIP_{Lab,tot}$ and $TIP_{Field,tot}$. We first evaporate 1 ml of the laboratory and field flowback water samples, and measure the mass of the remaining salts $(m_{salt,Lab}/m_{salt,Field})$. EC is linearly correlated to $m_{salt,Lab}$ and $m_{salt,Field}$ values (Figure 5-4).

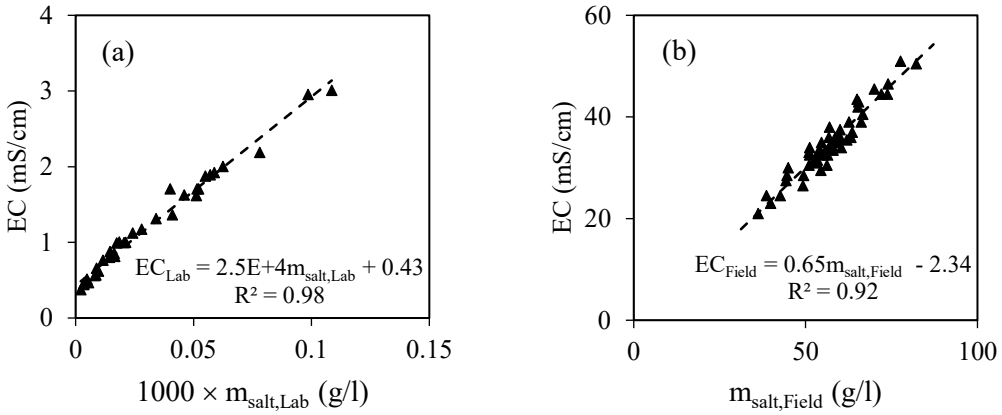

Figure 5-4. The EC of solutions versus (a) $m_{salt,Lab}$ and (b) $m_{salt,Field}$. EC_{Lab} and EC_{Field} represent the EC of the laboratory and field water samples, respectively. Both EC_{Lab} and EC_{Field} values are measured at $T = 23°C$ and $P = 14.7\ psia$. The accuracy of measured EC is ± 0.1 μS/cm.

Having the experimental value of EC_{Lab}, $m_{salt,Lab}$ is calculated using the $EC_{Lab} - m_{salt,Lab}$ correlation shown in Figure 5-4a. If DI water, which is ideally ion-free, is used in the experiments, one can approximate $TIP_{Lab,tot}$ using $TIP_{Lab,tot} = m_{salt,Lab} \times V_w$.

Similarly, the EC_{Field} of aqueous solutions is measured during flowback process. We calculate $m_{salt,Field}$ using the $EC_{Field} - m_{salt,Field}$ correlation which is shown in Figure 5-4b. Target wells in this study are fractured using slickwater (almost fresh water). During flowback process, the volume of recovered water $\left(V_{w,recov.}(t)\right)$ and its total ion content $\left(m_{salt,Field}(t)\right)$ change over time. Assuming that the initial ion concentration in the fracturing fluid is negligible, one can approximate $TIP_{Field,tot}$ using $TIP_{Field,tot} = \sum_t m_{salt,Field}(t) \times V_{w,recov.}(t)$.

5.4. Results and Discussions

5.4.1. Field Data vs. Laboratory Data

Figure 5-5 compares the concentration of selected ions (sodium, potassium, and barium) measured during flowback process and low-pressure isothermal imbibition experiments at $T =$

$23°C$. Field and laboratory results presented in Figure 5-5 belong to the OP well and OP_3 sample, respectively. We observed similar trends for other rock samples and also for the Ev well.

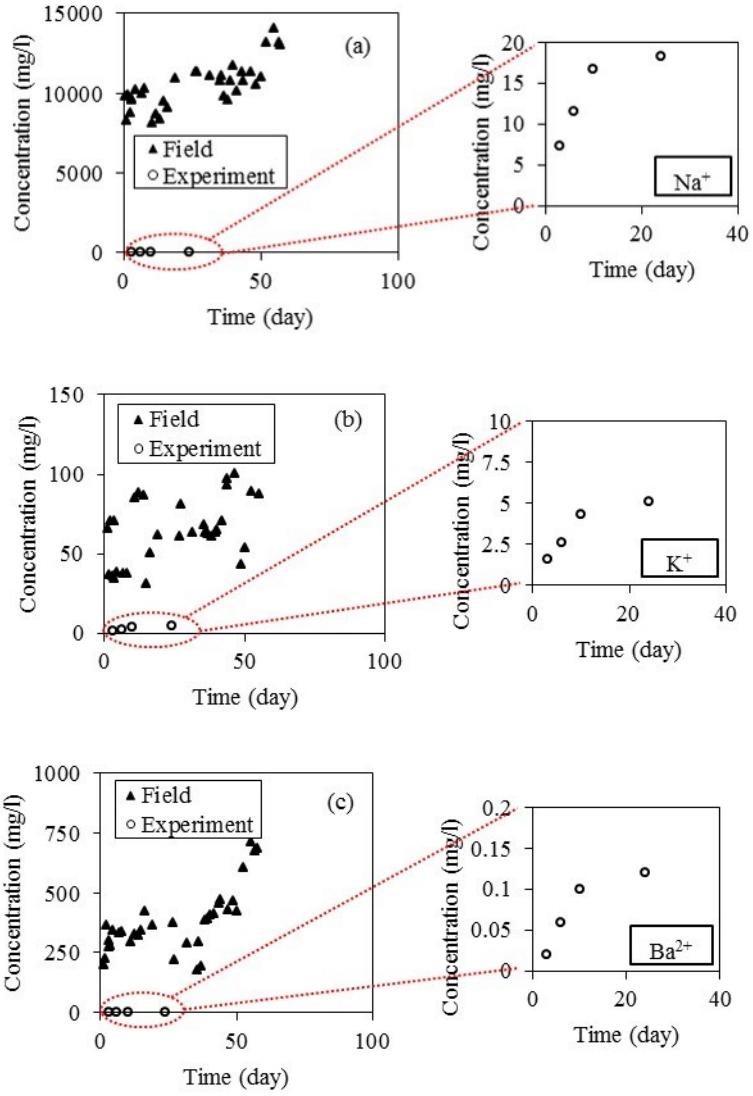

Figure 5-5.Comparison between concentrations of selected ions measured during low-pressure isothermal water imbibition experiment on OP_3 sample at $T = 23°C$ and that measured in the field during water flowback of OP well; (a) sodium ion, (b) potassium ion, and (c) barium ion. Laboratory and field data of ion concentrations are plotted against soaking time and flowback time, respectively. The accuracy of measured ion concentration is ± 0.1 mg/l.

According to Figure 5-5, the concentration of different ions during isothermal imbibition experiments at $T = 23°C$ are approximately 3 orders of magnitude smaller than that measured

during flowback process. The difference between the laboratory and field conditions (such as temperature, pressure, shale-water contact area, rock volume, and volumetric ratio of water and rock) can be responsible for the significant gap between the laboratory and field data of ion concentration.

Imbibition/leaching experiments are usually performed at lower temperature and pressure values than the reservoir (Ghanbari et al, 2013; Roshan et al., 2016; Yang et al., 2017). Different laboratory and field conditions (i.e. temperature and pressure) dictates different thermodynamic equilibrium states between water (or fracturing fluid) and rock sample (or reservoir rock); leading to different ion concentrations in laboratory and field.

Additionally, during water imbibition experiments, rock sample provides small A_s for rock-water interactions. In reservoir however, A_f is very large and provides considerable surface area for interaction of reservoir rock with the water residing in fractures. Roshan et al. (2016) concluded that the available surface area for shale-water interactions impacts the leached ions from shale samples. They calculated A_s using leached exchangeable cations, and suggested that A_f can potentially be calculated by analyzing the exchangeable cations in the recovered flowback water.

The concentration of individual ions provides information about the sources of the ions in the flowback water (Blaunch et al., 2009; Haluszczak et al., 2013) and can be used to characterize the fracture network (see Chapter 2). In addition to the individual ion concentration, the total mass of recovered salts/ions (i.e., TIP) during the production period may provide additional information for the fracture network. Figure 5-6 compares the calculated values of laboratory and field data of TIP. Similar to the individual ion concentration data (Figure 5-5) there is a significant gap between the TIP_{Field} and TIP_{Lab} values. For the OP well, the TIP_{Field} is more than 20 tonnes, while the TIP_{Lab} is less than 15 mg at the end of the imbibition experiments with OP_3 sample (Figure 5-6).

It must be noted that in both Figures 5-5 and 5-6, we plotted the experimental results of ion concentration and TIP versus soaking time, while the corresponding field data are plotted against the flowback time. These two time scales are not necessarily equivalent. We assume a pseudo-equilibrium state is achieved between rock and water under both laboratory and field conditions. More specifically, according to Figures 5-5 to 5-7, majority of the ion transfer from rock-to-water occurs during the first five days of the experiments; and after that, the net ion transfer slows down

significantly. Thus, we assume a pseudo-equilibrium state between rock and water after five days of soaking experiments. In the field, the target wells in this study are shut-in for more than two weeks. Similarly, we assume the pseudo-equilibrium state is achieved between the reservoir rock and fracturing fluid (i.e., water).

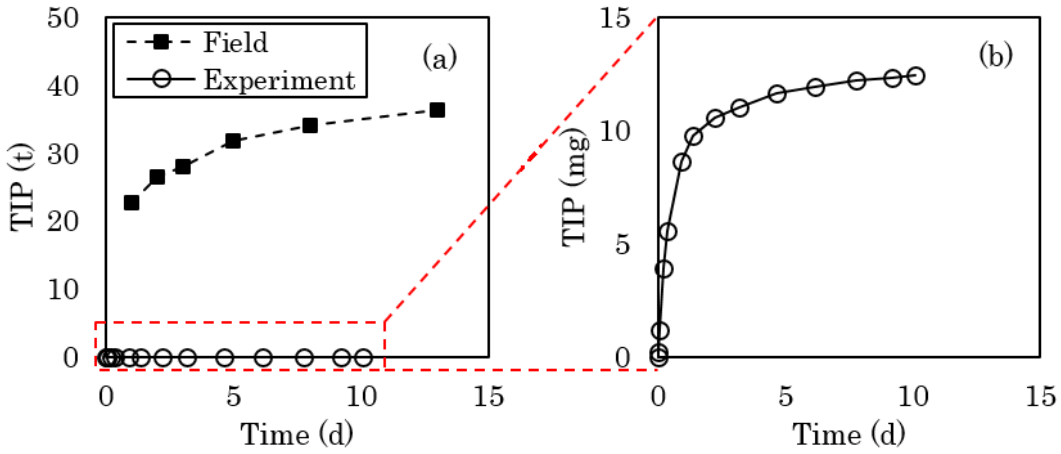

Figure 5-6. Comparison between TIP_{Lab} and TIP_{Field}. The TIP_{Lab} is calculated using the ion concentration values measured over soaking time during low-pressure isothermal water imbibition experiment on OP_3 sample at $T = 23°C$ and $P = 14.7\ psia$. The TIP_{Field} is calculated using the ion concentration values measured over flowback time of OP well. The units of TIP in Figures (a) and (b) are different to depict the difference between TIP_{Field} and TIP_{Lab}.

5.4.2. Results of Low-Pressure Experiments

Figure 5-7 shows the effects of temperature and A_s on the TIP_{Lab} values during the low-pressure water-rock interaction experiments on selected OP samples. We observe similar trends for the rest of OP samples as well as Ev samples.

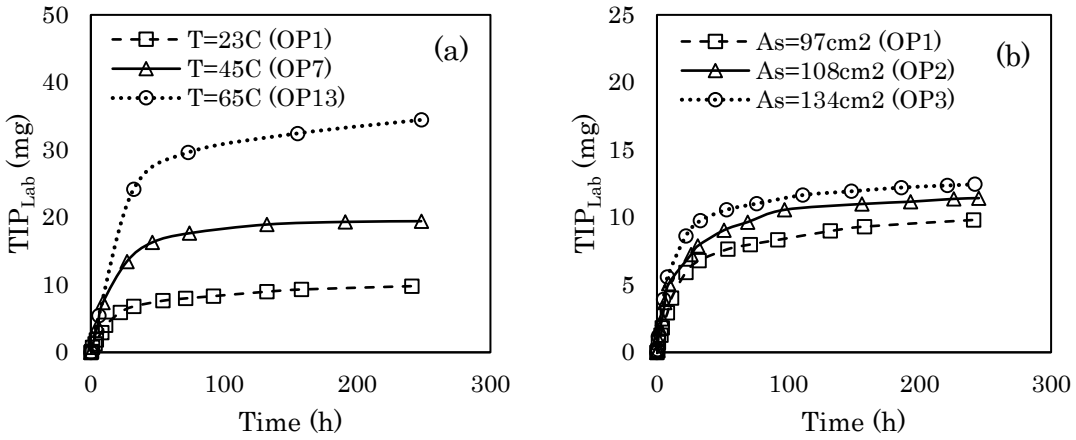

Figure 5-7. Effects of (a) temperature and (b) A_s on the TIP_{Lab} of the solution during low-pressure ($P = 14.7\ psia$) water-rock interaction experiments using representative OP samples. The Y-axis' units in Figures (a) and (b) are different to show the difference among the curves.

Increasing temperature increases the TIP_{Lab} (Figure 5-7a). High temperature generally (i) expedites the physiochemical reactions (Fogler, 2010) and (ii) increases the ion diffusion coefficients (Treybal, 1980); which can lead to high TIP_{Lab}. At late times, TIP_{Lab} stabilizes over time, where we consider its value as the $TIP_{Lab,tot}$.

Increasing A_s increases the TIP_{Lab} (Figure 5-7b), which can be due to mineral dissolution and ion-exchange reactions by clays. Furthermore, physiochemical reactions between rock constituents and water can potentially be increased by providing large mass transfer area; resulting in high TIP_{Lab}. Similarly, we consider $TIP_{Lab,tot}$ where the value of TIP_{Lab} stabilizes over time.

5.4.3. Results of High-Pressure Experiments

Figure 5-8a shows the effect of pressure on the TIP_{Lab} during the isothermal water-rock interaction experiments at $T = 140$℃. Pressure does not have significant impact on the TIP_{Lab}. More specifically, we increase the pressure incrementally every five days. TIP_{Lab} slightly increases with pressure. High-pressure may favor the dissolution of some minerals such as calcite (Peng et al., 2015), which can explain the gradual increasing trend of TIP_{Lab} with pressure.

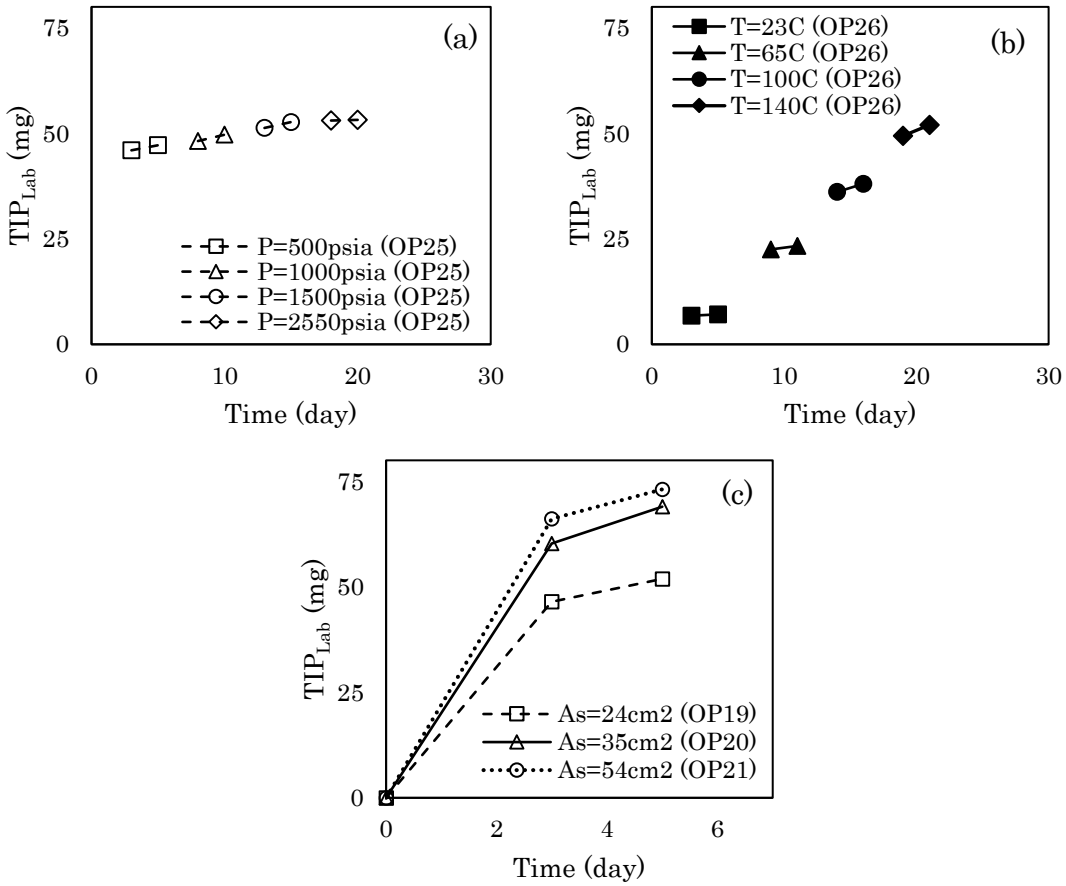

Figure 5-8. Effects of (a) pressure, (b) temperature, and (c) A_s on the TIP_{Lab} of the solution during high-pressure water-rock interaction experiments using representative OP samples.

For reactions without gaseous products, the equilibrium reaction constant (K_{eq}) does not depend on pressure (Eq. 5-3) (Levenspiel, 1999). Pressure independency of K_{eq} may explain the negligible variation of TIP_{Lab} with pressure (Figure 5-8c).

$$K_{eq} = exp(\frac{-\Delta_r G^{\circ}}{RT}) \tag{5-3}$$

Where, T is temperature, R is the universal gas constant, and $\Delta_r G^{\circ}$ is the standard Gibbs free energy change.

Since pressure does not significantly impact the TIP_{Lab}, we performed the rest of our $HTHP$ experiments at $P = 2550\ psia$, which is the maximum allowable pressure in our $HTHP$ reactor. Figure 5-8b shows the effect of temperature on the TIP_{Lab} at constant pressure of $2550\ psia$.

TIP_{Lab} sharply increases with increasing temperature. Mineral dissolution generally increases by increasing the temperature (Perry and Green, 2007), which can be responsible for the positive correlation of TIP_{Lab} with temperature in Figure 5-8b. Additionally, ion diffusion becomes faster at higher temperature (Treybal, 1980). Thus, increasing temperature can potentially improve the mass transfer from rock to water, increasing TIP_{Lab}.

Figure 5-8c shows the effect of A_s on the TIP_{Lab} at constant temperature and pressure values of $T = 140℃$ and $P = 2550\,psia$, respectively. Similar to the $LPLT$ tests (Figure 5-7b), increasing A_s increases the TIP_{Lab} at $HTHP$ conditions. High shale-water contact area (i.e., A_s) enhances the accessibility to the clay-rich zones (see Chapter 2), facilitating the ion-exchange reactions. Furthermore, the precipitated salts on the surface of natural fractures (Gale et al., 2014) or in the pore space (Fakcharoenphol, 2014) become more accessible to the water by increasing A_s. In addition, high A_s facilitates the physiochemical reactions between rock and water by providing more shale-water contact area, potentially leading to high TIP_{Lab}.

Comparing of Figure 5-7 with Figure 5-8 suggests that performing the shale-water interaction experiments at $HTHP$ conditions leads to significantly higher TIP_{Lab} compared with that performed at $LTLP$ conditions. For instance, OP_3 has more than five times A_s than OP_{19} (Tables 5-2 and 5-3). However, $TIP_{Lab,tot}$ is nearly seven times for $HTHP$ experiment with OP_{19} compared with that for $LTLP$ experiment with OP_3 (Figure 5-7b and Figure 5-8c).

5.5. Field Application

Experimental results indicate that TIP_{Lab} is significantly influenced by A_s and temperature (Figures 5-7 and 5-8). In this section, we scale-up the results of shale-water interaction experiments to estimate A_f for two wells completed in the HRB.

5.5.1. Estimation of A_f using Low-Pressure Experimental Data

Figure 5-9a shows the effect of A_s on the $TIP_{Lab,tot}$ for isothermal $(T = T_j)$ shale-water interaction experiments at $P = 14.7\ psia$ $\left(TIP_{Lab,tot}\big|_{T_j}\right)$ using OP samples.

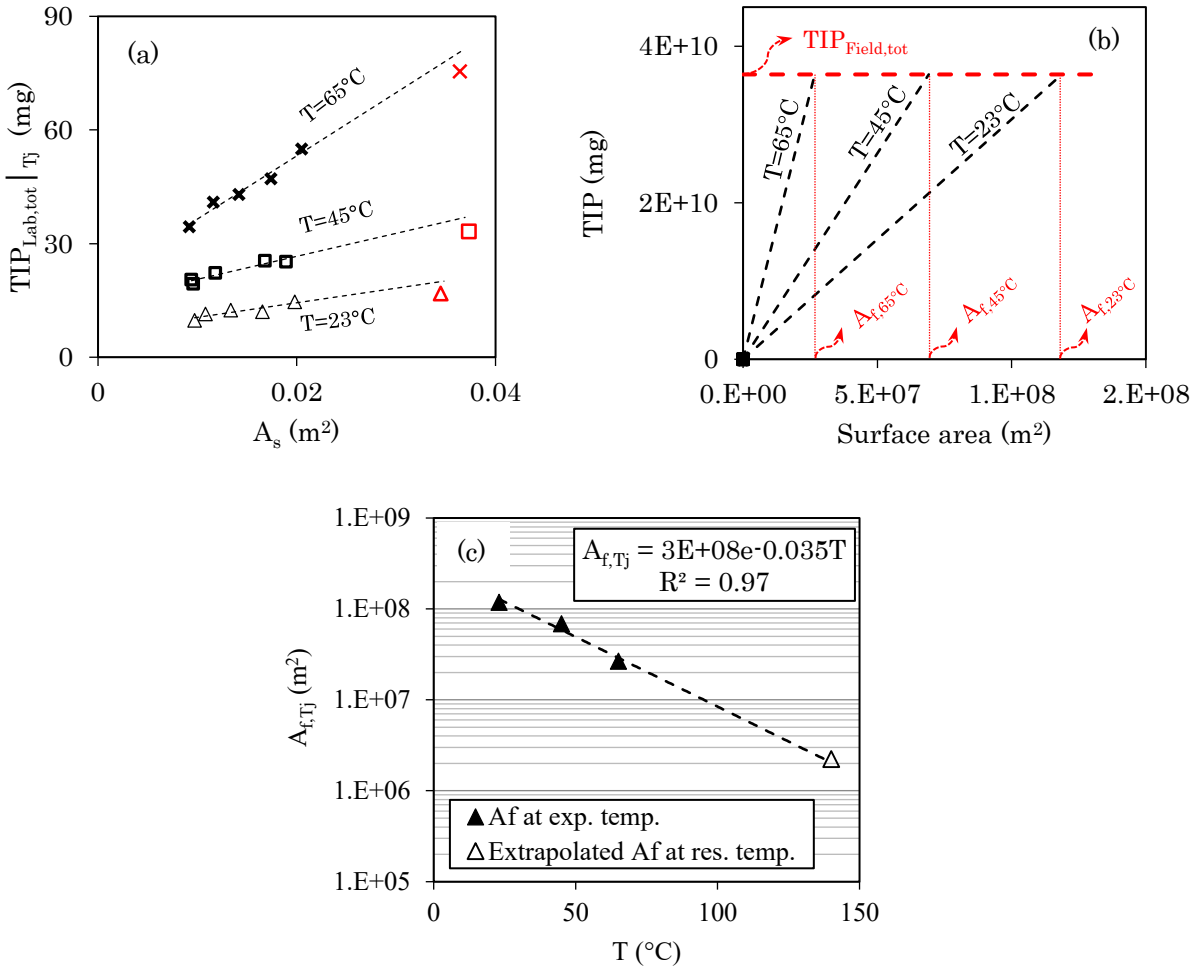

Figure 5-9. (a) Effect of A_s on the $TIP_{Lab,tot}\big|_{T_j}$ during isothermal $(T = T_j)$ shale-water interaction experiments at $P = 14.7\ psia$ using representative OP samples. The red color points represent the samples with known A_s values. (b) Estimated A_{f,T_j} using the $TIP_{Lab,tot}\big|_{T_j} - A_s$ correlations that are presented in Table 5-4. (c) Effect of temperature on the estimated A_{f,T_j} (solid-black triangle points). The correlation between $A_{f,T_j} - T$ is used to extrapolate $A_{f,Res.}$ (hollow-black triangle point).

We use linear regression to find the correlation between $TIP_{Lab,tot}\big|_{T_j}$ and A_s, which are provided in Table 5-4. In order to verify the accuracy of the regression, for each of the isothermal experimental data sets, we use the $TIP_{Lab,tot}\big|_{T_j} - A_s$ correlation to estimate the surface area of known sample $\left(A_{s,known}\big|_{est.}\right)$. Table 5-4 compares $A_{s,known}\big|_{est.}$ with $A_{s,known}$ and the corresponding error $\left(Err._{A_s}\right)$, which is defined as

$$Err._{A_s}\ (\%) = \left|\frac{A_{s,known}\big|_{est.} - A_{s,known}}{A_{s,known}}\right| \times 100 \tag{5-4}$$

Table 5-4. A comparison between $A_{s,known}$ and $A_{s,known}\big|_{est.}$ for each sets of low-pressure isothermal shale-water interaction experiments at $P = 14.7\ psia$.

Sample	$T\ (°C)$	$A_{s,known}$ (cm^2)	$TIP_{Lab,tot}\big\|_{T_j} - A_s$ correlation	$A_{s,known}\big\|_{est.}$ (cm^2)	$Err._{A_s}$ (%)
OP_6	23 ± 0.5	344.0 ± 0.25	$TIP_{Lab,tot}\big\|_{23°C} = 306.7A_S + 8.0$	287.5 ± 0.25	13.1
OP_{12}	45 ± 0.5	373.0 ± 0.25	$TIP_{Lab,tot}\big\|_{45°C} = 526.2A_S + 15.9$	329.3 ± 0.25	11.7
OP_{18}	65 ± 0.5	364.0 ± 0.25	$TIP_{Lab,tot}\big\|_{65°C} = 1363.3A_S + 25.1$	370.1 ± 0.25	1.6
Ev_6	23 ± 0.5	380.0 ± 0.25	$TIP_{Lab,tot}\big\|_{23°C} = 377.3A_S + 8.8$	434.5 ± 0.25	14.3
Ev_{12}	45 ± 0.5	353.0 ± 0.25	$TIP_{Lab,tot}\big\|_{45°C} = 690.8A_S + 16.4$	385.0 ± 0.25	9.0
Ev_{18}	65 ± 0.5	410.0 ± 0.25	$TIP_{Lab,tot}\big\|_{65°C} = 1137.1A_S + 32.2$	367.8 ± 0.25	7.8

The average error for estimation of $A_{s,known}$ is around 9.5%. According to Table 5-4, compared with the data set at $T = 23°C$, the error for estimation of $A_{s,known}$ deceases when we use experimental data sets at higher temperature values ($T = 45$ and 65°C).

$TIP_{Field,tot}$ for the OP and Ev wells are about 36.4 and 52.2 tonne, respectively. We place $TIP_{Field,tot}$ values in the $TIP_{Lab,tot}\big|_{T_j} - A_s$ correlations (presented in Table 5-4) to estimate A_f using each sets of isothermal tests $\left(A_{f,T_j}\right)$ (Figure 5-9b). It is worth mentioning that the $TIP_{Lab,tot}\big|_{T_j} - A_s$ correlations presented in Table 5-4 are specific to our samples, and might not be applicable to all samples from the target formations.

According to Figure 5-9b, the estimated A_{f,T_j} value decreases when we use experimental data set at higher temperature values $\left(A_{f,65°C} < A_{f,45°C} < A_{f,23°C}\right)$. Increasing temperature increases TIP per unit rock surface area; decreasing the estimated A_f values.

The average reservoir temperature in both OP and Ev wells is approximately $140°C$. The temperature-dependency of reaction rates usually describes by Arrhenius equation ($k = Aexp(-E_a/RT)$); where k is the reaction rate constant, A is pre-exponential factor, E_a is the activation energy, and R is the universal gas constant (Fogler, 2010). Thus, similar to Arrhenius equation, we use exponential regression to extrapolate A_f at reservoir temperature $\left(A_{f,Res.}\right)$, and the results are presented in Figure 5-9c for the OP well. There is a negative correlation between A_{f,T_j} and T. Using the low-pressure experimental results, the extrapolated $A_{f,Res.}$ values are $2.6 \times 10^6 m^2$ and $6.3 \times 10^6 m^2$ for the OP and Ev wells, respectively.

5.5.2. Estimation of A_f using High-Pressure Experimental Data

Figure 5-10a illustrates the effect of A_s on the $TIP_{Lab,tot}$ for OP samples at constant temperature and pressure values of $T = 140$℃ and $P = 2550\ psia$, respectively. We use the linear $TIP_{Lab,tot} - A_s$ correlation (shown on Figure 5-10a) to estimate the $A_{s,known}$ $\left(A_{s,known}\big|_{est.}\right)$ (red point on Figure 5-10a). The $Err._{A_s}$ is approximately 8.3% for estimation of $A_{s,known}$ using $HTHP$ experimental results. We extrapolate the $A_{f,Res.}$ by placing the $TIP_{Field,tot}$ into the linear $TIP_{Lab,tot} - A_s$ correlation (Figure 5-10b). Using the high-pressure experimental results, the calculated $A_{f,Res.}$ values are $7.9 \times 10^6 m^2$ and $1.3 \times 10^7 m^2$ for OP and Ev wells, respectively.

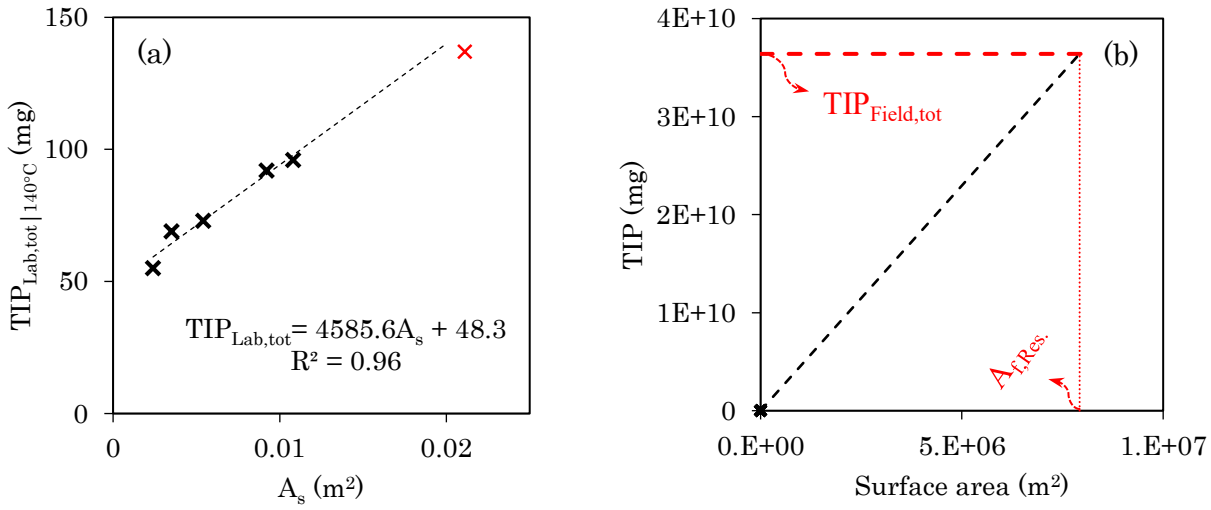

Figure 5-10. (a) Effect of A_s on the $TIP_{Lab,tot}|_{140°C}$ during isothermal shale-water interaction experiments at $T = 140°C$ and $P = 2550\ psia$ using OP samples. The red color point represent the sample with known A_s value. (b) Extrapolation of $A_{f,\text{Res.}}$ using the $TIP_{Lab,tot}|_{140°C} - A_s$ correlations that is shown on Figure (a).

5.5.3. Verification of the Estimated A_f Values

In order to verify the estimated $A_{f,\text{Res.}}$ results, we first compare them with those calculated from the production and flowback rate-transient-analysis (RTA). We also interpret the field data of water and gas recoveries along with the fracture network complexity analysis to qualitatively evaluate the estimated $A_{f,Res.}$ values.

***A_f from Rate-Transient Analysis* (*RTA*):** We calculated A_f for both target wells by RTA of the production data $(A_{f,RTA_{Production}})$. The calculated $A_{f,RTA_{Production}}$ values are $2.2 \times 10^6 m^2$ and $1.9 \times 10^5 m^2$ for the OP and Ev wells, respectively.

Flowback RTA is another method to calculate A_f. We did not have flowback RTA for our target wells. However, Xu et al. (2017) calculated A_f using flowback RTA $(A_{f,RTA_{Flowback}})$ of wells completed in the OP Formation in a well-pad adjacent to our target wells. Figure 5-11

compares the estimated $A_{f,Res.}$ values from $LTLP$ and $HTHP$ tests with those calculated from production and flowback $RTAs$ ($A_{f,RTA_{Production}}$ and $A_{f,RTA_{Flowback}}$).

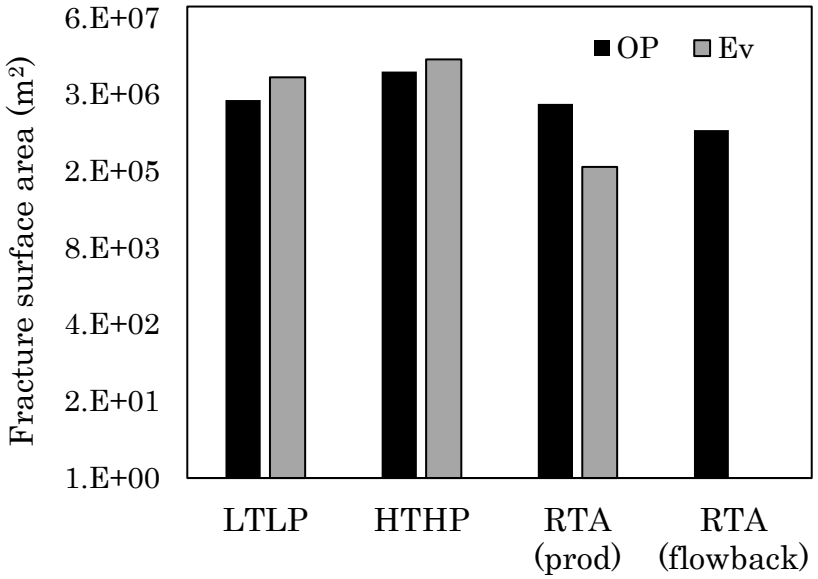

Figure 5-11. A comparison among the estimated $A_{f,Res.}$ from $LTLP$ and $HTHP$ imbibition tests and that calculated from the production RTA results for OP and Ev wells. The value presented for flowback RTA are the average A_f value reported by Xu et al. (2017) from flowback RTA of wells drilled in OP formations in a well-pad adjacent to our target wells.

The estimated $A_{f,Res.}$ from the scale-up of the $LTLP$ and $HTHP$ imbibition test results have similar orders of magnitude compared with those calculated from both production and flowback RTA results. Also, the estimated $A_{f,Res.}$ from the $HTHP$ imbibition tests are larger than that estimated from low-pressure imbibition tests. One possible explanation can be due to the slightly higher TIP per unit surface area of the rock sample at high-pressure conditions compared with that at low-pressure conditions (Figure 5-10a). More specifically, increased dissolution of certain minerals such as calcite at high-pressure conditions (Peng et al., 2015) lowers the $TIP - A_s$ slope, leading to slightly higher estimation of $A_{f,Res.}$ compared with that estimated using the low-pressure experimental data.

Water and Gas Recovery Data: Figure 5-12 compares the field data flowback water and gas recoveries for the OP and Ev wells. Ev well shows higher gas production ($\sim 5500\ m^3$) than OP well ($\sim 2700\ m^3$) during the 14-day flowback period. Higher estimated $A_{f,Res.}$ of the Ev well

corresponds to higher matrix-fracture contact which can facilitate gas production compared with the OP well. Moreover, higher $A_{f,Res.}$ of the Ev well enhances the chance of water leak-off into the matrix (see Chapter 2), resulting in lower water recovery ($\sim 1.8\%\ of\ TIV$) compared with the OP well ($\sim 6.9\%\ of\ TIV$) during the 14-day flowback period.

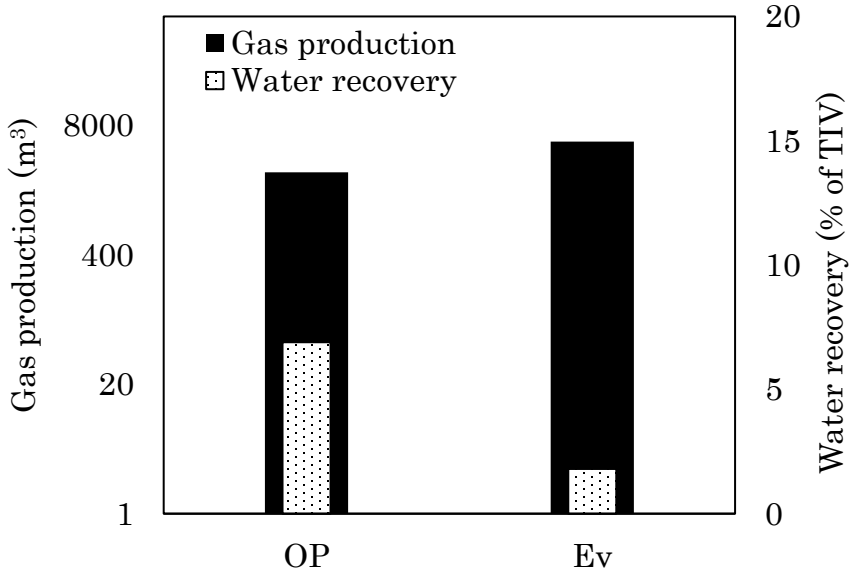

Figure 5-12. Gas production and water recovery during 14-day flowback period for OP and Ev wells.

Fracture Network Complexity Analysis: The estimated $A_{f,Res.}$ values also comply with the previous studies on analysis of fracture network complexity of these two wells. The experimental and modeling results presented in Chapters 2 and 4 suggested that the Ev well has more complex fracture network than the OP well. More complex fracture network in Ev agrees with its higher estimated $A_{f,Res.}$ value (Figure 5-11), as oppose to the simpler fracture network in OP and its lower estimated $A_{f,Res.}$ value (Figure 5-11).

5.6. Limitations of the Proposed Scale-up Technique

The proposed scale-up procedure for estimation of A_f based on the ion concentration data during $LTLP$ and $HTHP$ imbibition tests accounts for shale-water contact area (A_f), temperature, and pressure. However, in this chapter, the $LTLP$ and $HTHP$ experiments are conducted in

presence of air. The oxygen presented in the air can oxidize the redox-sensitive elements of the rock (such as iron, sulfate, and bromide) (Sun et al., 2013; Xu et al., 2018). In other words, we performed our experiments at oxic conditions. However, there is limited (or no) oxygen in the reservoir, and thus, it is initially at anoxic condition (Curtis, 2002). The dominant reactions controlling the water chemistry in the oxygen-rich laboratory environment could be different compared with those in the oxygen-poor reservoir conditions.

It must be noted that, fracturing fluid should be oxygen-rich as it is usually in contact with air for long time. Injection of oxygen-rich fracturing fluid can alter the redox state locally (i.e., at fracture-matrix face) during the fracturing and soaking periods. Thus, for the scale-up purpose, one should perform the experiments at controlled oxygen content if the reservoir contains significant amount of redox-sensitive minerals (such as pyrite) to best simulate the downhole condition.

There is a linear relationship between $TIP_{Lab,tot}$ and A_s at the experimental conditions (Figures 5-9a and 5-10a). The linear correlation is valid at the limited range of A_s values (less than 400 cm^2). Future studies should further investigate the linear $TIP_{Lab,tot} - A_s$ correlation at higher A_s values to ensure the validity of the proposed scale-up procedure at the reservoir scale.

5.7. Summary

This chapter presents the results of shale-water interaction experiments (i.e., water imbibition) at two different conditions of (i) low-temperature and low-pressure ($LTLP$) and (ii) high-temperature and high-pressure ($HTHP$). The experiments investigate the effects of rock surface area (A_s), temperature, and pressure on the total ion produced (TIP). $LTLP$ experiments include conducting

a. imbibition tests at different temperatures ($T = 23, 45$, and 65℃) using shale samples of similar A_s and volume (V_s) at $P = 14.7\ psi$.

b. isothermal imbibition tests using shale samples of different A_s but similar V_s at $P = 14.7\ psi$. Isothermal experiments are conducted at $= 23, 45,$ and $65℃$ to simultaneously investigate the effect of A_s and temperature on TIP.

$HTHP$ experiments include conducting

a. isothermal imbibition tests ($T = 140℃$) using shale samples of similar A_s and V_s. The pressure increased incrementally every five days to investigate the effects of pressure on TIP. The test pressures are $P = 5000, 1000, 1500,$ and $2550\ psia$.

b. imbibition tests at constant pressure of $P = 2550\ psia$ using shale samples of similar A_s and V_s. The temperature increased incrementally every five days to investigate the effects of temperature on TIP. The test temperatures are $T = 23, 65, 100,$ and $140℃$.

c. imbibition tests using shale samples of different A_s but similar V_s at $T = 140℃$ and $P = 14.7\ psi$.

Experimental results indicate that pressure has negligible impact on TIP, while both A_s and T are positively correlated to TIP. This chapter also presents a scale-up technique estimate the fracture surface area (A_f) using laboratory and field data of ion concentration. The estimated A_f is higher for the well with higher gas production and lower water recovery in the field as opposed to the well with lower gas production and higher water recovery. The estimated A_f values comply with the fracture network complexity analysis using barium ion concentration profiles (Chapter 2) and salinity profiles (Chapter 4). More specifically, the proposed scale-up procedure estimates higher A_f value for the Ev well which expected to have a more complex fracture network (Chapters 2 and 4) compared with that for the OP well.

In addition to the results presented in this chapter, a similar scale-up procedure is presented in Appendix C to estimate the invaded reservoir volume (IRV) using the laboratory and field data of ion concentration. The estimated IRV is higher for the Ev well compared with that for the OP well. The estimated IRV values comply with the field data of water recovery. More specifically, the Ev well (with higher estimated IRV value) has lower water recovery in the field compared with the OP well with higher field water recovery and lower estimation of IRV value.

Nomenclatures

A	Pre-exponential factor in Arrhenius equation
A_f	Fracture surface area
A_{f,T_j}	Fracture surface area estimated using experimental data of isothermal water imbibition at $T = T_j$
$A_{f,Res.}$	Extrapolated fracture surface area at reservoir temperature
$A_{f,RTA_{Production}}$	Estimated fracture surface area by production rate-transient-analysis
$A_{f,RTA_{Flowback}}$	Estimated fracture surface area by flowback rate-transient-analysis
A_s	Surface area of rock sample
$A_{s,known}$	Surface area of known sample
$A_{s,known}\big\vert_{est.}$	Estimated surface area of known sample by the scale-up procedure
C_i	Concentration of ion i
$C_{i,eqm.}$	Equilibrium concentration of ion i
DI	Deionized
E_a	Activation energy
EC	Electrical conductivity
EC_{Field}	Electrical conductivity of flowback water samples
EC_{Lab}	Electrical conductivity of aqueous solutions measured during imbibition experiments
$Err._{A_s}$	Error associated with estimation of surface area of the known sample
Ev	Evie
$HTHP$	High-temperature and high-pressure
$ICP-MS$	Inductively coupled plasma mass spectrometry
k	Reaction rate constant
K_{eq}	Equilibrium reaction constant
$LTLP$	Low-temperature and low-pressure

$m_{salt,Field}$	The mass of the remaining salts after evaporation of 1 ml of the flowback water sample
$m_{salt,Field}(t)$	The mass of the remaining salts after evaporation of 1 ml of the flowback water at time t.
$m_{salt,Lab}$	The mass of the remaining salts after evaporation of 1 ml of the solution used in the imbibition experiments
n	The number of ions
OP_i	OP sample number i
R	Universal gas constant
RTA	Rate transient analysis
t	Time
T	Temperature
TIP	Total ion produced
$TIP_{Field,i}$	The total mass of produced ion i in the flowback water
$TIP_{Lab,tot}\big\vert_{T_j}$	The total mass of ions produced during isothermal imbibition experiments at $T = T_j$.
$TIP_{Field,tot}$	The total mass of ion produced during flowback process
$TIP_{Lab,tot}$	The total mass of ion produced during imbibition experiment
TIV	Total injected volume
V_s	Volume of rock sample
V_w	The volume of water used in imbibition experiments
$V_{w,cum.}$	Cumulative produced water
$V_{w,recov.}(t)$	Volume of recovered flowback water as a function of time
XRD	X-ray diffraction
$\Delta_r G^\circ$	Standard Gibbs free energy change

Chapter 6

Water Sorption Behaviour of Gas Shales: I. Role of Clays

6.1. Introduction

Exploitations of the shale reserves have caused tremendous hydrocarbon production around the world, particularly in the United States and Canada. Advances in horizontal drilling and multistage hydraulic fracturing technologies paved the way towards economic oil and gas production from shales (Ning et al. 1993; King, 2012).

Although shales are considered to be a game changer in the energy industry (Rivard et al., 2014; Gevorkyana and Semmler, 2016), researchers face several challenges to design optimal field-scale operational procedure for hydrocarbon recovery from these unconventional reserves. Shales are challenging particularly due to their heterogeneous nature (Diaz, et al., 2010; Fathi and Akkutlu, 2009), low permeability and porosity (Naraghi and Javadpour, 2015; Pan et al., 2015), abundance of natural fractures (Gale et al., 2007), and presence of clay minerals (Chenevert, 1970; King, 2012).

Among the aforementioned parameters, presence of clay minerals has gained considerable research attentions. Li et al., (2016) showed that presence of clay minerals impacts water distribution in shales, which in turn alters methane adsorption capacity. Also, water activity of shales depends on the clay content (Chenevert, 1970; Wen et al., 2015) as water molecules can adsorb on the negatively-charged clay surfaces (Essington, 2005). Water adsorption by clays can cause swelling (Chenevert, 1970) and damage matrix permeability (Scott et al., 2007). Swelling of clay minerals can induce micro-fractures (Makhanov et al., 2014; Roshan et al., 2015; Sun et al., 2015; Ghanbari and Dehghanpour, 2015; Meng et al., 2015; Zhou et al., 2016) and deteriorate well integrity (Steiger and Leung; 1992). From the environmental point of view, presence of clay minerals in shale reservoirs is also important as they affect the fate of fracturing fluid (Ghanbari and Dehghanpour, 2016) and the chemistry of recovered flowback water (see Chapter 2).

Several past studies focused on sorption behavior of shales using different gases (i.e., N_2, CO_2, and argon) to investigate different properties of reservoir/shale samples. Yu et al. (2014 and 2016) used N_2-BET (Brunauer–Emmett–Teller) analysis to estimate original gas in place in Marcellus shale. Jin et al. (2015) performed N_2, CO_2, and argon sorption experiments on gas shale samples. They concluded that CO_2 has a very strong affinity to organic matter; and the presence of open fractures reduces the effect of gas sorption on the effective permeability. Lin and Kovscek

(2014) developed a numerical model to investigate the permeability change by gas adsorption. Their results indicated that permeability reduction is more prominent when CO_2 is used as adsorbent instead of N_2. They concluded that N_2 mainly forms a monolayer film on the pore surface, while CO_2 has strong multi-layer adsorption. It is worth mentioning that surface diffusion enhances adsorption process, especially in small capillaries (Wu et al., 2015 and 2016). For instance, they showed that over 90% of gas mass transfer in pores of <2 nm is controlled by surface diffusion process (Wu et al., 2015).

Water sorption behaviour of shales has been the focus of several studies to investigate the alteration of petrophysical properties, mechanical strength, and swelling potential of shale samples. Water adsorption by clay-rich shales can cause spalling and induce fractures (Chenevert, 1970, Ghanbari and Dehghanpour, 2015), reducing the mechanical strength of shale samples. Tandanand (1985) showed that tangent modulus and compressive strength of shales decrease linearly with the sample's moisture content. Al-Bazali et al. (2008) showed that water adsorption and leaching of ions out of shales weakens their mechanical strength. Lyu et al. (2015) investigated shale swelling caused by the water adsorption process. They concluded that maximum swelling rate occurs at shale's initial water content of 14%. Li et al. (2016) analyzed water adsorption isotherms in order to investigate the effect of water distribution on methane adsorption capacity. They concluded that due to hydrophilicity nature of clays, water uptake for clay-rich shales is high which in turn reduces the methane sorption capacity.

Interpretation of water sorption behaviour of shales is challenging as water molecules can be simultaneously condensed in pore space (Chenevert, 1970; Chen et al., 2012) and also adsorbed on the surface of clays. Kelvin equation commonly uses in the literature to describe capillary condensation during sorption process. Kelvin equation however, does not account for the clay adsorption process. In this study, we conduct a modified sorption experiment to investigate the role of clays during water sorption process in gas shales. We first describe the hypothesis in Section 6.2. Section 6.3 describes the materials and methods that we use to examine the hypothesis. Sections 6.4 and 6.5 cover experimental results and conclusions, respectively. We use the results obtained from this chapter to characterize the inorganic and organic pore size distributions of shale samples, which is presented in Chapter 7.

6.2. Hypothesis

When a porous medium is exposed to the vapor of a wetting fluid, vapor molecules can simultaneously (i) condense in the pore space (i.e., capillary condensation process) and (ii) adsorb on the surface of clay minerals (i.e., clay adsorption process). During the capillary condensation process, the vapor phase adsorbs as a multilayer film onto the porous medium. The process continues to the point at which the pores become filled with condensed liquid (Schramm, 1993). During clay adsorption process, polar molecules (such as water) can adsorb on negatively-charged surfaces of clay minerals. Clay adsorption process is particularly important in presence of water vapor molecules as clays have hydrophilic nature (Essington, 2005).

Kelvin equation (Eq. 6-1) commonly uses in the literature to describe the relationship between RH and the size of the water-filled capillary (Fisher and Israelachvili, 1979):

$$ln(RH) = \frac{-\gamma V_m \cos\theta}{RT}\left(\frac{1}{R_1}+\frac{1}{R_2}\right) \quad (6\text{-}1)$$

Where, γ is surface tension, V_m is the liquid molar volume, θ is contact angle, R is universal gas constant, T is temperature, and R_1 and R_2 are the principal radii of curvature.

According to Kelvin equation, water vapor condenses in small pores at low RH values. Larger pores fill with condensed water as RH increases during adsorption process. Kelvin equation however, does not account for water uptake by the clay adsorption process.

In this chapter, based on the hydrophilic nature of clay minerals, we hypothesize that clays primarily fill up their capacity for water uptake at early stages of the water adsorption process. In other words, we hypothesize that clay adsorption is the primary mechanism for water uptake at early stages of the adsorption process. The role of capillary condensation process for water uptake increases at later stages of the adsorption process.

6.3. Materials and Method

In order to analyze the hypothesis described in Section 6.2, we first perform conventional water sorption experiments using shale samples of different clay contents. We then conduct a modified water sorption experiments to investigate the role of clay adsorption process on the water uptake. We also performed water imbibition experiments using shale samples of different clay contents. We performed a comparative analysis between the results of imbibition and adsorption experiments to further scrutinize the role of clays on water uptake.

X-Ray Diffraction (XRD) Analysis: Downhole gas shale samples of different clay contents are collected from Otter-Park (OP), Evie (Ev), and Lower-Evie (LEv) formations of the Horn River Basin (HRB). Two sets of sample with different clay contents are selected from each formation. XRD analysis is used to characterize the rock mineralogy, and the results are presented in Table 6-1.

According to XRD results, illite, mica, and mixed-layer illite/smectite (I/S) are the major clay minerals in our shale samples. Total clay content of our shale samples varies from 5.8 Wt.% (OP1 sample) to 33 Wt.% (Ev2 sample). Table 6-1 also shows that the shale samples are heterogeneous as the rock mineralogy changes significantly even within a formation. For instance, Ev2 has over seven times more clay content compared with that of Ev1. It is worth mentioning that XRD uses small amount of rock volume for its analysis, and hence, the presented results in Table 6-1 might not be an accurate representation of all samples from target formations.

Table 6-1. Rock mineralogy of shale samples from XRD analysis (Wt.%). The XRD used for characterization of rock mineralogy has a signal-to-noise ratio of 400.

Minerals	OP1	OP2	Ev1	Ev2	LEv1	LEv2
Illite/Smectite (I/S)	0	5	0	14	0	3
Illite+Mica	5.8	11	4.5	19	4.9	9
Total Clay	5.8	16	4.5	33	4.9	12
Quartz	78.9	77	64	32	77.2	65
K-Feldspar	1.7	2	2	6	2.5	3
Plagioclase	5.4	2	5.1	6	0	6
Calcite	4.5	0	20.1	10	13	10
Ankerite/Fe-Dolomite	0	1	0	5	0	0
Dolomite	1.4	0	3.1	4	1.4	1
Pyrite	2.3	1	1.2	5	1	3
Total Non-Clay	94.2	84	95.5	67	95.1	88

N_2-BET Analysis: We use N_2-BET analysis to determine the total porosity of the shale samples (See Table 6-2). The total porosity of our shale samples ranges from 3.3% (OP2) to 5.6% (Ev1 sample) with an approximate value of 4.5%.

Table 6-2. Total porosity of shale samples from N_2-BET analysis. The accuracy of relative pressure measurements by N_2-BET analysis is 0.15%.

Sample	OP1	OP2	Ev1	Ev2	LEv1	LEv2
Total Porosity (%)	3.9	3.3	5.6	3.8	5.3	5.1

Conventional Sorption Experiments: We use a controlled-RH chamber to conduct the sorption experiments. To control RH, we use saturated salt solutions of known vapour pressure, as equilibrium vapour pressure is equivalent to RH. Table 6-3 lists the salts used in the water sorption experiments and their corresponding saturated vapour pressure (P^{sat}) at room temperature (23°C). We used silica gel and deionized (DI) water to preserve the RH at 0 and 1, respectively. All of the salts are purchased from Sigma-Aldrich Corporation with purity of > 93.0%.

Table 6-3. Salt solutions used in water sorption experiments and their relative P^{sat} at 23°C (Zhang et al., 2004).

Saturated solution	Silica gel	$ZnCl_2$	KCOOH	$MgCl_2$	$MnCl_2$	NaCl	KCl	KH_2PO_4	DI water
$P^{sat}(RH)$	≈0	0.1	0.215	0.32	0.56	0.755	0.85	0.960	1

We placed the oven-dried samples in the controlled-RH chamber (as schematically illustrated in Figure 6-1a). For conventional adsorption tests, we initially place the samples in the controlled-RH chamber with RH equal to 0.1 (the saturated salt solution of $ZnCl_2$). The samples reach to equilibrium conditions when their masses stabilized over time. Then, we increase the RH by switching the saturated salt solution to KCOOH ($RH \approx 0.215$). This procedure is repeated for different RH values corresponding to different salt solutions in Table 6-3. Once the conventional adsorption process completed (solid line in Figure 6-1b), the process is reversed to obtain the conventional desorption isotherm (dash line in Figure 6-1b). In other words, at the end of the adsorption process ($RH \approx 1$), we decrease the RH of the chamber in a step-wise manner to reach to $RH \approx 0$ according to Table 6-3.

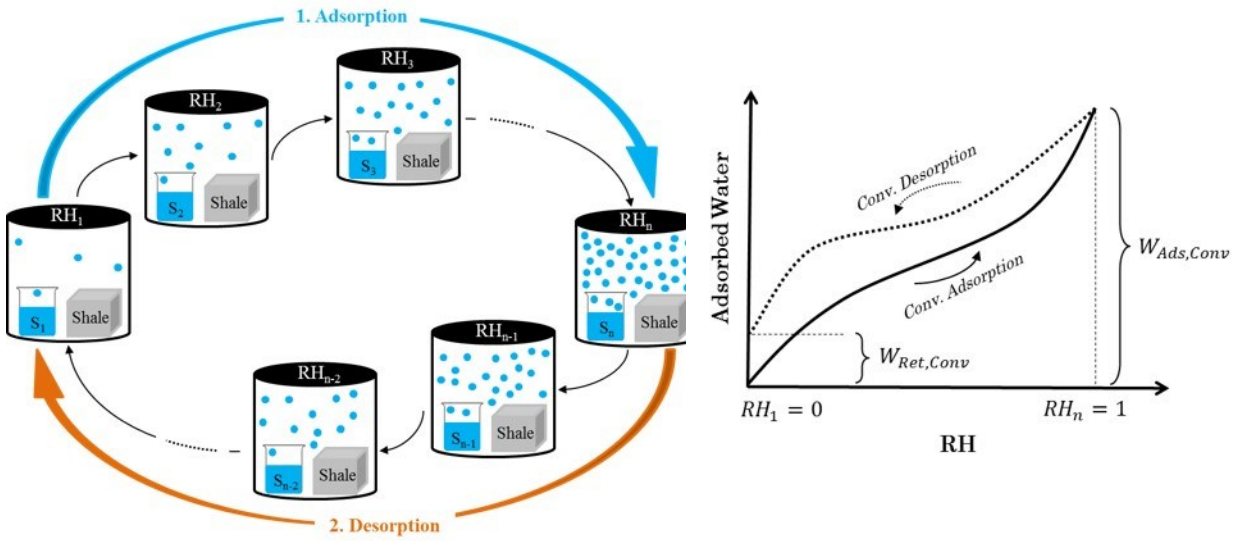

(a) (b)

Figure 6-1. Schematic illustration of (a) the conventional water sorption experiments and (b) the pertinent sorption isotherms ($RH_1 < RH_2 < \cdots < RH_{n-1} < RH_n$). S_i represents the saturated solutions of salt i.

Modified Sorption Experiments: We use a modified sorption technique (schematically illustrated in Figure 6-2) to investigate the role of clays on water uptake/depletion during water adsorption/desorption processes. The modified technique has an extra early sorption cycle (Stages 1 and 2 in Figure 6-2) compared with the conventional procedure (Figure 6-1b). The early sorption cycle consists of adsorption at $RH \approx 0.215$ (Stage 1) followed by desorption to $RH \approx 0$ (Stage 2). In other words, during Stage 1, the sample adsorbs total of $W_{Ads,Cyc}$ of water. During Stage 2, the amount of adsorbed water decreases from $W_{Ads,Cyc}$ to $W_{Ret,Cyc}$. It is worth mentioning that the primary goal of the early sorption cycle is to maximize water uptake by the clay adsorption process against the capillary condensation process. Ideally, one should use the smallest RH value for the end-point of the early sorption cycle. In our experiments however, we used $RH \approx 0.215$ instead of $RH \approx 0.1$ as the end-point of the early sorption cycle. More specifically, during the sorption experiments, we have to unseal the RH-chamber and weigh the samples. During this process, laboratory air (with an average RH value of 0.24) enters the RH-chamber. This excess RH can adversely impact our interpretation of the sorption data. More specifically, the excess RH in the air can be adsorbed by clays and also condensed in capillaries. However, the goal of this early sorption cycle is to minimize the effect of capillary condensation process.

After the early sorption cycle, we place the samples in the controlled-RH chamber for a full sorption experiment (Stages 3 and 4 in Figure 6-2). More specifically, during the modified adsorption process (Stage 3), the amount of adsorbed water increases from $W_{Ret,Cyc}$ to $W_{Ads,Mod}$. During the modified desorption process (Stage 4), the amount of adsorbed water decreases from $W_{Ads,Mod}$ to $W_{Ret,cyc} + W_{Ret,Mod}$. All experiments are performed twice to ensure reproducibility of the presented results.

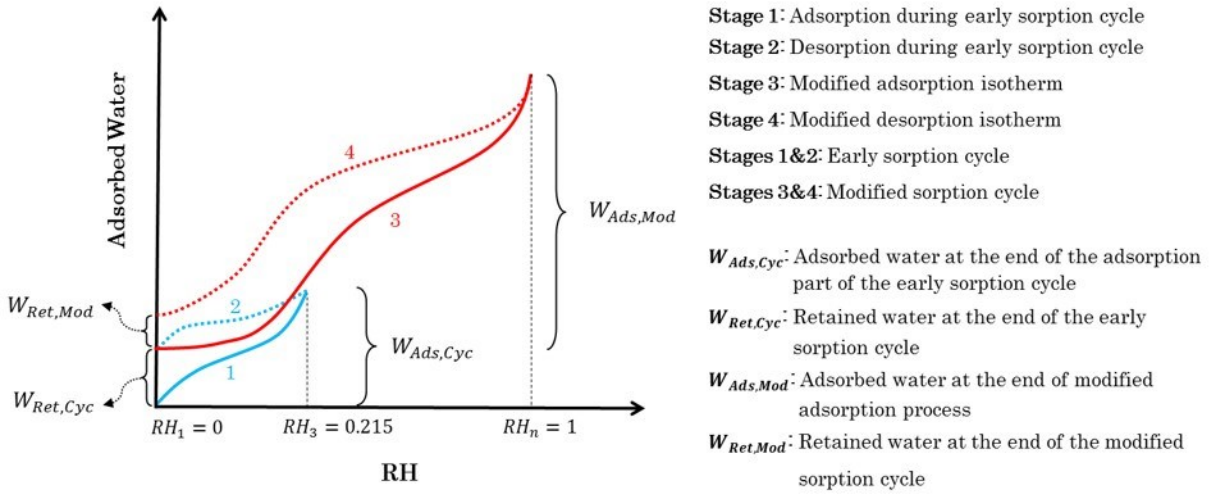

Figure 6-2. Schematic illustration of the modified sorption process. Dried samples initially go through an early sorption cycle of adsorption at $RH \approx 0.215$ (Stage 1) followed by desorption to $RH \approx 0$ (Stage 2). For stage 3, the samples obtained from stage 2 experience a full adsorption process from $RH \approx 0$ to $RH \approx 1$. At the end of Stage 3, RH will be reduced step-wise from $RH \approx 1$ to $RH \approx 0$ to complete the modified desorption process (Stage 4).

Spontaneous Imbibition Experiments: Several past studies performed water imbibition experiments using samples of different clay contents (Makhanov et al., 2014; Ghanbari and Dehghanpour, 2015; Javaheri et al., 2017a,b). We further analyze the role of clays on water uptake of shales by performing a comparative analysis between (i) spontaneous water imbibition and (ii) water adsorption experiments. We use twin samples from Set-2 samples (OP2, Ev2, and LEv2) for these experiments. For spontaneous water imbibition experiments, we fully immerse one pair of samples in deionized (DI) water, and measure the mass change over time. For water adsorption experiments, we place the other pair of samples in the sealed chamber with $RH \approx 1$, and measure the mass change over time. All experiments are performed twice to ensure reproducibility of the presented results.

6.4. Results and Discussion

Figure 6-3 compares the measured conventional and modified sorption isotherms. We only present the results for Set-1 samples (OP1, Ev1, and LEv) as the experimental data were reproducible.

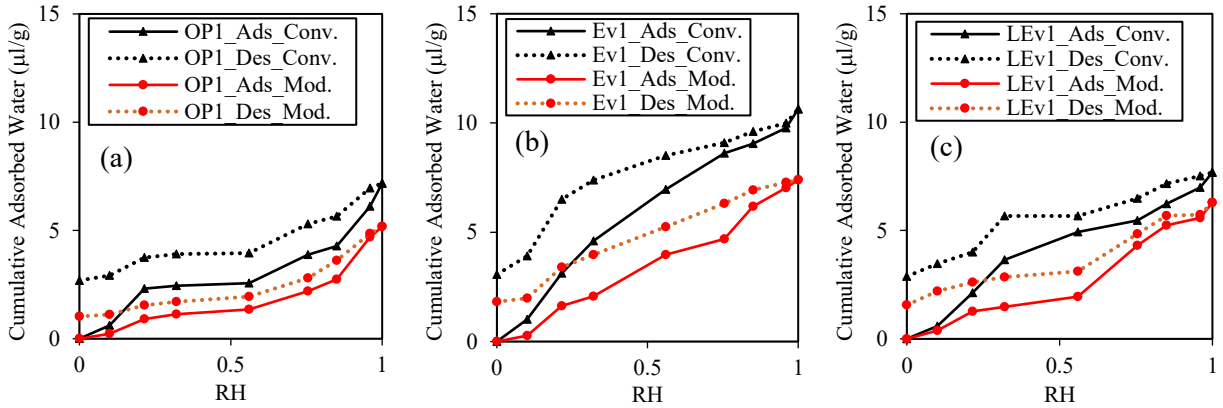

Figure 6-3. A comparison between the conventional (black curves) and modified (red curves) water sorption isotherms for Set-1 samples from (a) OP, (b) Ev, and (c) LEv formations. The early sorption cycle of the modified sorption technique is not presented in this Figure. The scale used for measuring the mass of the rock samples during water sorption experiments has an accuracy of ± 0.01 g.

6.4.1. Conventional Sorption Experiments

6.4.1.1. Early adsorption rate

According to Figure 6-3, conventional adsorption curves for all samples have relatively sharp increase rate at low RH values. On the other hand, clays' high affinity for water (Essington, 2005) increases the chance of clay adsorption at low RH values. In order to investigate the role of clays on the early water adsorption rate, we plot initial adsorption rate $(R_{Ads,i})$ against clay content for the conventional sorption process in Figure 6-4a (black rectangle points). We define $R_{Ads,i}$ as normalized water uptake at $RH \approx 0.1$ divided by 0.1.

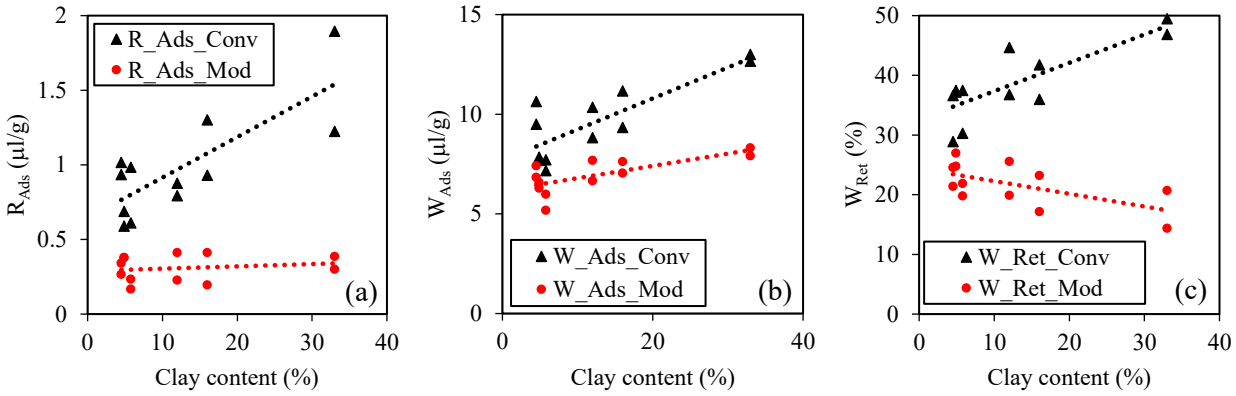

Figure 6-4. The effect of clay content on (a) the initial water adsorption rate, (b) the amount adsorbed water at the end of the adsorption process, and (c) the relative amount of retained water at the end of the desorption process compared with the maximum amount of adsorbed water during the adsorption process. Black and red points represent the results of conventional and modified processes, respectively.

According to Figure 6-4a, higher clay content increases $R_{Ads,i}$ in the conventional adsorption experiments. This observation suggests that clay minerals enhance water adsorption at early stages of the conventional adsorption process. One possible reason for this observation would be the use of oven-dried samples in conventional sorption experiments. To be specific, prior to the conventional sorption experiments, we dried the samples at 200°F which can potentially cause water loss from clays' interlayer (Hueckel, 2002). During conventional adsorption process, clays probably can rehydrate fast through adsorption of water molecules on the clays' surfaces; leading to a sharp increase in the adsorption curve.

6.4.1.2. Total amount of adsorbed water

Clay adsorption can affect the total amount of adsorbed water by the adsorption process (W_{Ads}). In order to investigate the role of clays on the total water uptake during adsorption process, we plot W_{Ads} against clay content for the conventional sorption experiments in Figure 6-4b (black rectangle points).

According to Figure 6-4b, increasing clay content increases W_{Ads} for the conventional adsorption process. Multilayer adsorption of water molecules on the surface of clay minerals can be a possible reason for this observation. Furthermore, in presence of water, clays can swell and adsorb more water (Essington, 2005). Swelling potential should be more pronounced in Set-2 samples (compared with Set-1 samples) as they have expandable mixed layer I/S clay mineral (Table 6-1).

6.4.1.3. Adsorption-desorption hysteresis

According to Figure 6-3, there is a hysteresis between the conventional adsorption and desorption isotherms. Huckel (2002) observed water hysteresis after thermal-dehydration of clay minerals. He explained this hysteresis by water retention in the interlayer of clay minerals. In order to investigate the role of clays on the hysteresis between sorption isotherms, we plot W_{Ret} against clay content for the conventional sorption experiments in Figure 6-4c (black rectangle points). W_{Ret} is the percentage of retained water after desorption process relative to W_{Ads}.

According to Figure 6-4c, increasing clay content increases W_{Ret} for the conventional adsorption process. High affinity of clay minerals for water may prevent depletion of interlayer water during desorption process; making the hysteresis for high-clay content samples more pronounced.

6.4.2. Modified Sorption Experiments

6.4.2.1. Early adsorption rate

According to Figure 6-3, modified adsorption curves have smoother increase rate at low RH values compared with that of conventional adsorption curves. We plot $R_{Ads,i}$ against clay content for the modified adsorption process in Figure 6-4a (red circular points). Unlike the conventional adsorption process; $R_{Ads,i}$ is almost independent of clay content for the modified adsorption process. This observation indicates that presence of an early sorption cycle in the modified process

reduces the tendency of shale samples for water uptake at low RH values. Insignificant affinity of $R_{Ads,i}$ to the clay content in the modified technique suggests that clays already filled-up (and retained) their capacity for water adsorption by the early sorption cycle. High tendency of clay minerals for water retention is also reported in clay-rich conventional rock samples (Shahrak and Piri, 2008, 2010, 2014 and 2015).

6.4.2.2. Total amount of adsorbed water

According to Figure 6-3, modified adsorption curves are always lower than conventional adsorption curves. In order to investigate the role of clays on the total water uptake during adsorption process, we plot W_{Ads} against clay content for the modified sorption experiments in Figure 6-4b (red circular points).

According to Figure 6-4b, although W_{Ads} generally increases with clay content in the modified process (red circular points), its raising rate is less than that of the conventional method (black triangle points). This observation along with the earlier results of independency of $R_{Ads,i}$ to clay content (red circular points in Figure 6-4b) suggest that clay minerals may already adsorb (and retain) enough water during the early sorption cycle of the modified process (Stages 1&2 in Figure 6-2).

6.4.2.3. Adsorption-desorption hysteresis

According to Figure 6-3, there is a hysteresis between the modified adsorption and desorption isotherms. In order to investigate the role of clays on the hysteresis between sorption isotherms, we plot W_{Ret} against clay content for the modified sorption experiments in Figure 6-4c (red circular points).

Unlike the conventional sorption experiments, W_{Ret} decreases with increasing clay content in the modified sorption process. Interestingly, the extrapolation of both fitted lines in Figure 6-4c at clay content of 0% suggests that around 25%-30% of the total condensed water cannot be depleted during desorption process. In other words, for clay-free shales (0% clay content),

capillary condensation should be the primary mechanism controlling the water uptake during adsorption. However, even for a clay-free sample, desorption process cannot deplete all of the condensed water in pores. A portion of this retained water can also be due to surface hydration. Short-range attractions between water molecules and pore-wall, such as hydrogen bonding, (Tuller et al., 1999; Meleshyn and Bunnenberg; 2005; Rao et al., 2013; Roshan et al., 2015) can impede complete water dehydration during the desorption process.

6.4.2.4. Early sorption cycle

According to Figure 6-4, presence of an early sorption cycle in the modified technique impacts the sorption behaviour of shales compared with the conventional sorption method. We investigate the role of clays on the water adsorption and adsorption-desorption hysteresis during the early sorption cycle by plotting $W_{Ads,Cyc}$ and $W_{Ret,Cyc}$ versus clay content in Figure 6-5, respectively. $W_{Ads,Cyc}$ is the total amount of adsorbed water during adsorption part of the early sorption cycle (end of Stage 1 in Figure 6-2). $W_{Ret,Cyc}$ is retained water relative to $W_{Ads,Cyc}$ after desorption part of the early sorption cycle (end of Stage 2 in Figure 6-2).

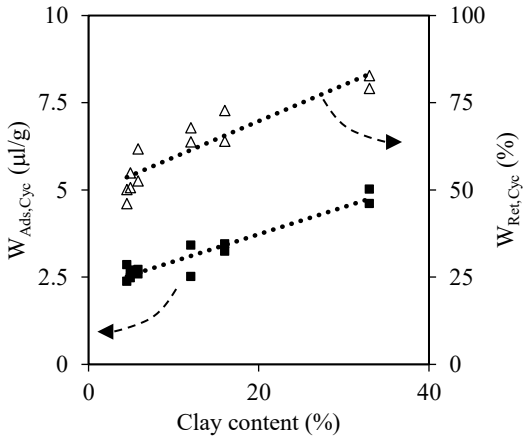

Figure 6-5**.** Effect of clay content on the adsorbed and retained water during the early sorption cycle of the modified technique. The adsorbed water (square points) is measured after the sample reached equilibrium at $RH \approx 0.215$. The samples then placed in $RH \approx 0$ and after equlibrium, the percent of retained water with respect to earlier adsortion part at $RH \approx 0.215$ is plotted on the second Y-axis (triangle points).

According to Figure 6-5, $W_{Ads,Cyc}$ is strongly correlated to clay content (square points). This observation may suggest that clay adsorption is an important mechanism for water uptake during the early sorption cycle of the modified process. Additionally, $W_{Ret,Cyc}$ is tightly correlated to clay content (triangle points in Figure 6-5); suggesting that the adsorbed water by clay minerals cannot be easily depleted by desorption.

Both $W_{Ads,Cyc}$ and $W_{Ret,Cyc}$ have stronger correlation with the clay content compared with those for the conventional technique (black points in Figures 6-4b,c). Furthermore, all of $W_{Ret,Conv}$ (black points in Figure 4-c) are less than 50%. However, majority of $W_{Ret,Cyc}$ (triangle points in Figure 6-5) are greater than 50%. These observations also suggest that water-clay interaction is more prominent at the early stages of the adsorption process, and clays tend to retain the adsorbed water.

6.4.3. Water Uptake Mechanisms during Water Sorption Experiments

The "total" water uptake in the modified sorption process can be expressed as $W_{Ret,Cyc} + W_{Ads,Mod}$. Figure 6-6 compares the "total" water uptake in the conventional and modified sorption experiments.

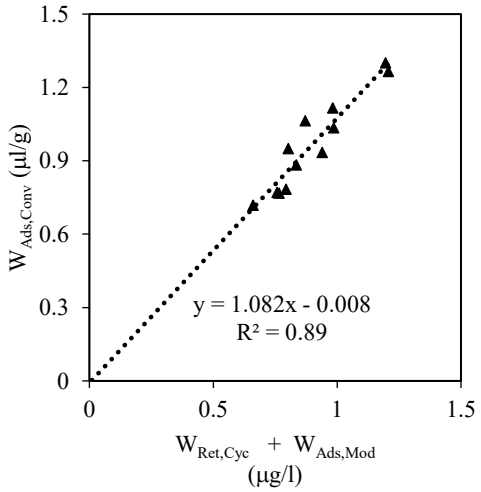

Figure 6-6. A comparison between the "total" adsorbed water by conventional and modified sorption processes. The "total" water uptake by the modified sorption technique is calculated by $W_{Ret,Cyc} + W_{Ads,Mod}$.

Interestingly, the fitted line in Figure 6-6 has slope of approximately one (~1.08), and it passes through origin (Y-axis intercept of ~ -0.008). In other words, both of the conventional and modified sorption processes result in similar total water uptake. Furthermore, in Section 6.4.2.4 we showed that water adsorption and retention are strongly correlated to the clay content during the early sorption cycle. The results may suggest that one can break the conventional water sorption process into (i) clay-dominant and (ii) capillary-dominant regions using the modified water sorption technique (schematically illustrated on Figure 6-7).

The strong correlation between $W_{Ads,Cyc}$ and clay content in the early sorption cycle (Figure 6-5) corresponds to adsorption at low RH values. This result may suggest that clay adsorption is the primary mechanism controlling water uptake at low RH values. The strong correlation between $W_{Ret,Cyc}$ and clay content in the early sorption cycle (Figure 6-5) suggests that clays retain majority of the adsorbed water after desorption process. Thus, the subsequent modified adsorption (and desorption) process mainly corresponds to capillary condensation (and depletion) phenomenon.

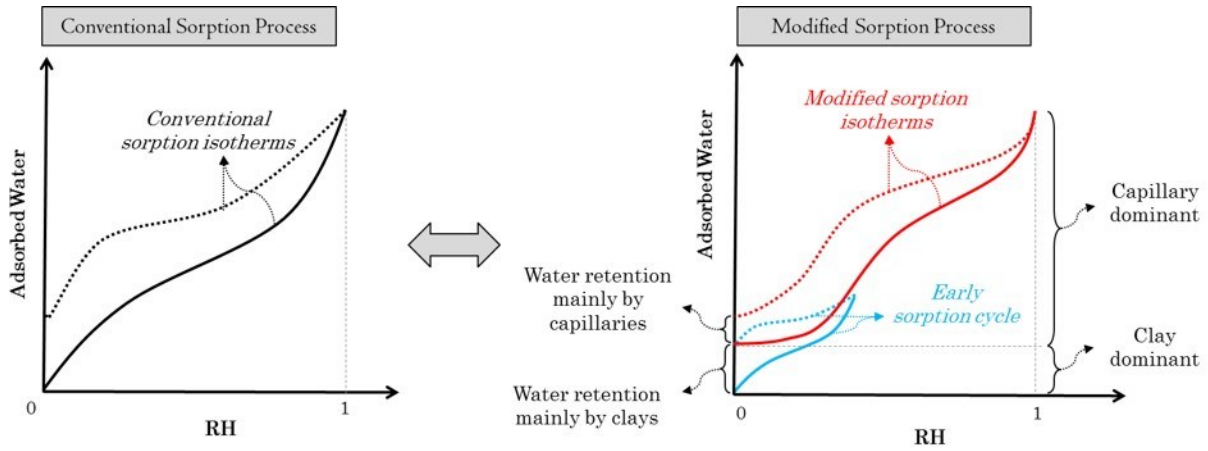

Figure 6-7. A schematic comparison between cconventional and modified water sorption processes. The modified water sorption process is divided into clay-dominant and capillary-dominant regions for water uptake.

6.4.4. Spontaneous Imbibition Experiments

Assuming the dried samples are moisture-free (negligible initial water saturation), the normalized water uptake curve with respect to pore volume can represent the water saturation (S_w). Figure 6-8 compares S_w during adsorption and imbibition experiments.

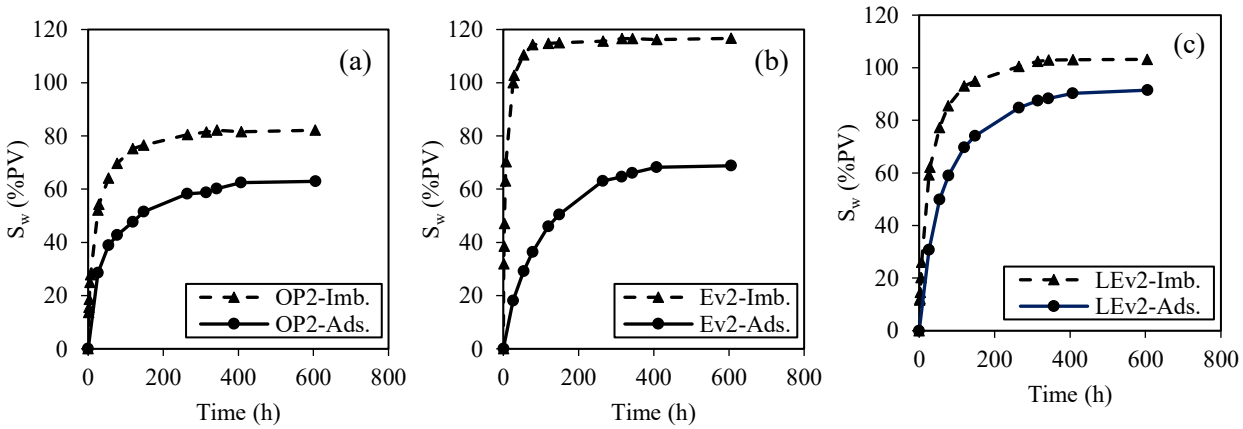

Figure 6-8. A comparison between water saturation curves during imbibition (solid line) and adsorption (dash line) processes for Set-2 samples from (a) OP, (b) Ev, and (c) LEv formations. The scale used for measuring the mass of the rock samples during water adsorption and imbibition experiments has an accuracy of ± 0.01 g.

According to Figure 6-8, water imbibition is higher and also faster than water adsorption in all three samples. For instance, for OP samples, the equilibrium S_w by water adsorption and imbibition are about 63% and 82% of PV, respectively. Also, it takes about 25 hrs for the imbibition process to fill out 50% of PV in OP sample; while this value is more than 145 hrs for the adsorption process. Possible reasons for different water uptake behaviors during adsorption and imbibition are different (i) swelling potentials, (ii) electric double layer (EDL) thickness around water molecules, and (iii) pore-filling sequences.

Swelling potential: Lyu et al. (2015) suggested that greater hydraulic force and higher ionic gradient can cause larger and faster shale expansion during water imbibition compared with that during water adsorption. Moreover, shale swelling can lead to induction of micro-fractures (Dehghanpour et al., 2013; Makhanov et al., 2014; Roshan et al., 2015; Sun et al., 2015; Ghanbari and Dehghanpour, 2015; Meng et al., 2015; Zhou et al., 2016). Therefore, higher swelling potential during imbibition can potentially induce more micro-fractures resulting in higher water uptake compared with adsorption.

The equilibrium S_w (plateau in the S_w curve) for the imbibition process in Ev and LEv samples are more than the total pore volume (PV) measured by BET analysis. More specifically, about 117% and 103% of PV is filled with water by imbibition process for Ev and LEv samples, respectively. Similar observations were also reported by other researchers which mainly attributed to the clay swelling and micro-fracture induction (Makhanov et al., 2014; Ge et al., 2015; Yang et al., 2016; Arshadi et. al., 2017). In order to investigate the role of clays on excess water uptake by imbibition compared with adsorption, we plot ΔS_w (the difference between equilibrium S_w of imbibition and adsorption processes) versus clay content in Figure 6-9. The results indicate that the sample with higher clay content has higher ΔS_w. In other words, water uptake is higher by imbibition compared with adsorption for high clay content shales.

It must be noted that all of our shale samples used in the imbibition and adsorption experiments were unconfined and allowed to swell freely. Previous studies indicated that micro-fractures induction is slower for samples under confined pressure compared with those that are allowed to swell freely (Ghanbari and Dehghanpour, 2015; Roshan et al., 2015).

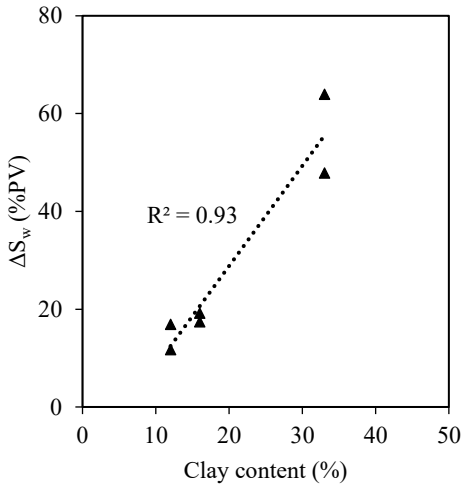

Figure 6-9. Effect of clay content on the excess water uptake by imbibition compared with adsorption. ΔS_w is the difference between the equilibrium S_w of the imbibition and adsorption processes.

Capillary condensation in hydrophilic inorganic pores, clay adsorption and swelling along with potential micro-fracture induction can improve water uptake by the adsorption process. However, the total PV probably cannot be filled during adsorption process (solid lines in Figure 6-8). Water molecules have low affinity to condense in organic pores due to their hydrophobic nature. In Chapter 7, we use the results obtained from this study to characterize the inorganic and organic pore size distributions of shale samples.

Electric double layer (EDL): During both water adsorption and imbibition experiments, water enters into the pores and dissolves (and reacts with) precipitated salts (rock constituents). During imbibition, the in situ formed brine dilutes as ions can leave the rock due to ionic gradient between bulk water and pore water. Low ion concentration forms a thick EDL around ions, which improves water uptake (Binazadeh et al., 2016). During adsorption however, ions cannot leave the shale; and therefore, in situ formed brine has high ion concentration. High ion concentration forms a thin EDL around ions, which hinders water uptake (Binazadeh et al., 2016).

Pore-filling sequence: Different pore-filling sequences during adsorption and imbibition can be another possible reason for different water uptake behaviors observed in Figure 6-8. During imbibition, large pores fill with water first (Handy, 1960; Gruener et al., 2016). Thus, there is a possibility for small pores to be trapped between two large water-filled pores. During adsorption

however, small pores fill with water first (Fisher and Israelachvili, 1979). Thus, there is a possibility for large pores to be trapped between two small water-filled pores. Trapping of large pores (with large pore volume) can be a possible reason for low water uptake during adsorption (circular points). Similarly, trapping of small pores (with small pore volume) can be a possible reason for high water uptake during imbibition (triangle points).

6.5. Summary

Interpretation of water sorption behaviour of gas shales is challenging as the water molecules can simultaneously be condensed in capillaries and adsorbed by clay minerals. This chapter presents a modified water sorption process to investigate the role of clays on water uptake of shale samples. Compared with the conventional water sorption process, the modified technique has an early sorption cycle between relative humidity (RH) of 0-0.215, where $RH = 0.215$ is approximately equal to the average ambient RH value of 0.24 in the laboratory.

Three sets of experiments are performed on downhole shale samples of different clay contents. Experiments include conventional water sorption, modified water sorption, and water imbibition. The comparative analysis of the results of conventional and modified water sorption experiments indicate that clay minerals adsorb and retain most of their capacity for water at low RH values. The modified water sorption process can be used to investigate the capillary condensation process.

Experimental results indicate that water imbibition is faster and higher compared with the water adsorption process. These results can be explained by (i) the higher swelling potential of shale samples during the water imbibition process compared with that during the water adsorption process, (ii) formation of large electric double layer around the ions during the imbibition process, and (iii) different pore-filling sequence during the imbibition and water adsorption processes.

Nomenclatures

BET	Brunauer–Emmett–Teller
DI	Deionized
Ev	Evie formation
HRB	Horn River Basin
LEv	Lower-Evie formation
OP	Otter-Park formation
PV	Pore volume
P^{sat}	Saturated vapour pressure
R	Universal gas constant
R_1, R_2	Principal radii of curvature
RH	Relative humidity
RH_i	Relative humidity corresponds to saturated solution of salt *i*
$R_{Ads,i}$	Initial adsorption rate
S_i	Saturated solution of salt *i*
S_w	Water saturation
T	Temperature
V_m	Liquid molar volume
W_{Ads}	Total amount of adsorbed water by conventional/modified adsorption process
$W_{Ads,Conv}$	Adsorbed water at the end of conventional adsorption process
$W_{Ads,Cyc}$	Adsorbed water at the end of the adsorption part of the early sorption cycle (end of Stage 1)
$W_{Ads,Mod}$	Adsorbed water at the end of modified adsorption process (end of Stage 3)
$W_{Ret,Conv}$	Retained water at the end of conventional desorption process
$W_{Ret,Cyc}$	Retained water at the end of the desorption part of the early sorption cycle (end of Stage 2)
$W_{Ret,Mod}$	Retained water at the end of modified desorption process (end of Stage 4)
XRD	X-ray diffraction

ΔS_w	The difference between equilibrium water saturation of imbibition and adsorption processes
γ	Surface tension
θ	Contact angle

Chapter 7

Water Sorption Behaviour of Gas Shales: II. Pore Size Distribution

7.1. Introduction

With the increasing demand in oil and gas, shale formations are emerging as an important resource of energy in the United States and Canada. These resources are characterized by their low permeability and porosity (Frantz and Jochen; 2005). Although challenging, petrophysical characterization of shales is essential for reserve estimation and production forecast. In particular, pore size distribution (PSD) controls the key petrophysical properties (such as permeability) and is essential for characterizing reservoir rocks (Archie 1950). PSD controls fluids' distributions at the pore-level and hence, impacts multi-phase flow characteristics (e.g., saturation paths and relative permeabilities) at the core-scale (Shahrak 2014; Zolfaghari and Piri, 2016a,b; Gesho et al., 2016).

Mercury injection capillary pressure (MICP) analysis is a common method to calculate the PSD of reservoir rocks (Donaldson et al., 1985; Terrace, 1997). In this technique, mercury is forced into the rock pore-space and the injected volume is measured at different pressures (Donaldson et al., 1985). Although several researchers utilized MICP analysis to calculate PSD in shales (Nelson, 2009; Al Hinai, 2014; Li et al., 2015; Lan et al., 2015; Moghaddam and Jamiolahmady, 2016), the validity of their results is questionable to due limited pore accessibility in shales (Pittman, 1992). Some researchers reported that mercury can hardly access small pores due to their extremely high capillary pressure (Al Hinai et al., 2014). Moreover, injecting mercury at high pressure could compress the rock and decrease the pore size, particularly when pores are small (Labani et al., 2013).

Brunaur-Emmett-Teller (BET) is another method for characterizing PSD of shales. Several researchers have applied BET analysis to either calculate the PSD or investigate the adsorption properties of shales (Adesida et al., 2011; Kuila and Prasad, 2011; Clarkson et al., 2013; Al Hinai et al., 2014; Sigal, 2015; Wang et al., 2015; Li et al., 2016; Chen et al., 2016). Adesida et al. (2011) used Monte Carlo simulation and N_2 adsorption experiments to calculate the PSD of shale samples. They concluded that the average organic pore size is less than ~10 nm. Clarkson et al. (2013) applied BET analysis using both N_2 and CO_2 adsorption isotherms to calculate PSD of several shale samples. They showed that BET analysis lead to different $PSDs$ when different adsorbing fluids (i.e., N_2 and CO_2) are used for the sorption experiments. Al Hinai et al. (2014) compared the

$PSDs$ obtained from both N_2 adsorption isotherm and MICP method. They detected different types of pores (micro-, meso-, and macro-pores) using BET analysis. Their results suggested that the MICP method is not able to discern between different types of pores. Also, during BET analysis, condensation begins in small capillaries mainly due to high van der Waals interactions between gas molecules and pore wall (Fisher and Israelachvili, 1979). Thus, there is a possibility for air trapping in a large pore when it is confined between to small fluid-filled pores.

Nuclear magnetic resonance (NMR) is another technique used to characterize the pore structure and PSD of shale samples (Prammer, 1994; Sigal et al., 2013; Sigal, 2015; Liu et al., 2015). Prammer (1994) applied NMR to determine PSD and permeability of shales. Sigal (2015) combined the NMR method and adsorption measurements to characterize PSD of shale samples. Several researchers reported the difficulties in using NMR for characterizing pore system of shales. Although NMR is considered to be a non-destructive technique for characterizing porous media (Elipe, 2003), nano-scale pores and complex surface chemistry of shales are challenges against determination of PSD using NMR (Firouzi et al., 2014).

Image processing is also widely used to visualize the pore structure of shales. Ambrose et al. (2012) conducted Scanning Electron Microscope (SEM) analysis to investigate the pore size of shales. Their results indicate that the pore system of shales encompasses two groups of pores: the small organic pores of less than 10 nm, and the large inorganic pores of about 100 nm. Milner et al. (2010) conducted SEM imaging on shale samples from different unconventional reservoirs. They concluded that the rock mineralogy and texture impact the pore size, which can be ranged from nanometer to micrometer. Saraji and Piri (2015) utilized multiple 2D SEM images to characterize PSD and simulate fluid flow in shale samples from the Bakken Formation. They classified the pore system into organic, intra-particle, and inter-particle pores.

Fluid imbibition experiments have been recently used to characterize shale properties (Dehghanpour et al., 2012 and 2013; Makhanov et al., 2014; Lan et al., 2015; Ghanbari and Dehghanpour, 2015; Binazadeh et al., 2016). Lan et al. (2015a) conducted a series of oil and water imbibition experiments to characterize hydrophilic and hydrophobic pore networks of several samples from the Montney Formation. Ghanbari and Dehghanpour (2015) studied the effect of rock fabric on the imbibition behaviour of shales. The imbibition data have been also studied using the fractal geometry method to investigate the pore size/structure of porous mediums. Cai et al.

(2010) predicted the maximum pore size of a porous medium by analyzing the imbibition data. Liu et al. (2015) applied fractal geometry method to investigate the pore structure of several shale samples. Gruener et al. (2016) developed a mathematical model to determine PSD of mesoporous silica using the shape of the imbibition front.

Application of different methods for characterization of pore space in shales usually yields different $PSDs$ (Clarkson et al., 2013; Al Hinai et al., 2014). For example, Clarkson et al. (2013) obtained different $PSDs$ when they applied BET and MICP analyzes on Barnette shale samples. Moreover, different fluids preferentially flow in different parts of the pore network, depending on the wettability of the pore surface (Lan et al., 2015; Javaheri et al., 2017a,b). For instance, Lan et al., (2015a) observed higher oil imbibition than water in Montney tight gas samples. They attributed the higher oil uptake to the smaller (and well-connected) hydrophobic pore network in contrast to the larger hydrophilic (and poorly-connected) hydrophilic pore network. Specific characterization of inorganic and organic pore networks and their $PSDs$ are of great interest to investigate fluid flow in porous medium; which can ultimately lead to more accurate determination of multi-phase flow parameters (such as capillary pressure and relative permeability). It must be noted that, although water prefers a hydrophilic pathway to flow (Lan et al., 2015; Javaheri et al., 2017a,b), it is still possible for water to enter the hydrophobic capillaries (Wu et al., 2017). In this case, non-slip boundary condition between water/pore-wall is less likely to be valid; and therefore, water flow capacity may increase in hydrophobic pores (Wu et al., 2017).

In this study, we first introduce the hypothesis for characterization of organic and inorganic $PSDs$ in Section 7.2. Section 7.3 describes the experimental procedure for investigation of the hypothesis. Section 7.4 shows the mathematical procedure to calculate PSD from water sorption isotherms. Section 7.4 also explains how to calculate the total, inorganic, and organic $PSDs$. Experimental results and the calculated $PSDs$ are presented in Section 7.5. Sections 7.6 and 7.7 discuss the limitations of the proposed procedure and the summary of this chapter.

7.2. Hypothesis

Shales usually contain clay minerals and have both inorganic and organic pores. We hypothesize that (I) BET analysis using N_2 can give the total pore volume (PV_{tot}) and the total PSD (PSD_{tot}), (II) the modified water sorption technique presented in Chapter 6 is applied to characterize the hydrophilic inorganic pore volume (PV_{inorg}) and PSD (PSD_{inorg}), and (III) the comparative analysis of BET and the modified water sorption results can lead to separate characterization of the hydrophobic organic pore volume (PV_{org}) and PSD (PSD_{org}).

7.3. Experiments

N_2-BET analysis is performed to characterize PV_{tot} and PSD_{tot}. Then, modified water sorption experiments (see Chapter 6) are conducted to distinguish between water adsorption by clays and capillary-condensed-water in inorganic pores. The capillary condensation concept (described in Section 7.4) is applied on the modified sorption isotherms to characterize PV_{inorg} and PSD_{inorg}. PV_{org} and PSD_{org} are calculated by comparative analysis of the results of N2-BET and modified water sorption experiments.

Rock Samples: Downhole gas shale samples belongs to three formations of Otter-Park (OP), Evie (Ev), and Lower-Evie (LEv) in the Horn River Basin (HRB). In order to remove the initial moisture content, the samples are dried at 200°F until the weight stabilization was achieved. X-ray diffraction (XRD) analysis is used to characterize the rock mineralogy, and the results are presented in Table 7-1. It must be noted that XRD uses small amount of rock samples for the analysis. Thus, the results presented in Table 7-1 might not be an accurate representation of all samples from the target formations.

Table 7-1. Mass of dried samples used for different experiments and their average mineralogy from XRD analysis. The XRD used for characterization of rock mineralogy has a signal-to-noise ratio of 400. The accuracy of relative pressure measurements by N_2-BET analysis is 0.15%.

	Sample Mass (g)		
Experiment	OP	Ev	LEv
N_2 Sorption (BET)	1.504	1.498	1.507
Modified Water Sorption	189.770	199.730	216.800
Clay Content (Wt.%)			
Illite/Smectite (I/S)	5	14	3
Illite+Mica	11	19	9
Total Clay	16	33	12
Non-Clay Content (Wt.%)			
Quartz	77	32	65
K-Feldspar	2	6	3
Plagioclase	2	6	6
Calcite	0	10	10
Ankerite/Fe-Dolomite	1	5	0
Dolomite	0	4	1
Pyrite	1	5	3
Total Non-Clay	84	67	88

N_2-BET Analysis: We perform N_2 sorption experiments using BET analysis to measure the PV_{tot} and PSD_{tot}. The N_2-sorption isotherms are obtained at 77 K. PSD can be obtained from both the adsorption and desorption isotherms. It has been shown that the calculated PSD from desorption curve is a better representation of the pore space (Clarkson et al., 2012; Schmitt et al., 2015). Thus, we calculate the PSD_{tot} from N_2 desorption isotherm using Dollimore and Heal (DH) method (Dollimore and Heal, 1964).

Modified Water Sorption Experiments: In order to obtain PV_{inorg} and PSD_{inorg}, the modified water sorption experiments, presented in Chapter 6, is conducted on the shale samples. In the modified process, the shale samples go through an early sorption cycle between RH=0 and

RH=0.215; where RH denotes relative humidity. Then, samples experience a full sorption cycle between RH=0 to RH=1 (i.e., the modified adsorption and desorption isotherms). The detailed procedure for the modified water sorption experiments is presented in Chapter 6 of this dissertation.

HIM-EDS Experiments: We visualize the inorganic and organic pores of our samples using Helium Ion Microscope-Energy Dispersive Spectrometer (HIM-EDS) analysis. The sample are cut into 1 cm × 1 cm × 0.5 cm cube. The 1 cm × 1 cm top surface of the sample are polished using 600-, 1000-, and 2000- grit sandpaper. The mechanical polished surface is then further polished using argon-ion milling, to minimize the effect of artifacts during mechanical polishing process, such as surface abrasion marks or grinding debris (Loucks et al., 2009). Several focus areas of the argon-ion-milled samples are imaged using Zeiss Orion NanoFab HIM under ~15 kV beam energy. The highest resolution for HIM imaging is 0.5 nm per pixel. The elemental map of the sample is collected using built-in EDS, to determine the mineralogy of the samples in the target focus areas.

7.4. PSD Calculation from Water Sorption Isotherms

In this section, similar to BET analysis, we utilize the capillary condensation concept to calculate PSD from the conventional water adsorption/desorption isotherms. Section 7.4.1 explains the relationship between the water adsorption/desorption process and the pore size of a porous medium. Section 7.4.2 describes a mathematical procedure to relate the volumetric fraction of adsorbed/depleted water to the probability density function (PDF) of the pore size. Section 7.4.3 explains how we apply the developed mathematical procedure on the modified desorption isotherm to characterize PSD_{inorg} and PSD_{org}.

7.4.1. Theory

When a porous medium is exposed to the vapor of a wetting fluid, the molecules start to condense within the pore space. This process is called capillary condensation in which the vapor phase is adsorbed as a multilayer film in porous medium (Schramm, 1993). Ideally, the process

continues to the point at which the pores become filled with condensed liquid (Schramm, 1993). The condensation process can occur at pressures lower than the saturation pressure at a given temperature (Chiu et al., 2006; Ayatollahi and Zolfaghari, 2006). Figure 7-1 schematically illustrates how the water vapor condenses within the pores of different sizes at different RH conditions. In order to describe the capillary condensation concept, we assume an ideal porous medium with uniform wettability for all pores. We will re-consider the assumption of uniform wettability for all capillaries in Section 7.4.3 and thereafter.

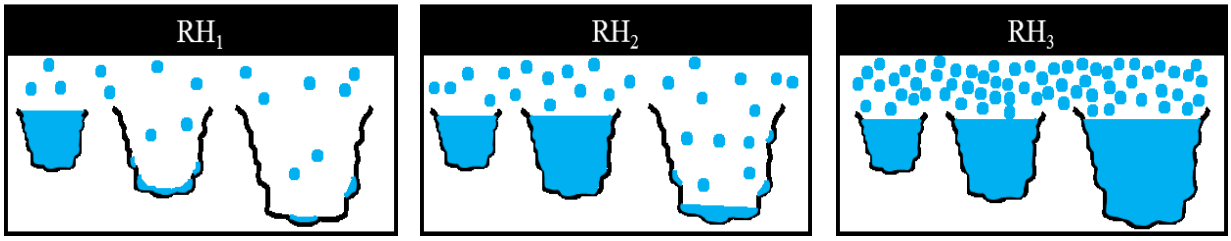

Figure 7-1. Capillary condensation in pores of different sizes at different RH environments ($RH_1 < RH_2 < RH_3$)

van der Waals forces are primarily responsible for short-range (<10 nm) molecular interactions between water molecules near a solid surface (Tuller et al., 2001). Thus, decreasing the capillary size enhances the van der Waals interactions between the water molecules and the pore wall. Furthermore, there are considerable van der Waals interactions between the water vapor molecules themselves in small capillaries. The significant molecule/molecule and molecule/solid interactions help the water vapor to condense at a vapor pressure below the saturation vapor pressure (Hunter, 2001). Due to significant van der Waals interactions in small capillaries, for a given RH condition, condensation first starts in smaller capillaries. The water vapor condenses in the larger capillaries as RH increases. Kelvin equation (Fisher and Israelachvili, 1979) describes the relationship between RH and the size of the water-filled capillary:

$$ln(RH) = \frac{-\gamma V_m \cos\theta}{RT}\left(\frac{1}{R_1} + \frac{1}{R_2}\right) \tag{7-1}$$

Here, γ is surface tension, V_m is the liquid molar volume, θ is contact angle, R is universal gas constant, T is temperature, and R_1 and R_2 are the principal radii of curvature. Assuming that the pores have spherical shape ($1/R_1 = 1/R_2 = 1/r_p$), Eq. 7-1 can be rearranged as

$$ln\left(\frac{1}{RH}\right) = \frac{2\gamma V_m \cos\theta / RT}{r_p} \quad (7\text{-}2)$$

Here, r_p is the pore radius. Eq. 7-2 shows that $\ln(1/\mathrm{RH})$ is inversely proportional to r_p $\left(ln(1/RH) \propto {}^{1}/_{r_p}\right)$. This relationship between the pore size and RH is similar to that between capillary pressure (P_c) and pore size of a porous medium through Young-Laplace equation $\left(P_c = 2\gamma|cos\theta|/r_p\right)$. $ln(1/RH)$ in a water adsorption process is inversely proportional to the pore size that is filled with condensed water vapor. Similarly, P_c measured during a mercury injection process is inversely proportional to the pore size of the invaded pore space. Moreover, the numerator of Eq. 7-2 $(2\gamma V_m \cos\theta/RT)$ does not depend on the pore size. Similarly, the numerator of Young-Laplace equation $(2\gamma|cos\theta|)$, does not depend on r_p. Therefore, the $ln(1/RH) - r_p$ relationship from the water adsorption test is "mathematically" analogous to the $P_c - r_p$ relationship from the mercury injection test. One can interpret the adsorption data to describe the PSD in a similar way that mercury injection data are interpreted to describe the PSD. In the following, we use this mathematical analogy to obtain PSD from the water adsorption data.

Now, we demonstrate how the water adsorption isotherm can be interpreted as a cumulative probability density function (CDF) for the pore size. Figure 7-2a schematically illustrates a typical water adsorption isotherm. The amount of water adsorbed in the porous medium increases by increasing RH. At lower RH values (RH_1), water condenses in small pores (Figure 7-1). Large pores start to be filled with condensed water at higher RH values (RH_2 and RH_3). Here, we assume that at the end of the adsorption process $(RH \approx 1)$, all pores will be filled with condensed water $(S_w = 1)$, and therefore, one can interpret the cumulative adsorbed water as the total effective pore volume. More specifically, the total mass of water adsorbed is considered as the total pore volume as the water density is considered to be $\rho = 1\ g/cc$. If the samples are completely dried (negligible initial water saturation), the normalized adsorption isotherm curve with respect to pore volume can represent the water saturation (S_w) during the adsorption process (Figure 7-2b). It must be noted that the shales are comprised of clays which can adsorb water. In Section 7.4.3., the modified sorption isotherms (see Chapter 6) is used to account for the water adsorption by clays.

Each arbitrary RH value on the horizontal axis (such as RH^* in Figure 7-2b) corresponds to a pore radius (r_p^*) according to Eq. 7-2. As $ln(1/RH)$ increases from right to left, r_p increases from left to right. Therefore, any value such as Q^* on the vertical axis represents the total volume of pores with the pore size equal or smaller than r_p^* $(r_p \leq r_p^*)$. Therefore, adsorption isotherm can be interpreted as the cumulative PDF of pore size.

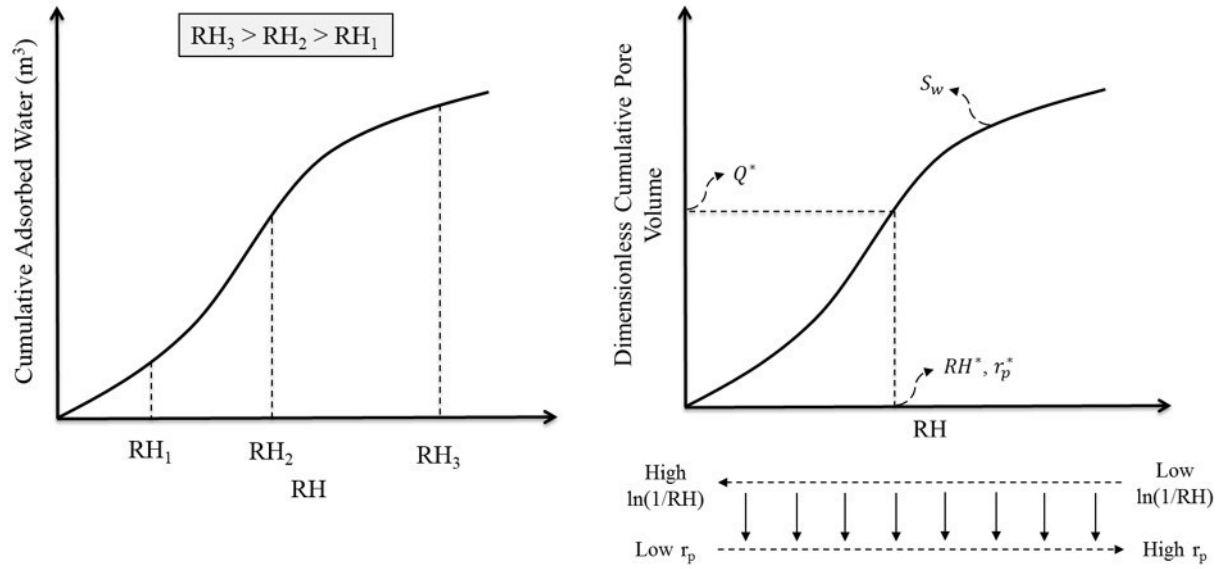

(a) (b)

Figure 7-2. (a) Schematic illustration of the adsorption isotherm curve, (b) adsorption isotherm may represent the cumulative PDF of pore size

7.4.2. *PSD* using Probability Density Function

In the previous section, we showed that at any value of r_p, S_w is the fraction of pore volume having the average size of less than or equal to r_p. If we assume that $f(R)$ is the PDF for the pore size, then

$$S_w = \int_{r_{p,min}}^{r_p} f(r_p) dr_p \tag{7-3}$$

where,

$$\int_{r_{p,min}}^{r_{p,max}} f(r_p)dr_p = 1 \tag{7-4}$$

Here, $r_{p,min}$ and $r_{p,max}$ are the minimum and maximum values for pore radius, respectively. Differentiating Eq. 7-4 using Leibnitz's rule for integral differentiation (Kate et al. 2006), the resulting PDF is given by

$$f(r_p) = \frac{dS_w}{dr_p} \tag{7-5}$$

We also know from Eq. 7-2 that

$$r_p\, ln(1/RH) = 2\gamma V_m\, cos\,\theta/RT \tag{7-6}$$

The right-hand side of Eq. 7-6 is constant. Therefore, differentiating Eq. 7-6 results in

$$r_p d\, ln(1/RH) + ln(1/RH)\, dr_p = 0 \quad \Rightarrow \quad dr_p = -r_p d\, ln(1/RH)/ln(1/RH) \tag{7-7}$$

Substituting Eq. 7-7 into Eq. 7-5 gives

$$r_p = -\frac{RT[ln(1/RH)]^2}{2\gamma V_m\, cos\,\theta}\frac{dS_w}{d\, ln(1/RH)} \tag{7-8}$$

Eq. 7-8 is derived based on Kelvin equation (Eq. 7-1), and can be used to calculate the size of the capillaries filled with condensed water vapour at each RH value during the adsorption process. Therefore, differentiating the water saturation curve (or normalized adsorbed water curve) with respect to $ln(1/RH)$ can lead to the PSD. It must be noted that all the parameters on the right-hand side of Eq. 7-8 are either constant or measurable. Therefore, adsorption isotherm curve can be used to calculate the PSD of the porous medium.

7.4.3. Characterization of PSD_{tot}, PSD_{inorg}, and PSD_{org}

Total (PSD_{tot})***:*** BET analysis uses the capillary condensation concept to calculate the pore filling/depletion sequence during adsorption/desorption processes (Brunauer et al., 1940). N_2 is an inert gas and it can condense in both hydrophobic and hydrophilic pores. Therefore, BET gives PV_{tot} and PSD_{tot} (Sujka, et al., 2016).

During sorption process, there is a hysteresis loop between the adsorption and desorption curves (Schmitt et al., 2015; Kuila, 2013). Although both adsorption and desorption isotherms can be used to determine PSD; it has been suggested that the calculated PSD from desorption isotherm can be a better representation of pore system as it can distinguish between pore throats and pore bodies (Kuila, 2013; Schmitt et al., 2015). Thus, in this chapter, we use the desorption isotherm (from both of the water and N_2 sorption experiments) to calculate PSD.

Inorganic (PSD_{inorg})***:*** Organic pores are hydrophobic and they are usually smaller than the inorganic pores (Ambrose et al., 2012). Therefore, water molecules can hardly condense in these small organic pores (Firouzi et al., 2014). Assuming negligible capillary condensation in organic pores; the water molecules can be adsorbed by clays (Chenevert, 1970; Van Meerveld et al., 2003; Deriszadeh and Wong, 2014) or condense in hydrophilic capillaries (Sujka, et al., 2016) during adsorption process.

A modified sorption technique is proposed in Chapter 6 to distinguish between clay-adsorbed water and capillary-condensed water in inorganic pores. The new technique has an early sorption cycle, allowing the clay minerals to saturate their interlayer space with water. The resulted samples then go through a full sorption cycle (i.e., the modified adsorption and desorption processes). Assuming that water molecules cannot condense in hydrophobic organic pores, the total amount of adsorbed water during the modified adsorption process represents PV_{inorg}. Thus, the mathematical procedure described in Sections 7.4.1 and 7.4.2 can be used to calculate PSD_{inorg} from both the modified adsorption and desorption isotherms. To be consistent with the BET analysis, we calculate PSD_{inorg} from the modified desorption isotherm.

Organic (PSD_{org})***:*** PV_{org} can be calculated by subtraction of PV_{inorg} from PV_{tot} as it is shown in Eq. 7-9.

$$PV_{org} = PV_{tot} - PV_{inorg} \quad (7\text{-}9)$$

Eq. 7-10 can be used to calculate PSD_{org}.

$$PSD_{org} = \frac{PV_{tot}PSD_{tot} - PV_{inorg}PSD_{inorg}}{PV_{org}} \quad (7\text{-}10)$$

7.5. Results and Discussion

N_2-BET- Analysis: Figure 7-3 illustrates N_2 sorption isotherms from BET analysis. The amount of adsorbed N_2 increases by increasing the relative pressure (P/P_0); where P is the equilibrium pressure and P_0 is the saturation pressure of the adsorbate at the experimental temperature. The amount of adsorbed N_2 decreases by decreasing the relative pressure (desorption isotherm). We observe hysteresis in the N_2 sorption isotherms; indicating that not all the N_2 adsorbed during the adsorption process can be released during the desorption process.

Modified Water Sorption Experiments: Figure 7-4 shows modified water sorption isotherms. Similar to BET results, we observe hysteresis between the modified water sorption isotherms (Figure 7-4); indicating that not all the water adsorbed during the modified adsorption process can be depleted during the modified desorption process. Generally, the adsorption and desorption curves diverge more at low P/P_0 or RH values; suggesting that desorption from smaller pores is more difficult than that from larger pores. This can be due to the strong van der Waals interactions between the condensed N_2/water and the host pore wall (Papadopoulos and Kuo, 1990).

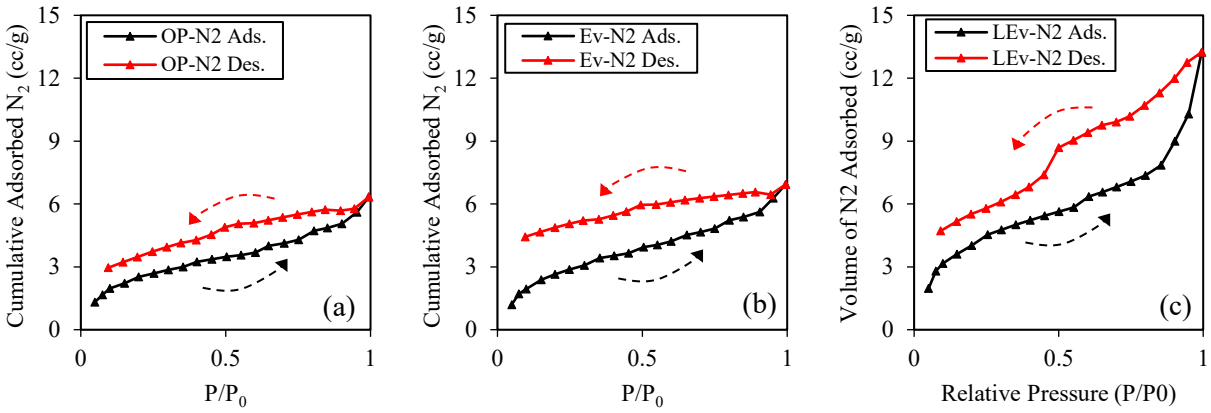

Figure 7-3. N_2 sorption isotherms measured by BET for the (a) OP, (b) Ev, and (c) LEv samples. Adsorption and desorption isotherms are plotted in black and red colors, respectively. The accuracy of relative pressure measurements by N_2-BET analysis is 0.15%.

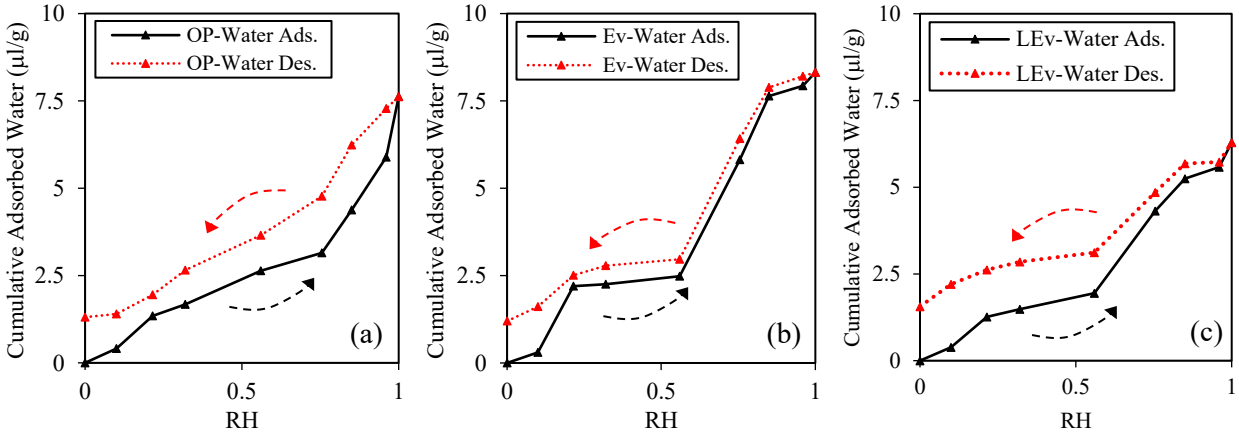

Figure 7-4. Modified water sorption isotherms of (a) OP, (b) Ev, and (c) LEv samples. The modified adsorption and desorption isotherms are plotted in black and red colors, respectively. The scale used for measuring the mass of the rock samples during water sorption experiments has an accuracy of ± 0.01 g.

Determination of PSD_{tot}: Total porosities measured by BET analysis ($\phi_{tot,BET}$) are 3.3%, 3.8%, and 5.1% for the OP, Ev, and LEv samples, respectively. We use DH method to calculate PSD_{tot} from N_2-desorption isotherm, and the results are presented by black bars in Figure 7-5. Sample LEv has the highest amount of N_2 adsorbed among our shale samples; which corresponds to its higher $\phi_{tot,BET}$ and PV_{tot} compared with that of the OP and Ev samples (black bars in Figure 7-6a). Furthermore, the LEv sample shows a sharp increase at high relative pressures in the N_2 adsorption isotherm (Figure 7-3c). This sharp increase corresponds to capillary condensation in

large pores; which is in agreement with the BET results of larger average pore size of the LEv sample compared with that of the OP and Ev samples (black bars in Figure 7-6b).

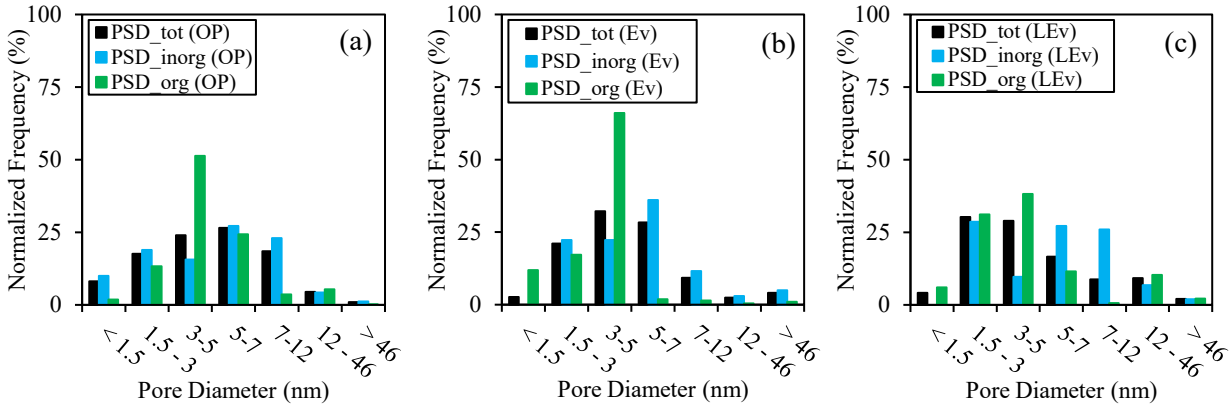

Figure 7-5. The calculated PSD_{tot}, PSD_{inorg}, and PSD_{org} for (a) OP, (b) Ev, and (c) LEv samples. PSD_{tot} is calculated from N_2-desorption isotherm measure by BET analysis. PSD_{inorg} is calculated from the modified water desorption isotherm. PSD_{org} is calculated from Eq. 7-10. The accuracy of relative pressure measurements by N_2-BET analysis is 0.15%.

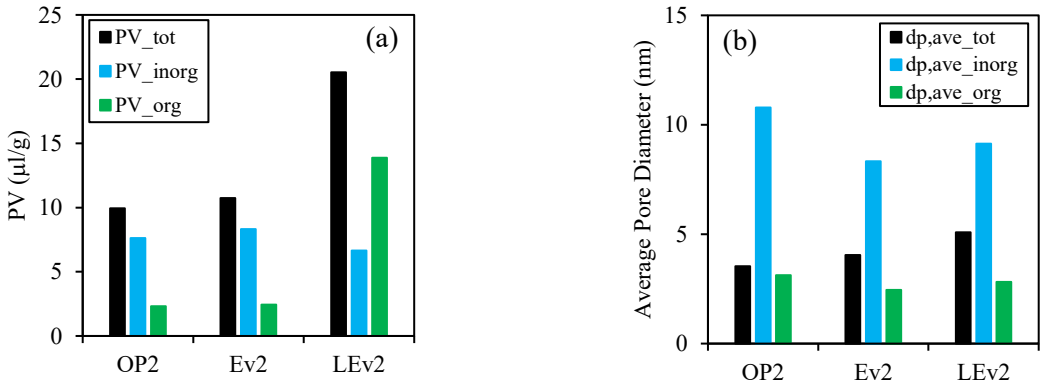

Figure 7-6. A comparison between the total, inorganic, and organic (a) pore volumes and (b) the average pore diameter for OP, Ev, and LEv samples. The total pore volume is measured by N_2-BET analysis. The maximum value of water adsorbed at the end of the modified adsorption process is considered to be the inorganic pore volume. The organic pore volume is calculated from Eq. 7-9.

Determination of PSD_{inorg} and PSD_{org}: Adsorbate affinity for pore wall affects the sorption process in nano-porous shales (Rezaveisi et al., 2014; Firouzi et al., 2014). Lan et al. (2015a) concluded that water and oil preferentially flow in the inorganic and organic pore

networks, respectively. In order to characterize PSD_{inorg}, we applied the model described in Section 7.4 on the modified water desorption isotherms; and the results are presented by blue bars in Figure 7-5. Eq. 7-10 is used to calculate PSD_{org}; and the results are presented by green bars in Figure 7-5.

According to Figure 7-5, the PSD_{inorg} has a wider distributions compared with PSD_{org}. Majority of small pores (< 5nm) are organic pores; while majority of the inorganic pores are large pores (> 10 nm). The average size for inorganic and organic pores are ~10 nm and ~3nm, respectively. These results are consistent with our HIM-EDS analysis results, showing that organic pores are generally smaller than the inorganic pores.

Except for the LEv sample, PV_{inorg} is larger than PV_{org} (Figure 7-6a). This complies with the previous experimental results showing that water imbibes more than oil into the HRB's shale samples (Dehghanpour et al., 2012 and 2013; Ghanbari and Dehghanpour, 2015). It must be noted that shales are very heterogeneous and their physiochemical properties can change significantly even in small scale (Diaz, et al., 2010). Therefore, the results presented in Figure 7-5 and 6 may not represent the pore system of all samples from the target formations.

HIM-EDS Analysis: We use HIM-EDS analysis in order to visualize organic and inorganic pores in our shale samples. Figure 7-7 shows the HIM-EDS results of Ev sample. Two magnified parts in Figure 7-7 show inorganic and organic pores. Visual observations indicate that organic pores are generally smaller than inorganic pores. An image processing technique (Zolfaghari et al., 2014c and 2018) is used to characterize the local organic porosity ($\phi_{org,local}$) and PSD $\left(PSD_{org,local}\right)$. To achieve this goal, the magnified HIM images of organic pores are processed by imaging processing package.

Image Processing of HIM Images: We use the image processing technique to generate binary (black and white) image from the color HIM image. In the binary image, black and white areas represent organic pores and rock-matrix, respectively. The binary image is then analyzed to characterize $PSD_{org,local}$. We also use the image processing package to determine $\phi_{org,local}$. $\phi_{org,local}$ is defined as the ratio of black area (the pore space) to the total area of the magnified HIM image of organic pores. We only applied the image processing technique on images of organic pores, as we were not able to detect areas with populated inorganic pores using HIM-EDS.

The calculated $PSD_{org,local}$ from the image processing analysis is shown in Figure 7-7e. About 78% of the local organic pores are smaller than 18 nm. Based on the image processing results, the average local organic pore size is ~13 nm which is larger than ~3 nm calculated from the modified water desorption isotherm. It must be noted that we were not able to visualize very small pores (<3 nm), due to the limiting resolution of HIM analysis (~15 KV). The complex mineral components in rock surface and uneven surface of rock samples also adversely affect the resolution of HIM images. Thus, there might be pores of smaller than ~3 nm that were beyond the detection limit of our HIM device.

Image processing yields $\phi_{org,local}$ of about 3.2%. This value is smaller than the total porosity of 3.8% which is measured by BET analysis. It is worth mentioning that although several past studies determined porosity of the porous medium using image processing technique (Saffari et al., 1993; Mlynarczuk et al., 2005; Saraji and Piri, 2015), it might not be a true representation of porosity as SEM/HIM images are 2D. One may recuperate this problem by analyzing augmented images obtained from SEM/HIM analyzes (Zolfaghari et al., 2014c and 2018).

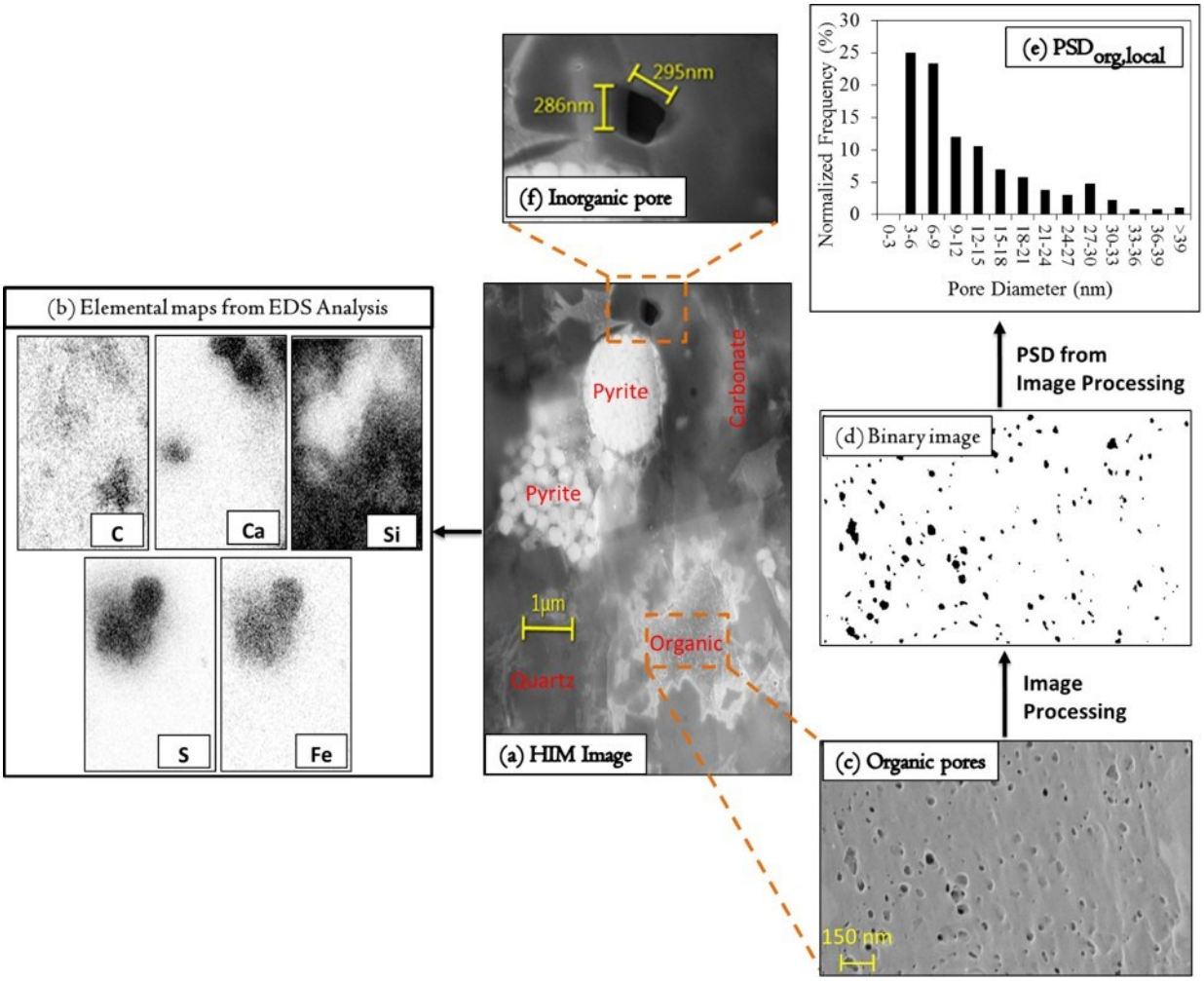

Figure 7-7. (a) HIM image of a focus area in the Ev sample. (b) Elemental maps of carbon, calcium, silica, sulfur, and iron from EDS analysis. Darker area in elemental maps represents higher density of the element. (c) Magnified HIM image showing organic pores. (d) Binary image of the magnified HIM image showing organic pores from image processing analysis. Black and white areas represent organic pores and rock-matrix, respectively. (e) The calculated $PSD_{org,local}$ from image processing. (f) Magnified HIM image showing an inorganic pore.

7.6. Limitations of the Proposed Method

Although the proposed method is helpful to estimate inorganic and organic $PSDs$ in shales, it uses several assumptions to characterize the pore space. For instance, it is assumed that the pore system does not alter during both water and N_2 sorption processes. However, water adsorption by

clays may induce micro-fractures (Ghanabri and Dehghanpour, 2015; Arshadi et. al., 2017), opening up more space for capillary condensation of water vapour. Therefore, the proposed method may over-estimate PV_{inorg} for clay-rich shales with expandable clay minerals (such as smectite).

The proposed method also assumes that "all" inorganic pores will be filled with condensed water during the modified adsorption process. However, some pores may be inaccessible for capillary condensation due to air trapping phenomena. To be specific, capillary condensation first commences in small pores due to high van der Waals interactions between water molecules and pore wall (Fisher and Israelachvili, 1979). Thus, there is a possibility for large pores to be trapped between two small water-filled pores, resulting to under-estimation of PV_{inorg}.

It is also assumed that the early sorption cycle in the modified water sorption experiments solely saturates the interlayer space of clay minerals. However, during early sorption cycle, condensed water in small capillaries may still be retained in the pore system. More specifically, the van der Waals interactions between the water molecules and pore wall are significantly high in small capillaries. Thus, desorption process may not be able to completely deplete the condensed water from small inorganic pores. In this case, the proposed method may under-estimate PV for the small inorganic pores; and also over-estimates water-adsorption by clays.

The proposed procedure also assumes that during the modified water adsorption process, water only condenses in inorganic pores. However, high solid-fluid attractions may lead to condensation of water molecules in very small organic pores of ~0.3 nm (Liu and Manson, 2005). In this research however, the detection limit for both BET and HIM analyzes was about 3 nm; and therefore, we assumed that water molecules do not condense in organic pores. It is also worth noting that there are multi-mineral pores in tight and shale formations (Habibi et al., 2015) that can accommodate both oil and water. In this study, we categorized multi-mineral pores into the inorganic pore system. This assumption needs to be modified if multi-mineral pore system exists in the samples.

The proposed procedure considers the bulk density of water ($\rho = 1\ g/cc$) for the water condensed in pores. However, there are several studies showing that capillary-confined fluid properties (i.e. density) are different compared with bulk properties (Spohr et al., 1998; Gad-el-

Hak, 1999; Gruener et al., 2009; Yang et al., 2017). This issue is particularly important when pore radius is smaller than 1 nm (Yang et al., 2017) mainly due to high fluid/wall intermolecular interactions (Spohr et al., 1998; Gad-el-Hak, 1999; Gruener et al., 2009). Therefore, for accurate calculation of PV, one should re-consider the water density assumption of $1\ g/cc$, especially for pores with radius of 1 nm or less.

7.7. Summary

This chapter characterizes the total, organic, and inorganic pores size distributions ($PSD_{tot}, PSD_{org},$ and $, PSD_{inorg}$) using the proposed modified water sorption process presented in Chapter 6. Furthermore, Helium Ion Microscope-Scanning Electron Microscope (HIM-SEM) analysis is used to visualize the pores of the shale samples. Additionally, the HIM-SEM images are analyzed by image processing to characterize the local organic pore size distribution $(PSD_{org.local})$.

Brunauer–Emmett–Teller (BET) analysis is conducted on the shale samples to characterize PSD_{tot} and the total pore volume (PV_{tot}). Then, the modified water sorption process is used to obtain the PSD_{inorg} and the inorganic pore volume (PV_{inorg}). The results of BET and modified water sorption experiments are compared to calculate PSD_{org} and the organic pore volume (PV_{org}). The results indicate that (i) majority of organic pores are smaller than 5 nm and (ii) majority of large pores are inorganic pores. The calculated $PSDs$ results comply with the visual observation of relatively larger inorganic pores than organic pores.

There is hysteresis between the adsorption and desorption isotherms of both N_2-BET and modified water sorption experiments. The hysteresis is more pronounced at low relative pressure/humidity values. These results indicate that the depletion of the condensed water/N_2 is harder for smaller pores. Strong van der Waals interactions between the condensed fluid and pore-wall can be a possible explanation for higher sorption hysteresis in small pores.

Nomenclatures

BET	Brunauer–Emmett–Teller
DH	Dollimore and Heal
EDS	Energy Dispersive Spectrometer
Ev	Evie formation
f(R)	Probability density function for the pore size
HIM	Helium Ion Microscope
HRB	Horn River Basin
LEv	Lower-Evie formation
MICP	Mercury injection capillary pressure
NMR	Nuclear magnetic resonance
OP	Otter-Park formation
P_c	Capillary pressure
PDF	Probability density function
PV	Pore volume
PV_{inorg}	Inorganic pore volume
PV_{org}	Organic pore volume
PV_{tot}	Total pore volume
PSD	Pore size distribution
PSD_{inorg}	Inorganic pore size distribution
PSD_{org}	Organic pore size distribution
$PSD_{org,local}$	Local organic pore size distribution
PSD_{tot}	Total pore size distribution
R	Universal gas constant
R_1, R_2	Principal radii of curvature
RH	Relative humidity
r_p	Pore radius
$r_{p,max}$	Maximum pore radius size

$r_{p,min}$	Minimum pore radius size
SEM	Scanning Electron Microscope
S_w	Water saturation
T	Temperature
V_m	Liquid molar volume
XRD	X-ray diffraction
$\phi_{org,local}$	Local organic porosity
$\phi_{tot,BET}$	Total porosities by BET analysis
γ	Surface tension
ρ	Density
θ	Contact angle

Chapter 8

Conclusions and Recommendations

The primary goal of this study is to investigate the source of ions in the flowback water. Also, the possibility of using flowback chemical data for characterization of the fracture network is investigated. Experiments are performed on downhole shale samples from gas shale wells drilled in the Horn River Basin. Flowback water samples are also collected from the same wells, and analyzed chemically in the laboratory.

8.1. Conclusions

The key conclusions of this study are summarized below

Chapters 2 and 3

- The barium ion in the flowback water is possibly originated from the precipitated salt crystals (likely witherite) in natural fractures.
- Logarithmic-scale cross-plot of Na^+ versus Cl^- in the flowback water is formation-independent.
- The molar ratios of Cl^-/Na^+ and Mg^{2+}/Na^+ in the flowback water are relatively close to those in the seawater; suggesting that chloride, sodium, and magnesium ions in the flowback water (of wells drilled in the Horn river Basin) are potentially sourced from formation water.
- The molar ratios of K^+/Na^+ and Ca^{2+}/Na^+ in the flowback water samples is significantly larger than that in seawater; suggesting that potassium and calcium ions in the flowback water (of wells drilled in the Horn river Basin) may originate from dissolution of rock constituents in fracturing fluid.
- The shape of the barium ion concentration profile during flowback process can be interpreted to characterize the complexity of the fracture network. More specifically, (i) a well with a steeper slope in the barium ion profile and relatively higher barium ion concentration at early flowback times has more complex fracture network

compared with (ii) a well with a smoother slope in the barium ion profile and relatively lower barium ion concentration at early flowback times.

- Leaching of clay minerals is a key mechanism for ion transfer from rock to water at the early stage of the water imbibition process.
- Presence of natural buffer systems such as calcite and dolomite can be a possible reason for the neutral pH range of the flowback water. Dissolution of natural buffer components (i.e., calcite and dolomite) can increase the ion content of the flowback water while helping the pH to remain around neutrality.

Chapters 4 and 5

- The shape of the salinity profile is potentially a signature of the complexity of the fracture network. The well with a continuous increase in the salinity (in flowback water) profile has a more complex fracture network compared with the well with a plateau in the salinity profile and a more simple fracture network.
- Pressure does not have significant impact on the total ion produced (TIP), while rock surface area, rock volume, and temperature are positively correlated to the TIP.
- The proposed scale-up procedure can accurately estimate the surface area of known samples based on the experimental results of ion concentration during the imbibition experiments. The scale-up results of fracture surface area (A_f) estimation ($\approx 5 \times 10^6 m^2$) have similar orders of magnitude compared with those estimated by rate-transient analysis ($\approx 10^6 m^2$).
- The proposed scale-up procedure was also able to accurately estimate the volume of unknown samples. The scale-up technique is then applied on the field flowback chemical data to estimate the invaded reservoir volume (IRV). The estimated IRV values are about $10^5 m^3$. The scale-up results lead to higher IRV value for the well with higher leak-off in the field as opposed to the lower IRV value for the well lower leak-off in the field.

Chapters 6 and 7

- The modified water sorption process can be used to
    - quantify the water uptake by clay minerals during water adsorption/desorption processes.
    - investigate the capillary condensation in shales.
    - to characterize the organic and inorganic pore size distributions in gas shale samples.
- Analysis of the hysteresis between the adsorption and desorption isotherms of water and nitrogen indicate that depletion of condensed fluid from smaller capillaries is more difficult than that from larger pores.

8.2. Recommendations

The following recommendations can help to further extent/improve the results of this research.

- The model presented in Chapter 4 lumps up the net effect of all possible sources of ions (i.e., leaching of clay minerals, mixing of fracturing fluid with formation water, and reaction of fracturing fluid with rock constituents) to investigate the ion transfer from rock matrix to the water-filled fractures. However, the experimental results presented in Chapter 2 indicate that clay leaching is a key ion transfer mechanism at early stages of the shale-water contact. Future studies should take into account for the leaching of clay minerals at the early stages of the shale-water fracturing operations (i.e., during fracturing and early times of the soaking period).
- The model presented in Chapter 4 assumes a constant diffusion coefficient for a single component. Future studies can extend the model by incorporation of multi-component mass transfer between reservoir rock and fracturing fluid.
- The model presented in Chapter 4 assumes slit-shape fractures. Future studies can incorporate different fracture geometries to further improve the model results.

- The presented scale-up procedure in Chapter 5 is based on the laboratory results of ion concentration during imbibition tests. Imbibition experiments were conducted in presence of air/oxygen (i.e., oxic condition). However, there is no (or limited) amount of oxygen at the reservoir conditions (i.e., anoxic condition). Future studies can improve the scale-up results by performing experiments at anoxic conditions to better represent the downhole conditions.

- The scale-up procedure presented in Chapter 5 applies the empirical linear $A_s - TIP$ correlation to estimate A_f. Although the linear $A_s - TIP$ correlation is valid for small shale rock samples, further thorough laboratory analysis is required to ensure that the linear $A_s - TIP$ correlation is still valid for medium-size, and ultimately reservoir-scale, rocks.

- The scale-up procedure presented in Chapter 5 for A_f estimation considers an exponential regression to extrapolate A_f at reservoir temperature. The exponential regression is selected to account for the temperature dependency of reactions similar to the Arrhenius equation. Future studies can extend the scale-up procedure by separately investigating the role of chemical reactions from other possible sources of ions such as mixing with formation water and leaching of clay minerals.

- The proposed model in Chapter 7 assumes that all inorganic pores will be filled with condensed water during the modified water sorption process. Future studies can improve the model results by taking into account for potential air trapping in pores during the adsorption process.

- The proposed model in Chapter 7 assumes that the adsorbed water at the early sorption cycle only saturates the interlayer of clay minerals. However, small hydrophilic pores may tend to retain the condensed water even at low RH values. Future studies can further improve the model results by taking into account for the possible water retention in small hydrophilic pores at the end of the early sorption cycle.

- The proposed model in Chapter 7 considers the bulk density of water ($\rho = 1\ g/cc$) for the water condensed in pores. However, the fluid density is generally higher near the pore wall. Future studies can improve the model results by incorporating the density profiles for the capillary-confined fluids.

- In this research, the impact of organic matters on the chemistry of flowback water is neglected. However, presence of organic matters in the produced flowback water impacts the flowback water chemistry. Organic matters can undergo complexation reactions, and lead to precipitation of salts especially in late flowback times where the produced flowback water is highly saline. Future studies should take into account for interaction of organic matters with inorganic ions for more accurate interpretation of the flowback chemical data.

References

Abbasi, M.A., Dehghanpour, H., Hawkes, R., Flowback analysis for fracture characterization, SPE 162661, SPE Canadian Unconventional Resources Conference, Calgary, Alberta, Canada 30 October-1 November 2012.

Abbasi, M. A., Ezulike, D. O., Dehghanpour, Hawkes, R., A comparative study of flowback rate and pressure transient behavior in multifractured horizontal wells completed in tight gas and oil reservoirs, Journal of Natural Gas Science and Engineering 17: 82–93, 2014.

Adesida A.G. Akkutlu, I.Y., Resasco, D.E., Rai, C.S., Kerogen Pore Size Distribution of Barnett Shale using DFT Analysis and Monte Carlo Simulations, SPE 147397, APE Annual Technical Conference and Exhibition, Denver, Colorado, USA, 30 October-2 November 2011.

Ahn, C. H., Chung, O. C., Dilmore, R., Wang, J. Y., A Hydraulic Fracture Network Propagation Model in Shale Gas Reservoirs: Parametric Studies to Enhance the Effectiveness of the Stimulation, URTeC: 1922580, Unconventional Resources Technology Conference (URTeC), Denver, Colorado, USA, 25-27 August 2014.

Akima, H., A New Method of Interpolation and Smooth Curve Fitting Based on Local Procedures, J. ACM, Vol.17, No. 4 (Oct. 1970) 589-602.

Alessi, D. S., Zolfaghari, A., Kletke, S., Gehman, J., Allen, D. M., Goss, G., Comparative analysis of hydraulic fracturing wastewater practices in unconventional shale development: Water sourcing, treatment and disposal practices, Canadian Water Resources Journal, Vol. 42, No. 2, 105–121, http://dx.doi.org/10.1080/07011784.2016.1238782, 2017.

Ali, M., Hascakir, B., Water-rock interaction for Eagle Ford, Marcellus, Green River, and Barnett Shale samples, SPE-177304-MS, SPE Eastern Regional Meeting, Morgantown, West Virginia, USA, 13-15 October 2015.

Al-Bazali, T., Zhang, J., Chenevertc, M.E., Sharma, M.M., Factors controlling the compressive strength and acoustic properties of shales when interacting with water-based fluids, International Journal of Rock Mechanics & Mining Sciences 45 (2008) 729–738, doi:10.1016/j.ijrmms.2007.08.012.

Al Hinai, A., Rezaee, R., Esteban, L., Labani, M., Comparisons of pore size distribution: A case from the Western Australian gas shale formations, Journal of Unconventional Oil and Gas Resources 8 (2014) 1–13, http://dx.doi.org/10.1016/j.juogr.2014.06.002.

Ambrose, R.J., Hartman, R.C., Diaz-Campos, M. Akkutlu, Sondergeld, C.H., Shale Gas in Calculations Part I: New Pore-Scale Considerations, SPE Journal, Volume 17 (1) 219-229, 2012.

Andrew M., Bijeljic, B., Blunt, B., J., Pore-scale Contact Angle Measurements at Reservoir Conditions using X-ray Microtomography, Advances in Water Resources 68 (2014) 24–31.

Archie, G.E., Introduction to Petrophysics of Reservoir Rocks", American Association of Petroleum Geologists Bulletin 34 (5): 943–961, 1950.

Arshadi, M., Zolfaghari, A., Piri, M., Al-Muntasheri, G.A., Sayed, M., The effect of deformation on two-phase flow through proppant-packed fractured shale samples: A micro-scale experimental investigation, Advances in Water Resources (2017), 105, 108-131, doi: 10.1016/j.advwatres.2017.04.022.

Asadi, M., Woodroof, R.A., Himes, R. E., Comparative study of flowback analysis using polymer concentrations and fracturing-fluid tracer methods: A field study, SPE 101614, SPE International Oil & Gas Conference and Exhibition, Beijing, China, 5-7 December 2006.

Ayatollahi, S., Zolfaghari, A., Simulation predicts condensate formation in Aghar field, Oil and Gas Journal, 104(47) 50, 2006.

Bai, B., Carlson, K., Prior, A., Douglas, C., Sources of Variability in Flowback and Produced Water Volumes from Shale Oil and Gas Wells, Journal of Unconventional Oil and Gas Resources 12 (2015) 1–5, DOI: http://dx.doi.org/10.1016/j.juogr.2015.07.001.

Bai, B., Elgmati, M., Zhang, H., Wei, M., Rock characterization of Fayetteville shale gas plays, Fuel 105 (2013) 645-652, http://dx.doi.org/10.1016/j.fuel.2012.09.043.

BC Oil and Gas Commission, Horn River Basin Unconventional Shale Gas Play Atlas, June 2014.

Balaba, R. S., Smart, R. B., Total arsenic and selenium analysis in marcellus shale, high-salinity water, and hydrofracture flowback wastewater, Chemosphere 89 (2012) 1437–1442.

Bearinger, D., Message in a bottle, SPE 168891, Unconventional Resources Technology Conference, Denver, Colorado, USA, 12-14 August, 2013.

Behmanesh, H., Hamdi, H., Clarkson, C.R., Production Data Analysis of Liquid Rich Shale Gas Condensate Reservoirs, SPE-167160, SPE Unconventional Resources Conference-Canada Calgary, Alberta, Canada, 5–7 November 2013.

Bello, R.O., Rate Transient Analysis in Shale Gas Reservoirs with Transient Linear Behavior, PhD Dissertation, Texas A &M U., College Station, Texas, 2009.

Bennion, D. B., Thomas, F. B., Bietz, R. F., Remediation of water and hydrocarbon phase trapping problems in low permeability gas reservoirs, J Can Pet Technol 38 (8): 39–48. PETSOC-99-08-01. http://dx.doi.org/10.2118/99-08-01, 1999.

Bertoncello, A., Wallace, J., Blyton, C., Honarpour, M., Kabir, C. S, Imbibition and water blockage in unconventional reservoirs: Well management implications during flowback and early production, SPE/EAGE European Unconventional Resources Conference and Exhibition, 2014.

Binazadeh, M., Xu, M., Zolfaghari, A., Dehghanpour, H., Effect of Electrostatic Interactions on Water Uptake of Gas Shales: The interplay of solution ionic strength and electrostatic double layer, Energy Fuels 2016, 30, 992−1001, DOI: 10.1021/acs.energyfuels.5b02990.

Binazadeh, M., Xu, M., Jiang, K., Zolfaghari, A., Dehghanpour, H., Effect of Electrostatic Interactions on Water Uptake of Gas Shales: The Interplay of Solution Ionic Strength, Electrostatic Double Layer, and Shale Zeta Potential, SPE-175926-MS, SPE/CSUR Unconventional Resources Conference, Calgary, Alberta, Canada, 2015.

Blaunch, M.E., Myers, R.R., Moore, T.R., Lipiniski, B.A., Houston, N.A., Marcellus shale post-frac flowback waters-where is all the salt coming from and what are the implications?, SPE 125740, SPE Eastern Regional Meeting, Charleston, West Virginia, USA (2009).

Brunauer, S., Deming, L. S., Deming, W. S., Teller, E., On a Theory of The van der Waals Adsorption of Gases, J Am Chem Soc, 62 (1940), pp. 1723–1732.

Cai, J. Yu, B., Zou, M. Luo, L., Fractal Characterization of Spontaneous Co-Current Imbibition in Porous Media, Energy Fuels 2010, 24, 1860–1867: DOI:10.1021/ef901413p.

Canadian Society for Unconventional Resources (2011), http://www.csur.com/wp-content/uploads/2018/02/TightOil_v3_wBleed.pdf, (accessed March 01, 2018).

Cao, P., Liu, J., Leong, Y. K., A multiscale-multiphase simulation model for the evaluation of shale gas recovery coupled the effect of water flowback, Fuel 199 (2017) 191-205, http://dx.doi.org/10.1016/j.fuel.2017.02.078.

Capo R. C., Stewart,B. W, Rowan E., R., Kohl C. A. K., Wall A. J., Chapman E. C., HammackR. W., Schroeder K. T., The strontium isotopic evolution of Marcellus Formation produced waters, southwestern Pennsylvania, International Journal of Coal Geology 126 (2014) 57–63.

Carman, P., S., Lant, K., S., Making the Case for Shale Clay Stabilization, SPE 139030, SPE Eastern Regional Meeting, Morgantown, West Virginia, USA, 12-14 October 2010.

Chen, Q., Zhang, J., Tang, X., Li, W., Li, Z., Relationship Between pore type and Pore Size of Marine Shale: An Example from the Sinian–Cambrian Formation, Upper Yangtze region, South China, International Journal of Coal Geology 158 (2016) 13–28, http://dx.doi.org/10.1016/j.coal.2016.03.001.

Chen, J-H., Zhang, J., Jin, G., Quinn, T., Frost, E., Chen, J., Capillary Condensation and NMR Relaxation Time in Unconventional Shale Hydrocarbon Resources, SPWLA 53rd Annual Logging Symposium, June 16-20, 2012.

Chenevert, M. E., Shale Alteration by Water Adsorption, Journal of Petroleum Technology, 22(9):240-247, SPE-2401-PA, http://dx.doi.org/10.2118/2401-PA.

Cheng, Y., Impact of Water Dynamics in Fractures on the Performance of Hydraulically Fractured Wells in Gas-Shale Reservoirs. J. of Can. Pet. Technol. 51 (2): 143-151. SPE-127863-PA, 2012.

Cheng, Y., Lee, W.J., MacVay, D.A., A New Approach for Reliable Estimation of Hydraulic Fracture Properties Using Elliptical Flow Data in Tight Wells. SPE Res. Eva. & Eng. J., (12):2, SPE-105767-PA, 2009.

Cheng, T., Saiers, J. E., Mobilization and transport of in situ colloids during drainage and imbibition of partially saturated sediments, Water Resources Research, Vol. 45, W08414, doi:10.1029/2008WR007494, 2009.

Chermak, J. A., Schreiber, M. E., Mineralogy and Trace Element Geochemistry of Gas Shales in the United States: Environmental Implications, International Journal of Coal Geology 126 (2014) 32–44.

Chiu C.Y., Chiang, A.S.T., Chao, K.J., Mesoporous Silica Powders and films - Pore Size Characterization by Krypton Adsorption, Microporous and Mesoporous Materials 91 (2006) 244–253.

Chou, C. L., Sulfur in coals: A review of Geochemistry and Origins, International Journal of Coal Geology 100 (2012) 1–13.

Cipolla, C. L., Warpinski, N. R., Mayerhofer, M. J., Hydraulic Fracture Complexity: Diagnosis, Remediation, and Exploration, SPE Asia Pacific Oil & Gas Conference and Exhibition, Perth, Australia, 20-22 October 2008.

Crafton, J.W., Gunderson, Stimulation Flowback Management: Keeping a Good Completion Good, SPE-110851, SPE Annual Technical Conference and Exhibition, Anaheim, California, 11-14 November 2007.

Clarkson, C.R., Bustin, R.M., Seidle, J.P., Production Data Analysis of Single-Phase (Gas) Coalbed-Methane Wells, SPE Res. Eval. & Eng. J., (10):3, SPE-100313-PA, 2007.

Clarkson, C.R., Wood J., Burgis S., Nanopore-Structure Analysis and Permeability Predictions for a Tight Gas Siltstone Reservoir by use of Low-Pressure Adsorption and Mercury-Intrusion Techniques, SPE Reservoir 40 Evaluation & Engineering, 2012, 15(06): 648-661.

Clarkson, C.R., Solano, N., Bustin, R. M., Bustin, A. M. M., Chalmers, G. R. L., He, L., Melnichenko Y. B., Radlinski, A. P., Blach, T.P., Pore Structure Characterization of North

American Shale Gas Reservoirs using USANS/SANS, Gas Adsorption, and Mercury Intrusion, Fuel 103 (2013) 606–616, http://dx.doi.org/10.1016/j.fuel.2012.06.119.

Clover Global Solutions, https://clovergs.files.wordpress.com/2012/09/shale-3.png, accessed March 01, 2018).

Council of Canadian Academies (CCA), Environmental impacts of shale gas extraction in Canada, Ottawa, ON: The Expert Panel on Harnessing Science and Technology to Understand the Environmental Impacts of Shale Gas Extraction, Council of Canadian Academies, pp. 292, 2014.

Curtis, J. B., Fractured shale-gas systems, AAPG bulletin, 86(11), 1921-1938, 2002.

Dauphinee, T. M., & Klein, H. P. The effect of temperature on the electrical conductivity of seawater, Deep Sea Research, 24(10), 891-902, 1977.

Dehghanpour, H., Lan, Q., Saeed, Y., Fei, H., Qi Z., Spontaneous Imbibition of Brine and Oil in Gas Shales: Effect of Water Adsorption and Resulting Microfractures, dx.doi.org/10.1021/ef4002814 | Energy Fuels 2013, 27, 3039−3049.

Dehghanpour, H., Zubair, H. A., Chhabra, A., Ullah, A., Liquid Intake of Organic Shales, dx.doi.org/10.1021/ef3009794, Energy & Fuels 2012, 26, 5750−5758.

Deriszadeh, M., Wong, R.C.K., One-dimensional Swelling Behavior of Clay and Shale under Electrical Potential Gradient, Transport in Porous Media (2014) 101:35–52.

Descourvières, C., Hartogc, N., Pattersonb, B. M., Oldhama, C., Prommer, H., Geochemical Controls on Sediment Reactivity and Buffering Processes in A Heterogeneous Aquifer, Applied Geochemistry 25 (2010) 261–275.

Diaz, E., Sisk, C., and Nur, A., Quantifying and Linking Shale Properties at a Variable Scale. Presented at the 44th US Rock Mechanics Symposium and 5th US-Canada Rock Mechanics Symposium, Salt Lake City, Utah, USA, 27–30 June, 2010, ARMA-10-272.

Dollimore, D., Heal, G. R., An improved method for the calculation of pore size distribution from adsorption data, ournal of Applied Chemistry, Vol. 14, Issue 3, pages 109–114, March 1964, DOI: 10.1002/jctb.5010140302.

Donaldson, E.C., Chilingarian, G.V., Yen, T.F., Enhanced Oil Recovery: Fundamentals and Analyses, Elsevier, Feb 1, 1985.

Ebrahimi, A. N., Sharak, A. Z., Mousavi, S. A., Shahrak, A. Z., Aghazadeh, F., Application of GA in Optimization of Modified Benzene Alkylation Process, Journal of Petroleum Science and Technology, Vol. 2, No. 1, 2012, 43-49.

Economides, M. J., & Martin, T. (2007). Modern fracturing: Enhancing natural gas production (pp. 978-1). Houston: ET Publishing.

Elipe, M.V.S., Advantages and Disadvantages of Nuclear Magnetic Resonance Spectroscopy as a Hyphenated Technique, Analytica Chimica Acta 497 (2003) 1–25, doi:10.1016/j.aca.2003.08.048.

Engelder, T., Cathles, L. M., Bryndzia, L. T., The Fate of Residual Treatment Water in Gas Shale, Journal of Unconventional Oil and Gas Resources 7 (2014) 33–48.

Engle M. A., Rowan, E. L., Geochemical evolution of produced water from hydraulic fracturing of the Marcellus Shale, northern Appalachian Basin: A multivariate compositional data analysis approach, International Journal of Coal Geology 126 (2014) 45-56.

Essington, M. E., Soil and Water Chemistry: An Integrative Approach, CRC Press, ISBN 0-8493-1258-2, 2005.

Estrada, J. M., Bhamidimarri, R., A review of the issues and treatment options for wastewater from shale gas extraction by hydraulic fracturing, Fuel 182 (2016) 292-303, http://dx.doi.org/10.1016/j.fuel.2016.05.051.

Ezulike, O. D., Complementary workflows for analyzing multiphase flowback and post-flowback production data in unconventional reservoirs, PhD Dissertation, University of Alberta, 2017.

Fakcharoenphol, P., Kurtoglu, B., Kazemi, H., Charoenwongsa, S., Wu, Y. S., The effect of osmotic pressure on improve oil recovery from fractured shale formations, SPE-198998-MS, SPE Unconventional Resources Conference, Woodlands, Texas, USA, 1-3 April 2014.

Fan, C., Analysis of microseismic events associated with hydraulic fracture propagation, MSc thesis, Louisiana State University, 2014.

Fathi, E., Akkutlu, Y., Matrix Heterogeneity Effects on Gas Transport and Adsorption in Coalbed and Shale Gas Reservoirs, Transport Porous Media (2009) 80:281-304, DOI 10.1007/s11242-009-9359-4.

Firouzi, M., Rupp, E.C., Liu, C.W., Wilcox, J., 2014b, Molecular Simulation and Experimental Characterization of the Nanoporous Structures of Coal and Gas Shale, International Journal of Coal Geology 121 (2014) 123–128, http://dx.doi.org/10.1016/j.coal.2013.11.003.

Fisher L. R., Israelachvili, J. N., Direct experimental verification of the Kelvin Equation for Capillary Condensation, Nature 277, 548 - 549 (15 February 1979); doi:10.1038/277548a0.

Fisher, M.K., Wright, C.A., Davidson, B.M., Goodwin, A.K., Fielder, E.O., Buckler, W.S., Steinsberger, N.P., Integrating Fracture-Mapping Technologies to Improve Stimulations in the Barnett Shale, SPE Production & Facilities J., (20):2 SPE-77441-PA, 2005.

Fogler, H. S., Essentials of chemical reaction engineering, Prentice Hall, 2010, ISBN: 978-0137146123.

Frantz, J.H., Jochen, J.V., Shale Gas, Schlumberger White Paper, 2005.

Gad-el-Hak, M., The Fluid Mechanics of Microdevices—The Freeman Scholar Lecture, J. Fluids Eng 121(1), 5-33, March 01, 1999, doi:10.1115/1.2822013

Gal, L. P., Jones, A. L., Evaluation of Oil and Gas Potential in the Deh Cho Territory: Northwest Territories Open-File Report, 2003-06, C. S. Lord Northern Geoscience Centre, p. 89, 2003.

Gale, J. F. W., Laubach, S. E., Olson, J. E., Eichhubl, P., and Fall, A., 2014, Natural Fractures in Shale: A Review and New Observations, AAPG Bulletin, v. 98, no. 11, p. 2165-2216. doi: 10.1306/08121413151

Gallegos, T.J., B.A. Varela, S.S. Haines,and M.A. Engle, Hydraulic fracturing water use variability in the United States and potential environmental implications, Water Resources. Research, 51, 2015.

Gdanski, R., Numerical Study of PDL-induced fracture-face damage using a fracture mimicator, SPE 132918, SPE Asia Pacific Oil & Gas Conference and Exhibition, Brisbane, Queensland, Australia, 18-20 October, 2010.

Ge, H.K., Yang, L., Shen, Y.H., Ren, K., Meng, F.B., Ji, W.M., Wu, S., Experimental Investigation of Shale Imbibition Capacity and the Factors Influencing Loss of Hydraulic Fracturing Fluids, Pet. Sci. (2015) 12:636–650, DOI 10.1007/s12182-015-0049-2.

Gesho, M., Zolfaghari, A., Piri, M., Pore Network Extraction and Upscaling: A Big Data Approach. CMWR Conference, University of Toronto, Toronto, ON, Canada, June 2016.

Gevorkyana, A., Semmler, W., Oil price, Overleveraging and Shakeout in the Shale Energy Sector — Game Changers in the Oil Industry, Economic Modelling 54 (2016) 244–259, http://dx.doi.org/10.1016/j.econmod.2015.12.029.

Ghanbari, E., Water Imbibition and Salt Diffusion in Gas Shales: A Field and Laboratory Study, Master of Science Thesis, University of Alberta, 2015.

Ghanbari, E., Abbasi, M.A., Dehghanpour, H., Bearinger, D., Flowback Volumetric and Chemical Analysis for Evaluating Load Recovery and its Impact on Early-time Production, SPE 167165, SPE Unconventional Resources Conference-Canada, Calgary, Alberta, Canada, 5-7 November, 2013.

Ghanbari, E., Dehghanpour, H., The fate of fracturing water: A field and simulation study, Fuel 163 (2016) 282-294, http://dx.doi.org/10.1016/j.fuel.2015.09.040.

Ghanbari, E., Dehghanpour, H., Impact of Rock Fabric on Water Imbibition and Salt Diffusion in Gas Shales, International Journal of Coal Geology 138 (2015) 55–67.

Goss, G., Alessi, D, Allen, D., Gehman, J., Brisbois, J., Kletke, S., Zolfaghari, A., Notte, C., Thompson, Y., Hong, K., Covalski, V., Neto, W. A., Prosser, C., Unconventional wastewater

management: A comparative review and analysis of hydraulic fracturing wastewater management practices across four north american basins, Canadian Water Network, October 2015.

Green, D. W., Perry, R. H., Perry: Perry's chemical engineers' handbook, Eighth Edition, McGraw-Hill Professional, 2008, ISBN: 9780071422949.

Gruener, S., Hofmann, T., Wallacher, D., Kityk, A.V., Huber, P., Capillary rise of water in hydrophilic nanopores, Physical Review E 79, 067301, 2009.

Gruener, S., Hermes, H.E., Schillinger, B., Egelhaaf, S.U., Huber, P., Capillary Rise Dynamics of Liquid Hydrocarbons in Mesoporous Silica as Explored by Gravimetry, Optical and Neutron Imaging: Nano-rheology and Determination of Pore Size Distributions from the Shape of Imbibition Fronts, Colloids and Surfaces A: Physicochem. Eng. Aspects 496 (2016) 13–27.

Habibi, A., Binazadeh, M., Dehghanpour, H., Bryan, D., Uswak, G., Advances in Understanding Wettability of Tight Oil Formations, SPE-175157-MS, SPE Annual Technical Conference and Exhibition, Houston, Texas, USA, 28-30 September 2015.

Haluszczak, L., Geochemical analysis of flow back and production waters from oil and gas wells in Pennsylvania, Department of Geosciences, BSc thesis, The Pennsylvania State University, 2011.

Haluszczak, L.O., Rose, A.W., Kump, L.R., Geochemical evaluation of fowback brine from Marcellus gas wells in Pennsylvania, USA, Applied Geochemistry J. 28 (2013) 55-61, http://dx.doi.org/10.1016/j.apgeochem.2012.10.002.

He, Y., Flynn, S. L., Folkerts, E. J., Zhang, Y., Ruan, D., Alessi, D. S., Martin, J. W., Goss, G., Chemical and toxicological characterizations of hydraulic fracturing flowback and produced water, Water Research 114 (2017) 78-87, http://dx.doi.org/10.1016/j.watres.2017.02.027.

He, C., Zhang, T., Vidic, R. D., Co-treatment of abandoned mine drainage and Marcellus Shale flowback water for use in hydraulic fracturing, Water Research 104 (2016) 425-431, http://dx.doi.org/10.1016/j.watres.2016.08.030.

Hensen, E. J. M., Smit, B., Why Clays Swell, Journal of Physical Chemistry B 2002, 106, 12664-12667.

Huntington H., emf 26: changing the game? Emissions and market implications of new natural gas supplies report, Stanford University, Energy Modeling Forum, 2013.

Hoffman, B. T., Chang, W. M., Modeling Hydraulic Fractures in Finite Difference Simulators: Application to Tight Gas Sands in Montana, Journal of Petroleum Science and Engineering 69 (2009) 107–116.

Holditch, S. A., Factors affecting water blocking and gas flow from hydraulically fractured gas wells, J Pet Technol 31 (12): 1515–1524. SPE-7561-PA. http://dx.doi.org/10.2118/7561-PA, 1979.

Horn River News, Encana Estimates up to 900 Trillion Cubic Feet in Horn River Basin, 2009.

Howarth, R. W., Ingraffea, A., Engelder, T., 2011. Natural gas: Should fracking stop? Nature 477 (7364), 271–275.

Hu, Q., Gao, X., Gao, Z., Ewing, R., Dultz, S., Kaufmann, J., Pore Accessibility and Connectivity of Mineral and Kerogen Phases in Shales, URTeC 1922943, Unconventional Resources Technology Conference, Denver, Colorado, USA, 25-27 August, 2014.

Hu, Y., Mackay, E., Modeling of geochemical reactions occurring in the Gyda field under cold-seawater injection on the basis of produced-water-chemistry data and implications for scale management, SPE Production & Operations, 2017.

Huang, P., M., Li, Y., Sumner, M. E., Handbook of Soil Sciences: Properties and Processes, Second Edition, CRC Press, ISBN 9781439803059 - CAT# K10170, November 17, 2011.

Huang, W. H., Kiang, W. C., Laboratory Dissolution of Plagioclase Feldspars in Water and Organic Acids at Room Temperature, American Mineralogist, Vol. 57, pp. 1849-1859, 1972.

Hueckel, T., Reactive plasticity for clays during dehydration and rehydration. Part 1: Concepts and options, International Journal of Plasticity 18 (2002) 281-312.

Hunter, R.J., Foundations of Colloid Science, 2nd Edition, Oxford University Press, ISBN: 978-0-19-850502-0, 2001.

Jackson, R. B., Vengosh, A., Darrah, T. H., Warner, N. R., Down, A., Poreda, R. J., Osborn, S. G., Zhao, K., Karr, J. D., Increased stray gas abundance in a subset of drinking water wells near Marcellus Shale gas extraction, Proc. Natl. Acad. Sci., USA 110 (28), 11250–11255, 2013.

Javaheri, A., Dehghanpour, H., Wood, J., Imbibition oil recovery from tight rocks with dual-wettability pore-network: A Montney case study, SPE-185076-MS, SPE Unconventional Resources Conference, Calgary, Alberta, Canada, 15-16 February 2017a.

Javaheri, A., Dehghanpour, H., Wood, J., Tight rock wettability and its relationship to other petrophisical properties: A Montney case study, Journal of earth Science, Vol. 28, No. 2, p. 381-390, April 2017b.

Jin, G., Perez, H.G., Agrawal, G., Khodja, M.R., Ali, A.Z., Hussaini, S.R., Jangda, Z.Z., The Impact of Gas Adsorption and Composition on Unconventional Shale Permeability Measurement, SPE-172744-MS, SPE Middle East Oil & Gas Show and Conference, Manama, Bahrain, 8-11 March, 2015.

Johnson, E.G., Johnson, L.A., Hydraulic fracture water usage in northeast British Columbia: Locations, volumes and trends, Geoscience Reports 2012, British Columbia Ministry of Energy and Mines, pages 41-63.

Jones, D. R., Chapman, B. M., Jung, R. F., Experimental and computer modeling studies of acid leaching of Rundle oil shale, Water Research, Vol. 26, No. 2, pp. 159-168, 1992.

Josh, M., Esteban, L., Delle Piane, C., Sarout, J., Dewhurst, D. N., Clennell, M. B., Laboratory Characterisation of Shale Properties, Journal of Petroleum Science and Engineering 88–89 (2012) 107–124.

Kate, K., Navare, S.D., Bandewar, S.R., Tambe, R.R., Acharya, R.S., Pawar, V.D., Engineering Mathematics-I, Second revised edition, Technical Publications Pune, 2006.

Karimi-Fard, M., Durlofsky, L.J., Aziz, K., An Efficient Discrete-Fracture Model Applicable for General-Purpose Reservoir Simulators, Society of Petroleum Engineer Journal, 9 (2), 227–236, 2004.

Keller, W.D., Da-Costa, L. M., Comparative chemical compositions of aqueous extracts from representative clays, American Mineralogist, Volume 74, pages I142-1 146, 1989.

King, G.E., Hydraulic fracturing: What every representative, environmentalist, regulator, reporter, investor, university researcher, neighbor and engineer should know about estimating frac risk and improving frac performance in unconventional gas and oil wells, SPE 152596, SPE Hydraulic Fracturing Technology Conference, Woodlands, Texas, USA, February 2012.

Kuila, U., Measurement and Interpretation of Porosity and Pore-Size Distribution in Mudrocks: The Hole Story of Shales, PhD Dissertations, Colorado School of Mines, 2013.

Kuila, U., Prasad, M., Surface Area and Pore-Size Distribution in Clays and Shales, SPE 146869, SPE Annual Technical Conference and Exhibition, Denver, Colorado, USA, 30 October-2 November, 2011.

Labani, M.M., Rezaee, R., Saeedi, A., Al Hinai, A., Evaluation of Pore Size Spectrum of Gas Shale Reservoirs using Low Pressure Nitrogen Adsorption, Gas Expansion and Mercury Porosimetry: A case Study from the Perth and Canning Basins, Western Australia, Journal of Petroleum Science and Engineering 112 (2013) 7–16, http://dx.doi.org/10.1016/j.petrol.2013.11.022.

Lan, Q., Dehghanpour, H., Wood, J., Sanei, H., Wettability of the Montney Tight Gas Formation, 2015 SPE Reservoir Evaluation & Engineering, REE171620 DOI: 10.2118/171620-PA.

Lan, Q., Ghanbari, E., Dehghanpour, H., Hawkes, R., Water loss versus soaking time: Spontaneous imbibition in tight rocks, SPE 167713, The SPE/EAGE European Unconventional Conference and Exhibition, Vienna, Austria, 25-27 February, 2014a.

Lan, Q., Xu, M., Dehghanpour, H., Wood, J., Advances in Understanding Wettability of Tight and Shale Gas Formation, SPE-170969-MS, APE Annual Technical Conference and Exhibition, Amsterdam, Netherlands, 27-29 October, 2014b.

Lange A., Bouzian, J., Bourbiaux, B., Tracer-Test Simulation on Discrete Fracture Network Models for the Characterization of Fractured Reservoirs, SPE 94344, SPE Europec/EAGE Annual Conference, Madrid, Spain, 13-16 June 2005.

Langille, D., Scheck, M., Berhad, S. S., Seligman, B., Slickwater chemistry concerns and field water management in tight gas, IPTC-181442-MS, International Petroleum Technology Conference, Kuala Lumpur, Malaysia, 10-12 December, 2014.

Levenspiel, O., Chemical reaction engineering, 3rd Edition, Nohn Wiley & Sons, ISBN 0-471-25424-X, 1999.

Le, T. D., Murad, M. A., Pereira, P. A., A new matrix/fracture multiscale coupled model for flow in shale-gas reservoirs, 181750-PA SPE Journal Paper, 2016.

Li, H., Son, J., Carlson, K. H., Concurrence of aqueous and gas phase contamination of groundwater in the Wattenberg oil and gas field of Northern Colorado, Water Research 88 (2016) 458-466.

Li, J., Yin, J., Zhang, Y., Lu, S., Wang, W., Li, J., Chen, F., Meng, Y., A Comparison of Experimental Methods for Describing Shale Pore Features — A Case Study in the Bohai Bay Basin of Eastern China, International Journal of Coal Geology 152 (2015) 39–49, http://dx.doi.org/10.1016/j.coal.2015.10.009.

Li, J., Li, X., Wang, X., Li, Y., Wu, K., Shi, J., Yang, L., Feng, D., Zhang, T., Yu, P., Water Distribution Characteristic and Effect on Methane Adsorption Capacity in Shale Clay, International Journal of Coal Geology 159 (2016) 135–154, http://dx.doi.org/10.1016/j.coal.2016.03.012.

Liao, X., Chigira, M., Matsushi, M., Wu, X., Investigation of Water–Rock Interactions in Cambrian Black Shale via a Flow-Through Experiment, Applied Geochemistry 51 (2014) 65–78.

Lin, W., Kovscek, A.R., Gas sorption and the consequent volumetric and permeability change of coal II: Numerical modeling, Transp Porous Med (2014) 105:23–42, DOI 10.1007/s11242-014-0356-x.

Liu, J.C., Manson, P.A., Does Water Condense in Carbon Pores?, Langmuir 2005, 21, 10219-10225.

Liu, X., Xiong, J., Liang, L., Investigation of Pore Structure and Fractal Characteristics of Organic Rich Yanchang Formation Shale in Central China by Nitrogen Adsorption/Desorption Analysis, Journal of Natural Gas Science and Engineering 22 (2015) 62-72, http://dx.doi.org/10.1016/j.jngse.2014.11.020.

Loucks, Robert G., et al. "Morphology, Genesis, and Distribution of Nanometer-Scale Pores in Siliceous Mudstones of the Mississippian Barnett Shale." Journal of sedimentary research 79.12 (2009): 848-861.

Lund, R., Fogler, H., S., Mccune, C., C., Acidization-I. The dissolution of Dolomite in Hydrochloric Acid, Chemical Engineering Science, 1973. Vol. 28, pp. 691-700.

Lyu, Q., Ranjith, P.G., Long, X., Kang, Y., Huang, M., A review of Shale Swelling by Water Adsorption, Journal of Natural Gas Science and Engineering 27 (2015) 1421-1431.

Makhanov, K., Habibi, A., Dehghanpour, H., Kuru, E., Liquid uptake of gas shales: A workflow to estimate water loss during shut-in periods after fracturing operations, Journal of Unconventional Oil and Gas Resources 7 (2014) 22–32.

Makinde, I., Lee, W. J., Forecasting production of liquid rich shale (LRS) reservoirs using simple models. Journal of Petroleum Science and Engineering, 157, 461-481, 2017.

Maxwell, S., Comparative Microseismic Interpretation of Hydraulic Fractures, SPE 162782-MS, SPE Canadian Unconventional Resources Conference, Calgary, Alberta, Canada, 30 October-1 November 2012.

McCaffrey, M. A., Lazar, B. H. D. H., Holland, H. D., The evaporation path of seawater and the coprecipitation of Br (super-) and K (super+) with halite, Journal of Sedimentary Research, 57(5), 928-937, 1987.

Medeiros, F., Ozkan, E., Kazemi, H., Productivity and Drainage Area of Fractured Horizontal Wells in Tight Gas Reservoirs, SPE Res Eval & Eng 11 (5): 902-911. SPE-108110-PA, 2008.

Medeiros, F., Kurtoglu, B., Ozkan, E., Kazemi, H., Analysis of Production Data from Hydraulically Fractured Horizontal Wells in Shale Reservoirs, SPE Res Eval & Eng 13 (3): 559-568. SPE-110848-PA, 2010.

Meleshyn, A., Bunnenberg, C., The Gap Between Crystalline and Osmotic Swelling of Na-Montmorillonite: A Monte Calro Study, Journal of Chemical Physics 2005;122:034705.

Meng, M., Ge, H., Ji, W., Shen, Y., Su, S., Monitor the process of shale spontaneous imbibition in Co-Current and counter-current displacing gas by using low field nuclear magnetic resonance method. Part 1, Journal of Natural Gas Science and Engineering 27, 336-345. 2015, http://dx.doi.org/10.1016/j.jngse.2015.08.069.

Milner, M., McLin, R., Petriello, J., Imaging Texture and Porosity in Mudstones and Shales: Comparison of Secondary and Ion-Milled backscatter SEM Methods, CSUG/SPE 138975, Canadian Unconventional Resources and International Petroleum Conference, Calgary, Alberta, Canada 19-21 October, 2010.

Mirchi, V., Saraji, S., Goual, L., Piri, M., Dynamic Interfacial Tension and Wettability of Shale in the Presence of Surfactants at Reservoir Conditions, Fuel 148 (2015) 127–138.

Mlynarczuk, M., Ratajczak, T., SZYdlak, T., Possible Replacing Traditional Rock Porosity Measurement by Rock Image Analysis, Polskie Towarzystwo Mineralogiczne, Prace Specjalne, 27, 37-49, 2005.

Moghaddam, R.N., Jamiolahmady, M., Fluid Transport in Shale Gas Reservoirs: Simultaneous Effects of Stress and Slippage on Matrix Permeability, International Journal of Coal Geology 163 (2016) 87–99, http://dx.doi.org/10.1016/j.coal.2016.06.018.

Mukerjee, P., Korematsu, K., Okawauchi, M., Sugihara, G., Effect of temperature on the electrical conductivity and the thermodynamics of micelle formation of sodium perfluorooctanoate, The Journal of Physical Chemistry, 89(24), 5308-5312, 1985.

Mulkern, M., Asadi, M., McCallum, S., Fracture Extent and Zonal Communication using Chemical Gas Tracer, SPE 138877, SPE Eastern regional Meeting, Morgantown, West Virginia, USA, 12-14 October 2010.

Naraghi, M.E., Javadpour, F., A stochastic permeability model for the shale-gas systems, International Journal of Coal Geology, Volume 140, 15 February 2015, Pages 111–124, https://doi.org/10.1016/j.coal.2015.02.004.

National Research Council, Rock Fractures and Fluid Flow: Contemporary Understanding and Applications, National Academy of Science Press, Washington D.C., ISBN: 0-309-56348-8, 2011.

Nguyen, T., Miska, S., Yu, M., Takach, N., Predicting Dynamic Barite Sag in Newtonian-Oil Based Drilling Fluids in Pipe, Journal of Energy Resources Technology, 133(2), 023102, 2011.

Nelson, P.H., It's A Small World After All - The Pore Throat Size Spectrum, Search and Discovery Article #50218, Adapted from oral presentation at AAPG Annual Convention and Exhibition, Denver, Colorado, June 7-10, 2009.

Ning, X., Fan, J., Holditch, S.A., and Lee, W.J., The Measurement of Matrix and Fracture Properties in Naturally Fractured Cores, SPE-25898, Low Permeability Reservoirs Symposium, Denver, Colorado, 26-28 April 1993.

Osborn, S. G., Vengosh, A., Warner, N. R., Jackson, R. B., Methane contamination of drinking water accompanying gas-well drilling and hydraulic fracturing, Proc. Natl Acad. Sci, USA 108, 8172–8176 (2011).

Pan, L., Xiao, X., Tian, H., Zhou, Q., Chen, J., Li, T., Wei, Q., A Preliminary Study on the Characterization and Controlling Factors of Porosity and Pore Structure of the Permian Shales in Lower Yangtze Region, Eastern China, International Journal of Coal Geology 146 (2015) 68–78, http://dx.doi.org/10.1016/j.coal.2015.05.005.

Papadopoulos, K.D., Kuo, C.C., The van der Waals Interaction Between a Colloid and its Host Pore, Colloids and Surfaces, 46 (1990) 115-125.

Parmar, J., Dehghanpour, H., Kuru, E., Displacement of Water by Gas in Propped Fractures: Combined Effects of Gravity, Surface Tension, and Wettability, Journal of Unconventional Oil and Gas Resources 5 (2014) 10–21.

Peña-Icart, M., Tagle, M. E. V., Alonso-Hernández, C., Hernández, J. R., Behar, M., Alfonso, M. S., P., Comparative study of digestion methods EPA 3050B (HNO3-H2O2-HCl) and ISO 11466.3 (Aqua Regia) for Cu, Ni and Pb contamination assessment in marine sediments, Marine Environmental Research 72 (2011) 60-66.

Peng, C., Crawshaw, J. P., Maitland, G. C., Trusler, J. M., Kinetics of calcite dissolution in CO_2-saturated water at temperatures between (323 and 373) K and pressures up to 13.8 MPa, Chemical Geology, 403, 74-85, 2015, 2015.

Perry, R. H., Green, D. W., Chemical engineerings' handbook, 8th Edition, McGraw-Hill, ISBN: 0-07-142294-3, 2007.

Petrowiki (2016), http://petrowiki.org/Fracturing_fluids_and_additives, (accessed March 04, 2018).

Pittman, E.,D., 1992, Relationship of Porosity and Permeability to Various Parameters Derived from Mercury Injection-Capillary Pressure Curves for Sandstone: AAPG Bulletin, vol. 76, no. 2, p. 191–198.

Poulsen, A. K., Lafond, K. B., Voight, N., Lundgaard, T., Pedersen, L. M., Characterization of Direct Fractures using Real Time Offshore Analysis of Deuterium Tracer Technology, SPE 154878-MS, SPE Europec/EAGE Annual Conference & Exhibition, Copenhagen, Denmark, 4-7 June 2012.

Prammer, M.G., NMR Pore Size Distributions and Permeability at the Well Site, SPE 28368, SPE 69th Annual Technical Conference and Exhibition, New Orleans, LA, USA, 25-28 September 1994.

Quirein, J. A., Grable, J., Cornish, B. E., Stamm, R., Perkins, T., Zannoni, S., Gordy, D., Dennis, S., Brewer, R., Microseismic Fracture Monitoring, SPWLA 47th Annual Logging Symposium, 4-7 June 2006.

Ramirez, J. S., Samaniego F. V., Rivera, J. R., Rodriguez F. G., Tracer Flow in Naturally Fractured Reservoirs, SPE 25900, 4 November 1993.

Ramirez, J. S., Samaniego F. V., Rodriguez F. G., Rivera, J. R., Tracer-Test Interpretation in Naturally Fractured Reservoirs, SPE 28691, SPE International Petroleum Conference and Exhibition, Veracruz, Mexico, October 10-13 1995.

Rao, S., Thyagaraj, T., Raghuveer, R.P., Crystalline and Osmotic Swelling of an Expansive Clay Inundated with Sodium Chloride Solutions, Geotech Geol Eng 2013;31:1399-404.

Reagan, M.T., Moridis, G.J., Keen, N.D., Johnson, J.N., Numerical simulation of the environmental impact of hydraulic fracturing of tight/shale gas reservoirs on near-surface groundwater: Background, base cases, shallow reservoirs, short-term gas, and water transport, Water Resources Research, 51,2543–2573, 2015, doi:10.1002/2014WR016086.

Rezaveisi, M. Javadpour, F., Sepehrnoori, K., Modeling Chromatographic Separation of Produced Gas in Shale Wells, International Journal of Coal Geology 121 (2014) 110–122, http://dx.doi.org/10.1016/j.coal.2013.11.005.

Reynolds, M. M., Munn, D. L., Development update for an emerging shale gas giant field-Horn River Basin, British Columbia, Canada, SPE 130103, SPE Unconventional Gas Conference. Society of Petroleum Engineers, Pittsburgh, Pennsylvania, USA, 23-25 February 2010.

Rimassa, S.M., Howard, P.R., Blow, K.A., Optimizing fracturing fluids from flowback water, SPE Tight Gas Completions Conference, San Antonio, Texas, USA, 15-17 June 2009.

Rivard, C., Lavoie, D., Lefebvre, R., Séjourné, S., Lamontagne, C., Duchesne, M., An Overview of Canadian Shale Gas Production and Environmental Concerns, International Journal of Coal Geology 126 (2014) 64–76, http://dx.doi.org/10.1016/j.coal.2013.12.004.

Rogers, S., Elmo, E., Dunphy, R., Bearinger, D., Understanding Hydraulic Fracture Geometry and Interactions in the Horn River Basin Through DFN and Numerical Modeling, SPE-137488, Canadian Unconventional Resources and International Petroleum Conference, Calgary, Alberta, Canada, 19-21 October 2010.

Roshan, H., Ehsani, S., Marjo, C.E., Andersen, M.S., Acworth, R.I., Mechanisms of Water Adsorption into Partially Saturated Fractured Shales: An Experimental Study, Fuel 159, 628-637, 2015, http://dx.doi.org/10.1016/j.fuel.2015.07.015.

Roshan, H., Sarmadivaleh, M., Iglauer, S., Shale fracture surface area measured by tracking exchangeable cations, Journal of Petroleum Science and Engineering 138 (2016) 97–103, http://dx.doi.org/10.1016/j.petrol.2015.12.005.

Ruiz, I.S., Juliao, T., García, F.S., Marquez, R., Ruiz, B., Porosity Development and the Influence of Pore Size on the CH_4 Adsorption Capacity of a Shale Oil Reservoir (Upper Cretaceous) from Colombia. Role of Solid Bitumen, International Journal of Coal Geology 159 (2016) 1–17, http://dx.doi.org/10.1016/j.coal.2016.03.020.

Saffari, N., Som, A., Green, D.T., Review of Progress in Quantitative Nondestructive Evaluation, pp 905-910, Image Processing Techniques for Improved Porosity Estimation, 1993.

Samandarli, O., Valbuena, E., Ehlig-Economides, C., Production Data Analysis in Unconventional Reservoirs with Rate-Normalized Pressure (RNP): Theory, Methodology, and Applications, SPE-155614, SPE Americas Unconventional Resources Conference, Pittsburgh, Pennsylvania, USA, 5-7 June 2012.

Sanaei A., Jamili, A., Callard, J., Effect of Pore Size Distribution and Connectivity on Phase Behavior and Gas Condensate Production from Unconventional Resources, SPE-168970-MS, SPE Unconventional Resources Conference, Woodland, Texas, USA,1-3 April, 2014.

Santos, H., Diek, A., Roegiers, J. C., & Fontoura, S., Can shale swelling be (easily) controlled?, In ISRM International Symposium-EUROCK 96. International Society for Rock Mechanics, 1996.

Saraji, S., Piri, M., The Representative Sample Size in Shale Oil Rocks and Nano-Scale Characterization of Transport Properties, International Journal of Coal Geology 146 (2015) 42–54, http://dx.doi.org/10.1016/j.coal.2015.04.005.

Schieber, J., Oxidation of detrital pyrite as a cause for Marcasite Formation in marine lag deposits from the Devonian of the eastern US, Deep-Sea Research II 54 (2007) 1312–1326.

Schmitt, M., Fernandes, C.P., Wolf, F.G., Neto, J.A.B.D.C., Rahner, C.P., 2015, Characterization of Brazilian Tight Gas Sandstones Relating Permeability and Angstrom-to Micron-Scale Pore Structures, Journal of Natural Gas Science & Engineering, 27.

Schramm, L.L., The Language of Colloid & Interface Science 1993, ACS Professional Reference Book, ACS: Washington, D.C.

Scott, H., Patey, I.T.M., Byrne, M.T., Return Permeability Measurements - Proceed with Caution, Paper SPE-107812-MS presented at European Formation Damage Conference, Scheveningen, Netherlands (2007), http: //dx.doi.org/10.2118/107812-MS.

Shahrak, A. Z., Pore-scale network modeling of two-and three-phase flow based on thermodynamically consistent threshold capillary pressures, PhD dissertation, University of Wyoming, 2014.

Shahrak, A. Z., Piri, M., Water Control in Carbonate Rocks by Polymer Gel Injection. SPWLA Spring Topical Conference, Skamania Lodge, Stevenson, WA, USA, 2015.

Shahrak, A. Z., Piri, M., Pore-scale Network Modeling of Two- and Three-phase Flow based on Thermodynamically Consistent Threshold Capillary Pressures. Gordon Research Conference - Flow & Transport in Permeable Media, Bates College, Lewiston, Main, USA, 2014.

Shahrak, A. Z., Piri, M., Effects of Thermodynamically Consistent Threshold Capillary Pressures and Composite Menisci on Residual Oil Saturation and Relative Permeability. Gordon Research Conference - Flow & Transport in Permeable Media, Bates College, Lewiston, Main, USA, 2010.

Shahrak, A. Z., Piri, M., Thermodynamically Consistent Threshold Capillary Pressures for Displacements in Mixed-wet Irregular Capillary Tubes. 17th International Conference on Computational Methods in Water Resources (CMWR), San Francisco, California, USA, 2008.

Shahrak, A. Z., Bozorgmehri, R., Ghotbi, S., Taghikhani, V., Design of a Comprehensive Artificial Neural Network in Modeling of the Polymer Solution VLE Using Virtual LLE Calculation, PPEPPD Conference, Hersonissos, Crete, Greece, 2007.

Shaver, S. A., Hower, J. C., Eble, C. F., McLamb E. D., Kuers, K., Trace Element Geochemistry and Surface Water Chemistry of The Bon Air Coal, Franklin County, Cumberland Plateau, Southeast Tennessee, International Journal of Coal Geology 67 (2006) 47–78.

Shook, G. M., Suzuki, A., Use of tracers and temperature to estimate fracture surface area for EGS reservoirs, Geothermics 67 (2017) 40–47, https://doi.org/10.1016/j.geothermics.2016.12.006.

Shrestha, N., Chilkoor, G., Wilder, J., Gadhamshetty, Stone, J. J., Potential water resource impacts of hydraulic fracturing from unconventional oil production in the Bakken shale, Water Research 108 (2017) 1-24, http://dx.doi.org/10.1016/j.watres.2016.11.006.

Sigal, R.F., Pore-Size Distributions for Organic-Shale-Reservoir Rocks from Nuclear—Magnetic-Resonance Spectra Combined with Adsorption Measurements, SPE Journal, http://dx.doi.org/10.2118/174546-PA, 2015.

Sigal, R.F., Akkutlu, Y., Kang, S. M., Diaz-Campos, M., Ambrose, R., The Laboratory Measurement of the Gas-Storage Capacity of Organic Shales, Petrophysics, Vol. 54, NO. 3, 2013, Page 224–235.

Singh, H., A critical review of water uptake by shales, Journal of Natural Gas Science and Engineering, 34, 751-766, 2016.

Smith, L., Mase, C. W., Schwartz, F. W., Estimation of fracture aperture using hydraulic and tracer test, 28th US Symposium on Rock Mechanics / Tucson/29 June- 1 July 1987.

Song, B., Ehlig-Economides, C., Rate-Normalized Pressure Analysis for Determination of Shale Gas Performance, SPE-144031, North American Unconventional Gas Conference, The Woodlands, Texas, 2011.

Soliman, M. Y., East L., Augustine, J., Fracturing Design Aimed at Enhancing Fracture Complexity, SPE EUROPEC/EAGE Annual Conference and Exhibition, Barcelona, Spain, 14-17 June 2010.

Spohr, E., Trokhymchuk, A., Henderson, D., Adsorption of water molecules in slit pores, Journal of Electroanalytical Chemistry 450 (1998) 281–287.

Stabile, T. A., Giocoli, A., Perrone, A., Piscitelli, S., Lapenna, V., Fluid injection induced seismicity reveals a NE dipping fault in the southeastern sector of the High Agri Valley (southern

Italy). Geophysical Research Letter, 2014, Vol. 41, Issue 16, 5847-5854, DOI: 10.1002/2014GL060948.

Steiger, R.P., Leung, P.K., Quantitative Determination of the Mechanical Properties of Shales, SPE Drilling Engineering, September 1992.

Subramani, A., Jacangelo, J. G., Emerging desalination technologies for water treatment: A critical review, Water Research 75 (2015) 164-187.

Sujka, M., Sokolowska, Z., Hajnos, M., Wlodarczyk-Stasiak, M., Characterization of Pore Structure of Rice Grits Extrudates using Mercury Intrusion Porosimetry, Nitrogen Adsorption and Water Vapour Desorption Methods, Journal of Food Engineering 190 (2016) 147-153.

Suliman, B., Meek, R., Hull, R., Bello, H., Portis, D., Richmond, P., Variable stimulated reservoir volume (SRV) simulation: Eagle Ford shale case study, Unconventional Resources Conference, Woodland, Texas, USA, 10-12 April, 2013.

Sullivan, R., Woodroof, R., Steinberger-Glaser, A., Fielder, R., Asadi, M., Optimizing fracturing fluid cleanup in the bossier sand using chemical frac tracers and aggressive gel breaker deployment, SPE 90030, SPE Annual Technical Conference and Exhibition, Houston, Texas, 26-29 September, 2004.

Sumner, M. E., Miller., W. P., Cation Exchange Capacity and Exchange Coefficients, In D.L. Sparks (ed.) Methods of Soil Analysis, Part 3, Chemical Methods, Soil Science Society of America, Book series no. 5, 1996.

Sun, L., Tuo, J., Zhang, M., Wu, C., Wang, Z., Zheng, Y., Formation and Development of the Pore Structure in Chang 7 Member Oil-Shale from Ordos Basin During Organic Matter Evolution Induced by Hydrous Pyrolysis, Fuel 158 (2015) 549–557, http://dx.doi.org/10.1016/j.fuel.2015.05.061.

Sun, M., Lowry, G.V., Gregory, K.B., Selective oxidation of bromide in wastewater brines from hydraulic fracturing, water research 47 (2013) 3723-3731, http://dx.doi.org/10.1016/j.watres.2013.04.041.

Tabrizi, F. F., Sharak, A. Z., Shahrak, A. Z., Thermodynamic analysis of combustion processes and pollutants emission using nonlinear optimization approach, Asia-Pacific Journal of Chemical Engineering, 7(1), 80-85, 2012.

Tafti, T. A., Aminzadeh, F., Characterizing Fracture Network in Shale Reservoir Using Microseismic Data, SPE 153814, SPE Western Regional Meeting, Bakersfield, California, USA, 19-23 March 2012.

Taleghani, A. D., Olsen, J. E., How natural fractures could affect hydraulic-fracture geometry, 167608-PA SPE Journal Paper – 2014.

Tandanand, S., Moisture Adsorption Rate and Strength Degradation of Illinois Shale, 26th US Symposium on Rock Mechanics, Rapid City, SD, 26-28 June 1985.

Tehrani, A., Popplestone, A., Ayansina, T., Barite sag in invert-emulsion drilling fluids, Offshore Mediterranean Conference and Exhibition, Offshore Mediterranean Conference, Ravenna, Italy, March 25-27, 2009.

Terrace, A., Pore Size Measurement, Springer Science & Business Media, 1997.

Tessier, A., Campbell, P. G. C., Bisson, Sequential extraction procedure for the speciation of particulate trace metals, Analytical Chemistry, 51 (7), pp 844–851, 1979.

Thomson, R. L., Bank, T., Roth, E., Granite, E., Resolution of rare earth element interferences in fossil energy by-product samples using sector-field ICP-MS, Fuel 185 (2016) 94-101, http://dx.doi.org/10.1016/j.fuel.2016.07.093.

Treybal, R. E., Mass transfer operations, Third edition, McGraw-Hill Kogakusha, Ltd, 1980.

Tuller, M., Or, D., Dudley, L. M., Adsorption and Capillary Condensation in Porous Media: Liquid Retention and Interfacial Configurations in Angular Pores, Water Resources Research, Vol. 35, NO. 7, Pages 1949–1964, July 1999.

Understanding Tight Oil, Canadian Society for Unconventional Resources, 2012, http://www.csur.com/sites/default/files/Understanding_TightOil_FINAL.pdf, accessed December 12, 2017.

Van der Baan, M., Dalton, D., Dusseault, D., Microseismic Monitoring Developments in Hydraulic Fracture Stimulation, International Conference for Effective and Sustainable Hydraulic Fracturing, http://dx.doi.org/10.5772/56444, 2013.

Van Meerveld, J., Molennar, M.M., Huyghe, J.M., Baaijens, F.P.T., Analytical Solution of Compression, Free Swelling and Electrical Loading of Saturated Charged Porous Media, Transport in Porous Media 50: 111–126, 2003.

Vengosh A. Jackson, R. B., Warner, N., Darrah, T. H., Kondash, A., A critical review of the risks to water resources from unconventional shale gas development and hydraulic fracturing in United States, Environmental Science & Technology, 48, 8384-8348, 2014.

Vidic, R.. Sustainable management of flowback water during hydraulic fracturing of Marcellus shale for natural gas production, University of Pittsburgh, PA (United States), 2015.

Wang, F., Pan, Z., Zhang, S., Impact of chemical osmosis on water leakoff and flowback behavior from hydraulically fractured gas shale, Journal of Petroleum Science and Engineering, 151, 264-274, 2017.

Wang, G., Ju, Y., Yan, Z. Li, Q., Pore Structure Characteristics of Coal-Bearing Shale using Fluid Invasion Methods: A Case Study in the Huainane-Huaibei Coalfield in China, Marine and Petroleum Geology 62 (2015) 1-13, http://dx.doi.org/10.1016/j.marpetgeo.2015.01.001.

Warner, N. R., Jackson, R. B., Darrah, T. H., Osborn, S. G., Down, A., Zhao, K., White, A., Vengosh, A. geochemical evidence for possible natural migration of Marcellus Formation brine to shallow aquifers in Pennsylvania, Proc. Natl. Acad. Sci., U. S. A. 2012, 109 (30), 11961−11966.

Weast R.C., Handbook of Chemistry and Physics, 53rd ed., Chemical Rubber, Cleveland, OH, 1974.

Wei, M., Xiong, Y., Zhang, L., Li, J., Peng, P., The Effect of Sample Particle Size on the Determination of Pore Structure Parameters in Shales, International Journal of Coal Geology 163 (2016) 177-185, http://dx.doi.org/10.1016/j.coal.2016.07.013.

Wellman, T. P., Shapiro, A. M., Hill, M. C., Effects of simplifying fracture network representation on inert chemical migration in fracture-controlled aquifers, Water Resources Research, Vol. 45, W01416, doi:10.1029/2008WR007025, 2009.

Wen, H. Chen, M., Jin, Y., Zhang, Y., Ge, W., Du, J., Zeng, C., Water Activity Characteristics of Deep Brittle Shale from Southwest China, Applied Clay Science 108 (2015) 165–172, http://dx.doi.org/10.1016/j.clay.2015.02.015.

Woodroof, R. A. Jr., Asadi, M., Warren, M.N., Monitoring Fracturing Fluid Flowback And Optimizing Fracturing Fluid Cleanup Using Chemical Frac Tracers, SPE-82221, SPE European Formation Damage Conference, The Hague, Netherlands, 13-14 May 2003.

Wu, K., Li, X., Wang, C., Yu, W., Chen, Z., Model for surface diffusion of adsorbed gas in nanopores of shale gas reservoirs, Industrial & Engineering Chemistry Research, 2015, 54 (12), 3225-3236.

Wu, K., Chen, Z., Li, J., Li, X., Xu, J., Dong, X., Wettability effect on nanoconfined water flow, 3358-3363, PNAS, March 28, 2017, vol. 114, no. 13.

Wu, K., Chen, Z., Li, X., Guo, C., Wei, M., A model for multiple transport mechanisms through nanopores of shale gas reservoirs with real gas effect–adsorption-mechanic coupling, International Journal of Heat and Mass Transfer 93 (2016) 408–426, http://dx.doi.org/10.1016/j.ijheatmasstransfer.2015.10.003.

Xiong, B., Zydney, A.L., Kumar, M., Fouling of microfiltration membranes by flowback and produced waters from the Marcellus shale gas play, Water Research 99 (2016) 162-170, http://dx.doi.org/10.1016/j.watres.2016.04.049.

Xu, M., Binazadeh, M., Zolfaghari, A., Dehghanpour, H., Effects of dissolved oxygen on water imbibition in gas shales, Energy & Fuels, 32(4), 4695-4704, 2018.

Xu, M., Dehghanpour, H., Advances in Understanding Wettability of Gas Shales, dx.doi.org/10.1021/ef500428y, Energy Fuels 2014, 28, 4362−4375.

Xu, Y., Dehghanpour, H., Ezulike, O., Virues, C, Effectiveness and time variation of induced fracture volume: Lessons from water flowback analysis, Fuel 210 (2017) 844–858, http://dx.doi.org/10.1016/j.fuel.2017.08.027.

Xu, Y., Ezulike, O. D., Zolfaghari, A., Dehghanpour, H., Virues, C., Complementary Surveillance Microseismic and Flowback Data Analysis: An approach to evaluate complex fracture networks, Annual Technical Conference and Exhibition. Society of Petroleum Engineers, 2016.

Yang, S., Dehghanpour, H., Binazadeh, M., Dong, P., A molecular dynamics explanation for fast imbibition of oil in organic tight rocks, Fuel 190 (2017) 409–419, http://dx.doi.org/10.1016/j.fuel.2016.10.105.

Yang, L., Ge, H., Shi, X., Cheng, Y., Zhang, K., Chen, H., Shen, Y., Zhang, J., Qu, X., The Effect of Microstructure and Rock Mineralogy on Water Imbibition Characteristics in Tight Reservoirs, Journal of Natural Gas Science and Engineering, 2016, http://dx.doi.org/10.1016/j.jngse.2016.01.002.

Yang, L., Lu, X., Luo, D., New method for inferring the mean pore size of shale using imbibition-diffusion data, 3rd Nordic Rock Mechanics Symposium (NRMS 2017), October 11-12, 2017, Helsinki, Finland, ISBN 978-951-758-622-1.

Yang, Y., Wu, K., Zhang, T., Xue, M., Characterization of the Pore System in an Over-Mature Marine Shale Reservoir: A Case Study of a Successful Shale Gas Well in Southern Sichuan Basin, China, Petroleum 1 (2015) 173-186, http://dx.doi.org/10.1016/j.petlm.2015.07.011.

Yarveicy, H., Haghtalab, A., Effect of amphoteric surfactant on phase behavior of hydrocarbon-electrolyte-water system-an application in enhanced oil recovery. Journal of Dispersion Science and Technology, 39(4), 522-530, 2018.

Yarveicy, H., Javaheri, A., Application of Lauryl Betaine in enhanced oil recovery: A comparative study in micromodel. Petroleum, 2017.

Yarveicy, H., Habibi, A., Pegov, S., Zolfaghari, A., Dehghanpour, H., Enhancing Oil Recovery by Adding Surfactants in Fracturing Water: A Montney Case Study, SPE-189829-MS, SPE Canada Unconventional Resources Conference, Calgary, Alberta, Canada, 13-14 June, 2018.

Yassin, M. R., Habibi, A., Eghbali, S., Zolfaghari, A., Dehghanpour, H., An Experimental Study of Non-equilibrium CO_2-Oil Interactions, SPE-187093-MS, SPE Annual Technical Conference and Exhibition, San Antonio, Texas, USA, 2017.

Yu, W., Sepehrnoori, K., Patzek, T.W., Evaluation of Gas Adsorption in Marcellus Shale, SPE Annual Technical Conference and Exhibition, Amsterdam, Netherland, 27-29 October 2014.

Yu, W., Sepehrnoori, K., Patzek, T.W., Modeling Gas Adsorption in Marcellus Shale with Langmuir and BET Isotherms, 170801-PA-SPE Journal, 2016.

Zhang, J., Chenevert, M.E., Al-Bazali, T., Sharma, M.M., SPE 89831, A new gravimetric-swelling test for evaluating water and ion uptake in shales, SPE Annual Technical Conference and Exhibition, Houston, Texas, USA, 26-29 September, 2004.

Zhou, Z., Abass, H., Li, X., Teklu, T., Experimental Investigation of the Effect of Imbibition on Shale Permeability During Hydraulic Fracturing, Journal of Natural Gas Science and Engineering 29, 413-430, 2016, http://dx.doi.org/10.1016/j.jngse.2016.01.023.

Zhou, W., Banerjee, R., Poe, B., Spath, J., Thambynayagam, M., Semianalytical production simulation of complex hydraulic-fracture networks, 157367-PA SPE Journal Paper, 2014.

Ziemkiewicz, P. F., He, Y. T., Evolution of water chemistry during Marcellus Shale gas development: A case study in West Virginia, Chemosphere 134 (2015) 224–231.

Zolfaghari, A., Ghanbari, E., Dehghanpour, H., Bearinger, D., Fracture Architecture from Flowback Signature: A Model for Salt Concentration Transient, SPE Hydraulic Fracturing Technology Conference, Woodlands, Texas, USA, 2014a.

Zolfaghari, A., Noel, M., Dehghanpour, H., Bearinger, D., Understanding of the Origin of Flowback Salts: A Laboratory and Field Study, SPE-171647-MS, SPE Unconventional Resources Conference Canada, Calgary, Alberta, Canada, 2014b.

Zolfaghari, A., Samimi, A., Mousavi, S.A., Bozarjamehri, R.B., Investigation of Membrane Preparation Condition Effect on the PSD and Porosity of the Membranes Using a Novel Image Processing Technique, Journal of Applied Polymer Science, 2014c, DOI: 10.1002/APP.39899.

Zolfaghari, A., Noel, M., Dehghanpour, H., Bearinger, D., Laboratory and field analysis of flowback water from gas shales, Journal of Unconventional Oil and Gas Resources, Journal of Unconventional Oil and Gas Resources 14 (2016a) 113–127.

Zolfaghari, A., Mousavi, S. A., Bozarjomehri, R. B., Bakhtiari, F., Gas-liquid membrane contactors: Modeling study of non-uniform membrane wetting, Journal of Membrane Science, Volume 555, 1 June 2018, Pages 463-472, https://doi.org/10.1016/j.memsci.2018.03.067.

Zolfaghari, A., Piri, M., Pore-scale network modeling of three-phase flow based on thermodynamically consistent threshold capillary pressures. I. Cusp formation and collapse, Transport in Porous Media, 116(3), 1093-1137, doi: DOI 10.1007/s11242-016-0814-8 (2016a).

Zolfaghari, A., Piri, M., Pore-scale network modeling of three-phase flow based on thermodynamically consistent threshold capillary pressures. II. Results, Transport in Porous Media, 116(3), 1139-1165, doi:10.1007/11242-016-0815-7 (2016b).

Zolfaghari, A., Dehghanpour, H., Holyk, J., Water Sorption Behaviour of Gas Shales: I. Role of Clays, International Journal of Coal Geology 179 (2017a) 130–138, http://dx.doi.org/10.1016/j.coal.2017.05.008.

Zolfaghari, A., Dehghanpour, H., Xu, M., Water Sorption Behaviour of Gas Shales: II. Pore Size Distribution, International Journal of Coal Geology 179 (2017b) 187–195, http://dx.doi.org/10.1016/j.coal.2017.05.009.

Zolfaghari, A., Dehghanpour, H., Bearinger, D., Fracture characterization using flowback salt-concentration transient, SPE Journal, J168598, DOI: 10.2118/168598-PA, 2016b.

Zolfaghari, A., Dehghanpour, H., Pore Size Distribution from Water Adsorption Isotherm, SPE Annual Technical Conference and Exhibition, 15ATCE-RD-3350-SPE, Houston, Texas, USA, 2015a.

Zolfaghari, A., Dehghanpour, H., A Comparative Study of Pore Size Distribution in Gas Shales, SPE-176908-MS, SPE Asia Pacific Unconventional Resources Conference and Exhibition, Brisbane, Australia, 2015b.

Zolfaghari, A., Holyk, J., Tang, Y., Dehghanpour, H., Bearinger, D., Flowback Chemical Analysis: An Interplay of Shale-Water Interactions, SPE-176911-MS, SPE Asia Pacific Unconventional Resources Conference and Exhibition, Brisbane, Australia, 2015a.

Zolfaghari, A., Tang, Y., Holyk, J., Binazadeh, M., Dehghanpour, H., Bearinger, D., Chemical Analysis of Flowback Water and Downhole Gas Shale Samples, SPE-175925-MS, SPE/CSUR Unconventional Resources Conference, Calgary, Alberta, Canada, 2015b.

Zolfaghari, A., Dehghanpour, H., Tang, Y., Holyk, J., Binazadeh, M., Bearinger, D., Advances in Flowback Chemical Analysis of Gas Shales, SPE Annual Technical Conference and Exhibition, 15ATCE-RD-3343-SPE, USA, Houston, Texas, USA, 2015c.

Zolfaghari, A., Tang, Y., He, J., Dehghanpour, H., Bearinger, D., Virues, C., Estimation of Fracture Network Surface Area and Invaded Reservoir Volume using Flowback Water Chemistry: Scale-Up of Experimental Data, SPE-185078-MS, SPE Canada Unconventional Resources Conference, Calgary, Alberta, Canada, 2017c.

Appendices

Appendix A Flowback Salt Analysis

In order to investigate the major flowback salts, the remaining salts after evaporation of the intact flowback samples are analyzed using XRD and SEM-EDS. The qualitative XRD and SEM-EDS results are shown in Figures A-1 and A-2, respectively. According to the XRD and EDS results it is very possible to have Na/K-bearing salts (such as NaCl and KCl). These results are in line with the ICP-MS analysis of the flowback samples (Figure 3-5) showing that the major cations in all of the samples are Na^+ and K^+. The major salts were similar for flowback samples taken at different times. Therefore, the XRD results are only presented for two flowback times in Figure A-1. According to the XRD results, the major salts in the flowback salt samples from Mu are NaCl and KCl. These results are also in agreement with the SEM-EDS elemental maps of salts from Mu; as both Na and K are present in similar areas where Cl occurs. The major salts in the flowback water samples from OP are $CaCO_3$ and NaCl (Figure A-1). According to the SEM-EDS results, Ca has a relatively high concentration. Also, Na and Cl occur in the similar locations. KCl is the major salt in the Ev flowback salts, which complies with the SEX-EDS results presented in Figure A-2. Both Na and Cl are observed in the similar locations.

According to the SEM-EDS results, sulfur is present in all samples. The concentration of SO_4^{2-} in all of the intact flowback water samples were less than 100 mg/l. After the fracturing operations, sulfate can be produced through reaction of pyrite with water in the presence of calcite and dolomite (see Chapter 2). As a reactive divalent anion, sulfate can react with cations with high surface charge density (such as Ca^{2+} and Ba^{2+}) to produce sulfate-bearing salts (such as $BaSO_4$ and $CaSO_4$). These salts are practically insoluble in water at our experimental conditions (Table A-1). However, one must note that, the redox reactions impact the mineral solubility after the fracturing operations. For example, sulfate reduction during the flowback process can increase the solubility of the barium-bearing components (Engle and Rowan, 2014).

Table A-1. Examples of the soluble, weakly-soluble, and insoluble salts. The solubility values are at 20°C and atmospheric pressure (Green and Perry, 2008). The salts are selected based on the results of XRD and SEM-EDS analyzes on the flowback salts presented in Chapter 3.

	Soluble		Weakly-soluble	Insoluble	
Salt	NaCl	KCl	K_2SO_4	$BaSO_4$	$BaCO_3$
Solubility (g/100 g H_2O)	35.89	34	11.11	0.00024	0.0022

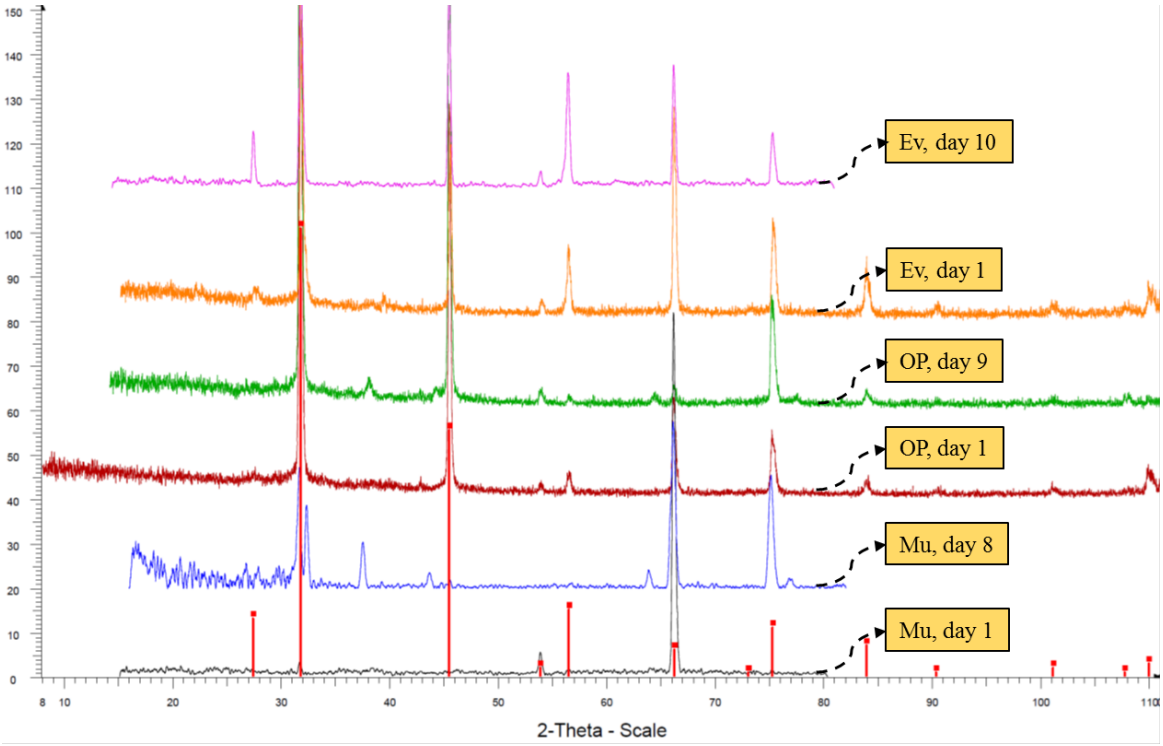

Figure A-1. XRD analysis of the flowback salts at two different flowback times. The results are from days 1 and 8 for the Mu samples, days 1 and 9 for the OP samples, and days 1 and 10 for the Ev samples. The XRD used for characterization of rock mineralogy has a signal-to-noise ratio of 400.

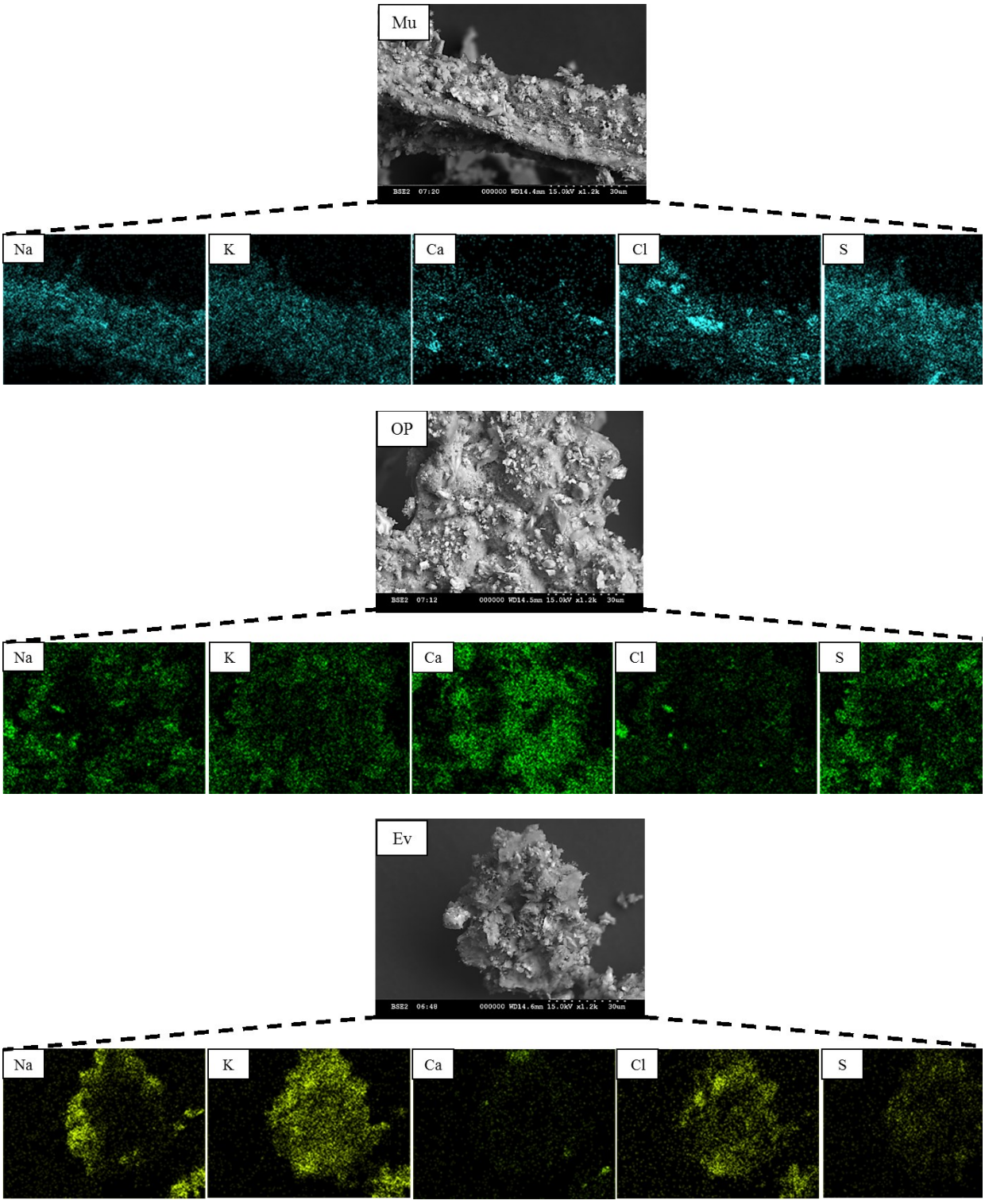

Figure A-2. Elemental maps of the salts obtained from the flowback water samples. The salts obtained from the flowback water samples are from the 8th, 9th, and 10th days of the flowback process for the wells completed in the Mu, OP, and Ev formations, respectively.

Appendix B Calculation of ASD using Fracture-in-Series Method

This section provides a step-by-step procedure to derive Eq. 4-12 which is the PDF for fracture aperture in the fracture in series method (approach 2).

For a connected fracture network, the PDF for ASD is defined as:

$$\int_0^\infty f(W_f)dW_f = 1 \tag{B-1}$$

The fractional number of fractures with width between W_f and $W_f + dW_f$ is $f(W_f)dW_f$. So, the number of fractures with width between W_f and $W_f + dW_f$ is $N_f f(W_f)dW_f$ where N_f is the total number of fractures making up the connected fracture network.

The volume of fractures with aperture size between W_f and $W_f + dW_f$ is given by:

$$dV_f = N_f \times W_f \times A_f \times f(W_f)dW_f \tag{B-2}$$

Where A_f is the half of the lateral area of the fracture with the aperture size of W_f. The total volume of the fractures is obtained by integrating Eq. B-2:

$$V_{f_t} = N_f \int_0^\infty W_f \times A_f \times f(W_f)dW_f \tag{B-3}$$

Considering $\overline{V_f}$ as the average fracture volume results in:

$$\overline{V_f} = \int_0^\infty W_f \times A_f \times f(W_f)dW_f \tag{B-4}$$

Where $\overline{V_f}$ is a constant value, therefore:

$$V_{f_t} = N_f \overline{V_f} \tag{B-5}$$

Considering Eq. 4-4, the corresponding volume of depleted fractures is given by:

$$V_d = N_f \int_{W_f}^{W_{f,max}} W_f \times A_f \times f(W_f) dW_f \tag{B-6}$$

So, normalized water recovery volume, $N_{P,w}$, is calculated by:

$$N_{P,w} = \frac{V_d}{V_{f_t}} = \frac{N_f \int_{W_f}^{W_{f,max}} W_f \times A_f \times f(W_f) dW_f}{N_f \overline{V_f}} = \frac{\int_{W_f}^{W_{f,max}} W_f \times A_f \times f(W_f) dW_f}{\overline{V_f}} \tag{B-7}$$

Rearranging Eq. B-7 results in:

$$\overline{V_f} \times N_{P,w} = \int_{W_f}^{W_{f,max}} W_f \times A_f \times f(W_f) dW_f \tag{B-8}$$

Differentiating Eq. B-8 with respect to W_f leads to:

$$\overline{V_f} \frac{dN_{P,w}}{dW_f} = \frac{d}{dW_f} \int_{W_f}^{W_{f,max}} W_f \times A_f \times f(W_f) dW_f \tag{B-9}$$

Leibnitz's rule for differentiation of definite integrals (Kate et al. 2006) is applied to evaluate the right-hand side of Eq. B-9.

$$\overline{V_f} \frac{dN_{P,w}}{dW_f} = -W_f \times A_f \times f(W_f) \tag{B-10}$$

Differentiating Eq. 4-4 with respect to W_f gives:

$$\frac{dC_f}{dW_f} = \frac{-2DC_m \Delta t / L_m}{W_f^2} \tag{B-11}$$

Dividing Eq. B-11 by Eq. B-10 gives:

$$\frac{dC_f}{dN_{P,w}} = \frac{2DC_m \Delta t \overline{V_f} / L_m}{W_f^3 \times A_f \times f(W_f)} \tag{B-12}$$

The PDF for the ASD can be obtained from Eq. B-12 as:

$$\frac{f(W_f)}{\bar{V}_f} = \frac{2DC_m\Delta t/L_m}{W_f^3 \times A_f\left[\frac{dC_f}{dN_{P,w}}\right]} \tag{B-13}$$

Eq. B-13 can be rewritten in the following alternative form by using Eq. 4-4.

$$\frac{f(W_f)}{\bar{V}_f} = \frac{{C_f}^3 L_m^2}{W_f^2 \times A_f\left[\frac{dC_f}{dN_{P,w}}\right]} \tag{B-14}$$

This equation can be rearranged as:

$$f(W_f) = \frac{{C_f}^3 L_m^2 \bar{V}_f}{(2DC_m\Delta t)^2 \times A_f}\frac{dN_{P,w}}{dC_f} \tag{12}$$

The step-by-step procedure for ASD calculations using the fracture in series method is shown Figure B-1.

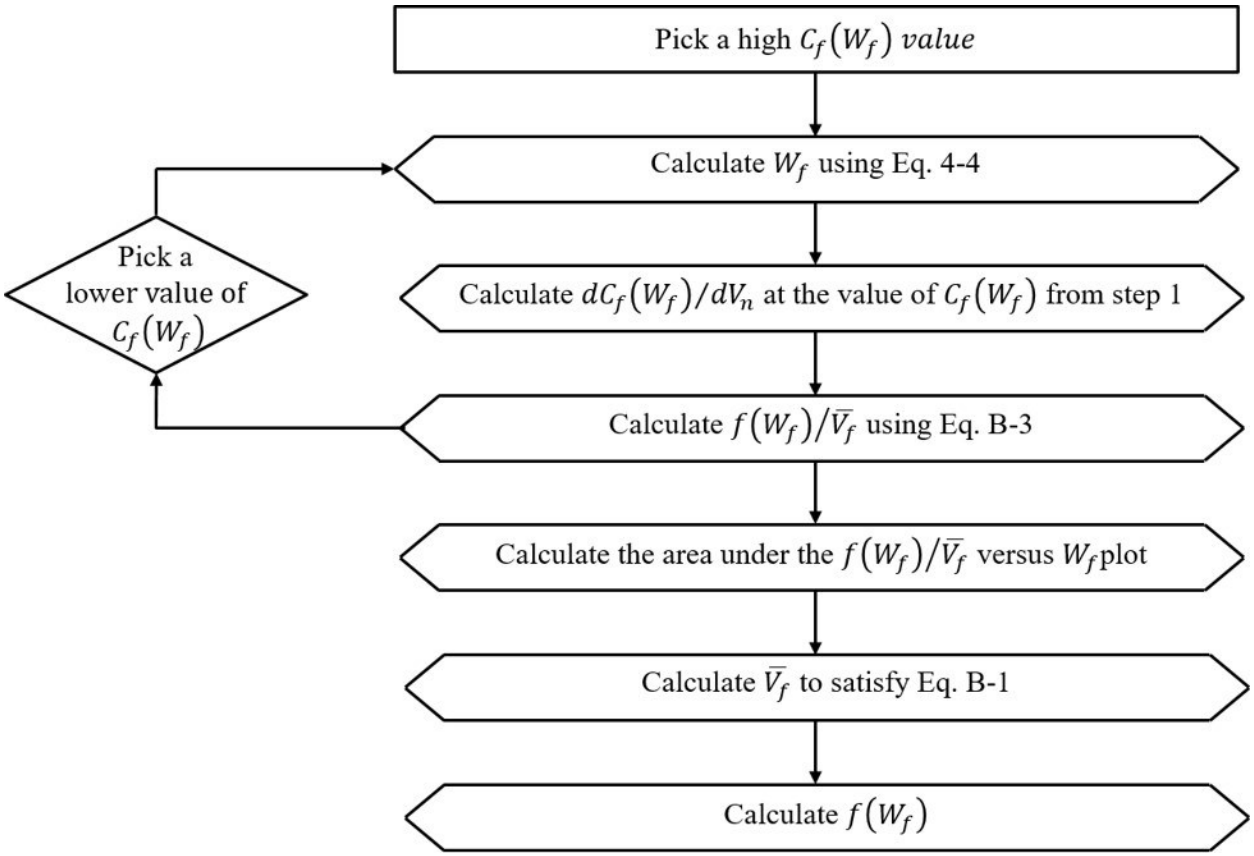

Figure B-1. ASD calculations flowchart using fractures in series method

Appendix C Estimation of IRV using the Ion Concentration Data

This section provides a step-by-step procedure to estimate the invaded reservoir volume (IRV) (shown in Figure C-1) by scaling up the experimental results of ion concentration.

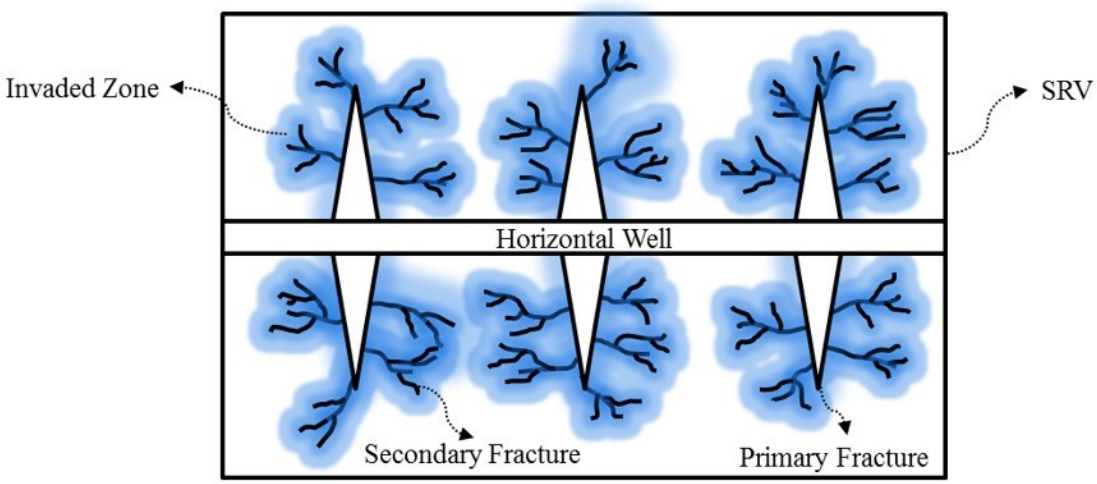

Figure C-1. Schematic illustration of IRV by fracturing fluid. The total volume of reservoir rock invaded by fracturing fluid (the blue color) is the IRV.

It is hypothesized that the TIP is proportional to the rock volume that is available for ion transfer from rock to water. In order to investigate this hypothesis, the ion concentration can be measured during imbibition experiments using samples of different V_s but similar A_s at constant temperature (i.e. isothermal) (schematically illustrated in Figure C-2a). Similar to A_f estimation procedure (presented in Chapter 5), one can calculate $TIP_{Lab,tot}\big|_j$ and $TIP_{Field,tot}$ using Eq. 5-1 and Eq. 5-2, respectively. Then, one can plot $TIP_{Lab,tot}\big|_j$ versus V_s as it is schematically illustrated in Figure C-2b. The value of $TIP_{Field,tot}$ can be placed in the experimentally obtained $TIP_{Lab,tot} - V_s$ relationship to estimate IRV_{T_j} (IRV estimated using experimental data of imbibition at $T = T_j$). The $IRV_{T_j} - T$ relationship can be used to extrapolate the IRV at reservoir temperature $\left(IRV_{T_{Res}}\right)$ (Figure C-2c).

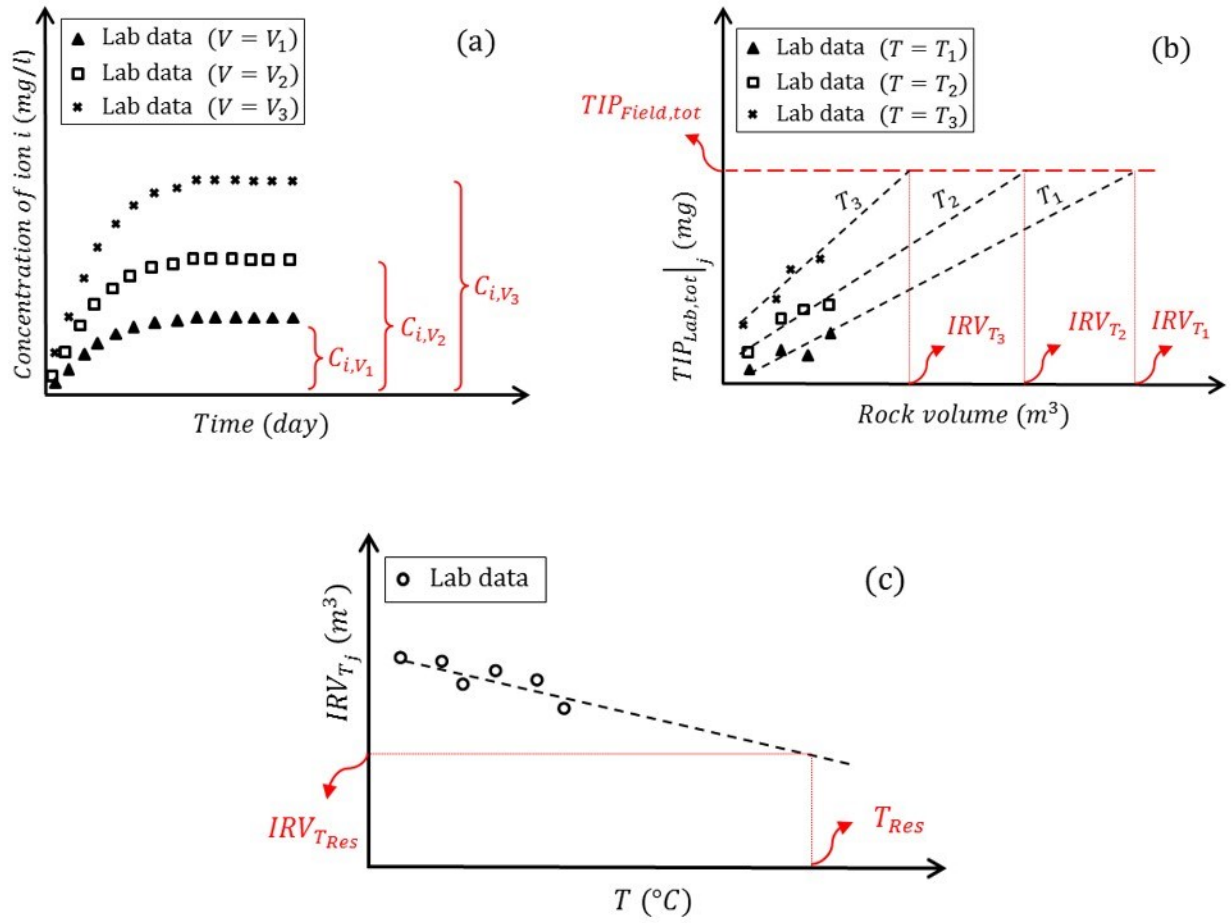

Figure C-2. Schematics of (a) ion concentration versus time during isothermal imbibition experiments using samples of different V_s values ($V_1 < V_2 < V_3$), (b) $TIP_{Lab,tot}|_j$ versus V_s for estimation of IRV_{T_j} ($T_1 < T_2 < T_3$), (c) IRV_{T_j} versus temperature for extrapolation of $IRV_{T_{Res}}$.

The physical properties of samples used in the experiments are presented in Table C-1.

Table C-1. Physical properties of selected OP and Ev shale samples used in the $LTLP$ imbibition experiments at room temperature and atmospheric pressure (23°C and 14.7 psia)

Sample	Mass (g)	$A_s(cm^2)$	$V_s(cm^3)$	$\varphi_{m,ave}$ *(%)*	*Matrix density* (g/cm^3)
Ev-V_1	131.8 ± 0.1	150.2 ± 0.25	52.7 ± 0.05		
Ev-V_2	162.9 ± 0.1	150.3 ± 0.25	65.17 ± 0.05	4.17	2.610
Ev-V_3	296.2 ± 0.1	150.7 ± 0.25	118.47 ± 0.05		
OP-V_1	115.2 ± 0.1	133.2 ± 0.25	46.07 ± 0.05		
OP-V_2	159.7 ± 0.1	127.8 ± 0.25	63.80 ± 0.05	4.29	2.616
OP-V_3	257.9 ± 0.1	134.0 ± 0.25	103.00 ± 0.05		

Figure C-3 shows the experimental results of $TIP_{Lab,tot}\big|_{23°C}$ versus V_s and their corresponding regression lines for the OP and Ev samples. Increasing V_s increases TIP. V_s is the only source for TIP as DI water is used for the imbibition experiments. Thus, samples with larger volume are larger source of ions compared with the samples with smaller volume.

Using the regression lines (shown on Figure C-3a,b) and the measured $TIP_{Field,tot}$ (presentd in Chapter 4), one can estimate the $IRV_{T_{23°C}}$ for OP and Ev wells (Figure C-3c,d). The estimated values of $IRV_{T_{23°C}}$ for the OP and Ev wells are $1.0 \times 10^5 m^3$ and $5.3 \times 10^5 m^3$, respectively.

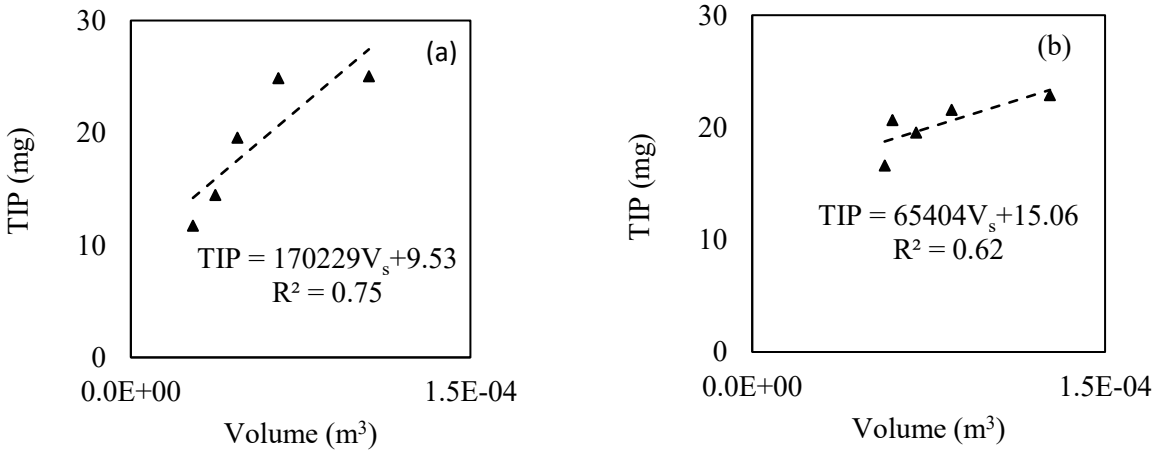

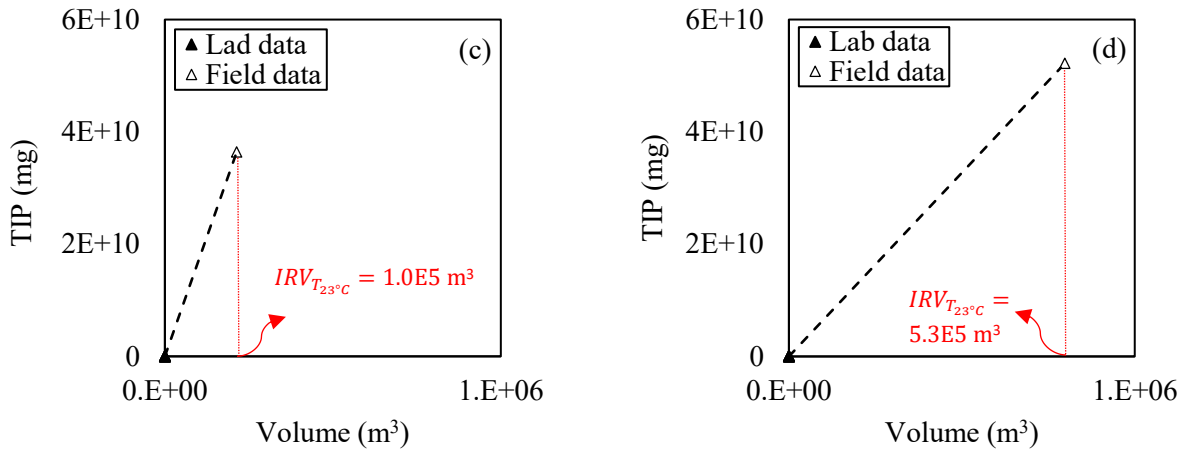

Figure C-3. The experimental results of $TIP_{Lab,tot}\big|_{23°C}$ versus V_s for the (a) OP and (b) Ev samples. The results of estimated $IRV_{T_{23°C}}$ for (c) OP and (d) Ev wells. Field data of $TIP_{Field,tot}$ reported in Chapter 5 are placed in regression equations shown on Figure C-3a,b to estimate $IRV_{T_{23°C}}$ values that are presented in Figure C-3c,d, respectively.

In order to verify the estimated $IRV_{T_{23°C}}$ values, one can estimate the average IRV (IRV_{ave}) using Eq. C-1:

$$IRV_{ave} = \frac{V_{w,m}}{\varphi_{m,ave}} \tag{C-1}$$

Where, $V_{w,m}$ and $\varphi_{m,ave}$ are the volume of water imbibed into the matrix and average matrix porosity, respectively. $V_{w,m}$ can be calculated by

$$V_{w,m} = TIV_{Ave} \times LOP_{ave} \tag{C-2}$$

Where TIV_{Ave} and LOP_{ave} are the average total injected volume and the average leak-off percentage, respectively. Combining Eqs. C-1 and C-2 leads to

$$IRV_{ave} = \frac{TIV_{Ave} \times LOP_{ave}}{\varphi_{m,ave}} \tag{C-3}$$

$\varphi_{m,ave}$ is about 4% for the samples used in the imbibition experiments (Table C-1). Assuming an average value of $5 \times 10^4 m^3$ for TIV_{Ave} and 25% for LOP_{ave} (Xu et al., 2016), the calculated IRV_{ave} will be $3.1 \times 10^5 m^3$. This value has similar order of magnitude compared with

those estimated from the scale-up of the experimental results (Figure C-3c,d). It must be noted that although both of the calculated IRV_{ave} and $IRV_{T_{23°C}}$ have similar orders of magnitude, the presented values of $IRV_{T_{23°C}}$ may not necessarily be accurate. Similar to estimation of A_f, different experimental conditions (such as temperature) can affect the scale-up results of IRV estimation. Furthermore, experiments can be done at $HTHP$ conditions to better represent the downhole conditions.

The estimated $IRV_{T_{23°C}}$ value for Ev is larger than that for OP (Figure C-3). In other words, more rock volume is invaded by fracturing fluid in Ev compared with that in OP. This observation complies with the experimental results of higher water imbibition in the Ev samples compared with that in the OP samples (Figure C-4). Figure C-4 presents the normalized imbibed volume $(V_{imb,n})$ of water versus time for OP and Ev samples of different V_s but similar A_s at room temperature $(T = 23°C)$. The results indicate that Ev samples have higher and faster water uptake than OP samples. Similar observations have been also reported previously (Ghanbari et al., 2013). In other words, higher tendency of water for the Ev samples (Figure C-4) results in larger IRV and lower water recovery compared with those of OP. These results are also in agreement with field observations of higher leak-off rate and lower water recovery from Ev compared to the lower leak-off rate and higher water recovery from OP (see Chapter 4).

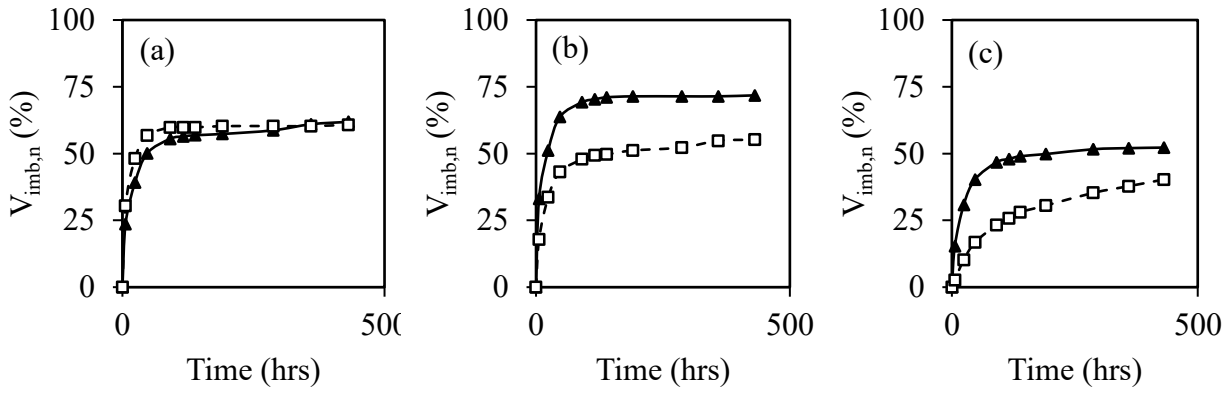

Figure C-4. Comparison between the normalized imbibed volume $(V_{imb,n})$ of water versus time for (a) OP-V_1 and Ev-V_1, (b) OP-V_2 and Ev-V_2, and (c) OP-V_3 and Ev-V_3 samples. Physical specifications of the samples are provided in Table C-1. $V_{imb,n}$ is the ratio of imbibed volume of water to the total pore volume of rock samples. Solid and dashed lines belong to Ev and OP

samples respectively. The scale used for measuring the mass of the rock samples during the imbibition experiments has an accuracy of ± 0.01 g.